Title

A STUDY OP THE INTERNAL CONVERSION ELECTRONS EMITTED WITHIN THREE NANOSECONDS AFTER THE SPONTANEOUS FISSION OF 252Cf

Author

Watson, Rand Lewis.

Publication Date

1966-07-01

UCRL-16798

(corrected)

University of California
Ernest O. Lawrence Radiation Laboratory

A STUDY OF THE INTERNAL CONVERSION ELECTRONS EMITTED WITHIN THREE NANOSECONDS AFTER THE SPONTANEOUS FISSION OF ^{252}Cf

Berkeley, California

DISCLAIMER

UNIVERSITY OF CALIFORNIA
Lawrence Radiation Laboratory
Berkeley, California

September 26, 1966

ERRATUM

TO: All recipients of UCRL-16798

FROM: Technical Information Division

Subject: UCRL-16798, "A Study of the Internal Conversion Electrons Emitted Within Three Nanoseconds after the Spontaneous Fission of ^{252}Cf" by Rand Lewis Watson, (Ph. D. Thesis), July 1966.

done

Please replace pages 31 and 32 with the attached sheet.

Please note the corrected figure (Fig. II-11).

UCRL-16798

UNIVERSITY OF CALIFORNIA

Lawrence Radiation Laboratory
Berkeley, California

AEC Contract No. W-7405-eng-48

A STUDY OF THE INTERNAL CONVERSION ELECTRONS EMITTED WITHIN THREE NANOSECONDS AFTER THE SPONTANEOUS FISSION OF ^{252}Cf

Rand Lewis Watson

(Ph.D. Thesis)

July 1966

A STUDY OF THE INTERNAL CONVERSION ELECTRONS EMITTED WITHIN THREE NANOSECONDS AFTER THE SPONTANEOUS FISSION OF ^{252}Cf

Contents

Abstract v

I. Introduction 1

II. Experimental Apparatus 10

A. Electronic System 11

B. Detectors 18

1. Electron Detector 18

2. Fission Fragment Detectors 20

C. Magnetic Steering Mechanism 23

1. The Motion of a Charged Particle in a Magnetic Field with Rotational Symmetry and Radial Dependence $1/r^n$ 23

2. Operation and Design 29

III. Experimental Methods 42

A. Experimental Procedures 42

1. Source Preparation 42

2. Energy and Efficiency Calibration 43

B. Experimental Effects 45

C. Data Processing 51

D. Mass Calculation 55

IV. Interpretation and Discussion of Results 66

A. The Electron Energy Spectra 66

1. The Gross Spectra 66

2. The Mass Sorted Spectra 69

3. Correlation with γ-ray Measurements 80

B. Analysis of the Electron Spectra 86
1. Determination of the Electron Peak Characteristics 86
2. Determination of the Electron Transition Characteristics 90
C. Discussion 103
V. Binding Energy Calculations of Highly Ionized Atoms . . . 109
A. Estimation of Fission Fragment Ionic Charges 111
B. The Hartree Fock S.C.F. Method 114
C. Results of Calculations 117
VI. Conclusions 131
Acknowledgements 133
VII. Appendices 134
A. The Motion of a Charged Particle in an Inhomogeneous Magnetic Field 134
B. Kinematic Relations for Electrons Emitted from Moving Fission Fragments 138
C. Hartree-Fock Theory 146
D. Experimental Conversion Electron Spectra 155
References 189

A STUDY OF THE INTERNAL CONVERSION ELECTRONS EMITTED WITHIN THREE NANOSECONDS AFTER THE SPONTANEOUS FISSION OF ^{252}Cf

Rand Lewis Watson

Lawrence Radiation Laboratory
University of California
Berkeley, California

July 1966

ABSTRACT

The spectra of internal conversion electrons of energies between 10 and 650 keV emitted in coincidence with the spontaneous fission of ^{252}Cf were measured and correlated to fragments of specific masses. A magnetic steering device was used to guide the electrons to a lithium-drifted silicon electron detector shielded against interference from fission fragments, alpha particles, gamma rays and x-rays. This device also made possible the measurement of the electron spectra in the specific time intervals of approximately 0 to 0.9, 0.1 to 1.7 and 1.1 to 2.9 nsecs after fission.

The measured spectra showed well-defined structure and were analyzed by means of a least-squares peak-fitting procedure. Many of the lines were identified as K and L conversion line pairs, thus facilitating multipolarity assignments on the basis of K-to-L ratios. Estimates of intensities and half-lives are also given for a large number of the electron lines. By correlating the electron spectra with the gamma-ray measurements of Bowman, it was possible to assign many of the electron lines to specific isotopes.

Several of the analyzed electron peaks were suggested as specific examples of possible 2+ to 0+ transitions in even-even nuclides. Two transitions thought to be associated with ^{110}Ru displayed energies and multipolarities that strongly suggest a region of stable deformation near mass 110.

Binding energy calculations were carried out employing a non-relativistic Hartree-Fock computer program developed by Roothaan. The K and L binding energies of Sr, Pd, Xe and Sm were calculated as a function of ionic charge ranging from the neutral atom to the fully ionized ion. It was found that the K and L binding energies are both increased over the neutral atomic values by approximately 0.9 keV for the most probable ionic charges of the fission fragments, and consequently that the K x-ray energies are almost unaffected.

I. INTRODUCTION

The fission process has long been utilized as a means of producing neutron-excess isotopes for the purpose of investigating their radioactive decay schemes. Most of the nuclear spectroscopic information which has evolved as a result of studies of fission product nuclides, however, pertains almost exclusively to those isotopes whose beta decay halflives are long enough for the application of chemical separation techniques, while very little detailed information has been obtained concerning the radiation emitted by the extremely short lived primary fission products.

Recently, advances in the technology of electronics and solid-state physics have led to the development of reliable multidimensional pulse-height analysis equipment, extremely low-noise pulse-preamplification devices, and to possibly the most important breakthrough yet in the problem of radiation detection--the development of high resolution semiconductor detectors. This timely state of affairs has brought about, for the first time, the possibility of examining the radiation energy spectra for fragments of specific masses by enabling the simultaneous measurement of the fission fragment and radiation energies with precision sufficient to identify individual nuclear transitions and the fragment masses from which they originate.

The consequences of these remarkable developments are numerous. It means, for example, that the methods of nuclear spectroscopy, previously limited to the regions of nuclides where fast chemistry and other separation techniques could be applied, may now be extended to a region of neutron-excess nuclides whose short halflives had, in the past, placed them entirely out of reach. It provides a method whereby information concerning the spins and de-excitation processes of primary fission fragments may be obtained. Moreover, it means that it is now possible to study the properties of individual fission fragments as identified by their characteristic radiations, rather than studying the average properties of fragment distributions.

The present studies were undertaken upon the successful demonstration by Bowman, Thompson and Rasmussen[1] of the capability of reducing the previously observed continuous gamma ray spectrum from ^{252}Cf fission fragments into spectra displaying discretely resolved structure when sorted with respect to fragment mass. Employing the simultaneous measurement of coincident fission fragment and electron energies by means of semiconductor detectors, a comprehensive investigation of the internal conversion electrons emitted within approximately 3 nsec after fission in association with the various gamma transitions observed by Bowman, et al.[1] has been carried out and is reported herein. Now, as a result of the present work, it has been possible to assign many of these observed gamma transitions to specific isotopes as well as to deduce certain information relating to conversion coefficients, multipolarities and life-times.

These studies have utilized ^{252}Cf as the fission source. The reason for this choice was that ^{252}Cf undergoes substantial spontaneous fission branching and hence the need for a reactor, along with the various experimental difficulties inherent with its use in an experiment of this type, is alleviated. The regions of nuclides constituting the heavy and light fission products of ^{252}Cf are roughly outlined on the section of the chart of the nuclides presented in Fig. I-1. The regions of interest in the present work are centered along the two dark lines delineating the most probable fission product isotopes as a function of mass.[2] As may be seen, the nuclei dealt with in these experiments are considerably removed from normally occurring stable nuclei and are generally not accessible in nuclear reactions. It is, therefore, one of the primary purposes of this research to obtain information relating to the nuclear level structure of nuclides in these regions.

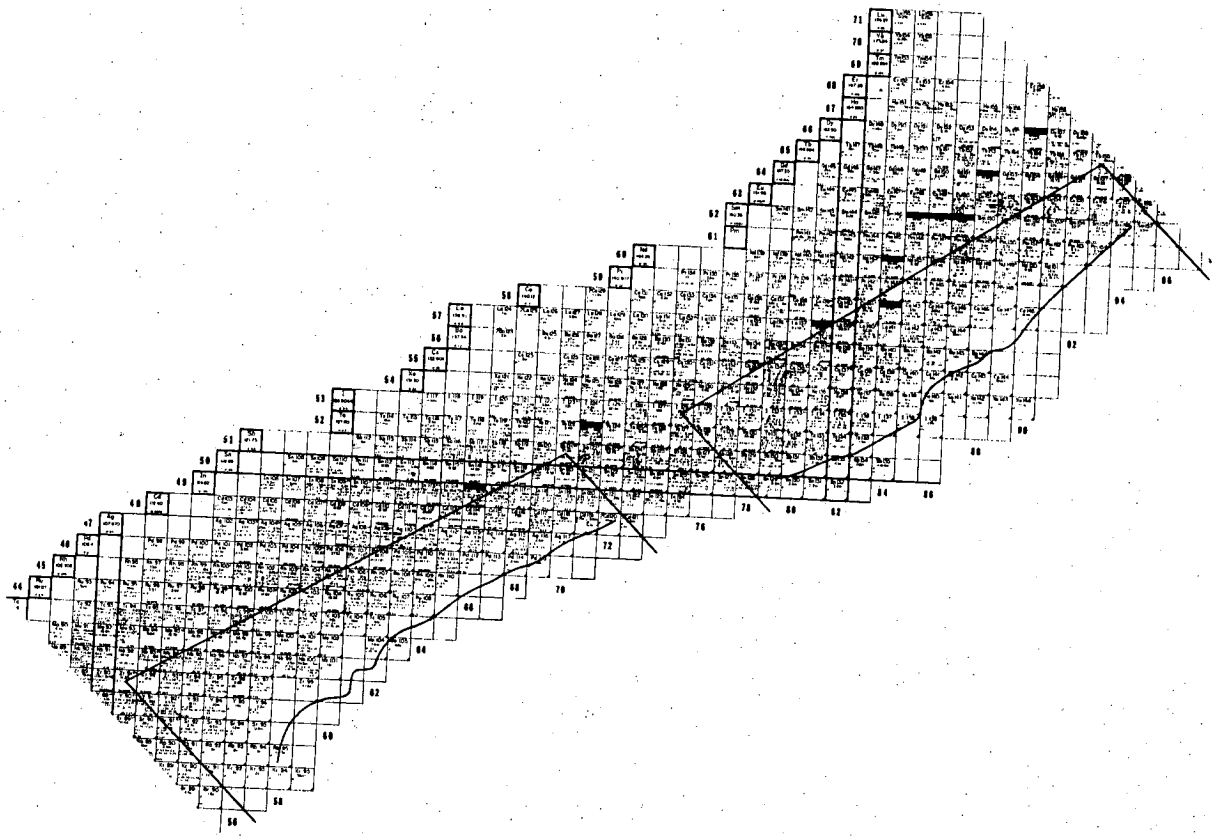

Fig. I-1. Outline of nuclides formed in the spontaneous fission of ^{252}Cf. The most probable primary fission product isotopes are indicated by the two dark lines spanning the delineated regions of heavy and light fission products.

The chronology of events in the spontaneous fission of ^{252}Cf leading up to and occurring after the emission of prompt gamma rays and internal conversion electrons is depicted in Fig. I-2 and a typical example of the resultant distribution of energy in the process is illustrated in Fig. I-3. As the fission barrier is penetrated, the nucleus distorts until it ruptures at the scission point. The two resulting fragments, each having on the average approximately 15 MeV of internal excitation, are then accelerated to relatively large kinetic energies by the Coulomb field of these positively charged nuclei. Promptly thereafter, approximately 10 MeV of internal excitation is lost by each fragment through the emission of neutrons. At this point, the fragments are still left with on the order of 4 to 5 MeV of internal excitation and begin to further de-excite by the emission of gamma rays and their associated internal conversion electrons. Subsequently, the fragments reach stability after a series of beta decays.

Although it has not been possible, in the past, to investigate gamma radiation from fission in great detail, the gross characteristics of this subject have been fairly well established. For example, the shape of the total energy spectrum for both ^{235}U and ^{252}Cf has been measured by a number of experimenters and the results of several such studies are compared in Fig. I-4 taken from the work of Smith, Fields and Friedman.[3] Fission gamma-ray energy release as a function of time has been another popular area of investigation, the results of which are summarized in Fig. I-5 taken from a review of the subject by Maienschein.[4] The observance of an unexpectedly high amount of energy release in the form of gamma-ray emission (8 to 9 MeV per fission) along with a multiplicity of approximately 9 to 10 gamma rays per fission by Smith et al.,[3] Bowman and Thompson[5] and others has led to the conclusion that the process of gamma emission in fission is characterized by cascades from relatively high-spin states. By comparison with the low-spin, low-

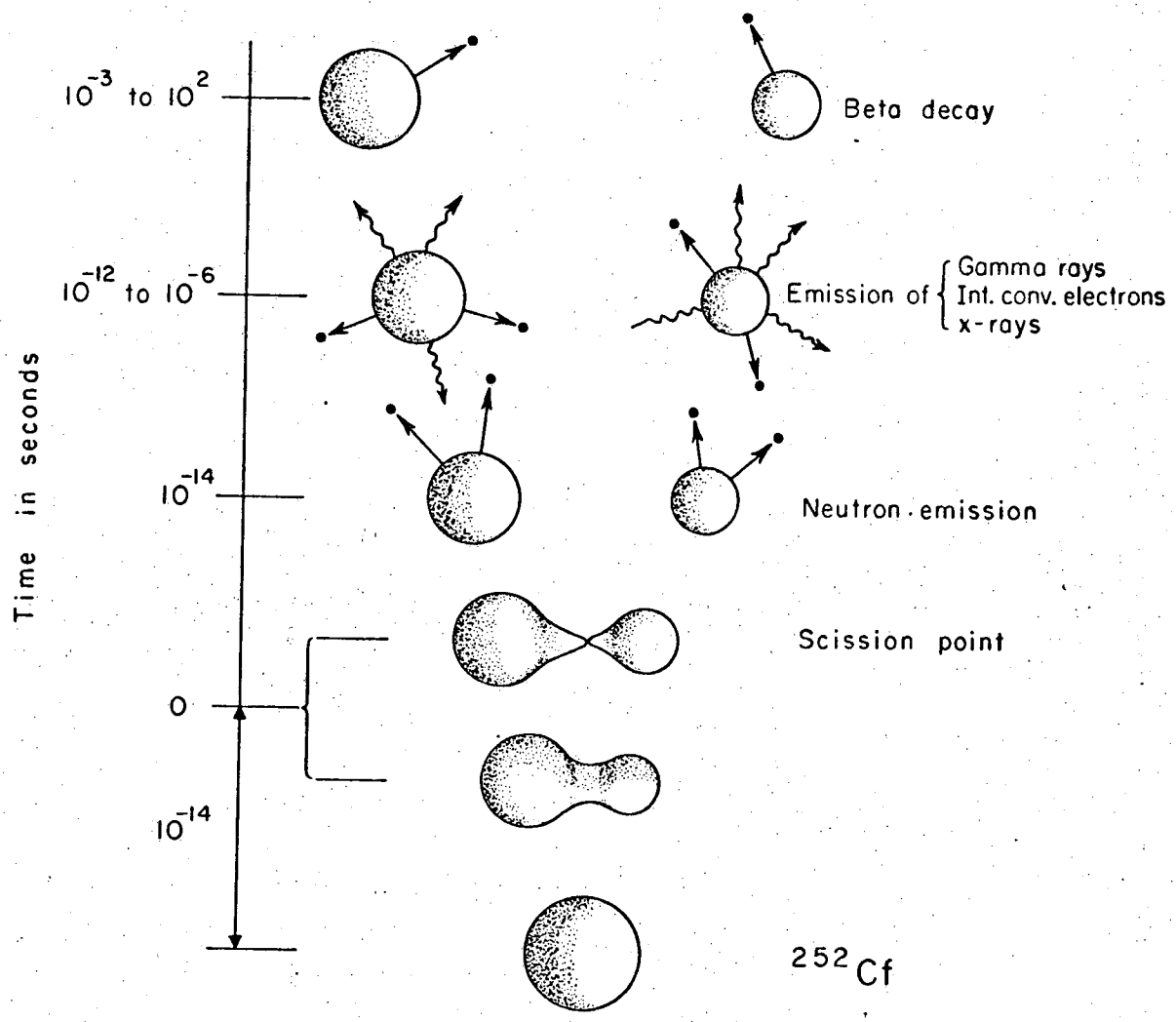

MUB-9746

Fig. I-2. Schematic time sequence of a ^{252}Cf nucleus undergoing spontaneous fission.

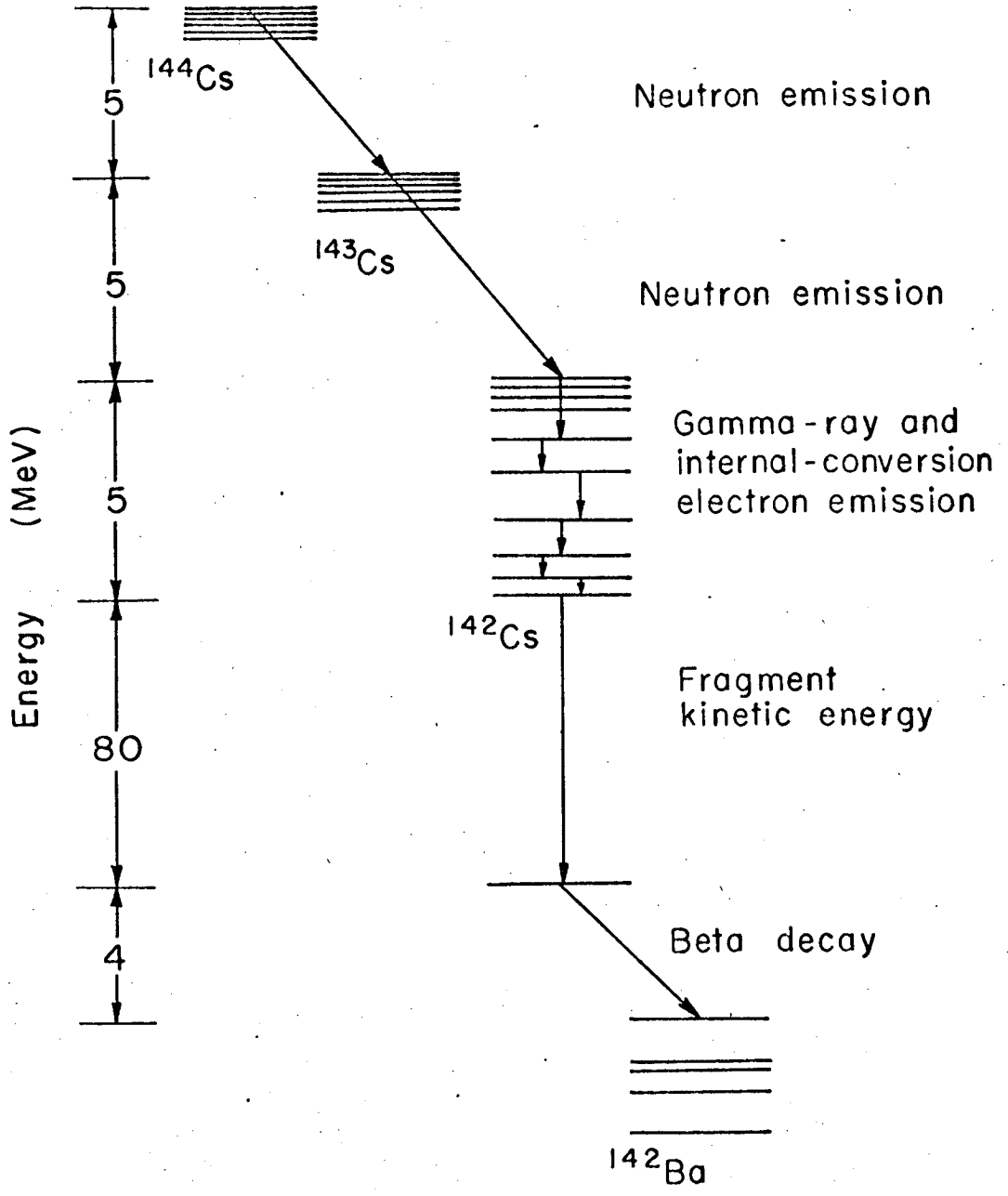

MUB-10558

Fig. I-3. An example of the distribution of the energy imparted to the heavy fragment in the spontaneous fission of a ^{252}Cf nucleus.

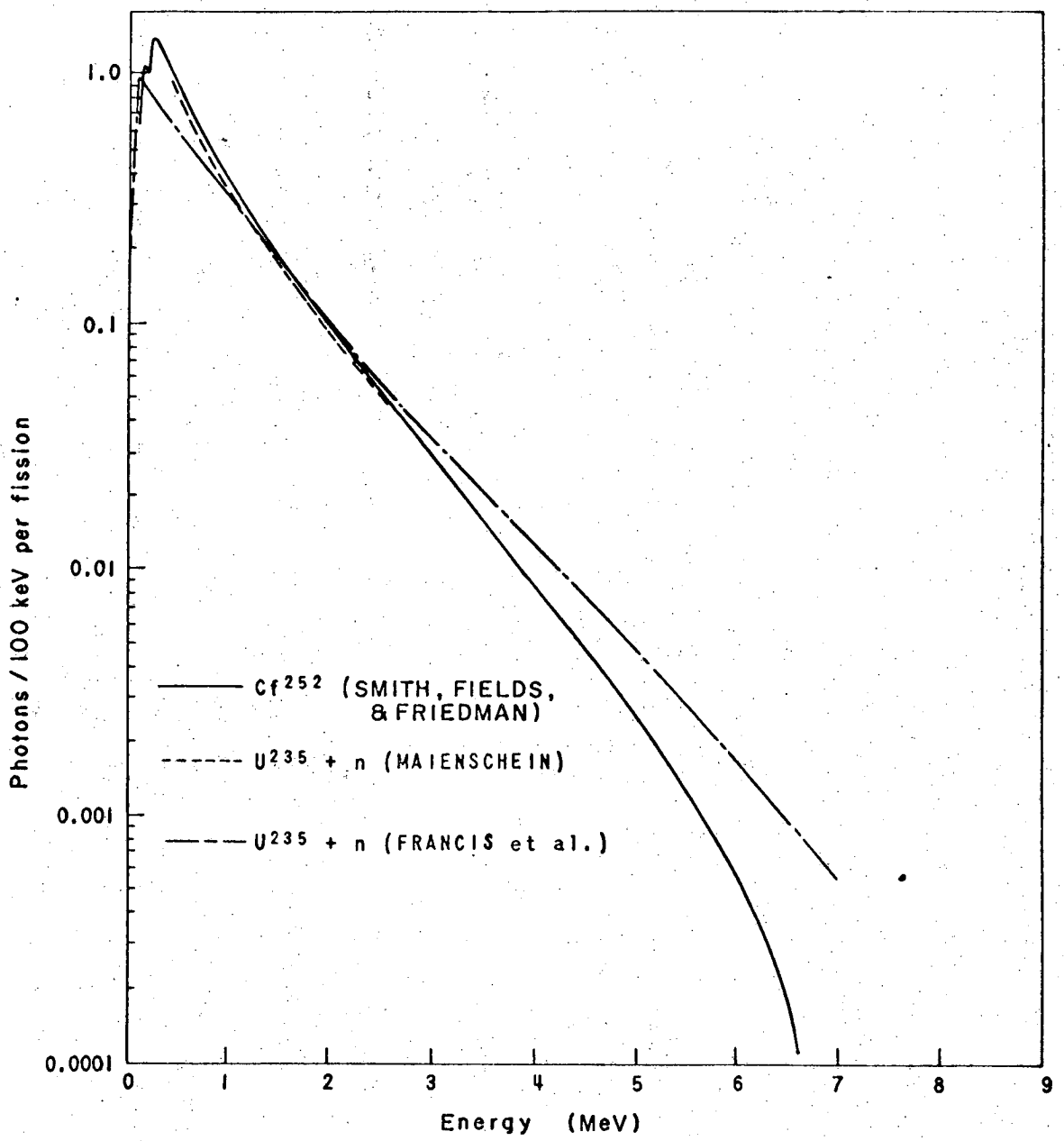

Fig. I-4. A comparison of the total gamma-ray energy spectra in coincidence with the fission of ^{252}Cf and ^{235}U taken from the work of Smith, Fields and Friedman.[3]

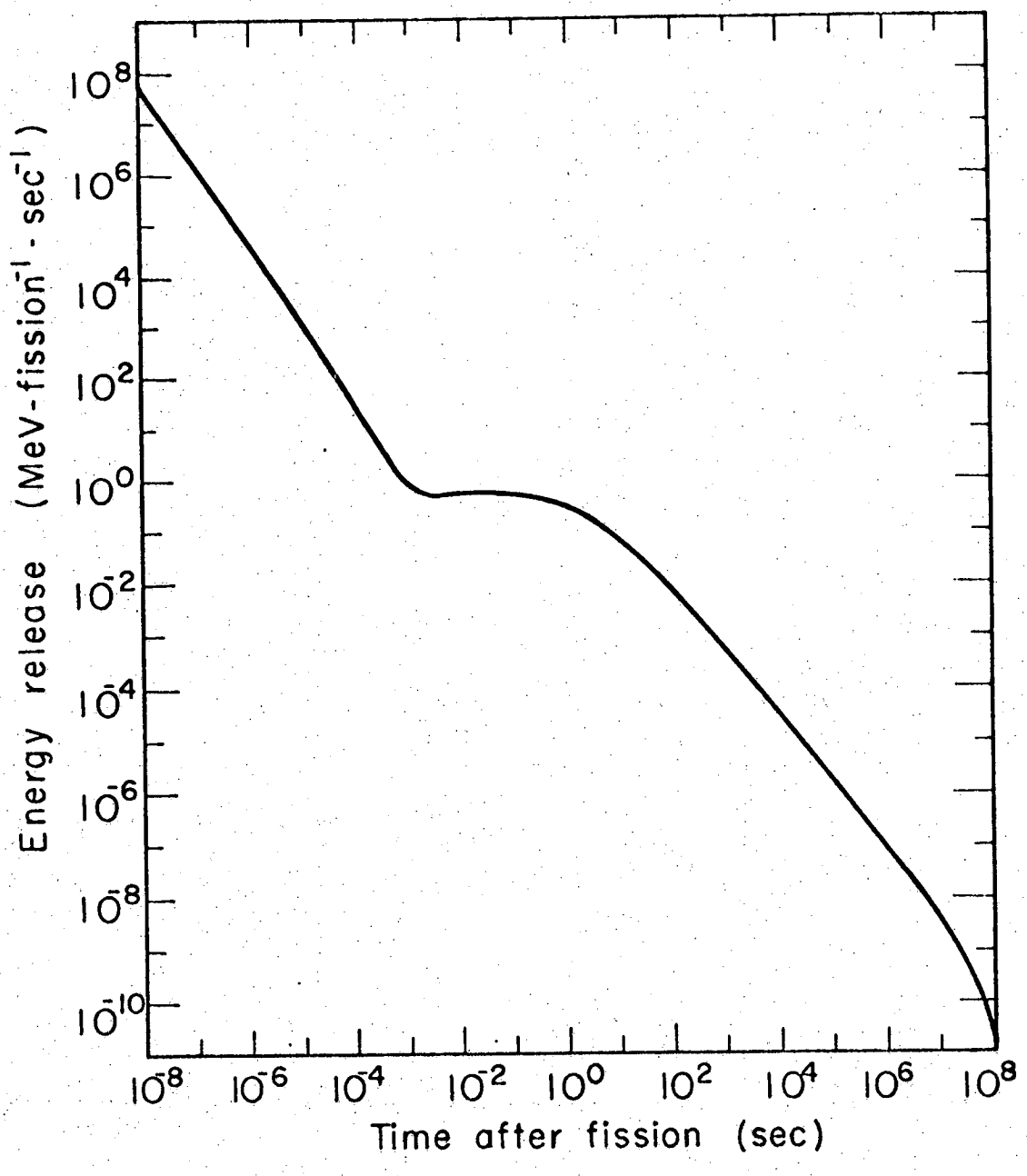

MUB-10565

Fig. I-5. Fission gamma-ray energy release as a function of time taken from Maienschein.[4]

multiplicity, high-average-energy de-excitation characteristics of neutron capture reactions and the high-spin, high-multiplicity, low-average-energy de-excitation characteristics of heavy-ion reactions, fission gamma de-excitation displays the properties of an intermediate reaction type. This fact, coupled with some speculation about the average gamma ray multipolarities in fission, has led to estimates of initial fragment spins on the order of 8 to 10 $\hbar$.[6]

Several puzzling questions have evolved from the limited information on prompt fission gamma radiation brought forward by studies such as those mentioned above. One fact which cannot be reconciled by past assumptions about the distribution of energy in fission is the magnitude of the total fragment excitation energy taken away by gamma emission. The usual assumption that neutron emission will occur much too rapidly for effective competition from gamma emission as long as the fragment retains sufficient energy to emit a neutron leads to the expectation of only 4 to 5 MeV of excitation left for gamma emission. Experimentally, however, approximately twice this amount is observed. The gamma multiplicity also poses certain theoretical problems. It is apparent, therefore, that the ability to investigate in detail the properties of prompt gamma ray and conversion electron emission from individual fission fragment isotopes would be of great value not only for investigations dealing with radioactive decay schemes but also for the further study of the various processes which give rise to the above anomalies.

II. EXPERIMENTAL APPARATUS

Experiments dealing with the measurement of the energy spectra of internal conversion electrons emitted from fission fragments of selected mass are fundamentally limited both by the energy resolution of the electron spectrometer and by the accuracy of the method used to ascertain the fragment masses. With the advent of semiconductor detectors and their inherently good resolution characteristics as well as their suitability for use with coincidence techniques, it has been possible, for the first time, to carry out experiments with sufficiently improved energy and mass resolution so as to enable a detailed study of the de-excitation characteristics of very short lived fission fragment isotopes.

The complexity of this type of experiment stems from the fact that not only must the energies of electrons and fission fragments evolving from the same fission events be individually measured and recorded, but also the event-by-event correlation between the electrons and fission fragments must be maintained. The fulfillment of these conditions necessitate the use of a rather elaborate electronic system. Furthermore, the precise measurement of electron energies requires the elimination of any window for the electrons to penetrate that would seriously degrade the experimental energy resolution. In the present experiments, this restriction necessitated that the electron detector be located inside the fission chamber, imposing the further complication of devising a means of shielding the detector from interference by fission fragments, alpha particles, x-rays and gamma rays. Conventional methods of shielding, such as placing the detector behind a lead collimator with a view of only a small portion of the fragment flight path, result in such a low detection geometry as to make any detailed study impractical. The problem was resolved, by employing a magnetic steering device to guide the electrons around a 90° arc, away from the

fission source region, to a shielded detector. In the sections which follow, the electronic system, detectors, and magnetic steering mechanism are discussed in detail.

A. Electronic System

In carrying out the conversion electron experiments, it was necessary to incorporate various electronic components into a system which would permit the following:

(a) The detection of coincidences between the fragment pairs and the emitted electrons;

(b) The measurement of fragment and electron energies for those events where a triple coincidence was detected;

(c) The assimilation of the energy measurements individually but in such a way that their coincidence correlation was retained;

(d) The optimization of energy and time resolution;

(e) The maintainance of electronic gain stability over long periods of time.

A simplified block diagram of the electronic arrangement used is shown in Fig. II-1.

Pulses from the fission fragment detectors were amplified by standard low-noise preamplifiers while those from the electron detector were sent to a specially designed preamplifier incorporating a field-effect transistor in the input stage. The details of this preamplifier are given by Elad.[7] The signals were then routed to transistorized linear amplifier systems via variable gain amplifiers.

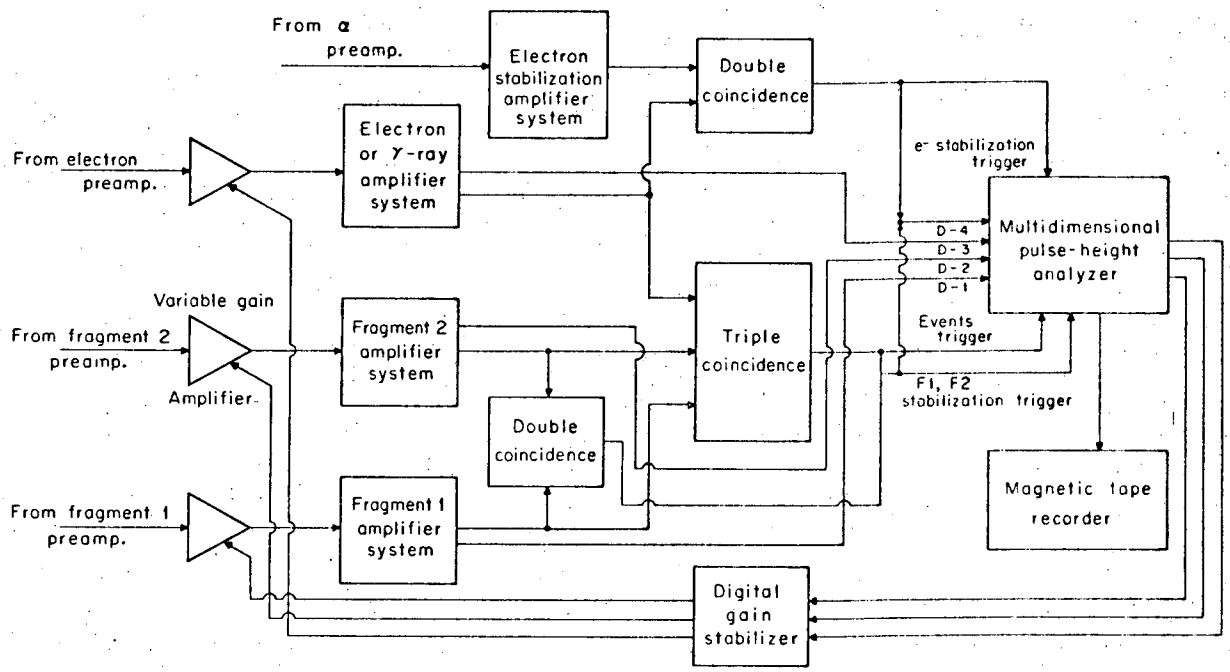

Fig. II-1. A simplified block diagram of the electronic system.

Zero crossover signals were generated in each amplifier and sent to a triple coincidence unit where it was required that an electron had to be detected within the time interval of 18 nsec after fission to 180 nsec after fission in order to generate a gating signal. (The large resolving time for electrons was needed because of the lengthy flight time required for the detection of low energy electrons in the magnetic steering device). The fission fragment zero crossover signals were further subjected to a fast double coincidence requirement having a 50 nsec resolving time. The triple coincidence accidental rate was always less than 3% of the total triple coincidence rate. Whenever an event occurred in which the triple and double coincidence requirements were satisfied, a gating signal was fed to the multidimensional pulse-height analyzer, which in turn analyzed serially the pulse-heights from the various amplifier systems. This information was stored in the analyzer memory even by event, so that the order of the detector pulses was maintained. Each time the analyzer memory became full, the output was written on magnetic tape. A picture of the various electronic components is given in Fig. II-2 and the multidimensional analyzer is pictured in Fig. II-3.

To avoid any possible gain shifts that would alter the detector energy calibrations during the long operation periods, a digital-gain stabilizer unit of the type described by Nakamura and La Pierre[8] was incorporated into the electronic system. This unit continuously monitored distributions of selected events from each detector and maintained the first moments of these distributions in prescribed positions by feeding back to the variable gain amplifiers preceding the

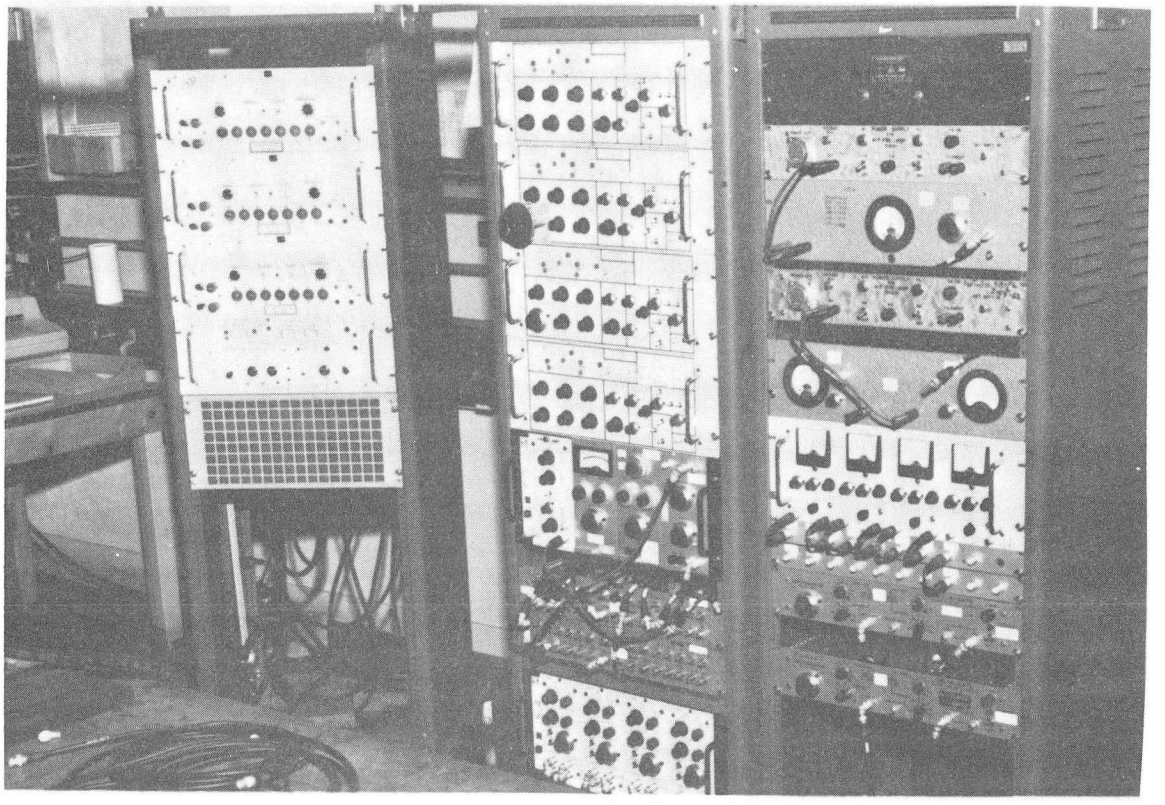

ZN-5645

Fig. II-2. A photograph of the electronic components comprising the electronic system.

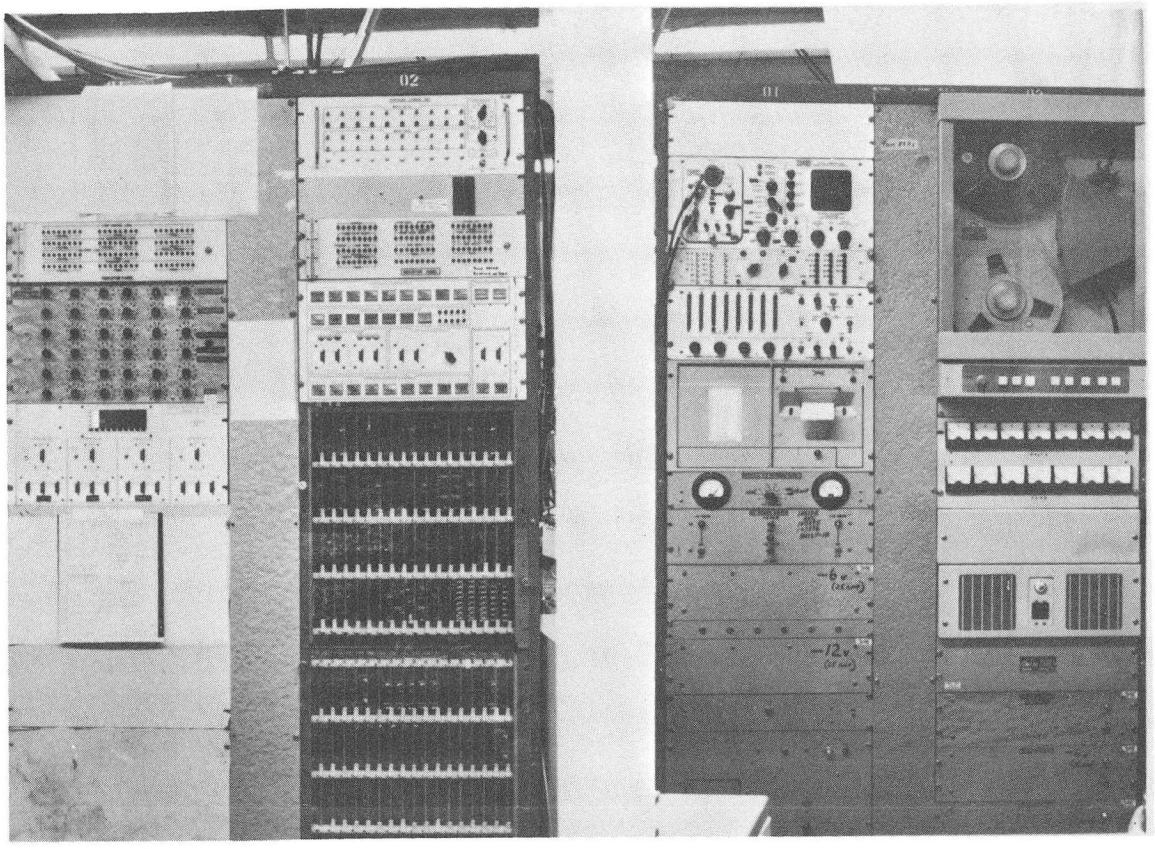

ZN-5649

Fig. II-3. A photograph of the multidimensional pulse-height analyzer system (center), digital gain stabilization unit (left), and magnetic tape recorder (right).

main amplifiers the analogue voltages corresponding to the differences in the number of pulses appearing above and below the pre-selected peak channels. The stabilizer was triggered by gating pulses generated in the double coincidence units in Fig. II-1.

The electron system was stabilized by monitoring the 277.6 keV gamma ray of a ^{243}Cm source mounted directly behind the electron detector on the surface of a semiconductor alpha detector. The stabilizer gating pulses were generated by requiring a double coincidence between gamma rays detected in the electron detector and alpha particles detected in the alpha detector. All ^{243}Cm gamma rays below the 277.6 keV line and any noise above was blocked by means of a single-channel analyzer. In the case of the fission fragment systems, stabilization was accomplished by monitoring the light-fragment distribution, and gating was achieved by means of a double coincidence requirement between fragments detected in detector 1 and fragments detected in detector 2. This also enabled the simultaneous recording of the double-coincidence fragment distributions along with the triple coincidence fragment distributions. Each time a γ-α or F1-F2 stabilization coincidence occurred, a marking pulse was sent to the fourth dimension of the multidimensional analyzer so that the stabilization events could later be sorted from the triple coincidence events.

As an example of the operation of the stabilization system, stabilized and unstabilized fission fragment spectra taken at two different times during an experiment are shown in Fig. II-4. As radiation damage to the detectors over the course of the run caused the detector leakage current to rise, the bias voltage across the detector decreased correspondingly. This decrease in detector bias caused a downward gain drift as evidenced by comparing the stabilized and unstabilized spectra in Fig. II-4a taken at 25°C after the detector had been exposed to 2.54×10^9 fissions/cm^2. By utilizing the stabilization system the

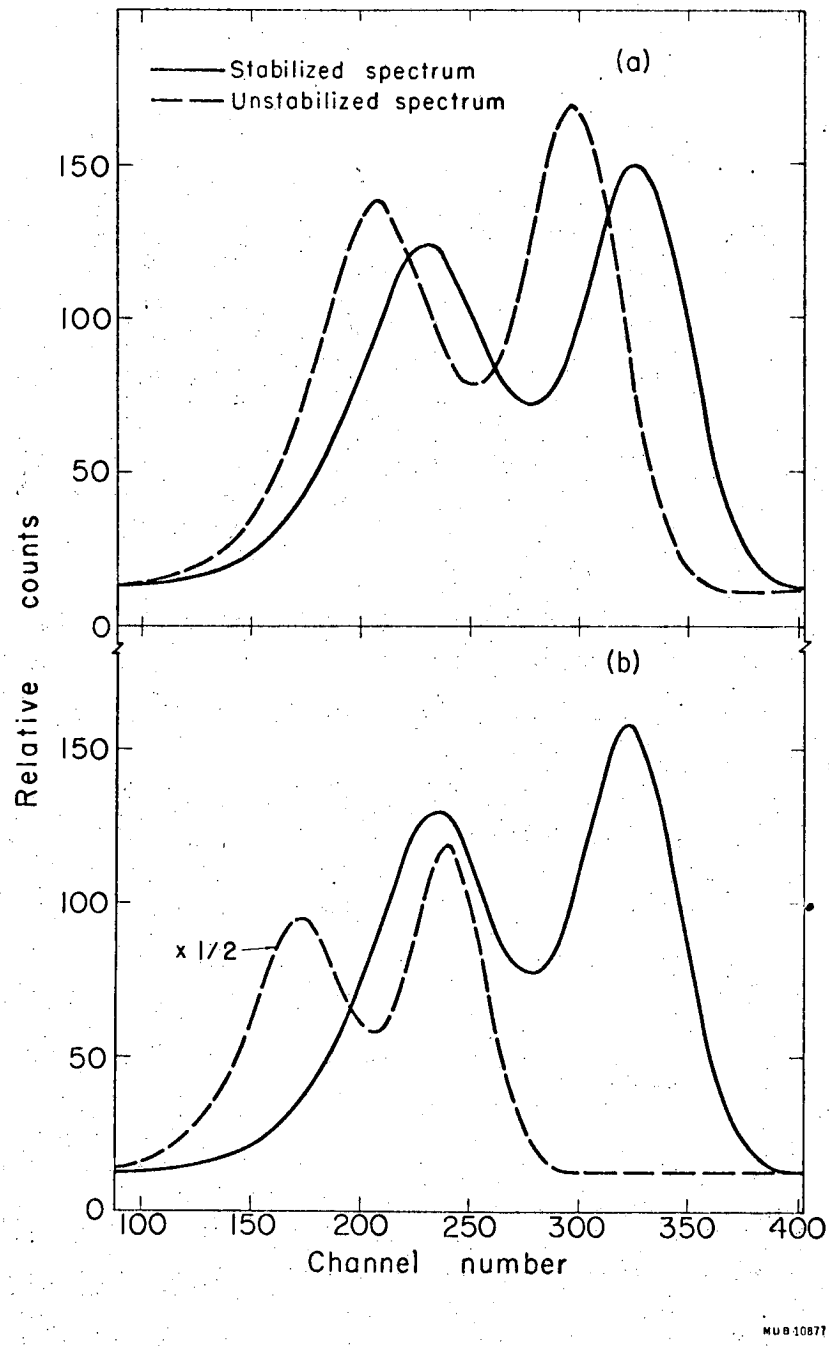

Fig. II-4. A comparison of the stabilized and unstabilized fission fragment spectra at times a) after the detector had been exposed to 2.54 10^9 fissions/cm^2 and b) after the detector had been exposed to 4.39 10^9 fissions/cm^2.

fission fragment distributions showed no detectable gain drift and remained nearly unaltered even after the unstabilized spectra had shifted down in gain by almost 30% as evidenced in Fig. II-4b after exposure to 4.39×10^9 fissions/cm^2.

B. Detectors

1. Electron Detector

The conversion electrons were detected through the use of a lithium-drifted silicon detector 17 mm in diameter and 2.5 mm in depletion depth. Its method of fabrication is described by Goulding.[9] The energy resolution was optimized through the application of a specially designed preamplifier which incorporated a field effect transistor (F.E.T.) designated 2N3823 in the input stage.[7]

In order to further optimize the detection system, a study of resolution as a function of bias voltage and temperature was undertaken. The F.E.T. temperature was held constant at -135°C while the silicon detector was operated at a number of different temperatures (ranging from -50°C to -160°C) maintained by means of an electrical heating system attached to the detector mount. Timed counts were made for a series of bias settings at each temperature and in this way the optimum bias was determined. The relative resolution could be measured quite accurately by comparing the peak heights of the 193.6 keV K-conversion electron line of ^{203}Hg for the various timed counts, care being taken to maintain the same system gain each time the bias voltage was changed. The results of these measurements are shown in Fig. II-5. As indicated, the best resolution was obtained at a temperature of -93°C and 318 V bias. The optimum operating temperature and bias have been found to vary considerably from case to case depending on the detector and experimental conditions, but the trends in the variation of resolution and bias with temperature appear to be general as can be seen by comparison of Fig. II-5 with the data given by Elad and Nakamura.[10]

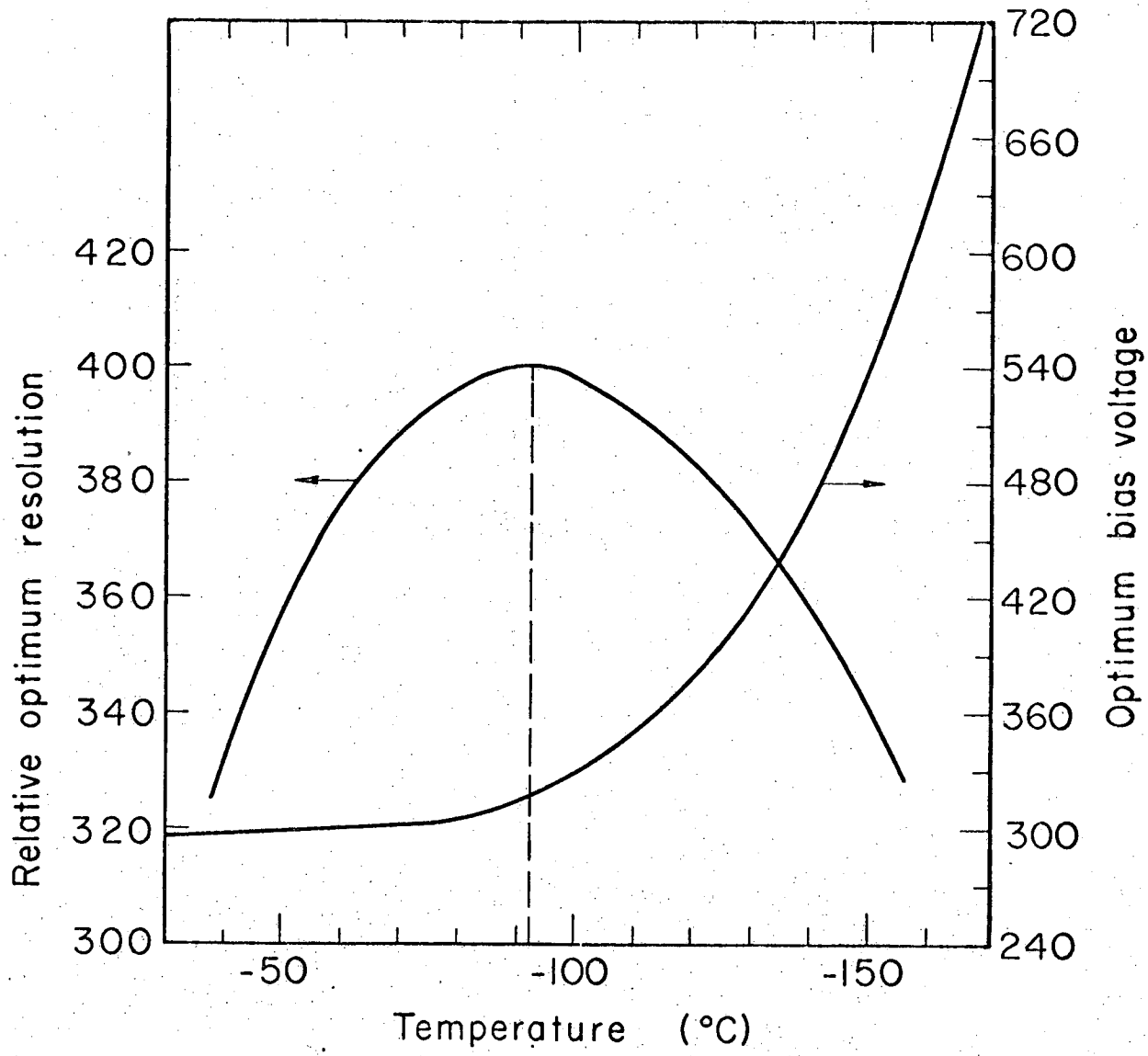

MUB-10855

Fig. II-5. Temperature and bias curves for the optimum operation of the lithium-drifted silicon electron detector used in the experiments.

The measured resolution (FWHM) at the optimum temperature and bias was 3.0 keV for the K line of ^{203}Hg as shown in Fig. II-6 where the K, L, M and a shoulder due to the N line may be seen. (This spectrum was taken using the magnetic steering device). The resolution capability of the electron detector, however, appears to be somewhat better than the electron measurements indicate, since an experimental resolution of 1.5 keV was obtained from measurements with 117-keV Pu $K\beta_1$-X-rays. The electron peaks in Fig. II-6 display a considerable amount of tailing, and this effect is probably partly responsible for the resolution difference between X-rays and electrons.

2. Fission Fragment Detectors

The fission fragment energies were measured through the use of phosphorus-diffused silicon detectors characterized by an extremely thin window (< 1 micron) and a depletion depth of approximately 200 microns. The particular detectors used in the present experiments were constructed from 400 ohm-cm silicon wafers 25 mm in diameter according to the method outlined by Goulding.[11] (The detectors were collimated to 15 mm in diameter).

The effect of radiation damage to the fission fragment detectors was studied as a function of the number of fragments detected in order to determine its consequences on fragment energy measurements during the electron experiments. The most apparent effect was found to stem from the rapid rise in leakage current (shown in Fig. II-7) when the detectors were operated at room temperature. The continuous increase in leakage current caused a corresponding drop in bias voltage across the detector and resulted in a continual downward drift in the gain of the system. Total loss of resolution occurred after the detectors had been exposed to 5.6×10^9 fissions/cm^2 (leakage current = 32 μ amp).

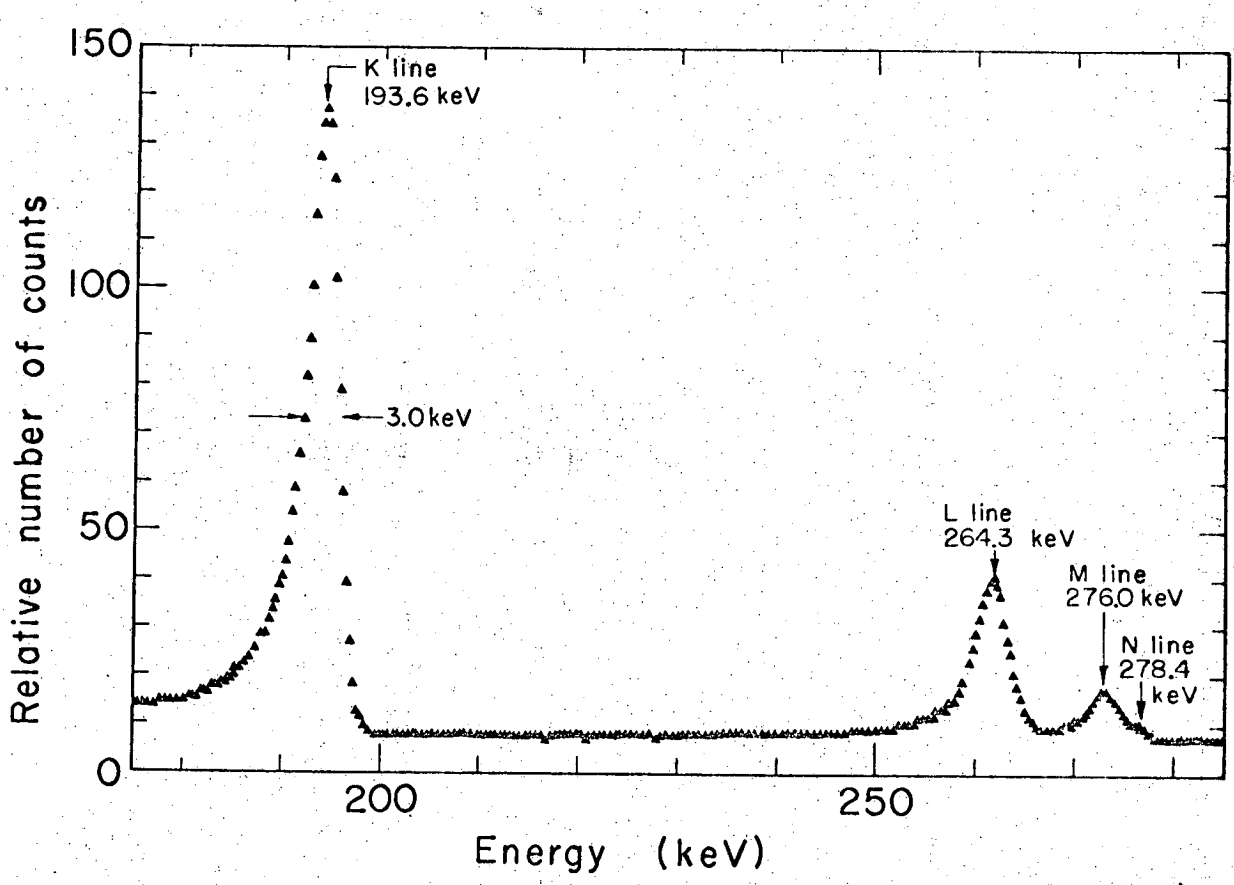

Fig. II-6. Spectrum of the internal conversion electrons associated with the 279.1 keV gamma-ray transition in ^{203}Tl taken with a lithium-drifted silicon detector in the magnetic steering device.

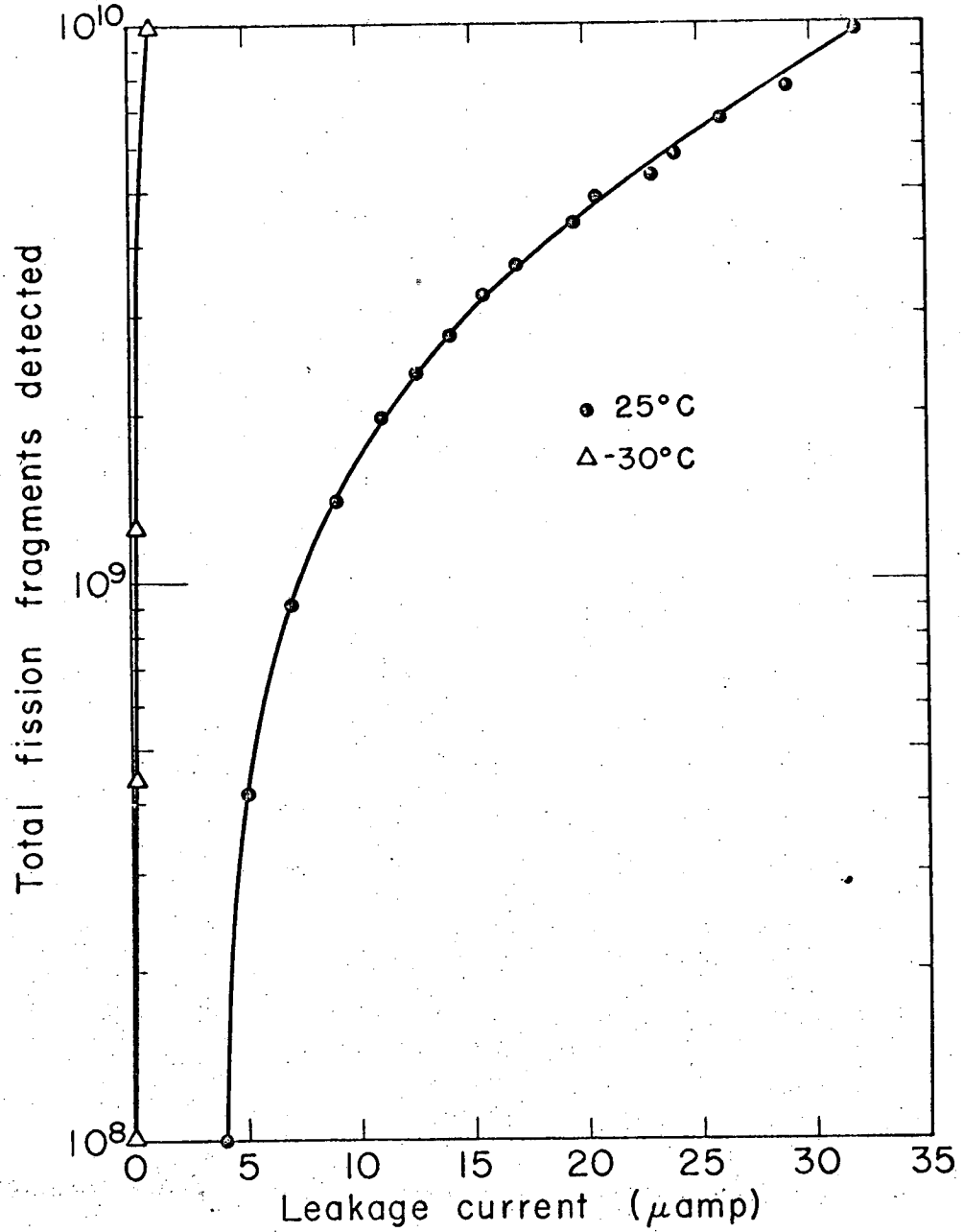

MUB-10883

Fig. II-7. A comparison of the leakage current characteristics of a phosphorus-diffused silicon fission fragment detector at two temperatures. (Bias = 300v).

By cooling the fragment detector, a great improvement was observed in the leakage current and rise time characteristics, while overall deterioration of the detectors was suppressed to the point of increasing the detector life by a factor of three or better.

The optimum operating temperature for the phosphorus-diffused detectors used in these experiments was found to lie in the range -30° to -50°C. At temperatures below -50°C, the operation of the detectors became hampered by polarization and trapping effects as evidenced by the appearance of slow-rise components in the detector output pulses and a rapid degradation in resolution. A typical fission fragment spectrum is shown in Fig. II-8. For reasonably good detectors, peak-to-valley ratios of around 2.4 and peak-to-peak ratios of around 1.3 were obtained.

C. Magnetic Steering Mechanism

1. The Motion of a Charged Particle in a Magnetic Field with Rotational Symmetry and Radial Dependence $1/r^n$.

The steering mechanism used in the present experiments employed a magnetic field with rotational symmetry and radial dependence $1/r^n$. A general treatment of the motion of a charged particle in an inhomogeneous magnetic field is given in Appendix A and from the two types of drift motion discussed in that section, it is expected that a charged particle moving in the fringing field would experience an azimuthal drift motion around the circumference of the magnet superimposed upon a spiralling motion along the magnetic lines of force. For trajectories with vertical components below a critical value, a "mirror effect" would occur resulting in reflection of the electrons back and forth across the plane of symmetry. Stated more concisely, the particle motion is a superposition of a trochoidal motion and a vertical oscillation through the symmetry plane.

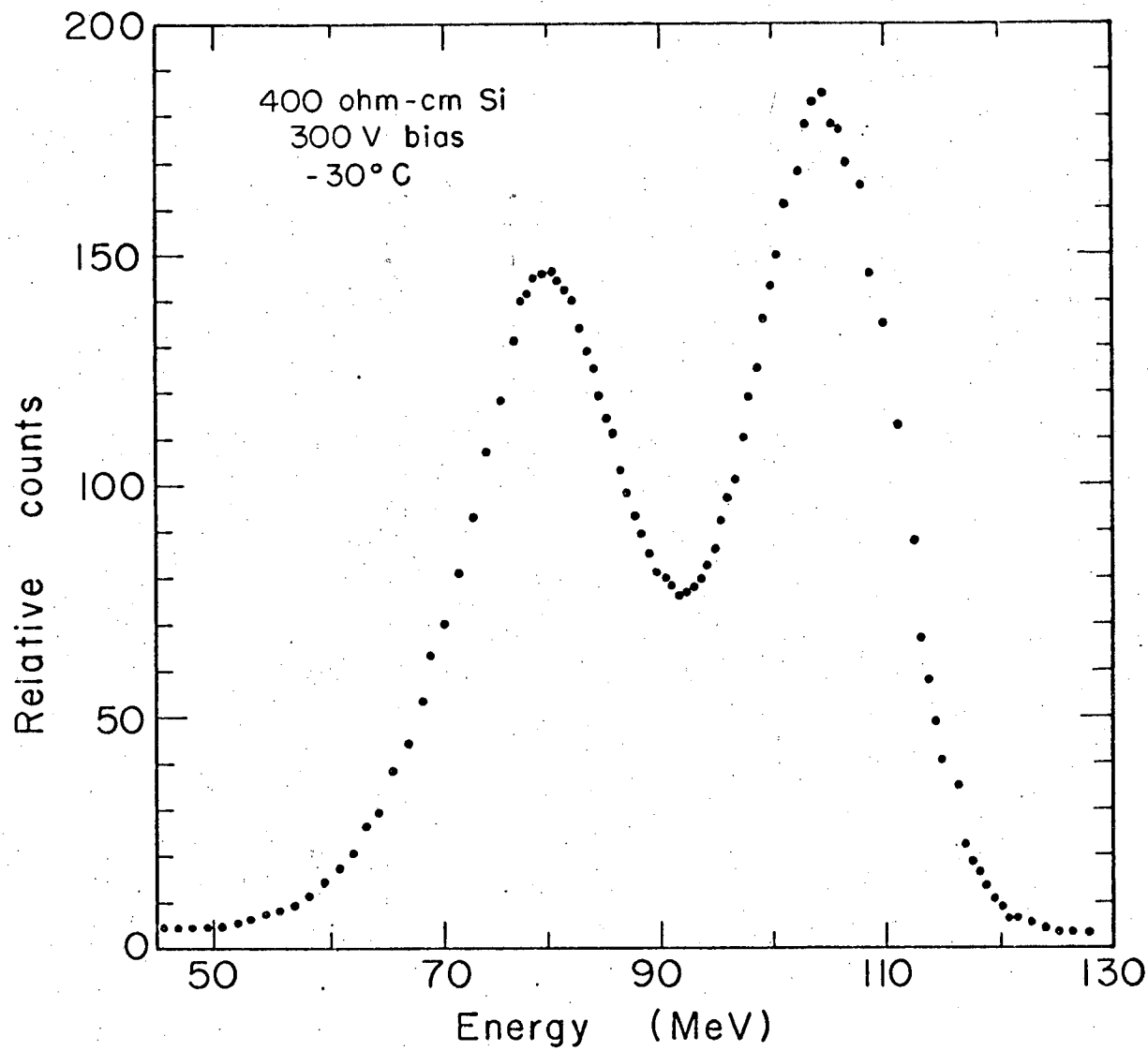

MUB-10878

Fig. II-8. A typical ^{252}Cf fission fragment spectrum taken with a phosphorus-diffused silicon detector.

The motion of a charged particle in such a field has been studied extensively by Malmfors.[12] Malmfors treated the problem by means of a perturbation method and obtained the following expression for the azimuthal angular displacement of a charged particle after one vertical oscillation through the symmetry plane:

$$\Lambda = \frac{2\pi}{r_o}\frac{mc}{eH_o}\sqrt{E}\sqrt{1+E/2}\left(1 - \frac{n^2-8n+4}{16}\cdot\frac{Z_R^2}{r_o^2} + \ldots\right) \quad . \qquad \text{(II-1)}$$

In this equation, r_o is the radial distance from the center of the magnet to the starting point in the plane of symmetry, B_o is the field strength at the starting point, Z_R is the oscillation amplitude (distance from the symmetry plane to point of reflection), and E is the particle energy in units of mc^2. The azimuthal angular displacement of a charged particle after one orbit in the plane of symmetry is given by

$$\Phi = \pi n \frac{\rho_o^2}{r_o^2}\left[1 + \left(\frac{3}{4}n^2+n-1\right)\frac{\rho_o^2}{r_o^2} + \ldots\right] \quad , \qquad \text{(II-2)}$$

where ρ_o is the radius of curvature in the plane of symmetry when the oscillation amplitude is zero. Another equation of interest gives the drift time required for a particle to precess 1/4 of the distance around the magnet. It is valid in the region of relativistic velocities and is expressed by

$$\tau = \frac{\pi r_o}{2v_{drift}} = \frac{\pi e}{2mc^2}\frac{H_o r_o^2}{n}\cdot\frac{E+1}{E(1+E/2)}\left(1 + \frac{n(n-2)}{4}\frac{Z_R^2}{r_o^2} + \ldots\right) \quad . \qquad \text{(II-3)}$$

An illustration of the region of acceptance into the steering device for a point source located on the symmetry plane is shown in Fig. II-9. All electrons emitted between the two cones are transmitted around the magnet. The transmission of the device may be calculated by integrating the surface area of a sphere over the region bounded by the two escape cones as follows:

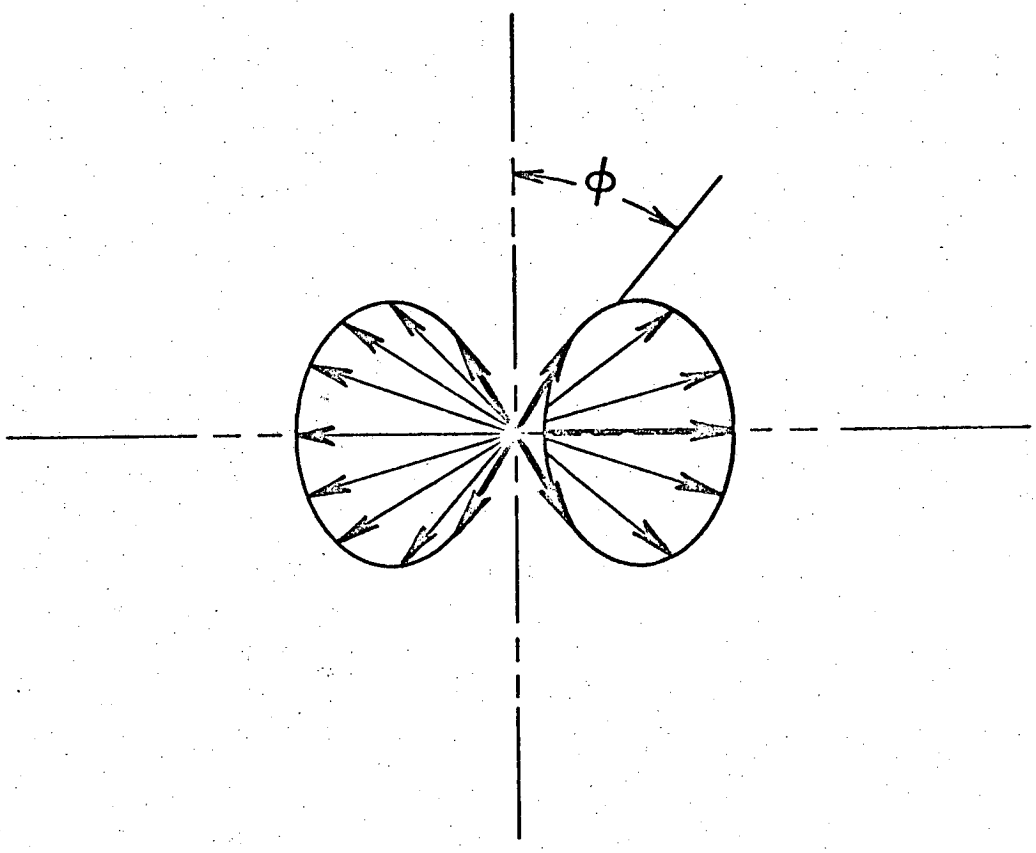

MUB-9749

Fig. II-9. An illustration of the region of acceptance into the magnetic steering device for electrons emitted from a point source located on the symmetry plane. All electrons emitted between the two cones are transmitted around the magnet to the electron detector.

$$\Omega = 8 \int_{\frac{\pi}{2} - \Phi}^{\frac{\pi}{2}} \int_{0}^{\frac{\pi}{2}} \sin\theta \, d\theta \, d\phi = 4\pi \sin \Phi$$

The total surface area of a sphere is 4π, thus the transmission is given by

$$T = \sin \Phi \quad . \tag{II-4}$$

Now, from Eq. (VII-12) it follows that

$$\sin^2 \Phi = \cos^2 \theta_c = 1 - \sin^2 \theta_c = 1 - \frac{B_{oz}}{B_{Rz}}$$

$$T = \sqrt{1 - \frac{B_{oz}}{B_{Rz}}} \quad . \tag{II-5}$$

Malmfors found that

$$\frac{B_{oz}}{B_{Rz}} = \left(1 - \frac{n^2 Z_R^{\,2}}{2 r_o^{\,2}} + \cdots \right) \quad , \tag{II-6}$$

and substituting the first two terms of this expansion into Eq. (II-5), the expression for the transmission becomes

$$T = \frac{n}{\sqrt{2}} \frac{Z_{R\,max}}{r_o} \quad . \tag{II-7}$$

It is seen, then, that the transmission of the steering device is independent of electron energy and is solely determined by the maximum oscillation amplitude of the reflection through the symmetry plane.

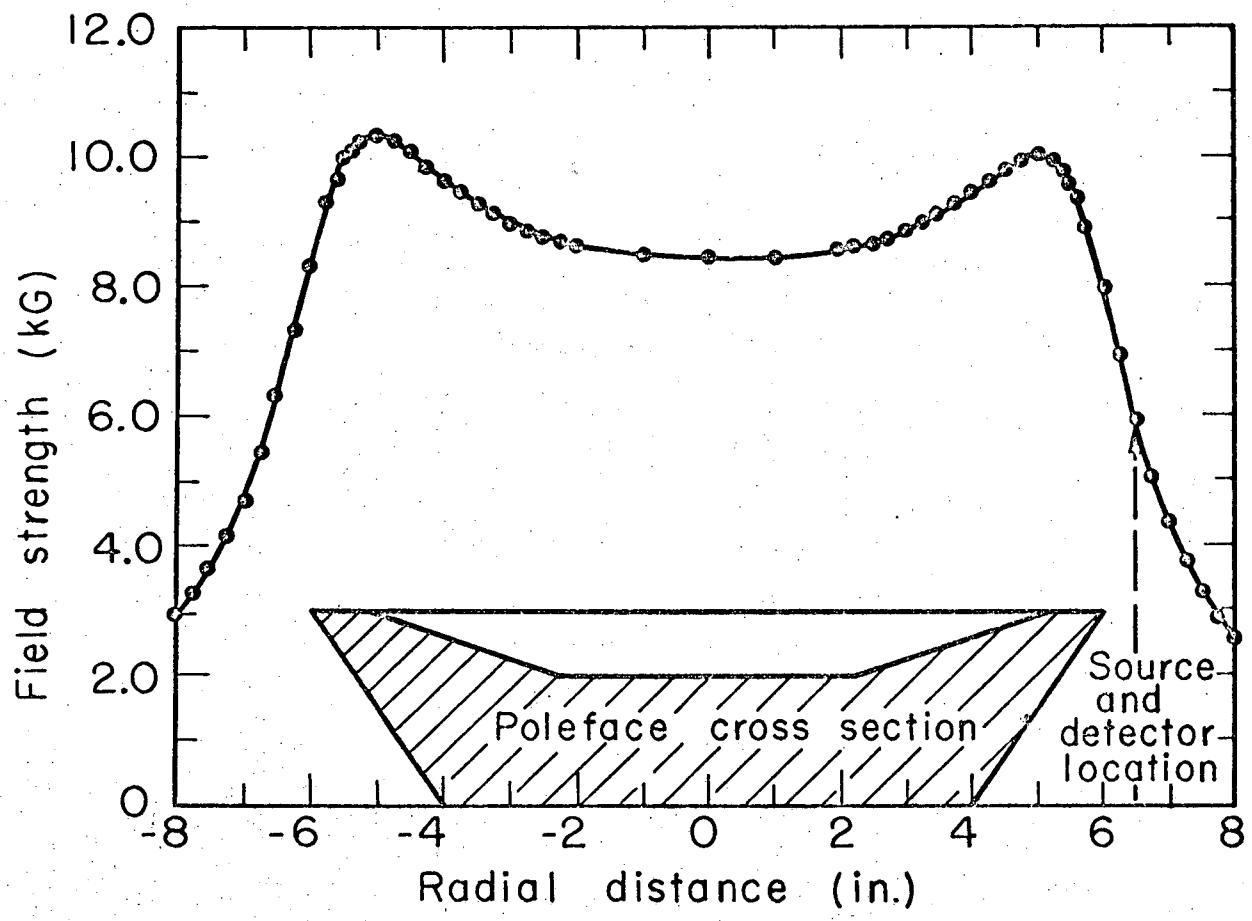

MUB-10882

Fig. II-10. Magnetic field profile and sketch of poleface cross section.

2. Experimental Design

The magnetic field used to steer the conversion electrons away from the fission source region was produced by a 100 KVA C-magnet. A plot of the magnetic field strength as a function of radial distance from the center of the magnet is shown in Fig. II-10 along with a cross section sketch of the poleface designed to create a nearly constant n fringing field with high convergence at the pole-tips. The radial position of the electron detector and fission source during the experiments is also indicated (r_o = 6.5 in.) and the field strength at this radius was 6000 gauss. The maximum oscillation amplitude of the electrons, Z_1, was limited to 1 cm by means of two deflectors. Since the field strengths at any two radii in a region of constant n are related by the expression

$$\frac{H_1}{H_2} = \frac{r_2^n}{r_1^n} \quad , \tag{II-8}$$

the value of n may be determined from

$$\frac{\log H_2 - \log H_1}{\log r_2 - \log r_1} = -n \quad . \tag{II-9}$$

The value of n in the region of the detector-source radius was found to be 3.35.

It was of interest in these experiments, to know the values of several quantities as a function of electron energy; namely, the radius of curvature in the symmetry plane ρ_o, the displacement, d, of an electron after one orbit in the symmetry plane, the maximum displacement, λ, of an electron after one complete vertical oscillation through the symmetry plane, and the time of flight 1/4 of the way around the magnet, $\tau_{90°}$. The radii of curvature were obtained from a table of magnetic rigidity for electrons[13] while the other quantities were calculated from Eqs. (II-1), (II-2) and (II-3). Inserting the appropriate constants into these equations yield the following expressions:

$$d = r_o \Phi = 0.6377\ \rho_o^2 \text{ cm} \qquad \text{(II-10)}$$

$$\lambda = r_o \Lambda = 1.7772\sqrt{E + E^2/2} \text{ cm} \qquad \text{(II-11)}$$

$$\tau_{90°} = 14.9789 \left[\frac{E+1}{E(1+E/2)}\right] \text{ nsec} \quad . \qquad \text{(II-12)}$$

Again, E is expressed in units of mc^2. These quantities are tabulated in Table II-1 as a function of electron energy.

A large discrepancy was found between the flight times calculated from Eq. (II-12) and those obtained experimentally at low electron energies. For example, the flight time calculated for a 20 keV electron was 390 nsec while the experimentally determined value was approximately 180 nsec. This difference was attributed to inaccuracies in the field measurements near r_o and to a variation in the ratio H_o/n along the electron flight path due to irregularities in the magnetic field. (In the region around r_o, the ratio H_o/n is changing very rapidly.)

A film study of the radial distribution of ^{203}Hg conversion electrons accepted into the steering device was conducted inside a vacuum chamber placed between the polefaces. A strip of X-ray film was mounted inside the vacuum chamber radially from the center of the magnet and an electron source, which consisted of ^{203}Hg amalgamated on the end of a thin copper wire, was mounted 90° around the magnet at a radial position of 6.5 in. One of the exposed film strips showing the distribution of electrons transmitted around from the source is presented in Fig. II-11.

A sketch of the basic layout used in the electron experiments is presented in Fig. II-12. As indicated, electrons starting at the symmetry plane precess in trochoidal orbits around the magnet in a 90° arc to the electron detector while being reflected from poleface to poleface along magnetic lines of force. (The trajectory of an electron leaving at the

Table II-1. Calculated quantities pertaining to the motion of electrons in the magnetic steering device. (6000 G, n = 3.35, r_o = 16.5 cm)

Energy (keV)	ρ_o (cm)	d (cm)	λ (cm)	$\tau_{(90°)}$ (nsec)
10.0	.056	.002	.250	772.8
50.0	.129	.011	.569	160.2
100.0	.186	.022	.824	83.4
150.0	.233	.035	1.031	57.6
200.0	.275	.048	1.216	44.5
250.0	.313	.063	1.387	36.6
300.0	.350	.078	1.549	31.3
350.0	.385	.095	1.704	27.4
400.0	.419	.112	1.855	24.5
450.0	.452	.131	2.002	22.2
500.0	.485	.150	2.145	20.3
550.0	.517	.170	2.287	18.8
600.0	.548	.192	2.426	17.5
650.0	.580	.214	2.564	16.4
700.0	.610	.238	2.700	15.4
750.0	.641	.262	2.835	14.5
800.0	.671	.287	2.969	13.8
850.0	.701	.314	3.102	13.1
900.0	.731	.341	3.234	12.5
950.0	.761	.369	3.366	11.9
1000.0	.791	.399	3.497	11.4

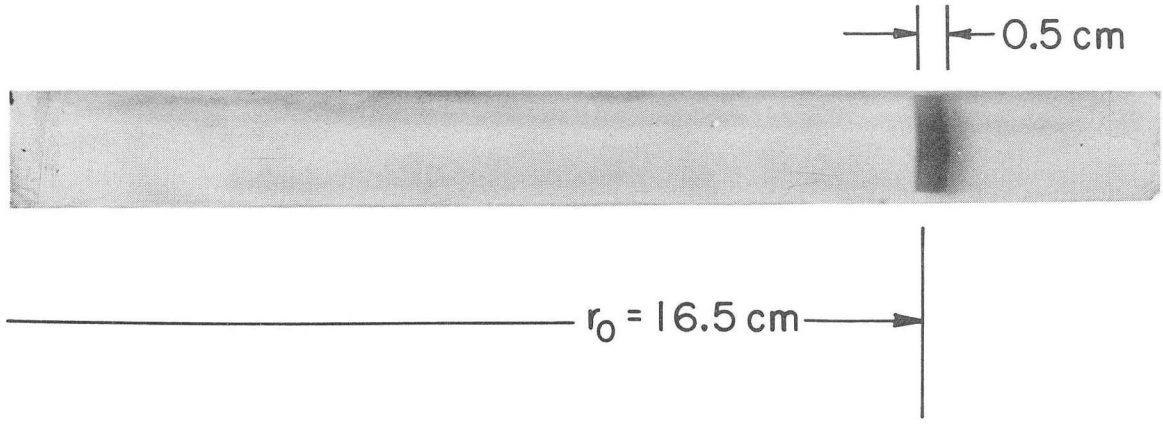

ZN-5859

Fig. II-11. A film strip which was exposed at the detector position to electrons transmitted around the magnet from the source position in the steering device.

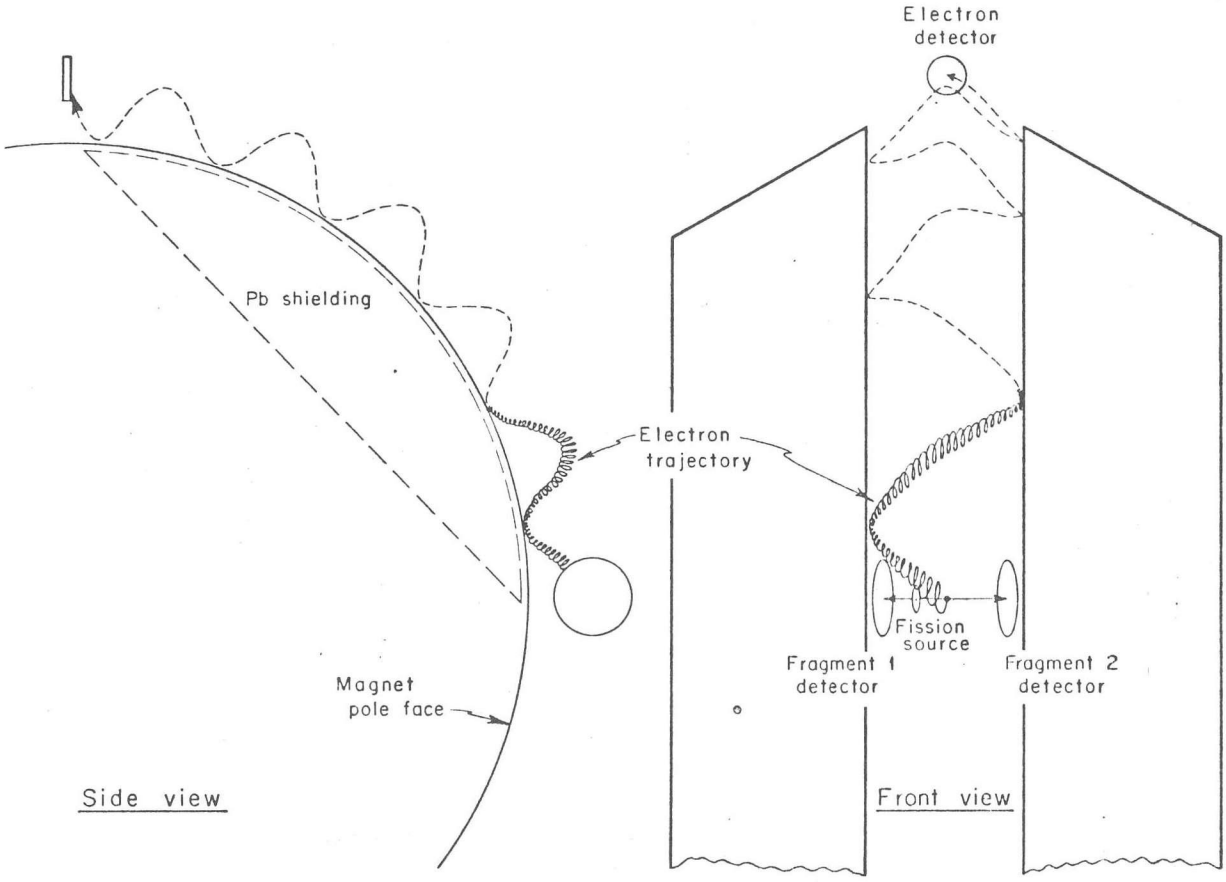

Fig. II-12. A diagram depicting the magnetic steering mechanism for an electron emitted at the critical reflection angle θ_c. The electron starts at the symmetry plane and precesses in trochoidal orbits around the magnet in a 90° arc to the detector while being reflected from poleface to poleface along magnetic lines of force.

critical reflection angle θ_c is depicted). The fission fragment detectors were placed parallel to the symmetry plane and only those electrons which were emitted near 90° with respect to the fragment detector axis were allowed to reach the electron detector. A large lead shield was located in a position which blocked any interfering radiation.

A very useful application was made of the fact that the transmission of the steering device can be controlled by varying the maximum oscillation amplitude. This property was employed, as illustrated in Fig. II-13 by moving the source off the symmetry plane and restricting the region of acceptance into the steering device by means of two deflectors. These two deflectors limited the maximum oscillation amplitude of the electrons and since the acceptance angle of the device is proportional to the maximum oscillation amplitude as depicted for electrons emitted at point 1 and point 2 in Fig. II-13, this restriction required that the fission fragments from which the electrons were emitted be near the symmetry plane at the time of emission. The transmission at any point between the deflectors may be calculated from Eq. (II-5) by replacing B_{oz} with the z component of the magnetic field at the source position. From Eq. (II-6), it is found that

$$\frac{B_{sz}}{B_{Rz}} = \frac{B_{oz}}{B_{Rz}} \times \frac{B_{sz}}{B_{oz}} = \frac{\left(1 - \frac{n^2}{2} \frac{Z_R^2}{r_o^2}\right)}{\left(1 - \frac{n^2}{2} \frac{Z_s^2}{r_o^2}\right)} \quad , \qquad \text{(II-13)}$$

where Z_s is the distance from the symmetry plane to the point of emission. It follows, after substitution of this expression into Eq. (II-5), that the transmission at any point between the deflectors is given by

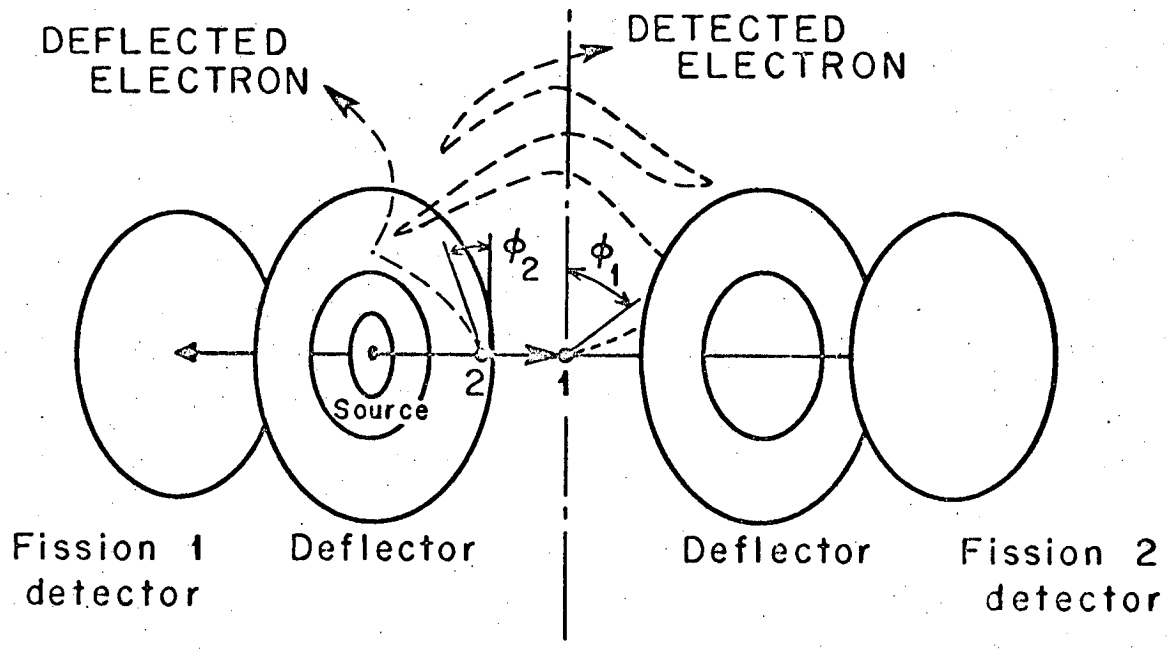

MUB-9748

Fig. II-13. A diagram of the fragment detector-source-deflector assembly. With the source positioned as shown, only those electrons which were emitted while the fragment was between the two deflectors could be detected. The limitation imposed upon the electron trajectories by the deflectors caused the critical angle of acceptance for electrons to vary from 0° at the deflector position to a maximum of 8° at the symmetry plane (position 1).

$$T(z) = n\sqrt{\frac{Z_{R\ max}^{2} - Z_s^{2}}{2r_o^{2} - n^{2} Z_s^{2}}} \qquad \text{(II-14)}$$

The deflectors were spaced 2 cm apart in the experiments and hence $Z_{R\ max}$ was 1 cm.

The calculated detection efficiency as a function of the distance of the fragment from the symmetry plane at the time of electron emission (Z_s) is plotted in Fig. II-14. It is seen that by positioning the deflectors 2 cm apart, a time resolution of approximately 1.7 nsec was achieved since the average fission fragment velocity is about 1 cm/nsec. Furthermore, it is apparent that only electrons emitted from that fragment of each fragment pair which passes through the symmetry plane have any probability of being detected. Hence, in this way total separation of electrons emitted from heavy and light fragments is accomplished.

A picture of the vacuum chamber and magnet is shown in Fig. II-15. The fission fragment detector-source assembly was mounted to a micrometer screw mechanism, the handle of which may be seen on the front flange of the vacuum chamber. This feature enabled the positioning of the source over a range of radial distances. Other details seen on the front flange include the fragment detector electrical connections, a thermocouple lead for monitoring the fragment detector temperature, and a liquid-nitrogen reservoir which supplied coolant to the fragment detectors. An inside view of the front flange is pictured in Fig. II-16 and shows the fission fragment detector-source-deflector assembly. The construction was such that the various components could be repositioned at any point along the detector axis. The fragment detectors were collimated to 15 mm in diameter by the detector mounts and cooled to -50°C. Three detector-source-deflector configurations were used in the electron experiments. In configuration 1, the californium source was

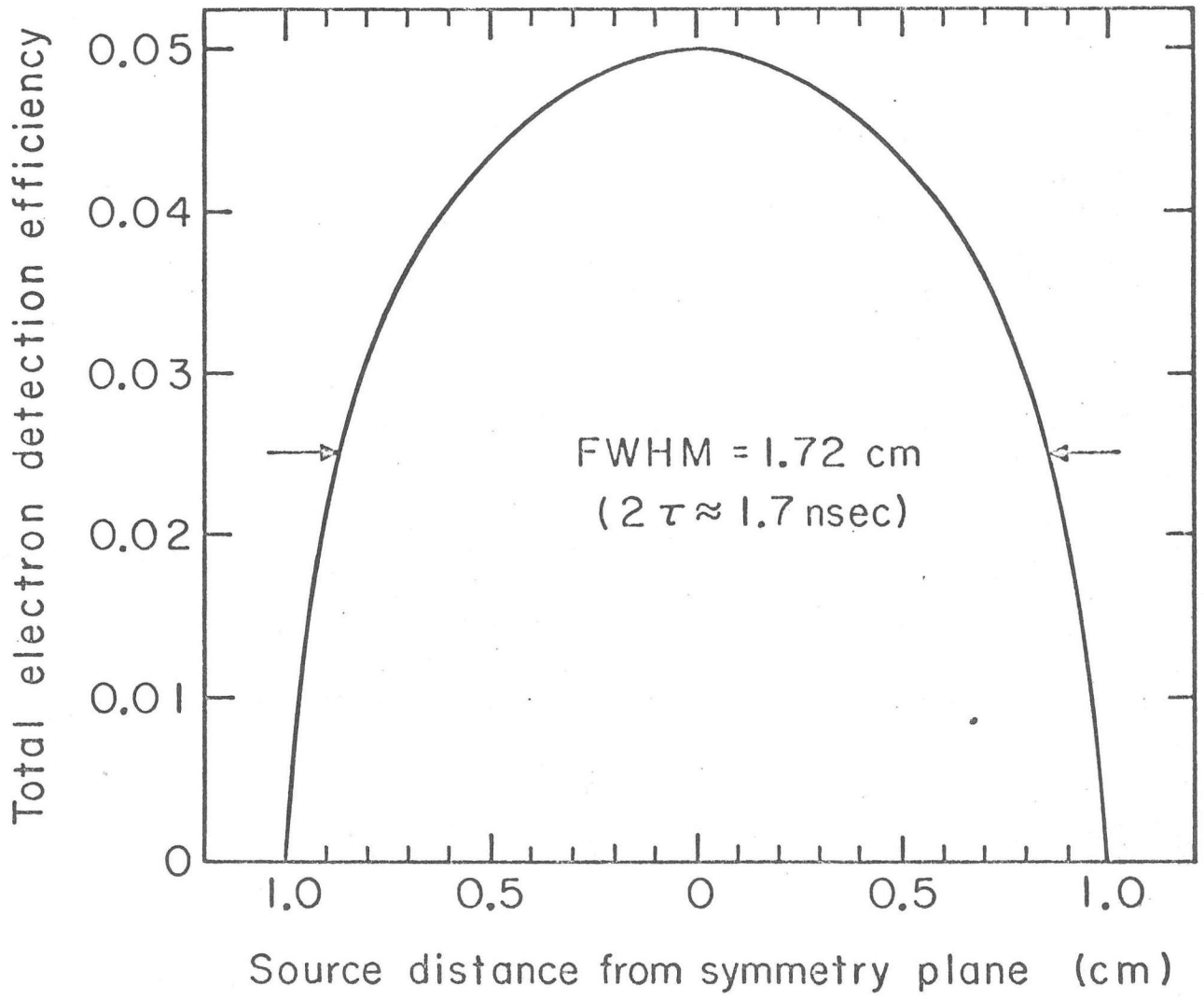

MUB-9904

Fig. II-14. The calculated detection efficiency for electrons emitted from fission fragments as a function of the distance of the fragment from the symmetry plane at the time of emission.

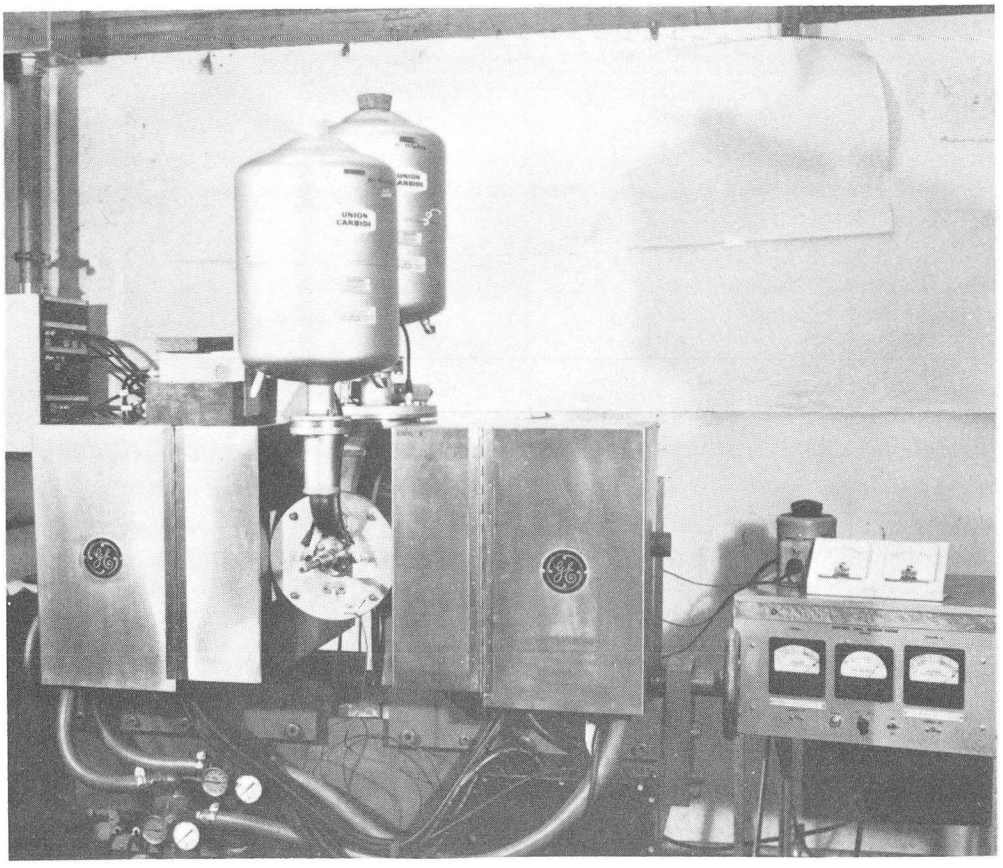

ZN-5646

Fig. II-15. A photograph of the magnetic steering device showing the magnet and vacuum chamber.

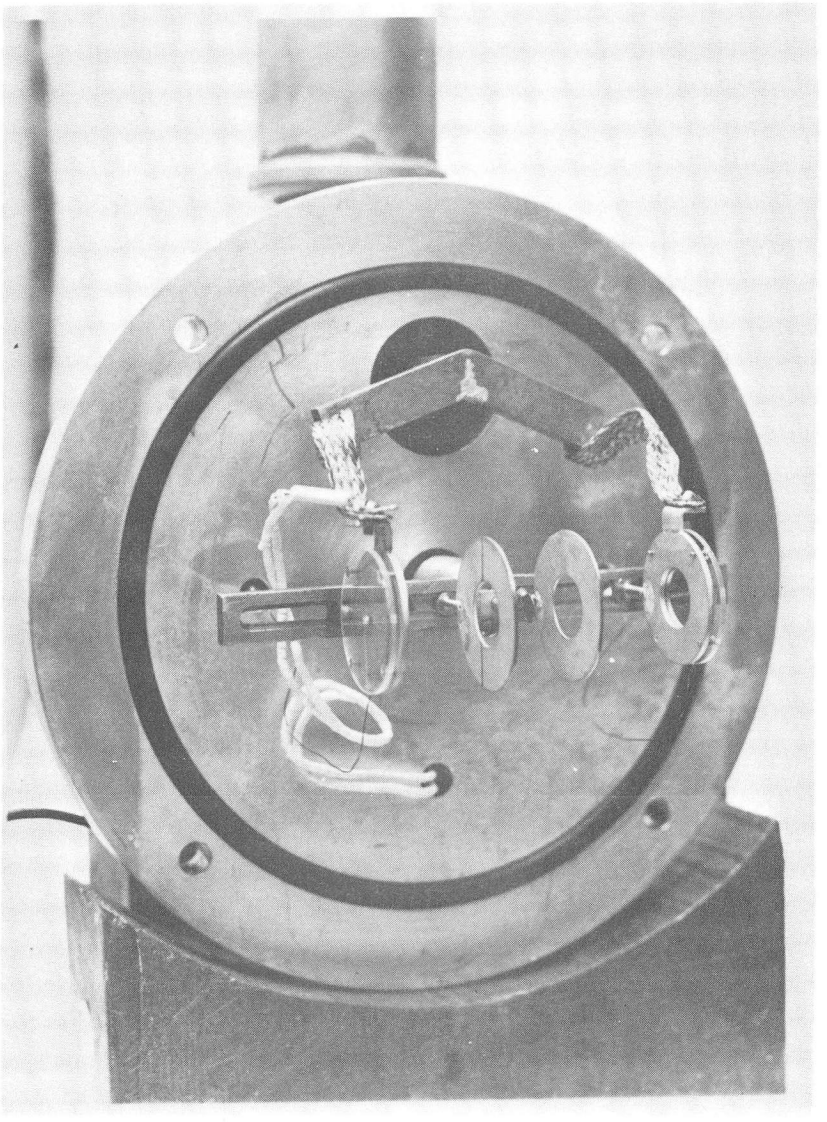

ZN-5647

Fig. II-16. A photograph of the front flange (inside view) showing the fragment detector-source-deflector assembly. Also shown are the detector cooling straps and thermocouple wire.

positioned on the symmetry plane with the deflectors at a distance of 1 cm on each side of the source. The fragment detectors were positioned at 2 cm on each side of the source. This arrangement allowed the detection of electrons emitted in less than 1 nsec after fission. Configuration 2 was used to detect electrons emitted near 1 nsec after fission. The source was positioned one cm from the symmetry plane, while detector 1 was located 2 cm from the symmetry plane on the same side as the source and detector 2 was located 1 cm from the symmetry plane on the other side. One deflector was mounted around the source and fragment detector 2 was utilized as the other deflector. Configuration 3, which was designed for the detection of electrons emitted near 2 nsecs after fission was attained by repositioning the source and fragment detector 1 at distances of 2 and 3.3 cm respectively from the symmetry plane.

The top flange, which may be seen in Fig. II-15, supported the electron detector mount and liquid nitrogen reservoir used to cool the detector. An upside down side view of the top flange assembly is pictured in Fig. II-17. The detector mount was constructed of copper and collimated the electron detector to 13 mm in diameter. It was attached to the liquid nitrogen cold finger through a block of teflon which acted as a resistance to heat transfer. By heating the detector mount through the large copper wire visible in Fig. II-17, the detector was maintained at -93°C. Since it was important to locate the F.E.T. near the detector in order to minimize stray capacitance and since the F.E.T. had to be cooled in order to optimize its low noise characteristics, the entire first stage of the preamplifier including the F.E.T. was mounted behind the detector and cooled to -135°C by attaching it to the cooled detector mount. The rest of the preamplifier is seen mounted on the outside of the flange. A portion of the silicon alpha particle detector which was used to detect ^{243}Cm alphas in coincidence with gamma rays detected through the back of the electron detector is visible immediately behind the electron detector mount in Fig. II-17. The $\gamma\alpha$ coincidence, as already mentioned, was used for gain stabilization purposes.

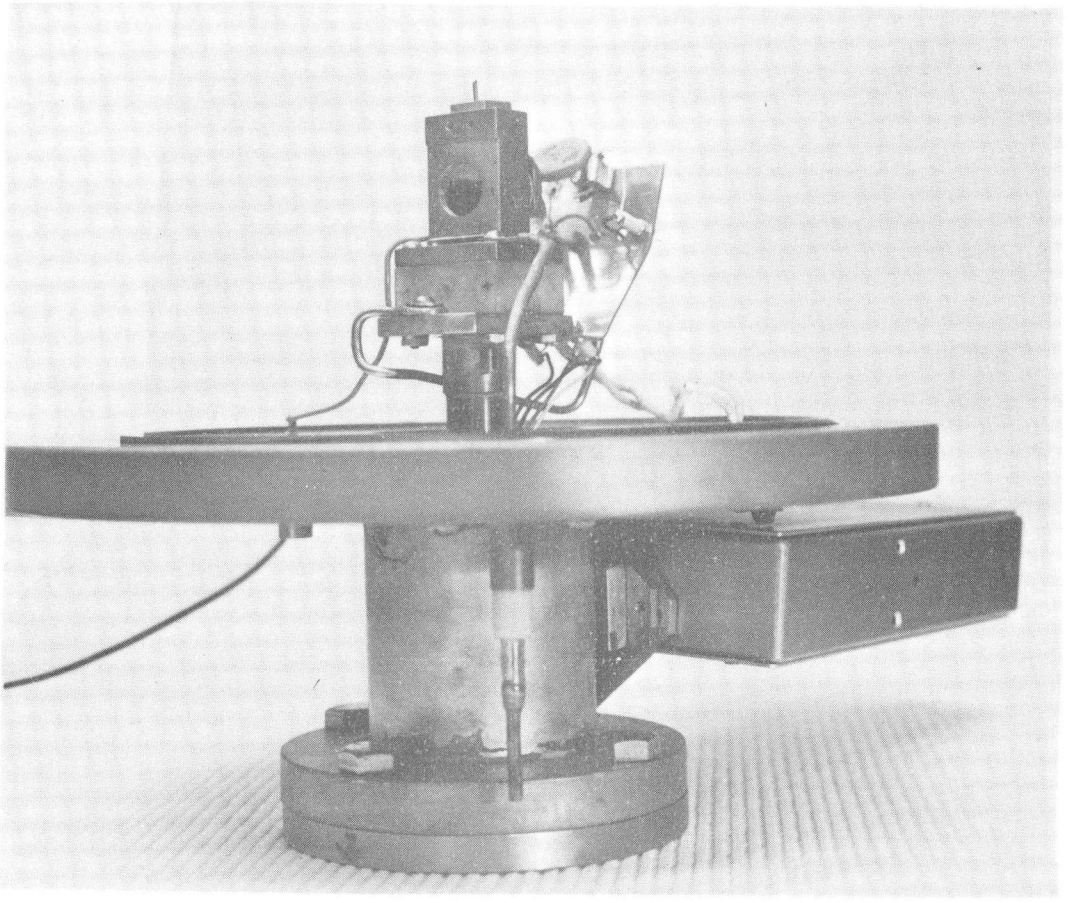

ZN-5648

Fig. II-17. A photograph of the top flange (upside-down side view) showing the electron detector and mount, the alpha detector (immediately behind electron detector mount), the heating wire, and the first stage of the preamplifier.

III. EXPERIMENTAL METHODS

A. Experimental Procedures

1. Source Preparation

Experiments with standard conversion electron sources disclosed the fact that serious restrictions are placed on the configuration of the source holder as a result of the trajectories imposed upon the electrons by the magnetic steering device. Specifically, these restrictions stem from the following two properties of the electron trajectories in the steering field:

(a) The electron drift displacement, d, in the azimuthal direction (around the magnet) after one orbit, is so small the electrons tend to reenter the source backing;

(b) The wavelength of the oscillation through the symmetry plane, λ, causes electrons having low energies or low takeoff angles to collide with the source holder.

Both of these effects cause serious tailing and peak displacement in measured electron spectra. Although these problems were not present in the detection of delayed electrons emitted from fission fragments, (since the source was positioned off the symmetry plane during the experiments, the electrons were emitted from single fragments which had traveled away from the source to the symmetry plane) it was still necessary to find a means of circumventing them in order to effectively calibrate the system for energy and detection efficiency. The solution finally emerged in the form of a satisfactory design for the source holder and source backing after many attempts with various configurations including wires and discs of different sizes.

The source holder consisted of a circular wire loop 1/4 in. in diameter constructed from 1/64 in. diameter stainless steel wire. A straight 5/8 in. length of stainless steel wire of the same diameter was soldered to the loop radially at a point along the perifery and

used to connect the loop to the fragment detector-source assembly. One such mounted source loop may be seen in Fig. II-16 centered between the two deflectors.

The source backing was mounted over the loop and the source deposited in the center. For the conversion electron standards, the source backing consisted of a 2 $\mu g/cm^2$ film of zapon enveloped over both sides of the source loop with approximately 10 $\mu g/cm^2$ of gold vaporized on each side over the zapon giving a total source backing thickness of about 24 $\mu g/cm^2$. The electron sources were prepared by evaporating to dryness small drops of the source solutions placed at the centers of the films.

The source backings for the ^{252}Cf sources were made from 4 μin. nickel films ($\sim$ 70 $\mu g/cm^2$). The nickel films, in the form of nickel plated over copper backings, were stamped into 3/8 in. diameter discs and attached to the source loops with epoxy cement. The copper backings were then dissolved in a solution of H_2SO_4 and $Na_2\ CrO_4$. Finally, electrical contact with the source loops was insured by overlapping small drops of conducting silver paint on the nickel films and source loops. Deposition of ^{252}Cf onto the nickel films was then accomplished by the "self-transfer" mechanism whereby the source loops were placed over a 7 μg source under vacuum. The sources prepared in this manner and used in these experiments typically had fission rates of 5×10^5 to 5×10^6 fission/min. Light and heavy fragments were found to lose on the average, 2.3 and 2.1 MeV respectively in penetrating the nickel films.

2. Energy and Efficiency Calibration

Energy calibration of the electron detector was accomplished through the use of conversion electron standards such as ^{109}Cd, ^{203}Hg, ^{207}Bi and ^{137}Cs. Simultaneous calibrations with electrons and gamma rays were also made at the beginning and end of each experiment by means of

the electron standards and a ^{243}Cm source mounted directly behind the electron detector. Utilizing the Pt X-rays arising from the ^{243}Cm platinum source backing and the Pu X-rays arising from the alpha decay product of Cm as well as the ^{243}Cm gamma rays, a 13 point X-ray-gamma calibration was obtained ranging from 14.3 keV to 277.6 keV (the higher energy electron experiments had to be calibrated by electron standards alone). As previously mentioned, the ^{243}Cm source was also used in conjunction with a digital gain stabilization system to insure that the energy calibration did not change due to electronic gain drift.

The fission fragment detectors were calibrated automatically during the experiments by the fission fragment distributions, since the energies of the light and heavy fragment peaks are well known for ^{252}Cf (see Section II-D). As with the electron detector, digital gain stabilization systems were also used to stabilize the fragment detector calibrations.

Although a satisfactory source holder and backing design was worked out for measuring electron energies without serious tailing and peak displacement effects, no means could be found by which the experimental geometry situation for fission fragments could be reproduced for electron standards. For this reason, it was not possible to measure directly the detection efficiency for electrons emitted from fission fragments. Several studies were conducted, however, in which efficiencies were measured with a series of calibrated electron sources mounted on source loops made with decreasing diameter wires. Extrapolations were then made to determine the efficiency for a source without a source loop (zero diameter wire).

The detection efficiency was also calculated. The transmission was first computed for the experimental configuration by means of Eq. (II-7) which gave T = 13.8%. By carefully tracing the coordinates of the field lines at the source radius in an electrostatic wedge tank

and measuring the magnetic field strengths along these coordinates by means of a Hall probe gaussmeter, another calculation of T was made from Eq. (II-5) utilizing the directly measured values of B_{oz} and B_{Rz}. This calculation yielded the value T = 13.5% in amazingly good agreement with the above result. From the knowledge of how the electrons are distributed as they precess around to the electron detector obtained from the film studies, the percentage of the transmitted electrons which actually impinged on the electron detector was then calculated. Correcting this value for the detector efficiency gave a calculated average detection efficiency of 5.0%. This value was in good agreement with the extrapolated results of the efficiency measurements. The detection efficiency should be nearly constant as a function of electron energy in the range from 0 to 300 keV since the only energy dependent factor is the detector efficiency and this has been found to be a very slowly varying function in this energy range.[14]

B. Experimental Effects

Several rather special effects had to be considered in carrying out the electron experiments. Of primary concern, was the question of electron energy loss between emission from the source and detection at the detector. The search for energy loss processes was instigated by the discovery of relatively large differences between simultaneous energy calibrations by X-rays and gamma rays and energy calibrations by electrons. After checking to make sure that the vacuum was sufficiently low so as to exclude electron energy loss due to collisions with gas molecules, the possibility of energy loss through radiation from the electrons as a result of their trochoidal motion in the magnetic field was investigated. The energy radiated per revolution was estimated from the following expression for energy radiated from electrons moving in circular orbits[15]

$$\Delta E = \frac{4\pi}{3} \frac{e^2}{4\pi\epsilon_o} \frac{1}{\rho} \beta^3 \gamma^4 \quad , \qquad \text{(III-1)}$$

where

ΔE = energy radiated/revolution ,

$\gamma = \frac{1}{\sqrt{1 - \beta^2}}$,

$\beta = v/c$,

ρ = radius of curvature .

This calculation for 500 keV electrons in a 6000 Gauss magnetic field yielded the value of 1.20×10^{-8} keV/revolution. Multiplying this quantity by the number of revolutions from source to detector for an electron moving on the symmetry plane, the negligible value of 2.08×10^{-6} keV for the total energy loss is obtained.

The discrepancy between the gamma ray and electron energy calibrations was finally discovered to be caused by a magnification of the effect of the intrinsic detector window. In tests where electrons were allowed to enter the detector along straight line trajectories in the absence of a magnetic field, the inherent detector window was found to shift the electron peak positions down in energy by one keV on the average. Electrons traveling in the magnetic steering field, however, were forced to enter the detector at very acute grazing angles on the average and hence "saw" a much larger window. The shifts experienced by the electrons in the magnetic steering device typically ranged from 2 to 6 keV depending on the detector age. Fortunately, the energy loss was ascertained to be linear as a function of energy from 0 to 650 keV.

The magnetic field had no observable effect on any of the detectors used in the electron experiments. The electron detector preamplifier, which was mounted near the detector, also showed no indication of magnetic field effects. The fission fragment trajectories were not altered to any significant extent by the magnetic field since the fragment flight paths were nearly parallel to the field and the radius of curvature of an average light fragment traveling in a 6000 gauss field directed perpendicular to the motion is more than 120 cm.

Another important consideration pertaining to the detection of electrons emitted by fission fragments in flight was the consequences of emission from a moving source. It is shown in Appendix B that the velocity of a relativistic electron in the laboratory coordinate system is related to its velocity in the center of mass coordinate system by the equation

$$V_{lab} = \frac{\left(\frac{V_F^2 - V_{cm}^2\beta^2}{V_F}\right)\cos\theta_{lab} + [(V_{cm}^2 - V_{cm}^2\beta^2\cos^2\theta_{lab} - V_F^2\sin^2\theta_{lab})(1-\beta^2)]^{1/2}}{1 - \frac{V_{cm}^2}{c^2}\beta^2\cos^2\theta_{lab} - \beta^2\sin^2\theta_{lab}} \qquad \text{(III-2)}$$

where V_F is the fragment velocity in the laboratory system, $\beta = V_F/c$ and θ_{lab} is the angle between the electron trajectory and the fragment trajectory (angle of emission) as measured in the laboratory system. Hence it is apparent that the laboratory energy of electrons emitted from moving fission fragments is a fairly rapidly varying function near $\theta_{lab} = 90°$. This fact is demonstrated in Fig. III-1 for a 40.0 keV transition arising from a fragment traveling at a velocity of 0.1036×10^{10} cm/sec (a mass 142 fragment) where the calculated difference between the electron energy as measured in the laboratory system and the electron energy in the center of mass system (transition energy) is plotted as a function of laboratory system emission angle. It is seen then that the shifts experienced by electrons emitted from moving fragments can be quite sizable.

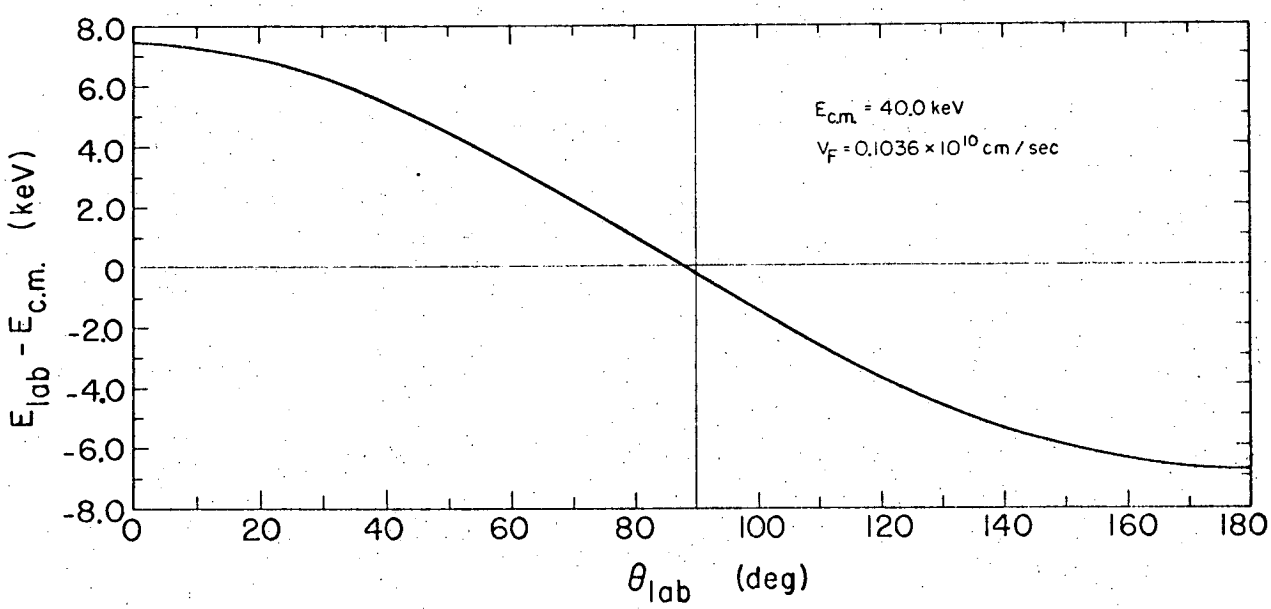

Fig. III-1. The difference between the laboratory and center of mass energies of an electron emitted from a moving fission fragment as a function of laboratory emission angle.

Since the acceptance angle of the magnetic steering device and size of the fission fragment detectors allowed the detection of electrons having a rather large spread of emission angles, it was expected that the measured electron peaks should show considerable broadening. Furthermore, this broadening effect should be smallest (on an absolute energy basis) for low energy electrons emitted from heavy fission fragments and increase rapidly with the electron energy and fragment velocity.

A rough estimate of the magnitude of this broadening effect in the present experiments may be obtained by using, for instance, the 40.0 keV example mentioned above. From Eqs. (II-4) and (II-7), the maximum acceptance angle Φ is calculated to be 8°. The average trajectory angle of fission fragments satisfying the coincidence requirement may be approximated from the calculations of Concus and Watson.[16] For configurations 1 and 2 the average fragment trajectory angle with respect to the detector-source axis is taken to be 13°. These two angles establish the approximate upper and lower limits of the average emission angle for an electron accepted into the steering device to be 111° and 69° respectively. By referring to Fig. III-1, it may be confirmed that the shifted energy difference between these two angles is 5.1 keV and combining this with a detector resolution of 3.0 keV (FWHM) ($\sigma^2_{total} = \sigma^2_{shift} + \sigma^2_{detector}$) results in a total resolution estimate of 5.9 keV. The experimentally measured resolution was found to be 4.7 keV. The variation of the energy resolution as a function of transition energy is considered in more detail in Section IV-B.

The relation between the angular distribution of the electrons emitted in the fragment system and the angular distribution of the electrons emitted in the laboratory system is given in Appendix B as

$$\frac{N(\theta_{lab})}{N(\theta_{cm})} = \frac{V_{lab}^2(V_{lab} - V_F\cos\theta_{lab})(1 - \beta^2)}{\left[V_{lab}^2(1 - \beta^2\sin^2\theta_{lab}) - 2V_{lab}V_F\cos\theta_{lab} + V_F^2\right]^{3/2}} \quad . \text{(III-3)}$$

Since the motion of the fission fragment causes an asymmetry about 90° in the angular distribution of electrons emitted in the laboratory system, it was important to determine how the measured electron peak positions were affected. Assuming an isotropic angular distribution in the fission fragment coordinate system, Eq. (VII-26) was used to calculate the anisotropy in the laboratory system. For the 40.0 keV electron example, the distribution was such that

$$\frac{N(0°_{lab})}{N(90°_{lab})} = 1.2108$$

$$\frac{N(0°_{lab})}{N(180°_{lab})} = 1.4468$$

As a result of this anisotropy, the average angle of emission in the laboratory system was shifted to an angle less than 90° and hence, the measured electron peaks were shifted up in energy. It was necessary to calculate corrections for this effect so that the true transition energies could be determined from the first moments of the measured peak positions. The details of these corrections are discussed in Section IV-B.

C. Data Processing

Upon completeion of an experiment, the data which had been recorded on magnetic tape, was processed by means of a series of four programs on an IBM 7094 computer. A flow chart of the operation is shown in Fig. III-2.

The data, which consisted of three correlated pulse heights for each $F_1F_2e^-$ triple coincidence event, two correlated pulse heights for each F_1F_2 double coincidence stabilization event and one γ pulse height for each $\gamma\alpha$ coincidence stabilization event, was first sent through Program 1. This program plotted the stabilization distributions on the printer and computed the 1st and 2nd moments and the standard deviations of the light and heavy fragment peaks of the stabilization distributions and of the gamma ray stabilization peak. It then computed linear calibration equations for the fragment distributions by using the first moments of the light and heavy peaks for calibration points.

Program 2 used the 1st moment and energy calibration information to compute the fission fragment mass maps. These maps consisted of arrays in which fragment masses were calculated for each D1, D2 channel combination for those pairs which resulted in a total fragment kinetic energy (ET) between the limits of 150 and 230 MeV. An example of the computer printouts for two such mass maps are shown in Table III-1 and III-2. In Table III-1, it is seen that the mass of a fission fragment giving rise to a channel 90 pulse in dimension 1 and detected in coincidence with a fragment giving rise to a channel 66 pulse in dimension 2 is calculated to be 107.2. The mass of the dimension 2 fragment is found to be 137.5 from Table III-2.

The output of program 1 was then sent through Program 3 where the mass maps from Program 2 were used to sort the $F_1F_2e^-$ triple coincidence events and the F_1F_2 double coincidence stabilization events into mass intervals of two mass units. Once this had been done, the

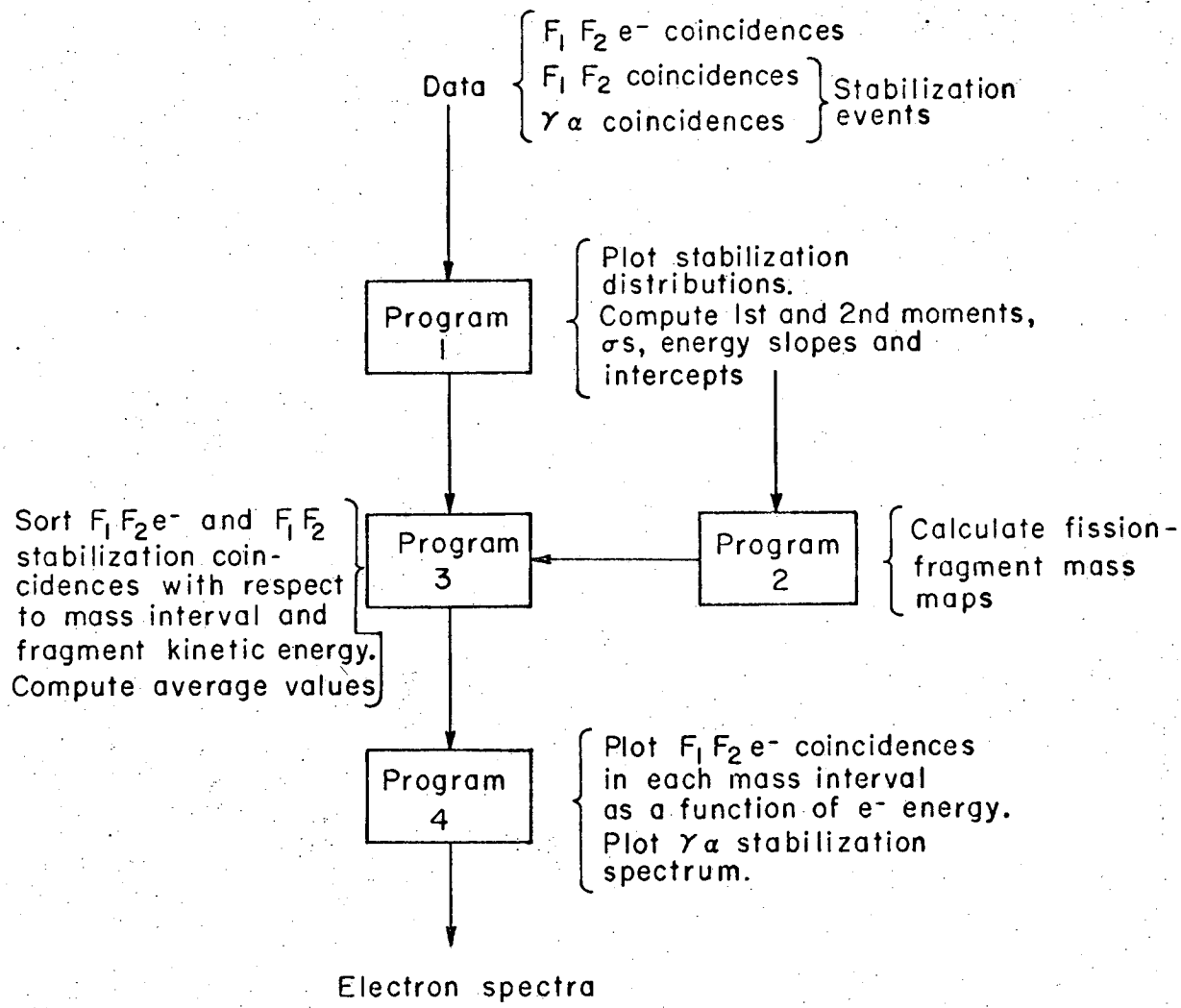

Fig. III-2. A flow chart of the computer processing operation.

Table III-1. MASS MAP WRT THE 1ST FISSION FRAGMENT IN TAPE DIMENSION 1..... 15C .LT. ET .LE. 230

DIM. 1	40	50	60	70	80	90	1C0	110	120	130
DIM. 2										
31	0.	0.	0.	0.	C.	0.	0.	0.	0.	0.
32	0.	0.	0.	0.	0.	0.	0.	0.	0.	0.
33	0.	0.	0.	0.	0.	0.	0.	79.075	0.	0.
34	0.	0.	0.	0.	C.	0.	C.	79.798	0.	0.
35	0.	0.	0.	0.	C.	0.	83.767	80.519	0.	0.
36	0.	0.	0.	0.	C.	0.	84.603	81.274	0.	0.
37	0.	0.	0.	0.	0.	0.	85.459	82.037	0.	0.
38	0.	0.	0.	0.	C.	0.	86.267	82.794	79.699	0.
39	0.	0.	0.	0.	C.	0.	87.005	83.549	80.368	0.
40	0.	0.	0.	0.	C.	0.	87.746	84.300	81.104	C.
41	0.	0.	0.	0.	0.	0.	88.491	85.103	81.750	0.
42	0.	0.	0.	0.	C.	91.422	89.114	85.913	82.492	79.573
43	0.	0.	0.	0.	C.	92.077	89.789	86.614	83.233	80.247
44	0.	0.	0.	0.	0.	93.055	90.475	87.347	83.966	8C.924
45	0.	0.	0.	0.	C.	94.021	91.149	88.081	84.697	81.627
46	0.	0.	0.	0.	C.	94.977	91.782	88.803	85.468	82.333
47	0.	0.	0.	0.	C.	95.785	92.429	89.475	86.240	83.037
48	0.	0.	0.	0.	C.	96.534	93.086	90.154	86.997	83.736
49	0.	0.	0.	0.	0.	97.284	93.794	90.839	87.700	84.431
50	0.	0.	0.	0.	C.	98.036	94.651	91.527	88.4C3	85.125
51	0.	0.	0.	0.	C.	98.695	95.497	92.181	89.105	85.854
52	0.	0.	0.	0.	100.420	99.257	96.321	92.829	89.773	86.575
53	0.	0.	0.	0.	100.936	99.913	97.081	93.484	90.433	87.288
54	0.	0.	0.	0.	101.466	100.546	97.795	94.146	91.096	87.959
55	0.	0.	0.	0.	102.008	101.119	98.507	94.888	91.761	88.626
56	0.	0.	0.	0.	102.526	101.687	99.214	95.657	92.422	89.291
57	0.	0.	0.	0.	103.022	102.271	99.897	96.416	93.053	89.942
58	0.	0.	0.	0.	103.538	102.868	1C0.495	97.166	93.687	90.574
59	0.	0.	0.	0.	104.069	103.369	1C1.099	97.883	94.323	91.208
60	0.	0.	0.	0.	104.642	103.917	1C1.708	98.550	94.961	91.84C
61	0.	0.	0.	0.	105.272	104.472	1C2.372	99.213	95.639	92.472
62	0.	0.	0.	0.	105.910	105.031	1C2.946	99.871	96.329	93.090
63	0.	0.	0.	105.480	106.559	105.556	1C3.526	100.525	97.010	93.696
64	0.	0.	0.	106.313	107.125	106.080	1C4.114	101.139	97.683	94.302
65	0.	0.	0.	106.933	107.605	106.614	1C4.708	101.726	98.345	94.907
66	0.	0.	0.	107.623	108.076	107.158	1C5.262	102.314	98.967	95.511
67	0.	0.	0.	108.933	108.582	107.715	1C5.818	102.902	99.583	96.132
68	0.	0.	0.	110.578	109.110	108.312	1C6.375	103.479	100.194	96.758
69	0.	0.	0.	115.717	109.744	108.913	1C6.934	104.036	100.800	97.377
70	0.	0.	0.	120.019	110.236	109.514	1C7.478	104.596	101.399	97.989
71	0.	0.	0.	123.991	110.716	110.1C6	1C8.CC9	105.158	101.965	98.594
72	0.	0.	0.	127.476	111.089	110.594	1C8.542	105.721	102.526	99.103
73	0.	0.	131.546	128.535	111.705	111.048	1C9.077	106.261	103.085	99.675
74	0.	0.	131.910	129.376	112.577	111.530	1C9.619	106.796	103.642	1C0.243
75	0.	0.	132.376	130.118	113.483	112.021	110.181	107.330	104.189	1C0.806
76	0.	0.	132.881	130.297	114.418	112.5C4	110.744	107.862	104.725	1C1.364
77	0.	0.	133.728	130.855	116.429	112.954	111.306	108.383	105.260	1C1.908
78	0.	0.	134.180	131.201	118.130	113.387	111.870	108.890	105.795	102.442
79	0.	0.	134.647	131.560	120.000	113.850	112.410	109.397	106.328	102.974
80	0.	0.	135.140	131.578	121.683	114.329	112.881	1C9.904	106.844	1C3.502
81	0.	0.	135.241	131.904	123.887	114.873	113.345	110.410	107.356	1C4.027
82	0.	0.	135.720	132.240	125.196	115.499	113.813	110.923	107.866	1C4.543
83	0.	140.157	136.228	132.570	126.612	116.221	114.288	111.442	108.373	1C5.055
84	0.	140.653	136.739	132.923	127.898	116.842	114.753	111.960	108.876	1C5.565
85	0.	141.164	137.259	133.296	128.847	117.5C8	115.186	112.475	109.366	1C6.073
86	0.	141.441	138.059	133.982	129.409	118.631	115.60C	112.989	109.853	106.577
87	0.	142.042	138.548	134.331	13C.013	119.679	116.018	113.474	110.337	1C7.C71
88	0.	142.643	139.044	134.695	130.718	120.733	116.440	113.908	110.820	1C7.614
89	0.	143.249	139.549	135.114	131.242	121.920	116.891	114.346	111.300	1C8.097
90	0.	143.898	140.063	135.551	131.613	123.012	117.360	114.785	111.786	1C8.577
91	0.	144.535	140.586	135.998	131.966	124.2C2	117.842	115.225	112.270	1C9.054
92	0.	145.160	140.898	136.451	132.330	125.361	118.337	115.654	112.791	1C9.525
93	150.654	145.778	141.444	136.910	132.683	126.163	118.822	116.058	113.230	1C9.989
94	151.228	146.390	141.920	137.372	133.049	127.1C0	119.356	116.671	113.706	110.450
95	151.801	146.994	142.407	137.622	133.425	128.0C4	120.082	117.075	114.166	110.908
96	152.371	147.610	142.899	138.087	133.792	128.727	120.821	117.477	114.591	111.364
97	152.938	148.280	143.393	138.547	134.154	129.265	121.521	117.890	115.015	111.818
98	153.502	148.930	143.889	139.014	134.301	129.777	122.301	118.309	115.439	112.272
99	154.065	149.566	144.383	139.481	134.708	130.290	123.111	118.731	115.861	112.724
100	154.622	150.188	145.021	139.948	135.119	130.792	123.877	119.156	116.281	0.
101	155.172	150.797	145.472	140.415	135.534	131.2C9	124.717	119.582	116.682	0.
102	155.714	151.394	145.928	140.883	135.955	131.578	125.608	120.002	117.064	0.
103	156.250	151.829	146.387	141.354	136.393	131.948	126.240	120.451	117.445	0.
104	156.777	152.442	146.848	141.824	136.834	132.347	126.860	120.985	117.824	C.
105	157.324	152.862	147.310	142.467	137.274	132.737	127.548	121.556	118.202	0.
106	157.861	153.287	147.785	142.909	137.713	133.127	128.224	122.092	118.587	0.
107	158.385	153.715	148.262	143.351	138.384	133.519	128.781	122.597	118.979	0.
108	158.897	154.144	148.734	143.771	138.794	133.910	129.313	123.242	119.370	0.
109	159.397	154.575	149.202	144.171	139.198	134.297	129.760	123.865	0.	0.
110	159.835	154.991	149.665	144.574	139.591	134.965	13C.197	124.467	0.	0.
111	160.253	155.395	150.124	144.979	139.983	135.319	130.649	125.108	0.	0.
112	160.666	155.797	150.578	145.386	140.377	135.677	131.086	125.790	0.	0.
113	161.071	156.199	151.039	145.794	140.771	136.040	131.493	126.440	0.	0.
114	161.468	156.599	151.505	146.202	141.166	136.4C5	131.856	126.963	0.	0.
115	161.856	156.997	151.964	146.601	141.562	136.774	132.548	127.494	0.	0.
116	162.243	157.394	152.417	146.999	141.957	137.154	132.875	128.051	0.	0.
117	162.626	157.788	152.863	147.397	142.352	137.536	133.217	128.605	0.	0.
118	163.003	158.179	153.303	147.793	142.746	137.917	133.563	0.	0.	0.
119	163.375	158.567	153.737	148.189	143.139	138.298	133.911	0.	0.	0.
120	163.741	158.952	154.168	148.583	143.530	138.678	134.261	0.	0.	0.
121	164.075	159.333	154.517	148.980	143.919	139.056	134.609	0.	0.	0.
122	164.479	159.709	154.877	149.375	144.306	139.433	134.955	0.	0.	0.
123	164.787	160.082	155.236	149.766	144.677	139.802	135.303	0.	0.	0.
124	165.093	160.451	155.595	150.154	145.043	140.168	135.652	0.	0.	0.
125	165.395	160.818	155.953	150.539	145.4C9	140.533	136.CC2	0.	0.	0.
126	165.693	161.183	156.309	150.920	145.774	140.896	136.353	0.	0.	0.
127	0.	161.541	156.665	151.298	146.138	141.259	136.7C4	0.	0.	0.
128	0.	161.894	157.017	151.673	146.5C0	141.620	137.057	0.	0.	0.
129	0.	162.242	157.352	152.050	146.860	141.979	137.413	0.	0.	0.
130	0.	162.584	157.685	152.423	147.285	142.337	C.	0.	0.	0.

Table III-2. MASS MAP WRT THE 2ND FISSION FRAGMENT IN TAPE DIMENSION 2..... 150 .LT. ET .LE. 230

DIM. 2 \ DIM. 1	40	50	60	70	80	90	100	110	120	130
31	0.	0.	0.	0.	0.	0.	0.	0.	0.	0.
32	0.	0.	0.	0.	0.	0.	0.	0.	0.	0.
33	0.	0.	0.	0.	0.	0.	0.	163.946	0.	0.
34	0.	0.	0.	0.	0.	0.	0.	163.328	0.	0.
35	0.	0.	0.	0.	0.	0.	157.834	162.740	0.	0.
36	0.	0.	0.	0.	0.	0.	157.116	162.141	0.	0.
37	0.	0.	0.	0.	0.	0.	156.414	161.555	0.	0.
38	0.	0.	0.	0.	0.	0.	155.783	160.970	164.710	0.
39	0.	0.	0.	0.	0.	0.	155.252	160.367	164.240	0.
40	0.	0.	0.	0.	0.	0.	154.736	159.782	163.771	0.
41	0.	0.	0.	0.	0.	0.	154.268	159.230	163.356	0.
42	0.	0.	0.	0.	0.	148.498	153.860	158.697	162.873	165.846
43	0.	0.	0.	0.	0.	148.180	153.449	158.263	162.359	165.458
44	0.	0.	0.	0.	0.	147.423	153.035	157.788	161.825	165.067
45	0.	0.	0.	0.	0.	146.687	152.622	157.319	161.296	164.653
46	0.	0.	0.	0.	0.	145.964	152.245	156.869	160.824	164.234
47	0.	0.	0.	0.	0.	145.394	151.854	156.449	160.367	163.813
48	0.	0.	0.	0.	0.	144.896	151.457	156.023	159.917	163.328
49	0.	0.	0.	0.	0.	144.400	150.992	155.591	159.472	162.841
50	0.	0.	0.	0.	0.	143.894	150.328	155.155	159.024	162.359
51	0.	0.	0.	0.	0.	143.473	149.678	154.730	158.573	161.944
52	0.	0.	0.	0.	138.084	143.120	149.119	154.292	158.136	161.524
53	0.	0.	0.	0.	137.706	142.749	148.562	153.843	157.694	161.097
54	0.	0.	0.	0.	137.313	142.347	148.031	153.383	157.244	160.657
55	0.	0.	0.	0.	136.912	141.986	147.502	152.820	156.787	160.213
56	0.	0.	0.	0.	136.583	141.640	146.975	152.198	156.323	159.763
57	0.	0.	0.	0.	136.284	141.274	146.478	151.586	155.853	159.307
58	0.	0.	0.	0.	138.942	140.881	146.044	150.981	155.375	158.851
59	0.	0.	0.	0.	135.566	140.676	145.599	150.403	154.890	158.388
60	0.	0.	0.	0.	134.826	140.201	145.145	149.861	154.399	157.918
61	0.	0.	0.	0.	134.501	139.723	144.524	149.321	153.839	157.441
62	0.	0.	0.	0.	134.129	139.245	144.089	148.784	153.252	156.952
63	0.	0.	0.	130.750	133.732	138.825	143.645	148.249	152.671	156.460
64	0.	0.	0.	130.261	133.632	138.409	143.191	147.742	152.097	155.963
65	0.	0.	0.	130.119	133.440	137.977	142.728	147.253	151.529	155.462
66	0.	0.	0.	129.892	133.199	137.531	142.210	146.760	150.987	154.958
67	0.	0.	0.	129.143	132.900	137.071	141.694	146.264	150.450	154.409
68	0.	0.	0.	128.018	132.565	136.626	141.179	145.776	149.916	153.850
69	0.	0.	0.	123.947	131.913	136.174	140.662	145.303	149.385	153.296
70	0.	0.	0.	119.935	131.669	135.720	140.168	144.825	148.858	152.748
71	0.	0.	0.	116.147	131.420	135.278	139.692	144.342	148.348	152.204
72	0.	0.	0.	112.445	131.386	134.941	139.212	143.857	147.844	151.737
73	0.	0.	104.395	111.563	130.895	134.602	138.730	143.348	147.340	151.214
74	0.	0.	104.431	110.887	130.219	134.215	138.253	142.838	146.837	150.694
75	0.	0.	104.475	110.345	129.490	133.814	137.783	142.329	146.340	150.177
76	0.	0.	104.519	110.380	128.762	133.420	137.308	141.823	145.852	149.663
77	0.	0.	104.555	110.227	126.905	133.056	136.830	141.330	145.363	149.157
78	0.	0.	104.553	110.163	125.433	132.694	136.348	140.851	144.874	148.656
79	0.	0.	104.536	110.098	123.725	132.278	135.867	140.372	144.386	148.156
80	0.	0.	104.500	110.284	122.163	131.826	135.429	139.893	143.883	147.659
81	0.	0.	104.445	110.229	120.159	131.343	135.002	139.414	143.384	147.163
82	0.	0.	104.505	110.162	119.015	130.781	134.566	138.936	142.888	146.676
83	0.	99.081	104.487	110.136	117.748	130.000	134.119	138.463	142.395	146.190
84	0.	98.977	104.446	110.094	116.664	129.422	133.669	137.990	141.905	145.707
85	0.	98.859	104.382	110.031	115.961	128.780	133.235	137.517	141.429	145.225
86	0.	98.715	104.267	109.800	115.640	127.656	132.822	137.046	140.956	144.745
87	0.	98.558	104.187	109.728	115.260	126.658	132.403	136.603	140.485	144.261
88	0.	98.382	104.091	109.637	114.765	125.673	131.982	136.179	140.015	143.727
89	0.	98.186	103.976	109.535	114.549	124.555	131.564	135.751	139.548	143.251
90	0.	97.917	103.844	109.404	114.454	123.608	131.088	135.319	139.086	142.778
91	0.	97.623	103.697	109.256	114.311	122.467	130.574	134.884	138.626	142.309
92	0.	97.325	103.570	109.095	114.163	121.460	130.046	134.462	138.168	141.845
93	89.395	97.022	103.411	108.922	114.018	120.789	129.532	134.056	137.711	141.387
94	89.170	96.714	103.230	108.737	113.859	120.018	128.969	133.317	137.257	140.932
95	88.930	96.401	103.026	108.637	113.688	119.297	128.187	132.889	136.811	140.480
96	88.676	96.070	102.808	108.442	113.522	118.775	127.434	132.461	136.386	140.031
97	88.410	95.674	102.575	108.237	113.355	118.401	126.740	132.034	135.960	139.586
98	88.133	95.285	102.331	108.018	113.318	118.131	125.999	131.600	135.533	139.143
99	87.844	94.898	102.077	107.788	113.107	117.841	125.279	131.131	135.108	138.703
100	87.540	94.514	101.756	107.548	112.886	117.483	124.561	130.656	134.683	0.
101	87.231	94.133	101.490	107.299	112.655	117.192	123.782	130.181	134.273	0.
102	86.917	93.755	101.215	107.048	112.411	116.991	122.959	129.708	133.872	0.
103	86.599	93.506	100.930	106.790	112.158	116.838	122.425	129.210	133.471	0.
104	86.277	93.135	100.639	106.525	111.899	116.625	121.901	128.614	133.069	0.
105	85.923	92.880	100.338	106.180	111.633	116.389	121.352	128.001	132.667	0.
106	85.560	92.615	100.001	105.910	111.360	116.148	120.813	127.451	132.260	0.
107	85.201	92.342	99.660	105.634	110.950	115.859	120.414	126.985	131.848	0.
108	84.843	92.061	99.319	105.348	110.681	115.645	120.033	126.359	131.418	0.
109	84.486	91.775	98.977	105.065	110.405	115.388	119.742	125.752	0.	0.
110	84.103	91.483	98.636	104.774	110.128	114.925	119.469	125.164	0.	0.
111	83.842	91.193	98.294	104.477	109.847	114.675	119.174	124.567	0.	0.
112	83.517	90.900	97.953	104.175	109.561	114.418	118.838	123.968	0.	0.
113	83.193	90.602	97.593	103.867	109.269	114.152	118.525	123.395	0.	0.
114	82.868	90.301	97.221	103.556	108.973	113.880	118.283	122.942	0.	0.
115	82.549	89.996	96.852	103.241	108.672	113.602	117.843	122.493	0.	0.
116	82.239	89.689	96.485	102.922	108.369	113.313	117.604	122.042	0.	0.
117	81.928	89.380	96.122	102.601	108.063	113.019	117.350	121.596	0.	0.
118	81.617	89.068	95.761	102.278	107.755	112.721	117.089	0.	0.	0.
119	81.306	88.752	95.403	101.953	107.443	112.420	116.822	0.	0.	0.
120	80.995	88.435	95.054	101.628	107.130	112.116	116.550	0.	0.	0.
121	80.709	88.118	94.756	101.295	106.814	111.809	116.272	0.	0.	0.
122	80.322	87.802	94.455	100.954	106.498	111.500	115.989	0.	0.	0.
123	80.048	87.486	94.153	100.615	106.181	111.191	115.701	0.	0.	0.
124	79.772	87.171	93.848	100.277	105.862	110.878	115.409	0.	0.	0.
125	79.494	86.844	93.543	99.940	105.541	110.564	115.114	0.	0.	0.
126	79.215	86.513	93.236	99.605	105.220	110.248	114.815	0.	0.	0.
127	0.	86.184	92.929	99.272	104.897	109.932	114.513	0.	0.	0.
128	0.	85.858	92.624	98.940	104.575	109.614	114.208	0.	0.	0.
129	0.	85.534	92.319	98.606	104.253	109.296	113.898	0.	0.	0.
130	0.	85.213	92.014	98.266	103.857	108.978	0.	0.	0.	0.

average numbers of emitted neutrons, kinetic energies, velocities, yields and masses of the fragments falling in each mass interval were computed.

Finally, by means of Program 4, the electron pulse heights were plotted for each mass interval on a Cal-Comp plotter and resultant electron spectra obtained. The gamma ray spectrum used for stabilization was plotted at the same time and used as a check against experimental or processing malfunctions. A representation of the final spectra obtained after the computer processing is presented in Fig. III-3 in the form of a picture of a three dimensional model constructed by cutting the resultant electron spectrum for each mass interval out of plastic and mounting them side by side in order of increasing mass.

D. Mass Calculation

Several problems complicate the conversion of fission fragment kinetic energies as measured by semiconductor detectors into fission fragment masses. First of all, it has been found that for heavy ions the output pulse heights of semiconductor detectors are not strictly linear functions of energy alone because of the existance of a pulse height defect.[17,18] Secondly, the measured energies are those of the post-neutron-emission fragments since neutron emission occurs in a time less than 10^{-14} sec after scission. Therefore, the exact conversion of these energies to masses requires a knowledge of the numbers of neutrons which have been emitted.

In the present experiments, the energy to mass conversion was carried out by means of an iterative process which incorporated a mass dependent energy calibration, proposed by Schmitt et al.[19] and neutron corrections based on the measurements of Bowman et al.[20] The process was initiated for any given pair of coincident fission fragment pulse heights, designated as X_1 and X_2, by first computing their approximate energies from linear calibration equations established from the known

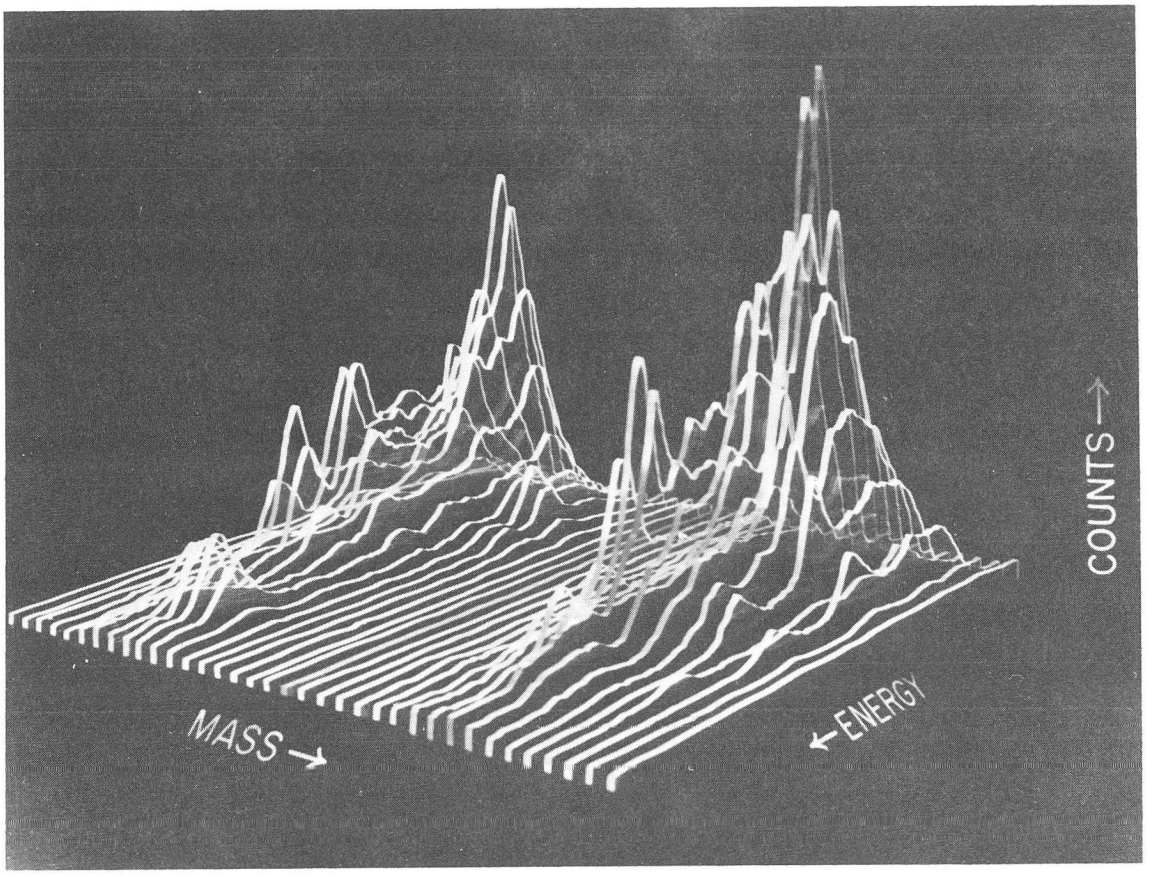

ZN-5696

Fig. III-3. A photograph of a three dimensional representation of the mass sorted electron spectra as a function of fragment mass.

energies of the 1st moments between the 3/4 points of the heavy and light fragment peaks. The 1st moments, P_L and P_H, were determined from the double coincidence stabilization distributions and set equal to energy values of 103.77 and 79.37 MeV, respectively.[19] Hence

$$E \simeq M X + b \qquad \text{(III-4)}$$

where

$$M = \frac{24.40}{(P_H - P_L)} \quad .$$

Conservation of momentum requires that

$$\frac{E_{1p}}{E_{2p}} = \frac{M_{2p}}{M_{1p}} \qquad \text{(III-5)}$$

where the subscript p denotes pre-neutron-emission quantities. Furthermore, it is obvious that

$$M_{1p} + M_{2p} = 252 \quad . \qquad \text{(III-6)}$$

Approximating E_{1p} and E_{2p} by substituting E_1 and E_2, approximate pre-neutron-emission masses were then calculated from the expressions

$$M_{1p} \simeq \frac{252}{\left(1 + \frac{E_1}{E_2}\right)} \quad , \quad M_{2p} \simeq 252 - M_{1p} \quad . \qquad \text{(III-7)}$$

Also, the total kinetic energy, E_T, was approximated by

$$E_1 + E_2 \simeq E_T = E_{1p} + E_{2p} \quad . \qquad \text{(III-8)}$$

The calculated values of M_{1p} and M_{2p} were next corrected for neutron emission from previous measurements of the average number of neutrons emitted as a function of E_T and the average number of neutrons emitted as a function of mass.[20] A fit of the experimental data of Bowman et al. yielded the following functional dependence of the average total number of neutrons, ν_T, emitted in a ^{252}Cf fission event:[21]

$$\nu_T(M,E_T) = A(M)e^{-B(M)(E_T - 150.0)} \quad . \tag{III-9}$$

Values of the parameters A(M) and B(M) as well as values of the ratio of the number of light fragment neutrons over the number of heavy fragment neutrons are given in Table III-3 as a function of pre-neutron-emission mass.

After determining the numbers of neutrons emitted, first approximation, post-neutron-emission masses were calculated such that

$$M_1 = M_{1p} - \nu_1 \quad , \quad M_2 = M_{2p} - \nu_2 \quad . \tag{III-10}$$

At this point, "mass corrected" energy values were calculated from the pulse heights and the post-neutron-emission masses by means of the following mass dependent calibration equation:[19]

$$E' = (24.0203 + 0.03574\ M)\frac{X}{P_L - P_H} - (24.0203 + 0.03574\ M)\frac{P_L}{P_L - P_H} + 0.1370\ M + 89.6083 \quad . \tag{III-11}$$

The iterative process was then entered into by returning to Eq. (III-8) using the energy values obtained from Eq. (III-11) and recalculating the post-neutron-emission masses. This procedure was repeated until the difference in the mass values resulting from two consecutive iterations was less than 0.05%. On the average, not more than 4 iterations were required for convergence.

Table III-3. Neutron correction data.

	MASS LT. FRAG.	RATIO(LT./HVY.) AVE. NO. NEUTRONS	AVE. TOTAL NO. NEUTRONS (ET) = A EXP (-B (ET -150.))	
			A	B
1	80.0000	0.1500		
2	82.0000	0.1900	9.6000	0.0120
3	84.0000	0.2200	9.9000	0.0160
4	86.0000	0.2500	10.2000	0.0200
5	88.0000	0.2630	10.6000	0.0230
6	90.3000	0.3080	10.9500	0.0280
7	93.3000	0.4090	11.4000	0.0327
8	96.1000	0.5470	12.0000	0.0380
9	99.0000	0.5250	12.6000	0.0415
10	102.0000	0.5940	13.3000	0.0435
11	104.5000	0.7510	14.1500	0.0450
12	107.0000	0.9880	14.9000	0.0455
13	109.5000	1.2100	15.8000	0.0460
14	112.0000	1.5560	17.8000	0.0455
15	114.7000	1.9440	19.4000	0.0445
16	117.3000	2.9620	20.3000	0.0437
17	119.3000	5.2660	20.4800	0.0405
18	120.0000	6.0000	19.7000	0.0365
19	121.0000	6.7000	19.1000	0.0350
20	122.0000	7.0000	17.5000	0.0325
21	123.0000	6.5500	15.6000	0.0300
22	124.0000	5.5000	15.3500	0.0275
23	125.0000	3.8500	15.3000	0.0260
24	126.0000	1.0000	15.4000	0.0255
25	127.0000	0.2590	15.6000	0.0250
26	128.0000	0.1820	16.0000	0.0255
27	129.0000	0.1530	16.5000	0.0260
28	130.0000	0.1430	17.0000	0.0275
29	131.0000	0.1490	17.6000	0.0295
30	132.0000	0.1670	18.1000	0.0320
31	132.7000	0.1900	18.7000	0.0335
32	134.7000	0.3380	19.1500	0.0355
33	137.3000	0.5150	20.2500	0.0390
34	140.0000	0.6430	20.5000	0.0420
35	142.5000	0.8260	19.5000	0.0445
36	145.0000	1.0120	18.1000	0.0455
37	147.5000	1.3320	16.0000	0.0460
38	150.0000	1.6840	14.8000	0.0455
39	153.0000	1.9050	14.0000	0.0448
40	155.9000	1.8280	13.4500	0.0435
41	158.7000	2.4440	12.8000	0.0410
42	161.7000	3.2460	12.2000	0.0380
43	164.0000	3.8020	11.6000	0.0335
44	166.0000	4.0000	11.2000	0.0300
45	168.0000	4.5450	10.9000	0.0265
46	170.0000	5.2630	10.7500	0.0225
47	172.0000	6.6670	10.6000	0.0195
			10.4000	0.0160

Since the fragment masses are derived from measured fragment kinetic energies, any dispersion introduced into the energy measurements will also be reflected in the calculated mass distributions. It has been pointed out by Terrell[22] that, besides arising from instrumental effects and intrinsic detector resolution, a great deal of dispersion in the energy measurements arises as a result of the varying directions, energies and numbers of emitted neutrons. The combination of these effects has been found to give rise to a mass resolution of 4.8 amu (FWHM) in the present work. This was determined, as illustrated in Fig. III-4, for the 162 keV electron peak, by plotting the intensities of several conversion electron lines from the spectra given in Appendix D as a function of mass. Since each conversion electron line in reality belongs to a single isotope, the experimental dispersion involved in measuring a fragment mass may, in this way, be directly ascertained.

In comparing an experimentally measured mass distribution with the "true" mass distribution, the former is generally considerably broader, especially in the valley and light and heavy peak tail regions, as a result of the experimental mass dispersion. The usual way of removing this dispersion is by the method of Terrell[22] which by a symmetrical distribution function having a negative second central moment equal to the variance of the measured mass resolution function is folded into the experimental mass distribution. This procedure has the effect of reducing the variance of the mass distribution by an amount exactly equal to the variance of the experimental resolution function.

Assuming that the radiochemical mass distribution as measured by Nervik[23] is a good representation of the "true" mass distribution, comparison of the "uncorrected" measured mass distribution from the present experiments and the "true" mass distribution, as shown in Fig. III-5, yields surprisingly good agreement. Apparently the method used to calculate the measured mass distribution has the same resolving effect as

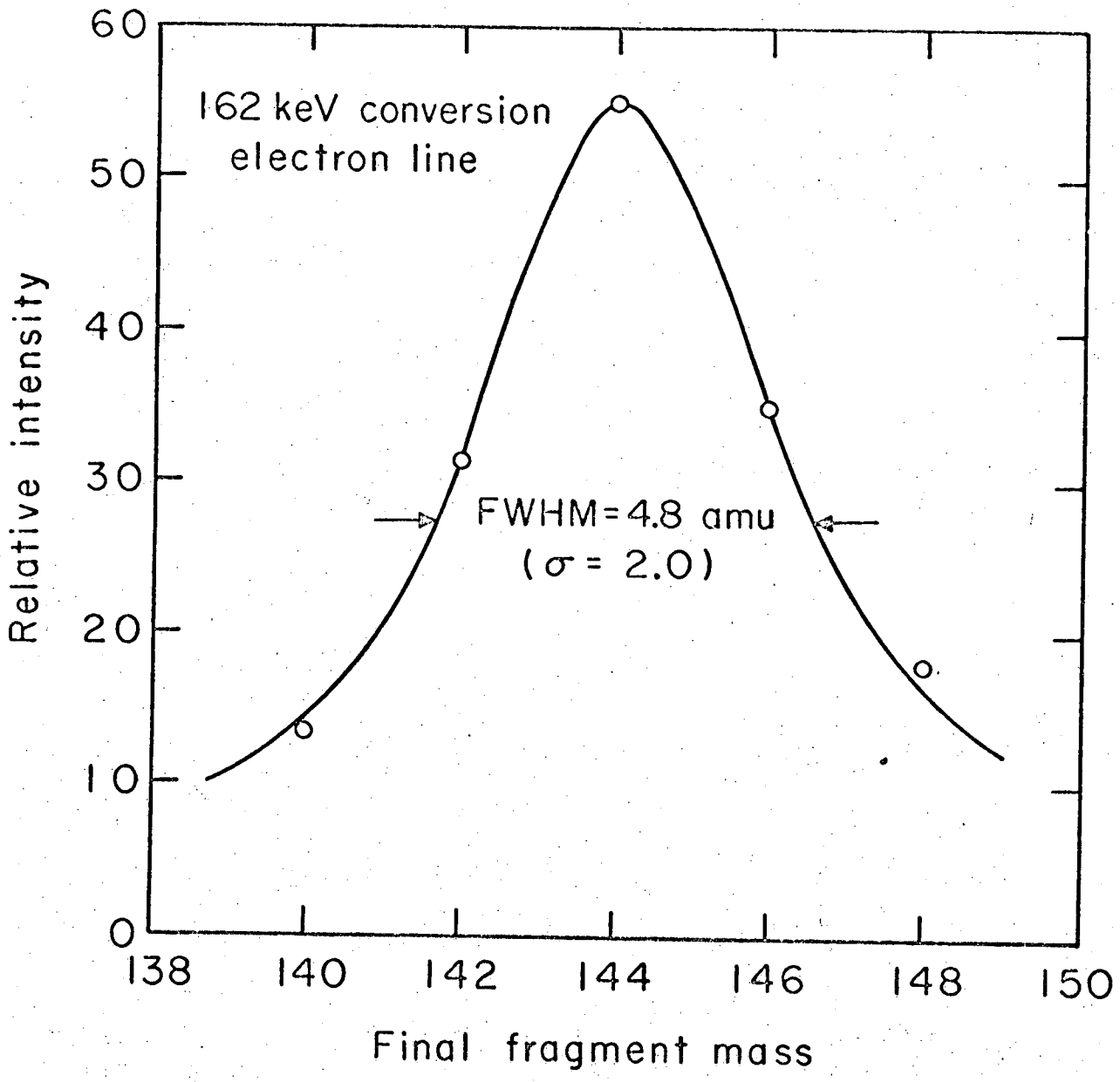

MUB-9905

Fig. III-4. An illustration of a direct determination of the experimental mass resolution by plotting the intensity of a single conversion electron as a function of the average mass of each mass interval in which it appears.

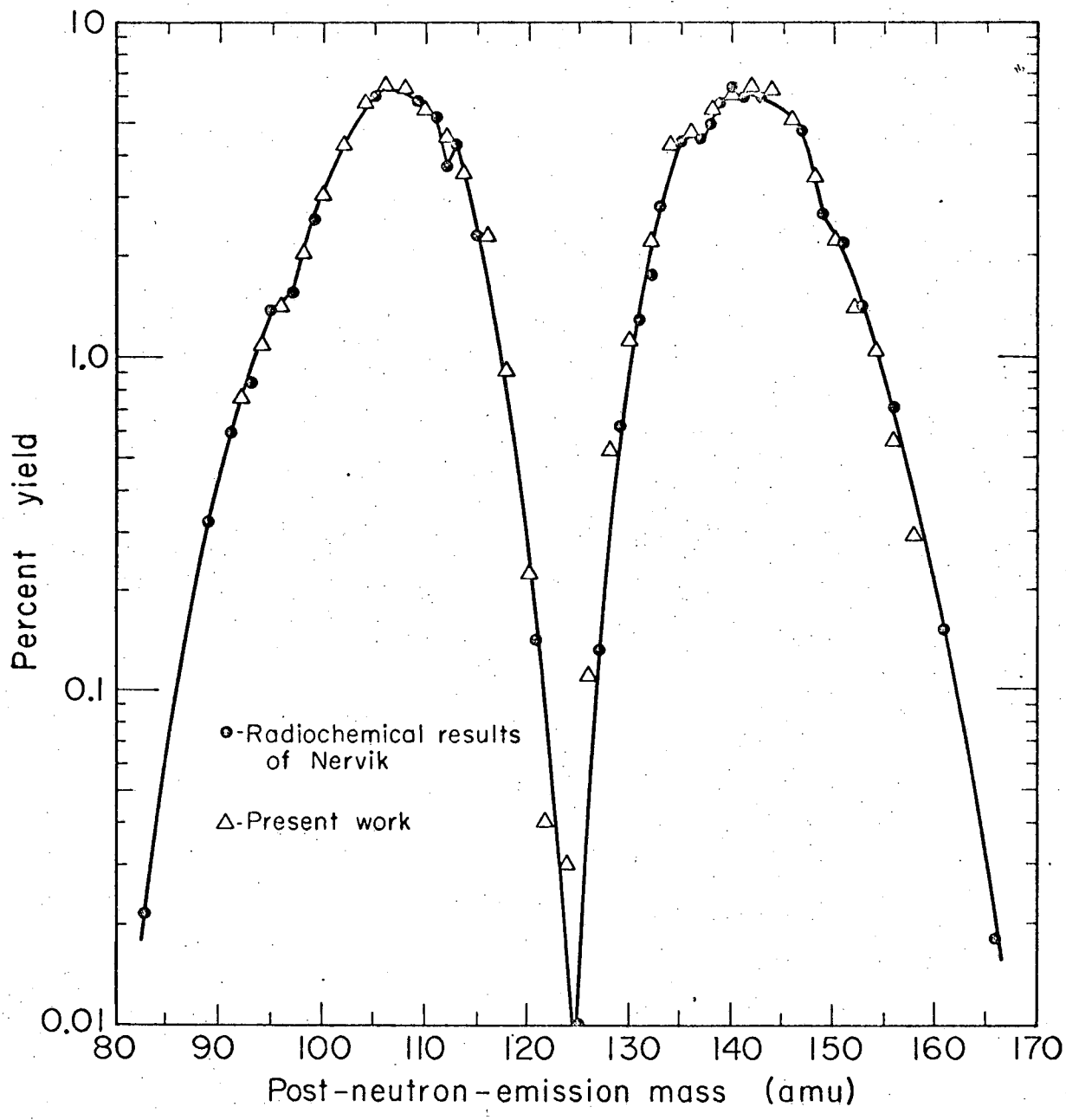

Fig. III-5. A comparison of the mass yields determined in the present experiments with the radiochemical results of Nervik.[23]

the procedure described above. On the basis of Fig. III-5, then, the usual mass dispersion correction was assumed to be unnecessary in these experiments. The average values arising from the mass calculations for a typical experiment are given in Table III-4 with respect to pre-neutron emission mass interval and in Table III-5 with respect to post-neutron emission mass interval. In both of these tables, number 2 quantities are with respect to the average mass of the listed mass interval, while number 1 quantities refer to the average coincident mass. The headings NU, E_T, E, and V refer to number of neutrons, total kinetic energy, fragment kinetic energy, and fragment velocity respectively.

Table III-4. D O U B L E C O I N C .

A V E R A G E V A L U E S

W R T. MASS B E F O R E NEUTRON EMISSION

MASS INTERVAL		TOTAL COUNTS	NU TOTAL	NU 1	NU 2	AFTER NU EMIT. MASS 1	MASS 2	BEFORE--AFTER NU EMIT. ET	E1	E2	V1	V2
91	93	504.	4.39	3.18	1.21	159.39	92.61	177.83	64.08	111.00	0.886	1.518
93	95	2534.	5.07	3.52	1.55	157.91	94.09	173.94	63.55	107.19	0.887	1.483
95	97	3589.	4.63	3.03	1.60	155.97	96.03	176.06	65.83	107.16	0.907	1.467
97	99	5276.	4.37	2.85	1.52	153.94	98.06	177.29	67.74	106.65	0.926	1.448
99	101	7809.	4.04	2.61	1.43	151.93	100.07	179.24	69.99	106.54	0.947	1.432
101	103	10448.	3.73	2.33	1.40	149.94	102.06	181.13	72.25	106.31	0.967	1.416
103	105	14213.	3.55	2.07	1.48	147.97	104.03	182.91	74.49	105.90	0.988	1.400
105	107	17438.	3.44	1.83	1.61	145.97	106.03	184.67	76.77	105.36	1.009	1.384
107	109	18048.	3.52	1.70	1.82	144.01	107.99	185.97	78.79	104.51	1.029	1.367
109	111	18051.	3.80	1.67	2.12	142.02	109.98	186.55	80.49	103.13	1.047	1.347
111	113	15889.	3.93	1.55	2.38	140.01	111.99	187.78	82.54	102.16	1.068	1.330
113	115	13679.	4.17	1.48	2.69	138.02	113.98	188.74	84.45	101.00	1.087	1.312
115	117	10994.	4.32	1.30	3.02	136.05	115.95	189.77	86.47	99.86	1.108	1.295
117	119	8369.	4.39	0.99	3.41	134.09	117.91	191.24	88.84	98.86	1.130	1.280
119	121	5175.	4.65	0.69	3.96	132.12	119.88	192.51	91.14	97.62	1.152	1.264
121	123	2403.	5.23	0.67	4.56	130.12	121.88	191.95	92.40	95.43	1.168	1.242
123	125	1088.	5.36	0.79	4.57	128.39	123.61	193.48	94.29	94.99	1.189	1.231
125	127	203.	4.82	2.03	2.80	126.34	125.66	197.12	96.64	96.71	1.220	1.222
127	129	1418.	5.13	4.36	0.77	123.76	128.24	192.40	94.54	93.88	1.230	1.182
129	131	2816.	4.72	4.12	0.60	121.86	130.14	191.85	95.81	92.31	1.247	1.163
131	133	4771.	4.55	3.88	0.67	119.95	132.05	192.18	97.52	91.00	1.267	1.147
133	135	9476.	4.27	3.35	0.92	117.93	134.07	191.19	98.87	88.88	1.284	1.126
135	137	12258.	4.19	2.97	1.22	115.97	136.03	189.25	99.62	86.30	1.298	1.102
137	139	15151.	3.98	2.58	1.40	113.98	138.02	188.61	101.01	84.46	1.317	1.083
139	141	17485.	3.86	2.35	1.51	111.99	140.01	187.94	102.27	82.65	1.335	1.064
141	143	19478.	3.73	2.09	1.63	110.00	142.00	186.65	103.20	80.57	1.352	1.044
143	145	20228.	3.46	1.79	1.66	108.02	143.98	186.00	104.52	78.84	1.372	1.025
145	147	18491.	3.40	1.60	1.80	106.01	145.99	184.65	105.37	76.76	1.389	1.005
147	149	14181.	3.57	1.50	2.08	104.02	147.98	182.79	105.81	74.43	1.405	0.984
149	151	10409.	3.74	1.41	2.33	102.05	149.95	181.12	106.31	72.24	1.421	0.964
151	153	6979.	3.96	1.40	2.56	100.06	151.94	179.35	106.64	70.04	1.438	0.943
153	155	4669.	4.27	1.48	2.79	98.08	153.92	177.40	106.74	67.82	1.454	0.923
155	157	3109.	4.51	1.56	2.94	96.08	155.92	176.06	107.16	65.90	1.472	0.904
157	159	2214.	4.93	1.52	3.40	94.10	157.90	174.12	107.32	63.67	1.489	0.884
159	161	1288.	5.27	1.42	3.85	92.11	159.89	173.16	108.17	61.81	1.510	0.867
161	163	739.	5.78	1.35	4.43	90.10	161.90	171.66	108.62	59.74	1.530	0.848
163	165	395.	6.26	1.32	4.94	88.08	163.92	170.52	109.24	57.84	1.552	0.831
TOTAL		321265.					AVE.	185.58				
							SIGMA	9.73				

Table III-5. D O U B L E C O I N C .

A V E R A G E V A L U E S

WRT. MASS A F T E R NEUTRON EMISSION

MASS INTERVAL		TOTAL COUNTS	NU TOTAL	NU 1	NU 2	AFTER NU EMIT. MASS 1	MASS 2	BEFORE--AFTER NU EMIT. ET	E1	E2	V1	V2
91	93	2406.	5.38	3.77	1.61	154.56	92.06	172.46	62.62	106.49	0.880	1.482
93	95	3496.	4.86	3.21	1.66	153.13	94.01	174.83	65.04	106.60	0.901	1.467
95	97	4587.	4.61	3.00	1.60	151.33	96.06	176.03	66.91	106.07	0.919	1.447
97	99	6621.	4.29	2.78	1.51	149.65	98.06	177.73	68.95	105.92	0.939	1.432
99	101	9770.	4.03	2.53	1.51	147.93	100.04	179.37	71.06	105.56	0.958	1.415
101	103	14047.	3.84	2.24	1.60	146.13	102.03	181.20	73.38	105.11	0.980	1.398
103	105	18141.	3.71	1.96	1.75	144.28	104.01	183.15	75.83	104.59	1.003	1.381
105	107	20891.	3.65	1.73	1.92	142.36	105.98	185.34	78.40	104.18	1.026	1.366
107	109	20622.	3.77	1.60	2.17	140.25	107.98	186.91	80.76	103.22	1.049	1.347
109	111	17685.	3.95	1.46	2.48	138.07	109.99	188.16	83.07	101.98	1.073	1.326
111	113	14731.	4.00	1.27	2.73	136.04	111.96	190.10	85.68	101.22	1.098	1.310
113	115	11461.	3.99	1.00	2.99	134.10	113.90	192.23	88.49	100.50	1.124	1.294
115	117	7420.	3.92	0.68	3.24	132.18	115.90	195.45	91.91	100.31	1.153	1.282
117	119	2916.	4.36	0.58	3.78	129.77	117.87	196.72	94.52	98.64	1.180	1.260
119	121	699.	4.52	0.67	3.85	127.76	119.72	199.22	97.12	98.43	1.206	1.249
121	123	128.	5.10	1.87	3.23	124.73	122.17	195.08	95.53	95.60	1.210	1.219
123	125	84.	4.32	1.98	2.34	124.22	123.46	201.05	98.76	98.84	1.233	1.233
125	127	340.	5.08	4.20	0.88	120.24	126.68	193.44	94.64	94.86	1.227	1.192
127	129	1675.	5.26	4.53	0.73	118.69	128.05	190.73	93.97	92.70	1.230	1.172
129	131	3585.	4.83	4.20	0.63	117.07	130.10	191.19	95.84	91.53	1.251	1.155
131	133	7114.	4.94	4.05	0.89	114.95	132.11	189.40	96.59	88.89	1.267	1.130
133	135	13687.	4.34	3.17	1.17	113.62	134.03	189.38	98.87	87.05	1.290	1.110
135	137	15137.	4.26	2.80	1.46	111.71	136.03	187.55	99.87	84.33	1.307	1.085
137	139	17407.	3.95	2.42	1.53	110.07	137.97	187.74	101.71	82.93	1.329	1.068
139	141	20005.	3.80	2.15	1.65	108.27	139.93	186.62	102.81	80.87	1.347	1.047
141	143	20861.	3.53	1.83	1.70	106.52	141.95	185.84	104.13	79.03	1.367	1.028
143	145	20473.	3.37	1.57	1.80	104.67	143.97	185.03	105.40	77.14	1.388	1.008
145	147	16257.	3.36	1.40	1.97	102.72	145.91	183.96	106.48	75.07	1.408	0.988
147	149	11196.	3.55	1.32	2.23	100.56	147.90	182.15	107.09	72.61	1.427	0.965
149	151	7104.	3.75	1.32	2.43	98.36	149.89	180.64	107.73	70.37	1.447	0.944
151	153	4396.	4.14	1.43	2.71	95.95	151.91	178.26	107.75	67.75	1.465	0.920
153	155	3354.	4.39	1.41	2.98	93.69	153.92	176.84	108.41	65.57	1.488	0.899
155	157	1800.	4.74	1.30	3.44	91.38	155.88	175.82	109.55	63.36	1.514	0.878
157	159	931.	5.32	1.23	4.09	88.85	157.82	174.18	110.33	60.78	1.541	0.855
159	161	387.	5.89	1.21	4.68	86.24	159.87	173.32	111.56	58.50	1.573	0.833
161	163	178.	6.43	1.20	5.22	83.74	161.83	172.50	112.70	56.39	1.604	0.813
163	165	44.	7.21	1.13	6.08	80.87	163.92	169.73	112.90	53.29	1.634	0.785
TOTAL		321636.					AVE.	185.56				
							SIGMA	9.74				

IV. INTERPRETATION OF RESULTS

A. The Electron Energy Spectra

1. Gross Characteristics

The total electron spectra unsorted with respect to fragment mass are compared in Fig. IV-1 for three of the low energy experiments. The three sets of data were taken (a) with the fission source at the magnet symmetry plane, (b) with the fission source 1 cm from the magnet symmetry plane, and (c) with the fission source 2 cm from the magnet symmetry plane. With the source in these positions, electron detection was restricted to those electrons emitted by fission fragments which had traveled to within the distance intervals of 0 to 0.9, 0.1 to 1.9 and 1.1 to 2.9 cm from the fission source, the average detection position in each interval being 0.4, 1.0 and 2.0 cm from the fission source, respectively. Hence these three curves represent the energy spectra of electrons emitted from fragments of all masses at the approximate times of (a) 0.4 nsec, (b) 1.0 nsec, and (c) 2.0 nsec after fission.

Clearly visible in the gross spectra of Fig. IV-1 are well-defined electron peaks characteristic of the internal conversion of nuclear gamma transitions. Specifically, peaks are seen at energies of 25, 33, 42, 75, 90, 102, 118 and 150 keV. Furthermore, the structure displays a rapid increase in intensity and complexity with decreasing energy in accordance with the well-known dictates of the internal conversion process. The appearance of well-defined structure in the gross spectra of Fig. IV-1 is somewhat surprising considering the number of possible nuclides involved and the extremely large number of different energy levels available for gamma de-excitation in highly excited fission fragments. This observation suggests that perhaps the conversion electrons in fission are predominantly associated with a restricted small fraction of the total number of gamma transitions possible.

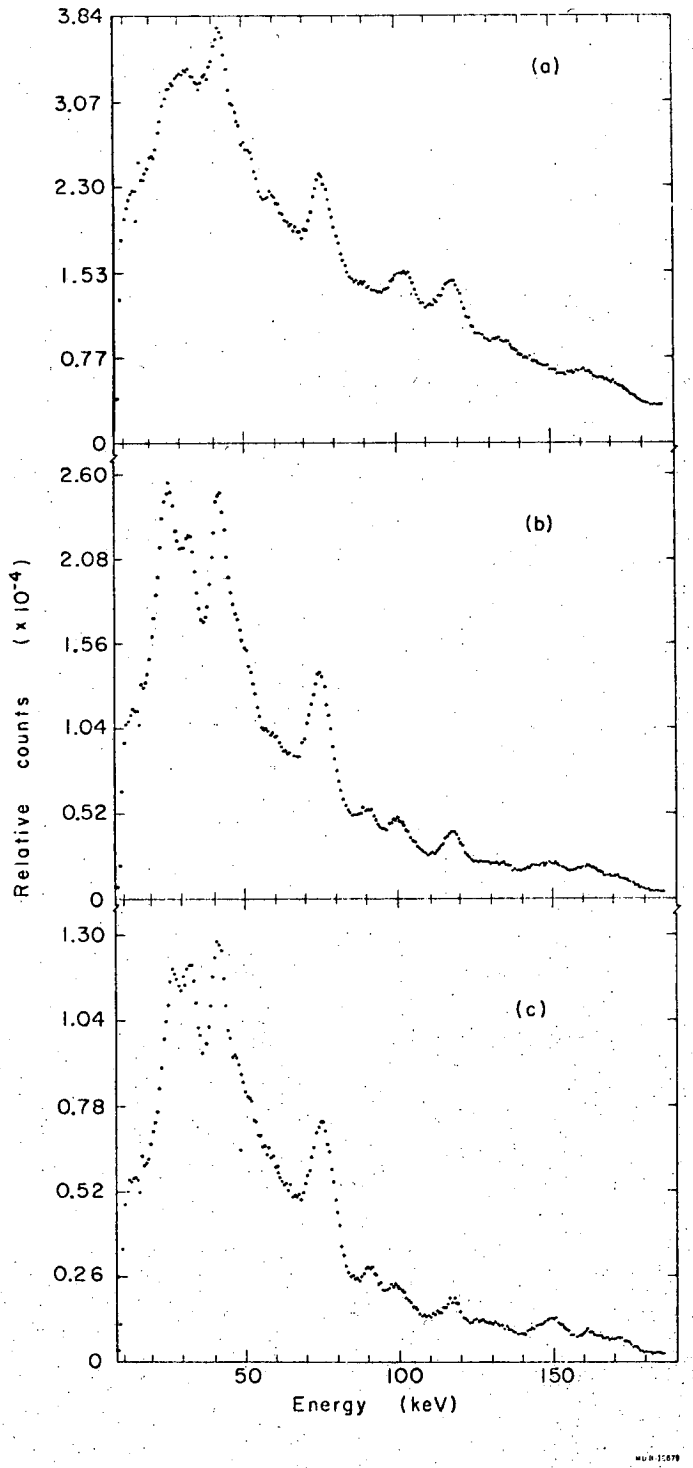

Fig. IV-1. Total energy spectra of electrons emitted in coincidence with fission fragments of all masses at the approximate average times of a) 0.4 nsec after fission b) 1 nsec after fission and c) 2 nsec after fission.

From an experimental standpoint, a particularly noteworthy feature of Fig. IV-1 is the extremely good energy reproducibility of the spectra considering they were obtained in three different experiments and under three different experimental configurations. It is also satisfying to note the easily discernable changes in relative peak intensities over the various time intervals represented by the three spectra. This observation lends confidence to the basic usefulness of the experimental method for determining halflives.

Using the total yields of electrons emitted in the three time intervals represented by the spectra in Fig. IV-1 a decay curve was constructed and found to be crudely analyzable in terms of a two component decay. The resulting halflives of the two components were found to be 0.17 and 2.6 nsec and the average yield of electrons per fission was calculated to be 0.60. Within the limits of error imposed by this greatly simplified treatment, these values are in agreement with the results reported by Atneosen et al.,[24] Glendenin and Griffin,[25] and Kapoor et al.[26] on measurements of K X-rays in coincidence with fission. These studies do indicate, however, that the electron yield per fission should be somewhat higher than the above value in order to account for internal conversion in the L shell and the emission of Auger electrons. The low energy cutoff in the present experiments was above the energies of the Auger electrons emitted from the light fragments and so these electrons are not included in the above yield estimate, but a yield of 0.60 electrons/fission still seems too low to account for contributions from L shell conversion and heavy fragment Auger electrons in light of the average X-ray yield per fission of 0.59 obtained by averaging the results of the above experimenters.

2. The Mass-Sorted Spectra

Mass-sorted spectra are shown in Fig. IV-2 for three heavy fragment mass intervals and in Fig. IV-3 for two light fragment mass intervals. They were obtained by sorting the data shown in the total spectrum in Fig. IV-1b (i.e. the experiment in which the source was 1 cm from the magnet symmetry plane) with respect to the masses of the coincident fragments. These spectra clearly display both well-resolved and complex structure which changes markedly from mass interval to mass interval. It is quite evident that sorting with respect to mass has indeed accomplished the desired effect of decreasing the complexity of the spectra to the point of making possible energy and mass assignments of numerous transitions.

Although the sorting process has greatly simplified the electron spectra, it has by no means reduced them to the realms of simple analysis for no restrictions have been placed upon the nuclear charges of isotopes contributing to the spectra. Therefore each spectrum contains possible contributions from at least three different elements. Moreover, complexity also arises from the fact that each electron peak is spread over 5 to 6 mass intervals due to the dispersion involved in measuring a fragment mass. The low energy portions of the heavy fragment spectra in Fig. IV-2 are further complicated by the appearance of KLL, KLM and KLN Auger electrons spanning roughly the energy region from 20 to 40 keV over the heavy fragment mass region.

A number of the electron peaks in Figs. IV-2 and IV-3 have been labeled alphabetically for use here in showing examples of possible K- and L-line combinations and for use in Section IV.A-3 in demonstrating the correlation between these electron data and the gamma ray measurements of Bowman[27] and Bowman et al.[28,29]. Possible K and L lines are denoted by the letters K and L preceding the identification letters.

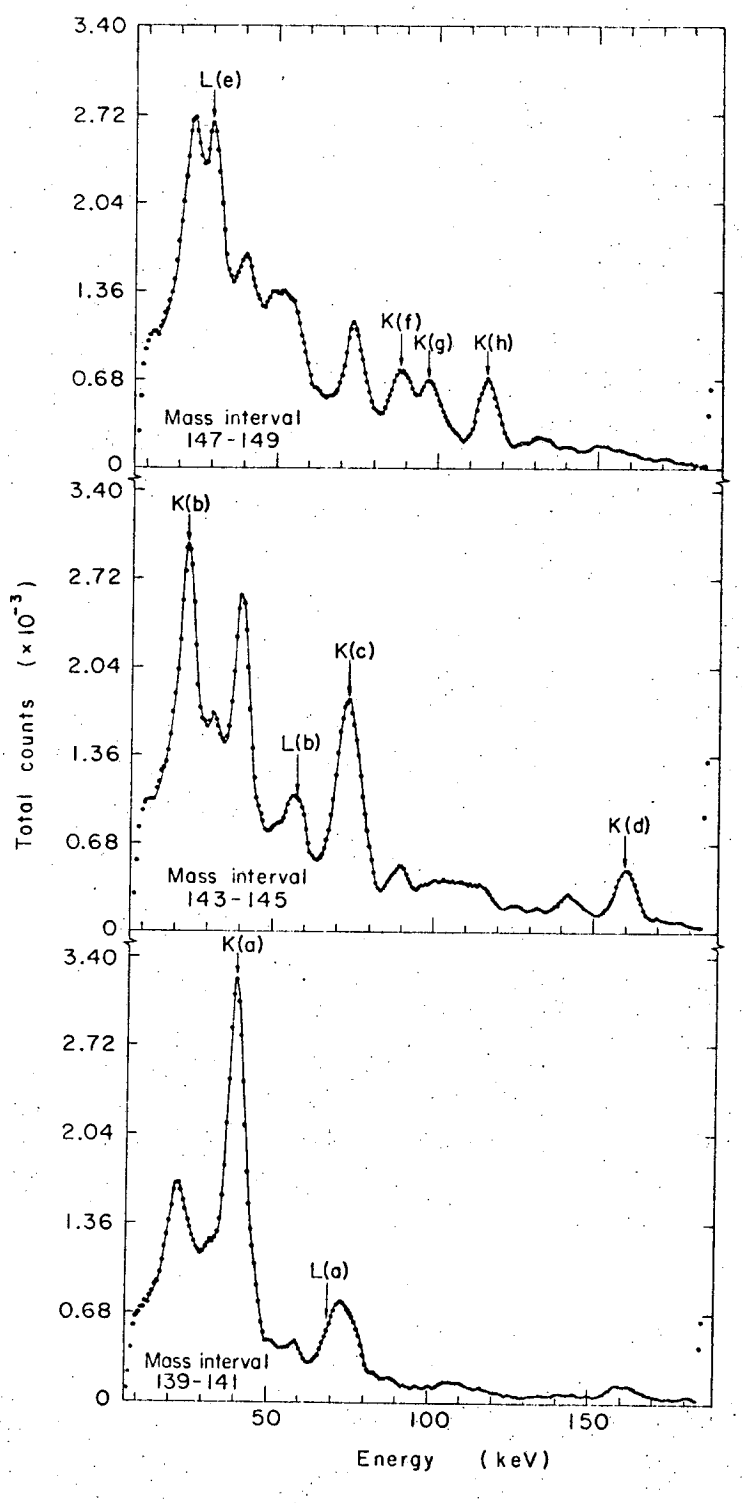

Fig. IV-2. Mass sorted spectra in coincidence with heavy fragments belonging to three different mass intervals taken at the approximate average time of 1 nsec after fission. A number of the peaks are labeled alphabetically for comparison with the associated gamma ray spectra and possible K and L conversion lines are indicated by the letters K and L preceding their identification letters.

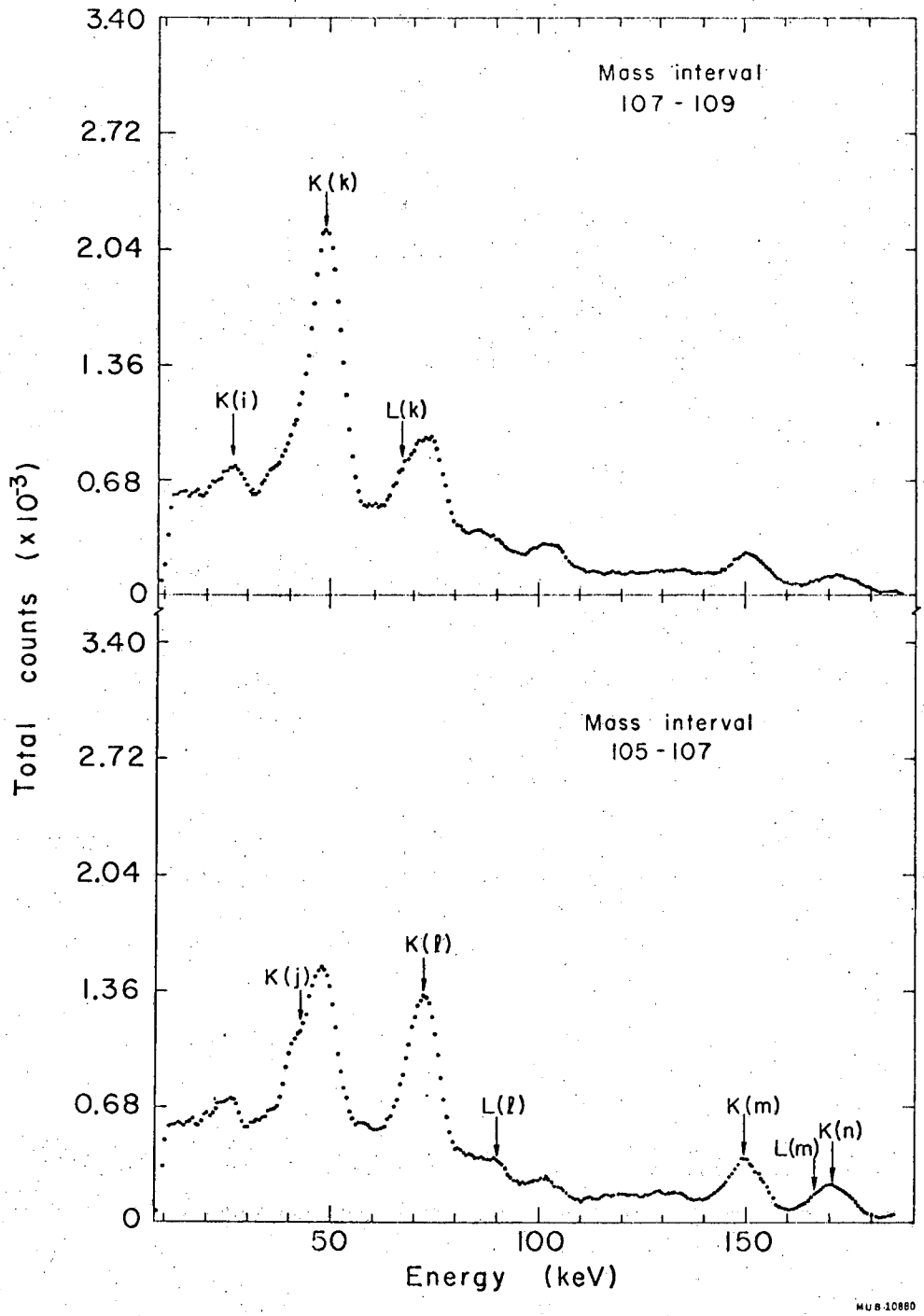

Fig. IV-3. Mass sorted spectra in coincidence with light fragments belonging to two different mass intervals taken at the approximate average time of 1 nsec after fission. Several examples of possible K and L conversion lines are indicated.

These tentative assignments were arrived at by looking for pairs of peaks displaying energy differences close to the differences in K and L binding energies of elements specified by the most probable charges for the given mass intervals. Theoretical values of K to L ratios were also useful in picking candidates for K and L pairs. Although the K to L ratio of a transition is quite sensitive to its multipolarity, the various ratios considered for these transitions can be limited, for the most part, to those arising for E1, M1 or E2 transitions, since higher multipolarity transitions can be ruled out on the basis of the lifetimes involved ($>>10^{-9}$ sec). Many of the peaks in these spectra quite obviously are complex and in order to obtain accurate K-L energy differences and K to L ratios account must be taken of the interfering structure. This problem is undertaken in Section IV-B.

In Fig. IV-4 are shown two spectra obtained in one of the high energy experiments. The electron intensities in this energy region are so low that it was only possible to obtain enough statistics to observe definite structure by using the experimental configuration in which the source was located at the magnet symmetry plane. Unfortunately, in this configuration, separation of electrons emitted by different members of fragment pairs is not possible and so these spectra contain contributions not only from the light fragments of mass 107-109 and 109-111 but also from the coincident heavy fragments of mass 137-139 and 139-141. Even so, these spectra are useful in illustrating the correspondence between the gamma-ray measurements and the electron measurements as will be seen.

Two low-energy spectra for the mass interval 145 to 147--one taken with the source 1 cm from the magnet symmetry plane ($\bar{t} \sim 1$ nsec) and the other taken with the source 2 cm from the magnet symmetry plane ($\bar{t} \sim 2$ nsec)--are compared in Fig. IV-5. It is interesting to note the changes in relative intensities of many of the peaks arising from their different rates of decay. In particular, the three sets of peaks located at 40, 55 and 73 keV show markedly different relative intensities in the two sets of data.

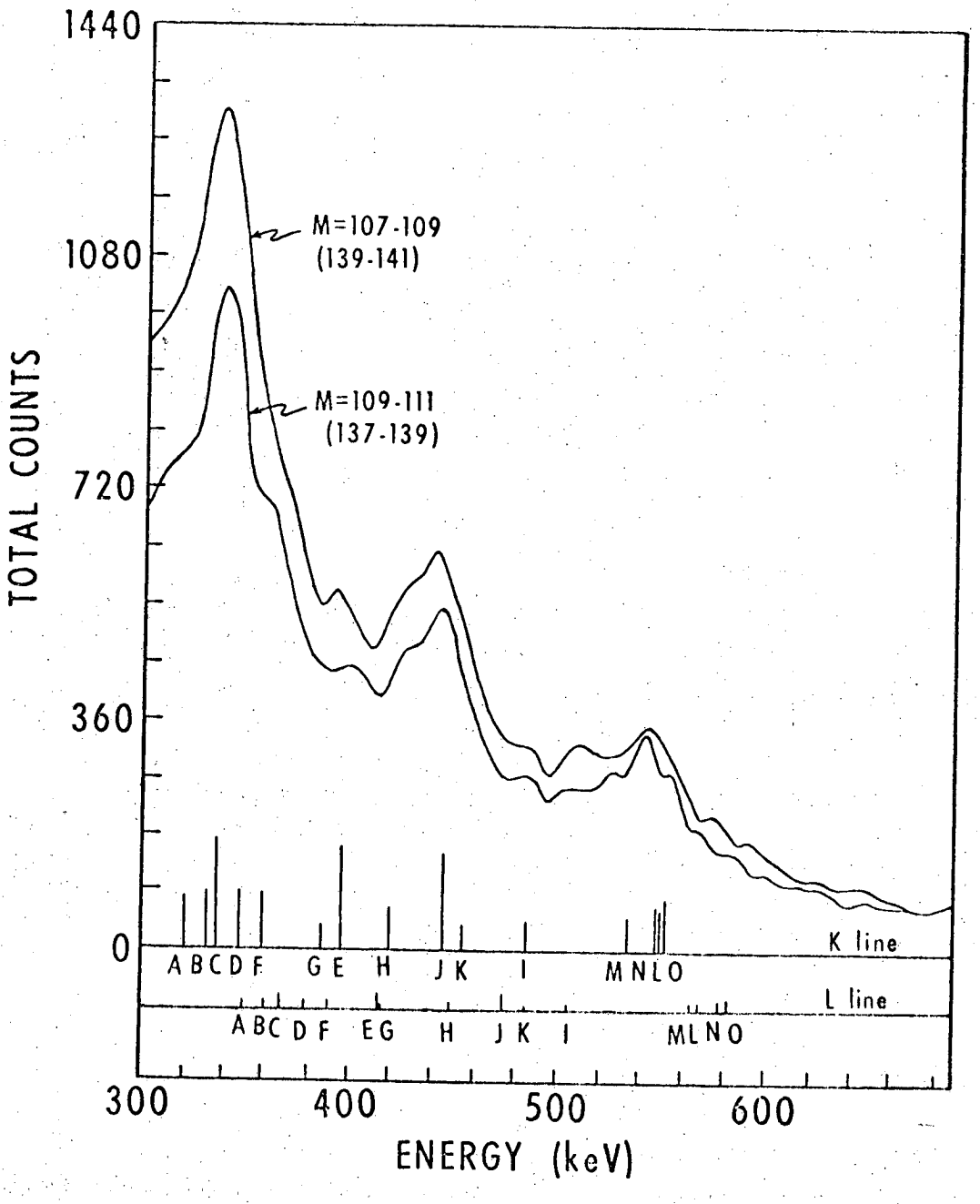

MUB-4811

Fig. IV-4. Combined electron spectra in coincidence with complimentary heavy and light fragment pairs having mass ratios of 1.25 and 1.30. The expected locations of K and L conversion lines as determined from their associated gamma rays are plotted below the spectra. As a rough guide, the line lengths are proportional to the gamma ray intensities.

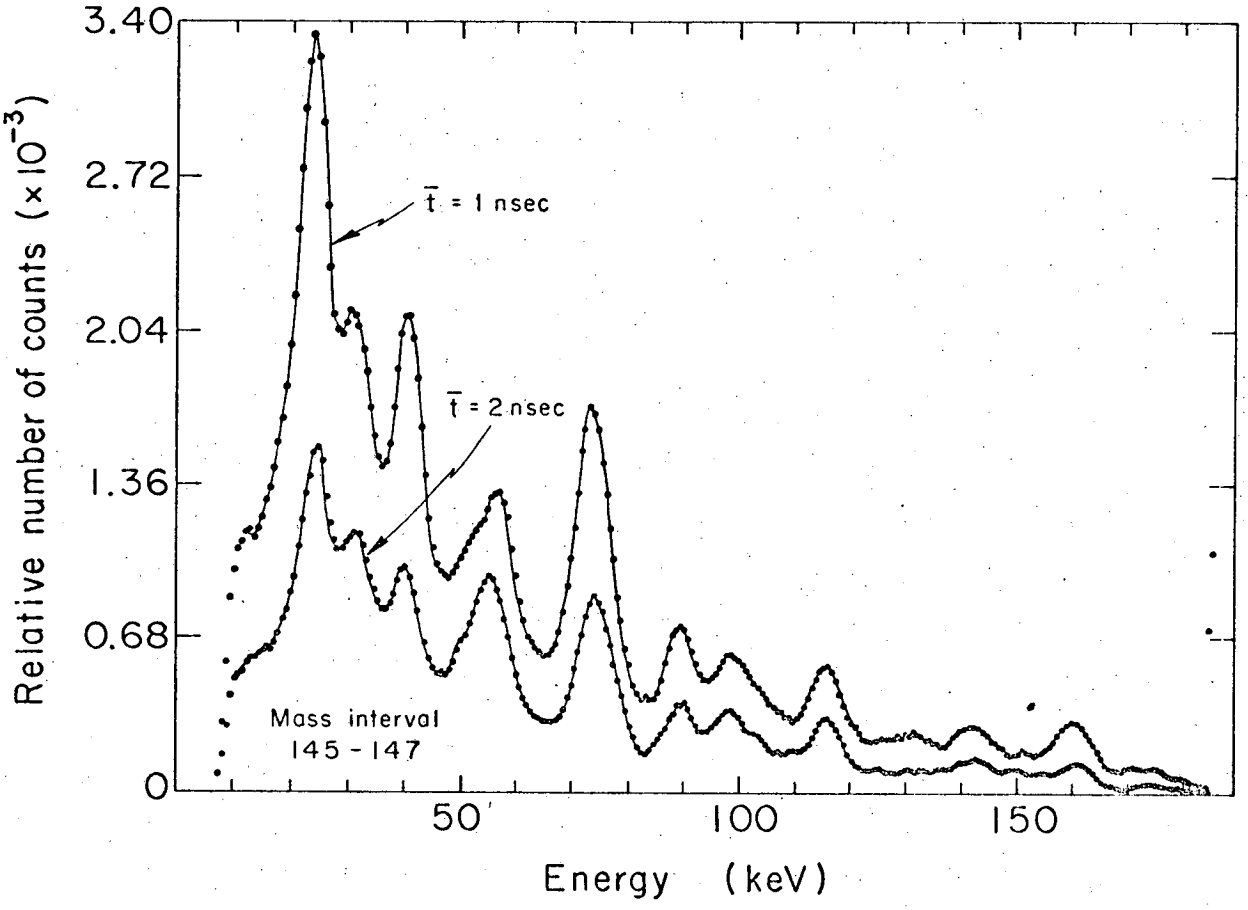

MUB-9908

Fig. IV-5. A comparison of two mass sorted spectra for a heavy fragment mass interval; one taken at an approximate average time of 1 nsec after fission and the other taken at an approximate average time of 2 nsec after fission.

Table IV-1. Observed electron peaks.

Observed Mass	Observed Electron or Electron Group Energy (keV)
100	193
102	132
104	24 127 272
106	43 72 150 170 290 448
108	25 48 101
110	38 126 216 234 545
112	51
114	22 301 312
116	100
134	257
136	223 320 261

Table IV-1. (cont'd)

Observed Mass	Observed Electron or Electron Group Energy (keV)
138	208
	338
	357
	450
140	41
	554
142	322
144	74
	144
	162
	193
	210
	243
	270
	292
	347
146	25
	57
148	90
	98
	117
	134
	153
	408
150	38
	51
154	157
156	44
	64
	84

The energies of all the peaks observed in these experiments over the energy range of 17 to 650 keV are listed in Table IV-1 along with the average masses of the mass intervals in which they appear in their highest intensities. Since many of the observed electron peaks are not single lines, but the sum of a number of lines, the energies of the peak centroids are not necessarily the correct electron transition energies, and the mass intervals at which the peaks appear in their highest intensities are not necessarily indicative of the true masses of the individual electron lines. For these reasons, the masses and energies listed in Table IV-1 are representative of the observed structure only as opposed to the analyzed structure to be presented in Section IV-B.

The complete set of electron spectra for all mass intervals taken in the low energy (10 to 180 keV) experiment with the source 1 cm off the magnet symmetry plane are given in Appendix D.

By summing the number of events in each electron spectrum over energy, the electron yield as a function of mass was obtained and is shown in Fig. IV-6 for the two time intervals 0.5 to 1.5 and 1.5 to 2.5 nsec after fission. These curves include only those electrons of energies between 10 and 180 keV. (Actually the low energy cutoff is somewhat higher than 10 keV since the Auger electrons from light fragments are not included in the yield curves of Fig. IV-6). The yields are seen to be quite sharply peaked at mass 108 and mass 150.5. Other noteworthy features included the extremely low yield observed near symmetric fission products, the slight discontinuities near masses 114 and 141, and the sudden drop in yield after mass 151.

In Fig. IV-7 the yield of electrons having energies from approximately 10 to 640 keV in the time interval 0.5 to 2.5 nsec after fission is compared with the X-ray measurements of Kapoor, Bowman and Thompson.[26] The solid line in this figure represents the number of K vacancies, resulting from internal conversion, as a function of mass and the dashed

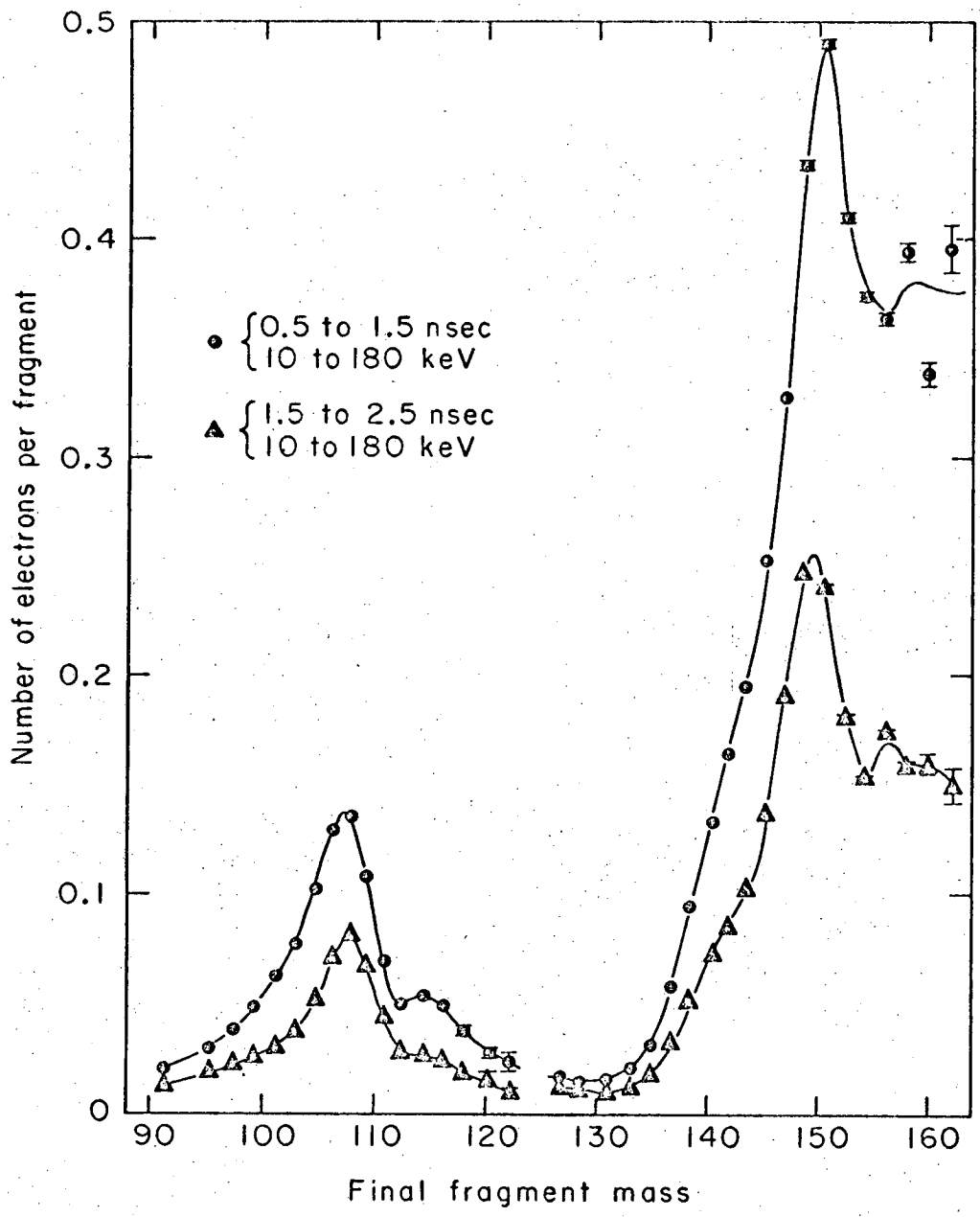

MUB-9906

Fig. IV-6. The low energy electron yield as a function of fragment mass over the two approximate time intervals of 0.5 to 1.5 nsec after fission and 1.5 to 2.5 nsec after fission.

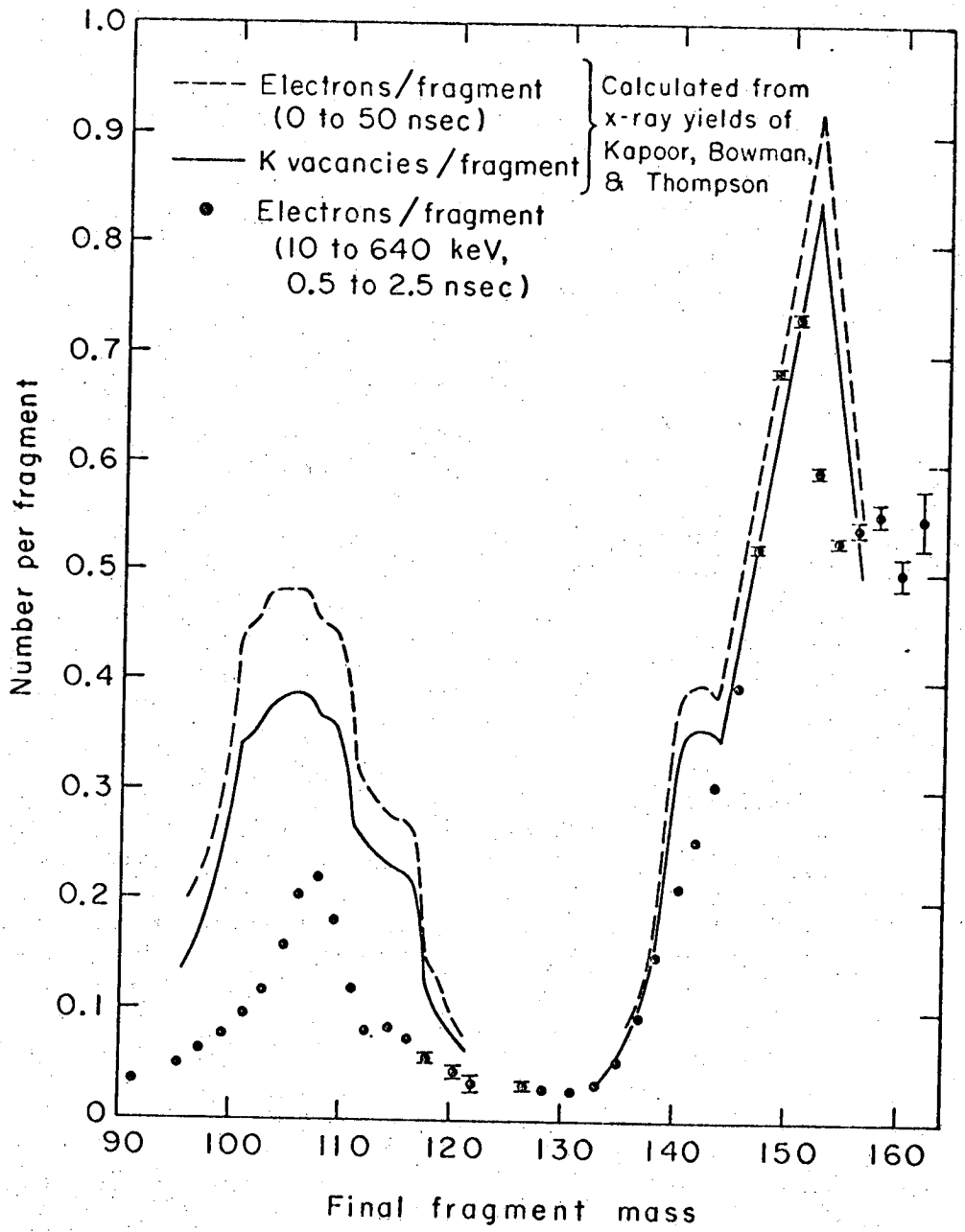

MUB-9907

Fig. IV-7. The total electron yield as a function of fragment mass over the approximate time interval of 0.5 to 2.5 nsec after fission. Also shown for comparison are the yield of K electrons and the yield of K vacancies as functions of mass over the time interval of 0 to 50 nsec after fission as calculated from the X-ray yields of Kapoor, Bowman, and Thompson.[26]

line represents the yield of K conversion electrons plus Auger electrons as a function of mass. Both of these curves have been calculated from the X-ray yields of Kapoor et al.[26] which cover the time interval from 0 to 50 nsec after fission. Although these curves are not useful in demonstrating quantitative agreement with the electron data, general qualitative agreement is quite evident. The general features of the electron yield as a function of mass presented in this figure also agree well with the data of Atneosen, Thomas, Gibson and Perlman.[24]

3. Correlation with γ-ray Measurements

Several experiments have been reported by Bowman et al.[28,29] in which the gamma rays emitted by ^{252}Cf fission fragments in flight within 50 nsec after fission have been measured. These experiments were basically similar to the present electron experiments in that the gamma rays were detected in coincidence with the fission fragments (by means of a lithium-drifted germanium detector), the fragment energies were measured and recorded with the energies of the coincident gamma rays, and the data were processed and sorted in a similar fashion. Spectra were taken with the detector positioned at 90° and at 0 and 180° with respect to the fragment flight path.

Three gamma-ray spectra obtained by Bowman[27] at 90° to the fragment flight path are shown in Fig. IV-8 for the same mass intervals as the electron spectra of Figs. IV-2 and IV-3. Since in the gamma-ray experiments there was no way in which detection could be limited to only those gamma rays emitted by a selected member of each fragment pair, these spectra contain gamma-ray lines from both the light fragments and the coincident heavy fragments belonging to the mass intervals specified in the figure.

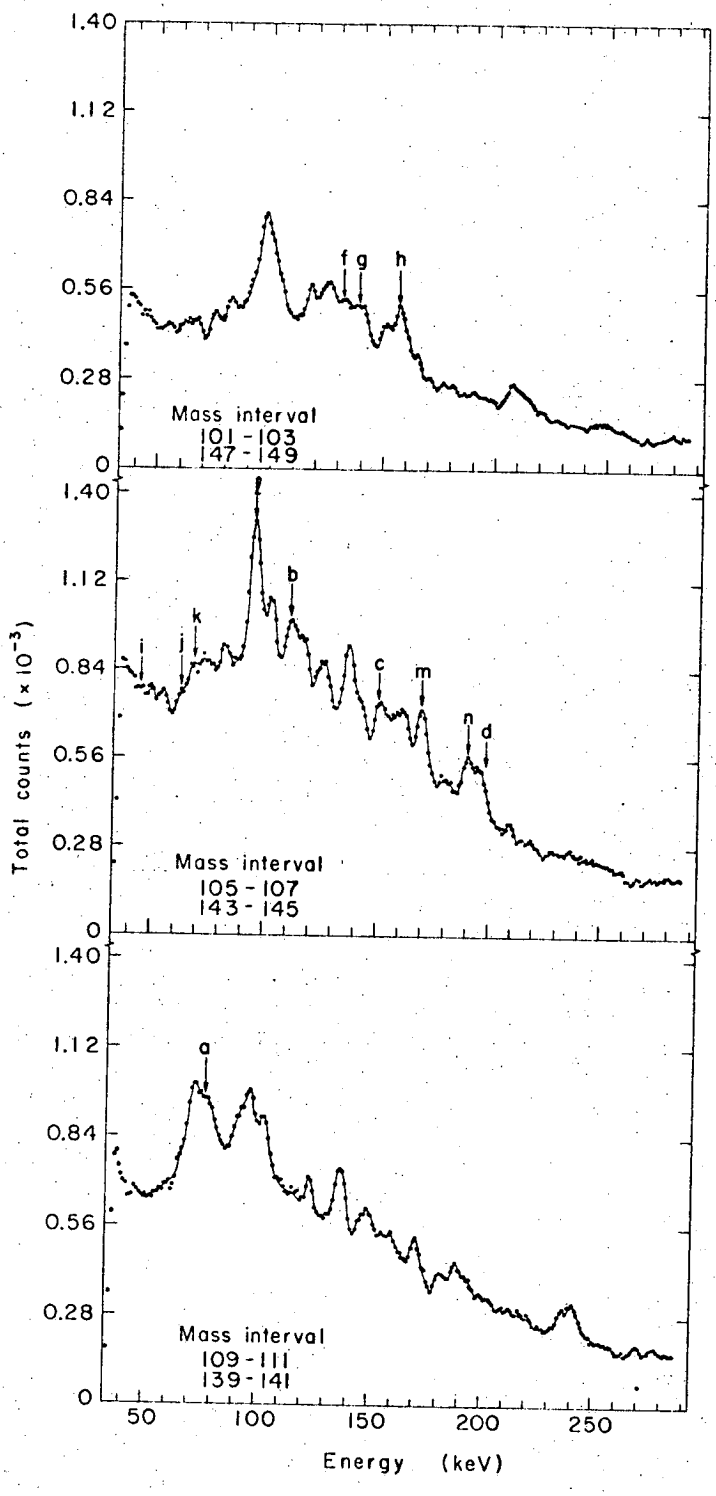

Fig. IV-8. Mass sorted gamma ray spectra in coincidence with complimentary heavy and light fragment pairs belonging to three different mass intervals. A number of the peaks are labeled alphabetically for comparison with the associated electron spectra.

In order to demonstrate the agreement between the electron results and the gamma-ray results, the approximate energies of gamma rays giving rise to the labeled K and L conversion electron lines in Figs. IV-2 and IV-3 were calculated from the binding energies of the most probable charge elements. The resulting gamma-ray energy positions are indicated by arrows and identified by the letters of the corresponding electron peaks in Fig. IV-8. As can be seen, excellent agreement is obtained in most cases. This test is extremely crucial for both sets of data and it is particularly reassuring at this point to find order evolving amidst the various complexities and uncertainties associated with these experiments.

Tentative assignment of gamma-ray-conversion-electron sets may be further tested by identifying the gamma rays as belonging to light or heavy fragments. For example if it could be shown that gamma ray ℓ in Fig. IV-8 does indeed belong to a light fragment, then its apparent correlation with the conversion electron peak ℓ in the light mass interval of 105-107 in Fig. IV-3 could be considered rather conclusive. If, on the other hand, it was shown that gamma ray ℓ was emitted by a heavy fragment, then most assuredly the correlation between these two peaks would be a mere coincidence. The method by which the gamma rays may be assigned to either light or heavy fragments is based upon observing their Doppler shifts in the 0 and 180° spectra. The 0 and 180° gamma ray measurements were made in an experimental configuration in which the fission fragment detectors were located 1 cm from the source. Therefore, any gamma rays which were emitted before the fragments had reached the detector received a Doppler shift due to the motion of the fragment. By sorting the data such that only those events were selected in which the heavy fragment was traveling toward the gamma detector (light fragment away from the detector) or in which the heavy fragment was traveling away from the gamma detector (light fragment toward the detector), the gamma rays can be identified as belonging to either light or heavy fragments by observing the directions of their Doppler shifts. An example

of this type of analysis is presented in Fig. IV-9 for the heavy fragment mass interval 143-145 and its complementary light fragment mass interval 103-105. In the top, middle and bottom spectra, the heavy fragment is moving toward, perpendicular to and away from the gamma-ray detector, respectively. The peaks are labeled alphabetically and those peaks which show either a light fragment shift or a heavy fragment shift are specified by the letter L or H following their identification letter. Those peaks displaying an unshifted component denoting emission after the fragment has stopped in the detector are specified by the letter U. It may be seen that peak ℓ (peak A in Fig. IV-9) does indeed belong to a light fragment in agreement with the evidence supplied by the previous comparison with the conversion electrons.

The same type of analysis has been applied to the mass 109-111 (137-139) interval spectra covering the energy range of 300 to 620 keV shown in Fig. IV-8. The spectrum in Fig. IV-10a is for the case of the heavy fragment traveling away from the detector (180°) and the spectrum in Fig. IV-10b is for the case of the heavy fragment traveling toward the detector (0°). Inspection of these spectra shows three peaks identified with light fragments (E,I,L) and twelve identified with heavy fragments. Using the gamma-ray energies as determined from these measurements, the expected location of the associated K and L conversion lines have been plotted below the high energy electron spectra in Fig. IV-4 assuming a most probable heavy Z of 53 and a most probable light Z of 44. As a rough guide, the line lengths are taken from the intensities of the gamma rays in Fig. IV-10. Again it is seen that there is good agreement between the two sets of data.

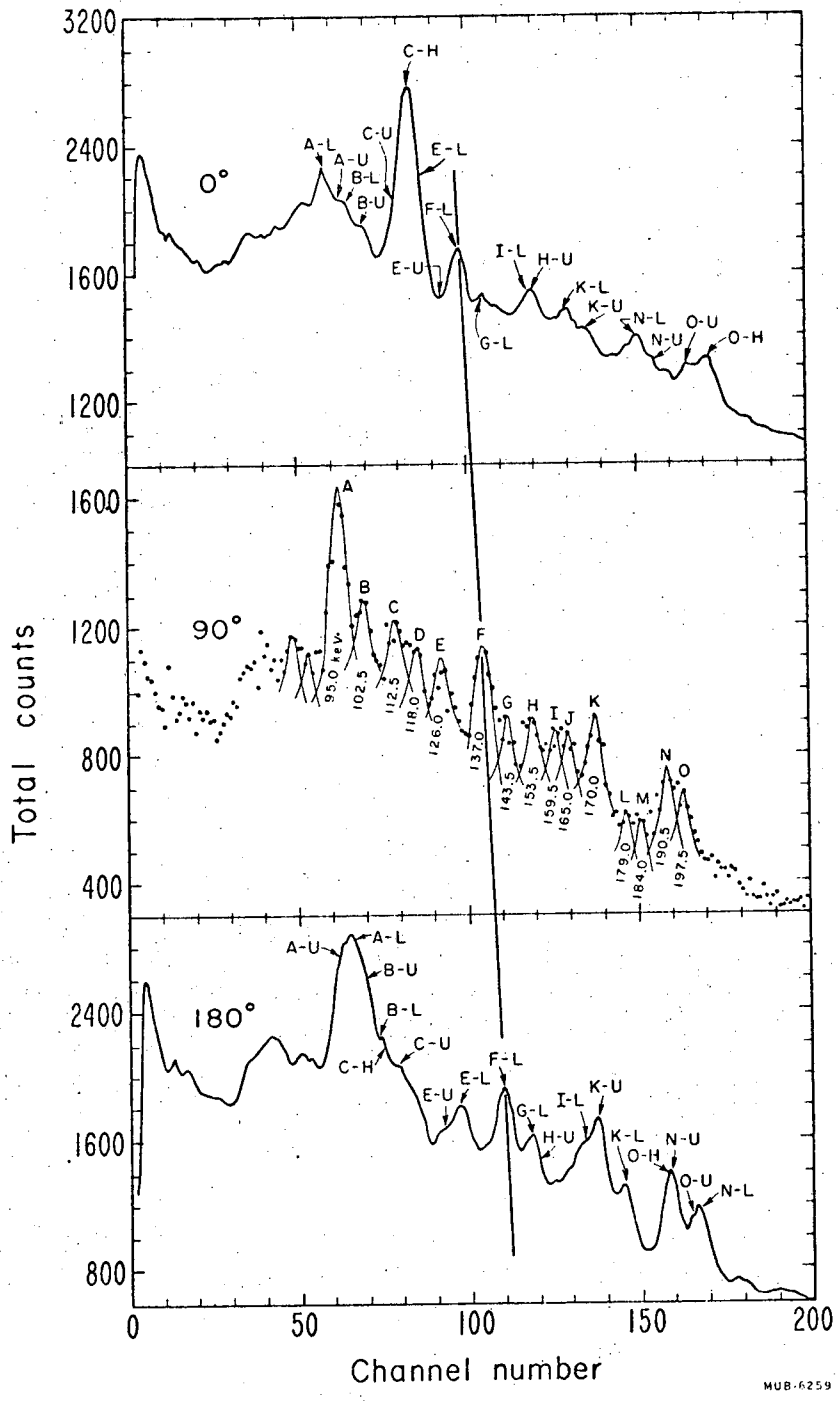

Fig. IV-9. Mass sorted gamma ray spectra in coincidence with mass (143-145)--mass (103-105) complimentary fission fragment pairs with heavy fragment moving toward (top), at 90° (center) and away (bottom) from the gamma ray detector. The gamma ray peaks are labeled alphabetically followed by the Letter L, H or U for peaks in a light fragment Doppler shifted position, a heavy fragment Doppler shifted position or an unshifted position respectively.

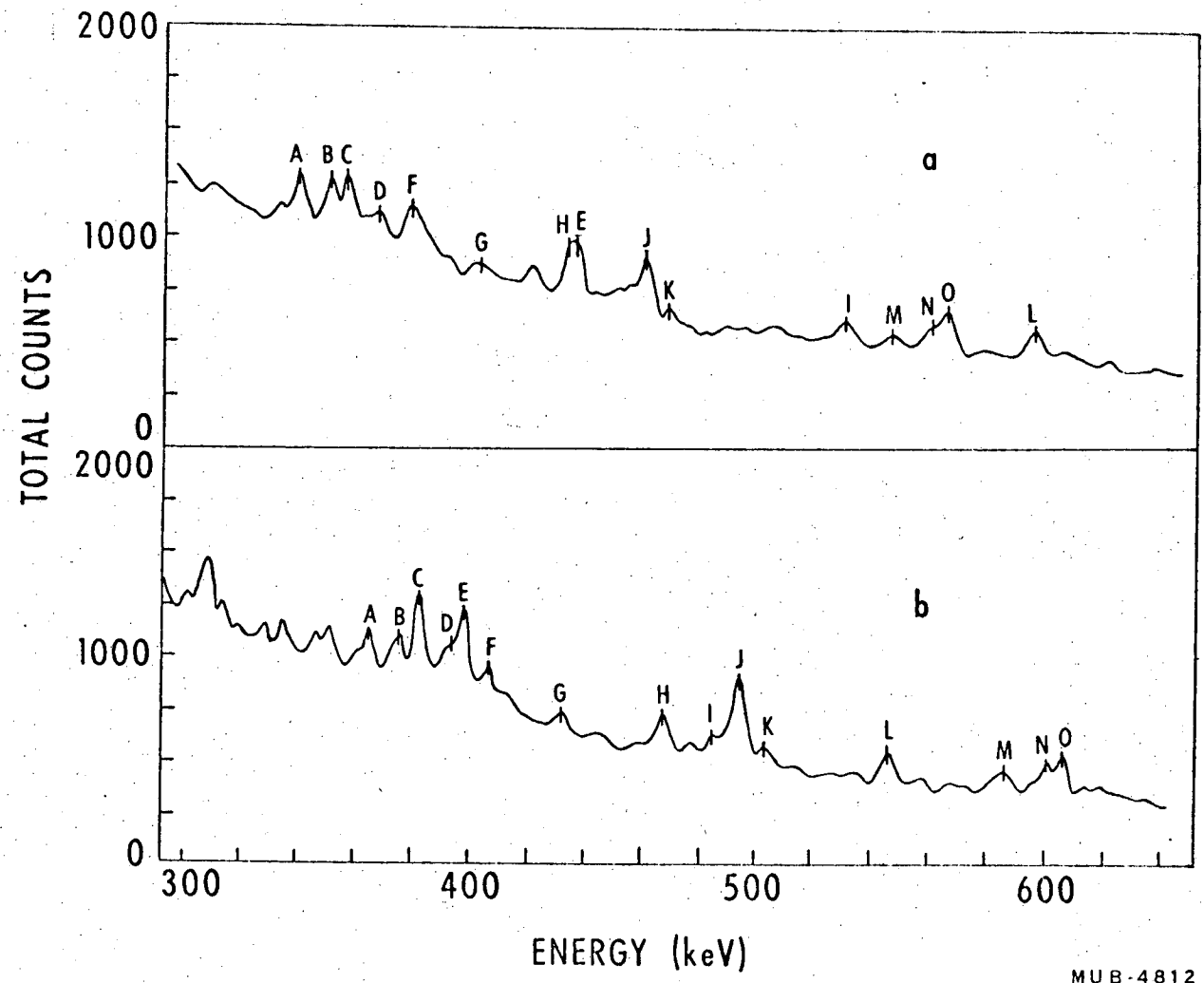

Fig. IV-10. Mass sorted gamma ray spectra in coincidence with mass (137-139)--mass (109-111) complimentary fission fragment pairs taken at a) 180° and b) 0° with respect to the fragment flight path.

B. Analysis of the Electron Spectra

1. Determination of the Electron Peak Characteristics

In order to untangle the complexities associated with the number of isotopes contributing to the electron spectra, it is important to have a knowledge of the shape and width of a single electron line measured under the same experimental conditions. Since, as was pointed out in Section III-V, detection was possible for electrons having a large spread of emission angles, and since the laboratory energy of an electron emitted from a moving source is a function of its angle of emission, it is evident that the peak shapes pertaining to these experiments are primarily dependent upon the way in which the relative probability of detection varies as a function of emission angle. The only recourse, under the circumstances, was to find some means of identifying a single line in the electron spectra for use in establishing the experimental peak shape characteristics.

As might have been expected from an inspection of Figs. IV-2, IV-3 and the figures of Appendix D, the electron peaks were found to be very nearly the shape of Gaussian functions. This fortunate state of affairs reduced the problem to that of establishing the standard deviation or width of a single electron line as a function of electron energy and fragment velocity. A satisfactory solution was obtained by formulating the problem in terms of an "effective" upper and lower limit to the range of experimental emission angles which resulted in electron detection. These "effective" angles are defined such that electrons emitted at the upper or lower effective emission angle receive energy shifts exactly equal to one half the full width at half maximum (FWHM) of the experimental electron peak (measured from the first moment energy of the peak). The procedure by which the effective emission angles in the center of mass system ($\theta_{cm\ 1}$ and $\theta_{cm\ 2}$) were calculated for a given

experimental electron peak associated with a fragment of average velocity V_F and having a first moment laboratory energy $\bar{E}_{lab}$, and standard deviation σ is outlined as follows:

1. Calculate the laboratory energies of the electron when emitted at the lower and upper effective emission angles ($E_{lab\ 1}$ and $E_{lab\ 2}$ respectively). By definition

$$E_{lab\ 1} = \bar{E}_{lab} + \frac{FWHM}{2} = \bar{E}_{lab} + 1.18\ \sigma_{shift}$$

$$E_{lab\ 2} = \bar{E}_{lab} - \frac{FWHM}{2} = \bar{E}_{lab} - 1.18\ \sigma_{shift} \quad ,$$

where $\sigma_{shift} = \sqrt{\sigma^2 - \sigma_{det}^2}$, σ_{det} being associated with the intrinsic detector resolution (the FWHM of a Gaussian function is equal to 2.36 σ). Then, convert these energies to velocities by means of the equation

$$V = \left[1 - \left(\frac{m_o c^2}{E + m_o c^2}\right)^2\right]^{1/2} c \quad . \qquad \text{(IV-1)}$$

2. Assume the average angle of emission in the laboratory system ($\bar{\theta}_{lab}$) is 90° and calculate the velocity of the electron in the center-of-mass system using Eq. (VII-16) of Appendix B.
3. Calculate the center-of-mass emission angles, $\theta_{cm\ 1}$ and $\theta_{cm\ 2}$, using Eq. (VII-20).
4. Calculate the average angle of emission in the center of mass system (θ_{cm}) by assuming that the probability of electron emission from moving fission fragments is a nearly constant function of emission angle for angles near 90° with respect to the fragment trajectory. Hence

$$\bar{\theta}_{cm} = \frac{\theta_{cm\ 1} + \theta_{cm\ 2}}{2}$$

5. Using the $\bar{\theta}_{cm}$ obtained in step 4, calculate $\bar{V}_{lab}$ by means of equation (VII-14), convert this to energy by means of the equation

$$E = m_o c^2 \left[\frac{1}{\sqrt{1 - (V/c)^2}} - 1 \right] \qquad \text{(IV-2)}$$

and compare with the initial $\bar{E}_{lab}$.

6. Based upon the comparison of step 5, assume a new $\bar{\theta}_{lab}$ and repeat steps 2 through 5.

7. Reiterate until self-consistency is reached.

Since the effective angles $\theta_{cm\ 1}$ and $\theta_{cm\ 2}$ are specified solely by the experimental configuration and hence do not depend upon the electron energy or fragment velocity, they may, once determined, be used to calculate the $\bar{E}_{cm}$ and σ_{shift} for any $\bar{E}_{lab}$ and V_F.

The determination of $\theta_{cm\ 1}$ and $\theta_{cm\ 2}$ was accomplished by applying the procedure outlined above to a large number of the experimental peaks over a range of energies and fragment velocities. The $\bar{E}_{lab}$'s and σ's of the various peaks used were accurately ascertained by fitting the peaks with Gaussian functions by means of a least squares computer program. A number of different values were obtained for $\theta_{cm\ 1}$ and $\theta_{cm\ 2}$ as was expected since it was not known beforehand which peaks were single lines and which were complex. However, it was easy to conclude which choice of values to take based upon the close consistency they displayed throughout the spectra. These values were 77° and 103°. The calculated dependence of σ on energy is shown in Fig. IV-11 for a number of fragment velocities (mass intervals) and it is noted that σ is a rather rapidly increasing function of both the electron energy and the fragment velocity.

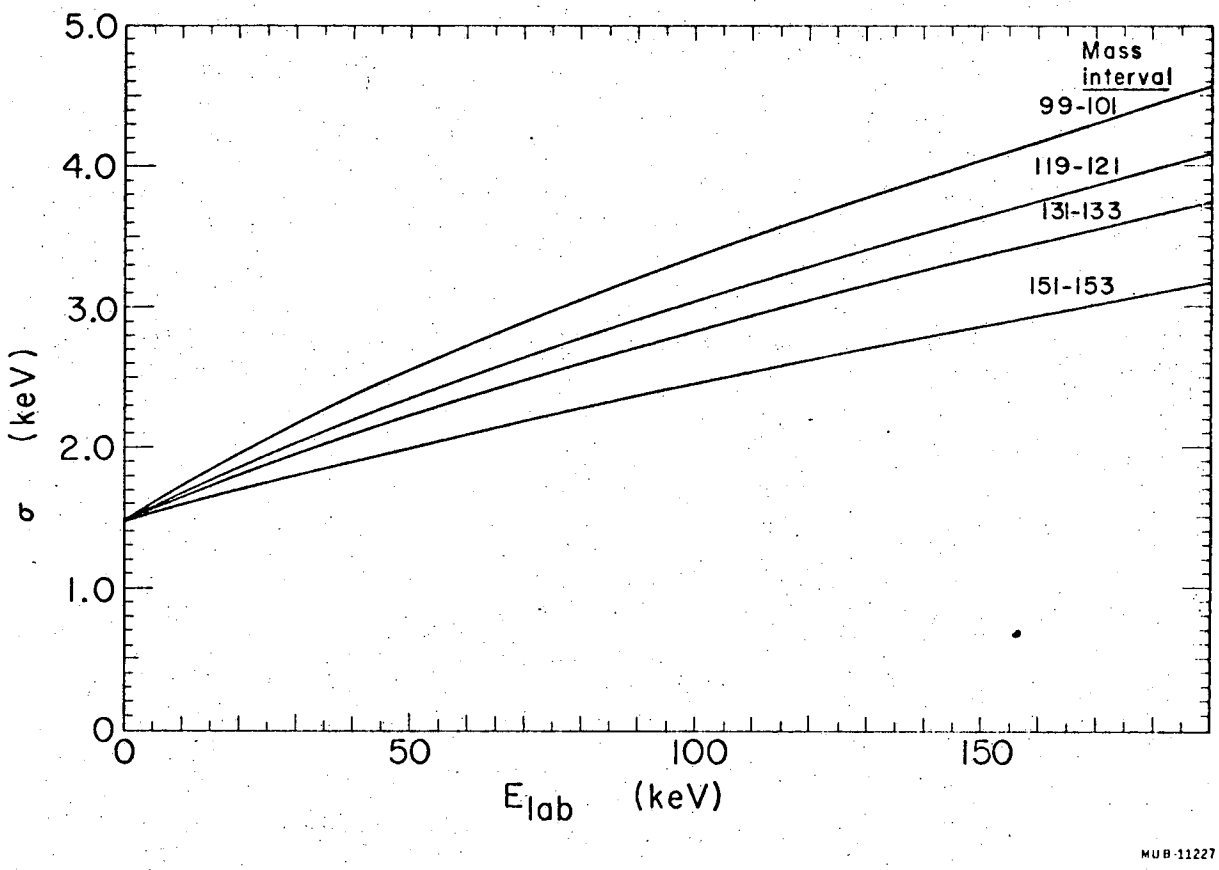

Fig. IV-11. The calculated dependence of the measured electron peak width (σ) on electron energy and fragment velocity.

The average angle of emission in the center of mass system as determined by the above procedure turned out to be 90° as a direct consequence of the fact that the experimental peak shapes were symmetrical. This indicates that the emission probability was symmetrical about 90° with respect to the fragment trajectory. The energy corrections needed to convert the laboratory peak energies to center of mass transition energies are now directly calculable from the measured $\bar{E}_{lab}$ and the knowledge of $\bar{\theta}_{cm}$ through the use of the equation [see Eq. (VII-19) of Appendix B]

$$V_{cm} = \frac{\left(\frac{V_{lab}^2\beta^2 - V_F^2}{V_F}\right)\cos\theta_{cm} + [(V_{lab}^2 - V_{lab}^2\beta^2\cos^2\theta_{cm} - V_F^2\sin^2\theta_{cm})(1-\beta^2)]^{1/2}}{1 - \frac{V_{lab}^2}{c^2}\beta^2\cos^2\theta_{cm} - \beta^2\sin^2\theta_{cm}} \qquad \text{(IV-3)}$$

Table IV-2 lists energy corrections for laboratory energies up to 200 keV. To obtain the transition energies represented by electron peaks in the spectra of Appendix D, subtract the correction given in Table IV-2 for the appropriate mass interval from the measured peak energy ($\bar{E}_{lab}$).

2. Determination of the Electron Transition Characteristics

A knowledge of the characteristics of an electron peak arising from a single electron line can be used as a powerful tool for resolving complex structure. This information was applied to the electron spectra resulting from the present experiments through the use of a Gaussian fitting program developed especially for this purpose. Utilizing the method of least squares, the program was constructed such that any number of peaks up to and including ten, each individually specified by a σ consistent with its peak energy and associated fragment velocity, could, in combination, be varied in their intensities and first moments to obtain the best possible fit to the experimental data.

Table IV-2. Electron energy shift corrections.

Average mass	100	104	108	112	116	120	132	136	140	144	148	152	156	160
E_{lab}(keV)	Correction (keV)													
20.00	0.59	0.56	0.54	0.51	0.49	0.46	0.38	0.35	0.32	0.30	0.28	0.25	0.23	0.21
40.00	0.61	0.59	0.56	0.53	0.50	0.48	0.39	0.36	0.34	0.31	0.29	0.26	0.24	0.21
60.00	0.64	0.61	0.58	0.55	0.52	0.50	0.41	0.37	0.35	0.32	0.30	0.27	0.25	0.22
80.00	0.66	0.63	0.60	0.57	0.54	0.51	0.42	0.39	0.36	0.33	0.31	0.28	0.25	0.23
100.00	0.68	0.65	0.62	0.58	0.56	0.53	0.43	0.40	0.37	0.35	0.32	0.29	0.26	0.24
120.00	0.70	0.67	0.64	0.60	0.58	0.55	0.45	0.41	0.39	0.36	0.33	0.30	0.27	0.24
140.00	0.73	0.69	0.66	0.62	0.60	0.57	0.46	0.43	0.40	0.37	0.34	0.31	0.28	0.25
160.00	0.75	0.71	0.68	0.64	0.61	0.58	0.48	0.44	0.41	0.38	0.35	0.32	0.29	0.26
180.00	0.77	0.73	0.70	0.66	0.63	0.60	0.49	0.45	0.42	0.39	0.36	0.33	0.30	0.27
200.00	0.79	0.76	0.72	0.68	0.65	0.62	0.51	0.47	0.43	0.40	0.37	0.34	0.31	0.27

There are, of course, always a number of uncertainties involved in fitting data of this sort since any given region composed of more than one peak may usually be fit equally well, from a statistical point of view, by several different combinations of peaks. In the present situation, however, a rigid constraint exists in the requirement that each individual peak of any combination of peaks exhibit a distinct behavior as a function of mass. Specifically, any given peak must display a constant first moment over all the mass intervals in which it appears and its intensity when plotted as a function of mass must be approximately Gaussian in shape with a σ of 1.7 to 2.0. (The above specifications were determined by plotting the intensities of a number of single electron peaks vs. mass as illustrated in Section III-D and these plots were used to establish a "standard" mass resolving function). These properties were enough to lend considerable confidence to the results obtained from the peak fitting analyses.

The procedure found to work best in analyzing the electron spectra was to first fit all of the spectra by allowing the first moments and intensities of the various trial peaks to be varied so as to obtain the best least squares fit to the experimental data. Next, the average first moments of the individual peaks were determined by weighting the values of the first moments resulting from this initial fit by their resultant intensities and averaging them over all the mass intervals in which they appeared. Having established the peak-average first moments to a fair degree of accuracy, the last step was to again fit all of the spectra--this time with the peak first moments fixed at their average values--in order to obtain accurate values for the peak intensities. As an example of the "goodness" of the fits obtained in the first step of the above procedure, a completely fitted spectrum for the mass interval 145-147 (1 nsec experiment) is shown in Fig. IV-12. The first moments and intensities of the fitted peaks appearing in this figure are given in

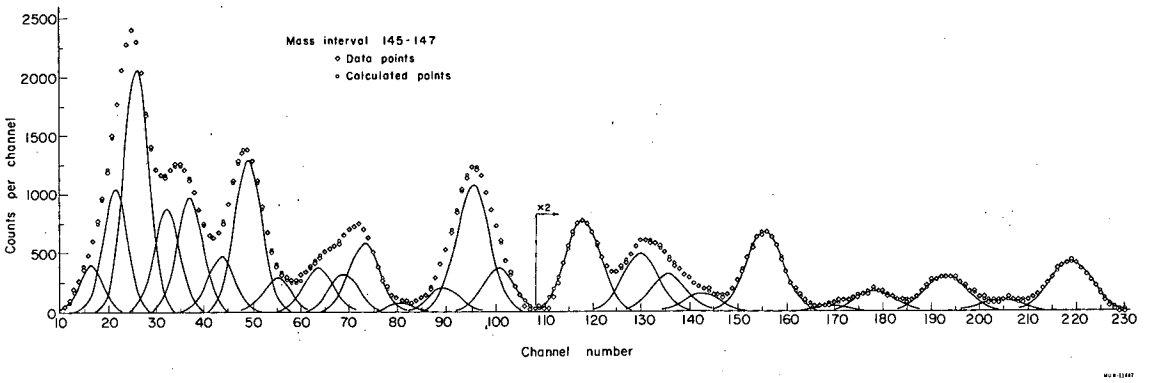

Fig. IV-12. Gaussian fitted electron spectrum.

Table IV-3 along with their FWHM's. The error limits specified in this table are to be taken only as an indication of the "goodness" of the least squares fit.

The final results of two complete peak-fitting analyses of each of 75 individual electron spectra are presented in Table IV-4. In the first column is listed the mass assignment of each electron line. These masses were determined by plotting the peak intensities vs. the average masses of each of the mass intervals in which the peaks appeared and fitting the "standard" mass resolving function through the experimental points. The mass coinciding with the first moment of this fitted resolving function was taken as the mass of the fragment to which the electrons belonged. The error estimated to be associated with these mass determinations is ±1 mass unit. The second column of Table IV-4 lists the corrected transition energies of those electron peaks attributed to K-conversion lines. These energies were acquired by the weighted average procedure described above and are estimated to be as accurate as ±0.5 keV in most cases based upon a comparison of the energy values obtained for the same transition by means of two independent experiments.

The third and fourth columns of Table IV-4 give the average electron emission rates for each transition over the time intervals specified by the experimental configurations in which the source was located 1 cm from the magnet symmetry plane (R_1) and 2 cm from the magnet symmetry plane (R_2) respectively. These quantities were determined by summing the intensities specified by the fitted mass resolution functions over all contributing masses, adjusting this quantity for mass yield and detection efficiency and then dividing by $1.72/V_F$ where 1.72 cm is the width of the detection interval (FWHM) and V_F is the fragment velocity. Because of the number of variables affecting these quantities, they are, for the most part, presented only as rough estimates.

Table IV-3. Electron peak energies and intensities for gaussian fit of mass 145-147 spectrum.

Corrected Energy (keV)	Intensity (10^{-3} electrons/fragment)	FWHM (keV)
18.9±0.2	3.1±0.2	4.08
22.4±0.1	8.5±0.3	4.18
25.4±0.1	17.2±0.3	4.25
29.9±0.1	7.6±0.3	4.39
33.3±0.1	8.4±0.2	4.46
37.8±0.3	4.2±0.2	4.58
41.7±0.1	11.9±0.2	4.70
45.8±0.4	2.6±0.2	4.79
49.4±0.4	2.2±0.1	4.89
53.6±0.2	4.1±0.1	5.00
58.0±0.1	6.9±0.1	5.10
62.5±0.6	1.0±0.1	5.22
69.9±0.4	2.0±0.2	5.38
74.1±0.1	11.6±0.2	5.50
77.7±0.2	4.0±0.3	5.57
90.2±0.0	4.26±0.02	5.86
98.4±0.1	2.8±0.1	6.04
102.5±0.4	1.76±0.08	6.14
107.3±0.4	0.9±0.1	6.23
116.5±0.0	4.06±0.03	6.44
126.4±1.0	0.33±0.08	6.66
132.6±0.3	1.02±0.07	6.77
142.8±0.1	1.96±0.04	6.99
150.9±0.5	0.57±0.06	7.15
160.9±0.1	2.88±0.03	7.36

Table IV-4. Results of the analysis of the electron spectra.

Mass Number	K Line Energy (keV)	R_1 (10^{-3} electrons/fragment/nsec)	R_2 (10^{-3} electrons/fragment/nsec)	$t_{\frac{1}{2}}$ (nsec)	I_{tot} (10^{-2} electrons/fragment)	L Line Energy (keV)	I_K/I_L	Multipolarity	Gamma Energy (keV) A	B	Z
99	198.0	7.1				(207.7)			209.5	210.0	39
100	79.1	37				(94.8)			97.2	98.0	40
102	131.9	12	9.2	1.7	4.0	(148.4)			(151.8)		
	186.7	6.2				(203.2)			211.2		
105	169.7	18	12	1.2	13	(187.0)			190.2	190.6	42
106	71.0	43	27	1.1	10	87.3	4.8	E2	94.2	94.0	44
	148.8	24	16	1.4	6.7	(167.1)			(170.8)		
107	41.6	40	24	1.0	9.5	(59.9)			(63.6)		
108	47.1	74	43	1.0	17	(66.3)			(70.1)		
	100.2	7.4				(119.4)			123.7	123.2	44
110	50.2	34	27	2.2	14	(69.4)			73.2	73.2	44
	74.5	19	11	0.9	4.2	94.5	5.7	E2	97.7	97.5	44
	125.8		3.3			(145.0)			149.2	148.8	44
	215.1	8.7				235.4	4.0	E2	238.0	238.1	44
113	36.1	22				(55.8)			60.0	60.2	45
115	21.4	20	7.8	0.6	3.8	43.3	2.4	E2	47.2	47.7	47
136	51.8	4.9	1.1	0.4	1.1	(80.4)			85.7	85.9	51
139	247.7	0.63				(277.2)			(283.2)		
140	40.8	69	36	1.0	18	69.6	14		75.7	76.3	54
144	77.6	28	22	2.6	14	110.4	5.3	M1	116.2	115.9	56
	104.3	4.6				(136.1)			142.6	142.6	56
	160.8	14	12	1.0	3.8	192.5	4.1	E2	198.2	197.7	55
	242.4	0.42				(274.2)			(280.7)		
145	143.4	7.2	4.4	1.4	2.3	(175.2)			(181.7)		
146	73.5	45	26	1.2	14	106.9	13		(113.3)		
	24.8	71	24	0.6	17	57.9	2.5	E2	64.7	64.6	57
	57.8	25	16	1.7	12	90.2	1.8	E2	97.7	97.6	57
	253.2	0.3				(286.2)			(293.0)		
147	211.1	1.1				242.4	4.0	E2	252.2	252.4	58
148	116.2	27	16	1.3	8.6	151.6	3.7	E2	157.2	157.5	58
149	98.3	26	17	1.8	9.9	133.4	3.6	E2	141.7		59
	200.9	1.1				235.6	4.1	E2	(242.2)		
150	31.1	119	70	1.4	39	(66.7)			(74.0)		
152	119.5	21				(155.1)			162.7	162.4	59
156	23.3	66	51	2.9	36	61.6	1.7	E2	(69.5)		
	42.6	37	25	1.9	15	83.3	1.8	E2	87.2	87.1	60
158	63.5	200	130	1.9	81	(103.0)			(111.2)		
	68.3		65			109.3	14		(116.0)		

Listed in column 5 are the transition half-lives. These half-lives were calculated in the following way:

Since the number of fragments which have not decayed via a given transition at any time t is given by

$$N = N_o e^{-\lambda t} \quad ,$$

where N_o is the total number of fragments formed and λ is the decay constant associated with the transition in question, the numbers of fragments which decay via this transition in the time intervals t_1 to t_2 and t_3 to t_4 are given by

$$\begin{aligned} \Delta N_1 &= N_o[e^{-\lambda t_1} - e^{-\lambda t_2}] = N_o e^{-\lambda t_1}[1 - e^{-\lambda(t_2 - t_1)}] \\ \Delta N_2 &= N_o[e^{-\lambda t_3} - e^{-\lambda t_4}] = N_o e^{-\lambda t_3}[1 - e^{-\lambda(t_4 - t_3)}] \quad . \end{aligned} \tag{IV-4}$$

In these experiments $t_2 - t_1 = t_4 - t_3$ so

$$\frac{\Delta N_2}{\Delta N_1} = \frac{e^{-\lambda t_3}}{e^{-\lambda t_1}} = e^{-\lambda(t_3 - t_1)}$$

$$\ln\left(\frac{\Delta N_2}{\Delta N_1}\right) = -\lambda(t_3 - t_1)$$

$$\lambda = \frac{-\ln\left(\frac{\Delta N_2}{\Delta N_1}\right)}{(t_3 - t_1)} \quad , \tag{IV-5}$$

but $t_{1/2} = 0.693/\lambda$ and

$$t_3 - t_1 = \frac{1.14}{V_F} - \frac{0.14}{V_F} = \frac{1}{V_F} \quad ;$$

hence

$$t_{1/2} = \frac{-0.693}{V_F \ln\left(\frac{\Delta N_2}{\Delta N_1}\right)} \quad . \tag{IV-6}$$

The error limits attached to the half-lives determined in these experiments are ±20% and are attributable mainly to the inaccuracies associated with measuring the source and deflector positions.

In the sixth column, are listed the total emission intensities per fragment mass. These quantities were calculated from the equation obtained by solving for N_o in Eq. (IV-4); namely

$$I_{tot} = N_o = \frac{\Delta N_1 \, e^{\lambda t_1}}{[1 - e^{-\lambda(t_2 - t_1)}]} \quad . \tag{IV-7}$$

Substituting Eq. (IV-5) for λ yields

$$I_{tot} = \frac{\Delta N_1 \, e^{\frac{-\ln(\Delta N_2/\Delta N_1)t_1}{(t_3 - t_1)}}}{\left[1 - e^{\frac{\ln(\Delta N_2/\Delta N_1)(t_2 - t_1)}{(t_3 - t_1)}}\right]} \tag{IV-8}$$

but

$$\frac{t_1}{(t_3 - t_1)} = 0.14$$

and

$$(t_2 - t_1)/(t_3 - t_1) = \frac{1.86 - 0.14}{1} = 1.72 \quad ;$$

therefore,

$$I_{tot} = \frac{\Delta N_1 \, e^{-0.14 \ln (\Delta N_2/\Delta N_1)}}{\left[1 - e^{1.72 \ln (\Delta N_2/\Delta N_1)}\right]} \quad . \qquad \text{(IV-9)}$$

As with the quantities R_1 and R_2, the values listed for I_{tot} are presented only as rough estimates.

The seventh column of Table IV-4 contains a listing of the L-conversion electron energies associated with the K lines of column 2. Those numbers not in parentheses give the energies of the L lines which have been located in the electron spectra. The numbers in parentheses are the calculated L-line energies (for those cases where identifiable L lines could not be found). They were obtained by adding the K-L binding energy differences of the most probable charge elements to the K line energies of column 2. There are a number of reasons why L lines frequently could not be identified. Interfering structure, for example, commonly made it impossible to pin down definite L line energies in some cases, while in other instances it is possible that lines attributed to K lines were really L lines. The factor considered to be most frequently responsible for missing L lines, especially in the light fragment region, was large K-to-L ratios. Theoretical conversion coefficients and K-to-L ratios are listed as a function of energy for an average light fragment Z of 43 in Table IV-5 and for an average heavy fragment Z of 55 in Table IV-6.[30] From these tables, it can be seen that for light fragments, the large K-to-L ratios for E1 and M1 transitions make it unlikely that L lines would be identifiable for transitions of these multipolarities. It is also evident that throughout the energy range listed for both the heavy and light fragments, E2 transitions consistently display the smallest K-to-L ratios and therefore E2 transitions should be the easiest to identify in the spectra on the basis of K-to-L ratio. This is indeed the case as may be seen by inspecting columns 8 and 9 of Table IV-4 where the measured K to L ratios and the multipolarity assignments deduced from them are listed.

Table IV-5. Conversion coefficients and K to L ratios for Z = 43.

Energy (keV)	E1 K/L	α1(K+L)	M1 K/L	β1(K+L)	E2 K/L	α2(K+L)
30	80	4.0	24	21	2.9	135
40	91	2.1	27	10	3.4	52
50	107	1.1	24	4.5	4.8	23
60	113	0.64	19	2.0	4.9	11
70	97	0.35	12	0.87	4.6	4.9
80	80	0.20	9.6	0.52	4.2	2.5
90	83	0.15	8.9	0.35	4.5	1.6
100	86	0.12	10	0.26	5.4	1.2
150	129	0.058	16	0.14	12	0.48
200	194	0.035	21	0.080	20	0.25
250	106	0.010	11	0.024	8.1	0.048
300	84	0.0047	9.2	0.013	7.5	0.024
350	85	0.0033	9.2	0.0093	7.8	0.014

Table IV-6. Conversion coefficients and K to L ratios for Z=55.

Energy (keV)	E1 K/L	α1(K+L)	M1 K/L	β1(K+L)	E2 K/L	α2(K+L)
30	5.5	5.3	3.2	16	0.25	200
40	6.3	3.0	5.0	9.6	0.39	53
50	7.9	1.7	6.1	5.8	0.67	20
60	8.0	0.99	6.8	3.7	1.0	9.8
70	7.8	0.59	7.0	2.4	1.2	5.5
80	7.1	0.36	7.5	1.7	1.4	3.4
90	7.2	0.26	7.1	1.1	1.8	2.3
100	7.7	0.21	7.8	0.88	2.0	1.6
150	13	0.11	7.4	0.28	3.6	0.41
200	17	0.063	7.3	0.13	4.5	0.16
250	8.0	0.018	7.6	0.070	5.2	0.074
300	7.4	0.010	7.6	0.043	5.4	0.041
350	7.8	0.0071	7.6	0.028	5.8	0.026

In column 10 are listed energies of the gamma rays associated with the conversion electron lines. Those numbers in column 10a not in parentheses are the measured energies of gamma rays identified in the data of Bowman[27] while those numbers in parentheses are values calculated from the binding energies of the most probable charge elements. It is important to note that the binding energies used in calculating gamma ray energies must be corrected for the state of ionization of the fragments involved since the binding energies of highly ionized ions are considerably increased over those of neutral atoms. The problem of calculating these corrections is taken up in Section V where it is found that the K binding energy increase remains an approximately constant 0.9 keV over the entire range of fragment atomic numbers. This correction has been used both in calculating the gamma ray energies and in assigning the atomic numbers listed in column 1 of Table IV-4 on the basis of the energy differences between the gamma ray energies and the K conversion line energies (i.e. the K binding energies). The energy values given in column 10b are the calculated gamma energies for the Z assignment specified in column 12. As can be seen, close agreement is obtained in most instances and the Z assignments are felt to be accurate to better than ±1 atomic number.

Table IV-4 is by no means presented as a complete listing of all the electron structure appearing in the various spectra. Included in this table are only those lines which showed enough consistency in the analysis to promote reasonable confidence in the accuracy of the listed quantities. Moreover, for many of the electron lines below 50 keV in the heavy fragment spectra, analysis was not possible because of the interference from very complex Auger electron structure.

C. Discussion

A number of features pertaining to the gamma de-excitation processes of fission fragments may be deduced from the electron yield curves given in Figs. IV-6 and IV-7. It is reasonable, for example, to expect the variation of electron yield as a function of mass to reflect the relative importance of low-energy transitions in the de-excitation processes of the various fragments, based upon the behavior of conversion coefficients as a function of transition energy. Pursuing this line of reasoning, it follows that low-energy transitions are particularly abundant in the regions of mass 108 and mass 152. It was further pointed out by Atneosen et al.[24] that the existence of closely spaced levels is not in itself a sufficient condition for the production of a relatively large number of conversion electrons, but that it is also necessary for de-excitation to take place through a sequence of these levels. These properties are characteristics of rotational transitions and, although in no way conclusive, the above deductions are consistent both with the proposal by Johansson,[31] that there exists a region of stable deformation near mass 110, and with the known deformed region beginning around mass 150. The low electron yields near mass 132 are most likely attributable to the sharp rise in energy characteristic of single particle transitions associated with the doubly closed shell configuration of 50 protons and 82 neutrons.

If, indeed, the above deductions are correct, then evidence of rotational transitions might be perceptible in the electron spectra for mass intervals near 110 and 152. Referring to Table IV-4, it is seen that a number of transitions have been identified for mass 110. Two of these transitions, namely the 97.7 and 238.0 keV gamma rays assigned to ^{110}Ru are particularly good candidates for 2^+ to 0^+ and 4^+ to 2^+ rotational transitions since they appear to have the required E2 multipolarity. The energies of these two transitions are somewhat lower than the 300 keV

Table IV-7. Systematics of even-even first 2+ states in rare earth region.

Nuclide	First 2+ Energy (keV)	$t_{\frac{1}{2}}$ (nsec)
$^{142}_{58}Ce_{84}$	640	0.006
$^{144}_{60}Nd_{84}$	696	0.008
$^{146}_{60}Nd_{86}$	453	0.06
$^{148}_{62}Sm_{88}$	334	0.05
$^{148}_{60}Nd_{88}$	300	0.2
$^{150}_{62}Sm_{88}$	334	0.05
$^{152}_{64}Gd_{88}$	344	0.05
$^{150}_{60}Nd_{90}$	132	1.6
$^{152}_{62}Sm_{90}$	122	1.4
$^{154}_{64}Gd_{90}$	123	1.2
$^{154}_{62}Sm_{92}$	82	3.0
$^{156}_{64}Gd_{92}$	89	2.2
$^{160}_{64}Gd_{96}$	75	2.5

4^+ to 2^+ and the 130 keV 2^+ to 0^+ transitions estimated by Johansson[31] but agree well with the value (~100 keV) obtained by extrapolating from a plot of known first 2+ energies of ruthenium isotopes as a function of neutron number. The energy ratio is also consistent with rotational behavior in this region.

Assuming the above mentioned transitions are associated with a rotational band of ^{110}Ru, an idea of the magnitude of the deformation involved may be obtained by calculating the intrinsic quadrupole moment Q_o implied by the transition energy and lifetime and correlating it with the quadrupole deformation parameter ϵ given by Nathan and Nielsson.[32]

The value of Q_o calculated on the basis of the measured half-life of the 97.7 keV transition is 4×10^{-24} cm^2. The quadrupole deformation parameter ϵ is given by the equation[32]

$$\epsilon = -1 \pm \sqrt{1 + 2\,\delta} \qquad \text{(IV-10)}$$

where

$$Q_o = (4/3)Z \langle r^2 \rangle \delta \quad . \qquad \text{(IV-11)}$$

Solving for ϵ results in a value of 0.3 which is comparable in magnitude to the distortion parameter found for ^{158}Gd and other nuclides in the deformed rare-earth region.

A survey of the known systematics of even-even nuclides in the rare-earth deformed region indicate that for deformed nuclei, the first 2+ state commonly ranges between 100 and 150 keV above the ground state and occasionally dips as low as the 75 keV 2+ state evidenced in ^{160}Gd.[33] Based upon extrapolations of the first 2+ energies of neighboring isotones, the 2+ states of the most probable charge even-even nuclides lying between masses 150 and 160 are estimated to fall between 70 and 100 keV while the 4+ and 6+ states are expected to lie near 250 and 500 keV respectively. Referring to Table IV-4, it is seen that many of the

observed electron lines are associated with or imply association with gamma rays having energies near those estimated for 2+ to 0+ rotational transitions. Unfortunately, the large conversion coefficients inherent with low energy E2 gamma transitions and the low mass yields in this region makes it difficult to locate with confidence gamma-ray lines which would further substantiate the K-line assignments and establish the Z of the emitting nuclide.

Another quantity which is frequently of help in evaluating evidence for 2+ to 0+ transitions of even-even nuclides in the heavy fragment region is the transition half-life. By plotting the log of known 2+ energies versus the log of their half-lives it was found that the points approximately lie along a straight line. The data used for the present half-life estimates are summarized in Table IV-7.[33] (A more general study of the behavior of E2 transitions from the first 2+ state in even-even nuclides as a function of transition probability has been reported by Grodzins.[34])

Two transitions in Table IV-4 appear to be particularly good candidates for even-even 2+ to 0+ transition from the standpoint of energy; namely the 157.2 keV gamma transition assigned to ^{148}Ce and the 87.2 keV transition assigned to ^{156}Nd. The half-life estimates for transitions of these energies are 0.7 and 4 nsec respectively which are in reasonable agreement with the measured half-lives of 1.3 and 1.9 nsec. The values of Q_o and ϵ calculated for the 157.2 keV transition in ^{148}Ce are, however, unreasonably low ($Q_o = 1.3 \times 10^{-24}$ cm^2, $\epsilon = 0.1$).

A complex peak which appears to be associated with fragments of mass 158 (see spectrum for mass 157-159 interval in Appendix D) bears pointing out because of its unusually high intensity. The peak has been found to be comprised essentially of two lines having energies of 63.5 and 68.3 keV. For all of their intensity, however, no evidence of associated L conversion lines could be found in the spectra. This fact

excludes their being E2 transitions since the K to L ratios for E2 transitions of these energies are around 2.0. M1 and E1 K to L ratios for these transitions, on the other hand, are on the order of 8 and hence the transitions probably arise from deformed odd-mass nuclides, where M1 transitions in rotational cascades should be quite common.

The known transitions of ^{153}Eu[33] provide an insight into the character of typical odd-mass transitions in the heavy mass region. The ground state has spin and parity 5/2+ while the first two excited levels are a 7/2+, 83 keV state and a 9/2+, 191 keV state. De-excitation proceeds via a two transition M1-E2 cascade and a crossover transition from the 9/2+ level to the ground state in relative amounts of 26% and 74% respectively. The 9/2+ level has a half-life of 0.24 nsec and the 7/2+ level has a 0.7 nsec half-life. Strong cross-over transitions are known for a number of other odd-mass nuclides in this region, for example the crossover transition (64% relative intensity) having an energy of 256 keV and a half-life of 0.9 nsec in ^{151}Pm,[33] and hence the character of odd mass de-excitation occurring in the nuclides of most probable charge may be assumed to display similar properties.

It becomes evident that in order to account for the large number of low energy transitions having lifetimes in the range of 1 to 2 nsecs observed in these experiments it must be postulated that a large percentage of the lines arise from the decay of odd-mass nuclides. In searching for lines having these characteristics, a number of possible crossover transitions were found as may be seen by again referring to Table IV-4. In particular, the gamma ray lines indicated for masses 139, 144 and 145 at energies of 283.2, 280.7, 181.7 respectively are of about the right energies for crossover transitions while the 116.2 keV gamma ray at mass 144 and the 113.3 keV gamma ray indicated at mass 146 look about right for cascade transitions. There were, however, no clear cases where all three transitions for any one nuclide could be found.

Returning once again to the electron yield curve of Fig. IV-7, one should like to explain the puzzling drop in electron yield beyond mass 151 on the basis of the present data. The fact that the yield does not continue to drop, but levels out around mass 153 suggests the possible existance of highly converted low energy rotational transitions in a number of nuclei spanning the heavy mass region. As the heavier mass nuclides are approached, it is reasonable to expect these levels to move down in energy. Perhaps the sudden drop could be explained by assuming that as the mass 150 nuclei are approached, the predominant cascade transitions move below the K binding energy and hence abruptly reduce the electron yield. The yield would level out in the observed manner due to the large contribution from electrons converted in the L shell. (This suggestion was first put forth by Vandenbosch.[35]) Rotational transitions fitting the above description were looked for in the present data, but no conclusive evidence could be found in support of this proposal.

V. BINDING ENERGY CALCULATIONS OF HIGH IONIZED ATOMS

Due to the high velocities attained by fission fragments ($\sim 10^9$ cm/sec) immediately upon fissioning, they are unable to carry along many of their outer orbital electrons and hence become highly ionized. In attempting to ascertain the nuclear charges of fission fragments by measuring the difference in energy between associated gamma rays and internal conversion electrons, it is important to be aware of how the K electron binding energies are affected by this high state of ionization.

Qualitatively, the effect on the binding energies of stripping a number of outer electrons from a neutral atom may be understood by picturing the electronic charge as residing on the surfaces of spheres centered about the nucleus. Figure V-1a illustrates the repulsive potential due to the electron shells which would be felt by a test charge as it was brought toward the nucleus of such an atom. Before the first shell of charge is reached, the potential is given by $38\ e^2/r$. As this shell is penetrated, its contribution to the potential becomes a constant C_1 and the further increase is due to the remaining charge 36e. The repulsive potential continues to increase in the same fashion until the K shell is penetrated at which point, it becomes constant. The attractive potential on the other hand, is given by $-38e^2/r$ and is due to the nuclear charge. By adding these two potentials, the binding potential is obtained and this potential establishes the binding energies of the various electrons.

In Fig. V-1b is shown the same potentials for a strontium atom with its two outer electron shells stripped. It is seen that the net effect is to lower the binding potential by the amount $C_1 + C_2$. It is expected, then, that the binding energies of an ionized atom will be higher than those of a neutral atom and furthermore, that these increases in binding energies should be nearly the same for all occupied orbitals of the ion.

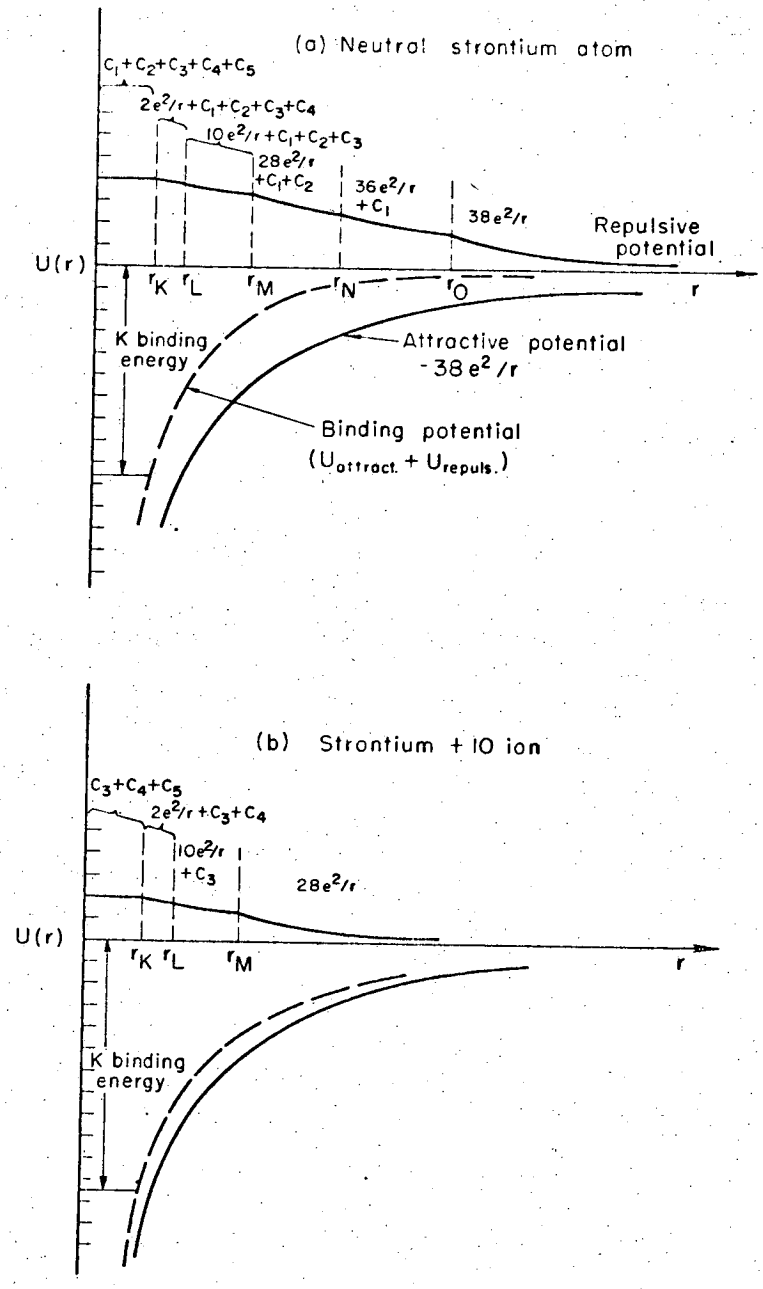

MUB-10567

Fig. V-1. Idealized electrostatic potential energy diagram for a) a neutron strontium atom b) a strontium +10 ion.

A. Estimation of Fission Fragment Ionic Charges

The first problem in considering the ionization effect is in determining the degree of ionization itself. Very little experimental data are available on fission fragment initial ionic charges, and no satisfactory method for calculating them precisely from a theoretical or empirical formula has yet been devised. In fact, about the only means of estimating the initial ionic charge of a fission fragment in a vacuum is based on the assumption first brought forth by Bohr[36]--that only those electrons whose orbital velocities are greater than the translational velocity of the fission fragment will remain bound. In this connection, Bohr approximated the velocity of an electron in an atom by

$$v = \frac{e^2}{\hbar} \frac{Z^*}{n^*} = v_o \frac{Z^*}{n^*} \quad , \tag{V-1}$$

where Z^* is the effective charge on the electron in question, n^* is its effective principle quantum number and v_o is the orbital velocity of an electron in the ground state of the hydrogen atom. Solving for the Z^* of the electron whose velocity v is equal to the velocity V of the fragment, the result is,

$$Z^* = \frac{V}{v_o} n^* \quad . \tag{V-2}$$

Bohr then approximated n^* with $Z^{1/3}$ based on the Thomas-Fermi statistical model of the atom and obtained

$$Z^* = Z^{1/3} \frac{V}{v_o} = \frac{Z^{1/3} V}{2.2 \times 10^8} \quad . \tag{V-3}$$

Extensive experimental studies by Lassen[37,38] involving the measurement of the curvature in the paths of ^{235}U fission fragments in a magnetic field have yielded initial charge values of 22 and 20 for the most probable heavy and light fragment respectively. Since the time that

these measurements were made, however, more reliable mass and velocity data have become available. If the most probable mass and velocity data of Milton et al.[39] are used in conjunction with Lassen's Hρ measurements, the most probable light and heavy fragment ionic charges become 21 and 23, respectively. An ionic charge of 21 for the most probable light fragment of ^{235}U(mass 96) is in very good agreement with the measurements of Cohen et al.[40] on ^{97}Zr. The values obtained from Eq. (V-3), on the other hand, are 23 for the light fragment and 17 for the heavy fragment. These values not only deviate substantially from the experimental values, but also are reversed in their trend, resulting in a larger charge for the light fragment than for the heavy fragment. Table V-1 summarizes the fragment charge values presented here as well as the data used in obtaining them.

Before attempting to determine the nuclear charges of fission fragments from the energy differences between corresponding gamma ray and internal conversion electron lines, the binding energy increases due to the high state of ionization of the fragments must be known. For this reason, detailed calculations of the K binding energies for various fission product atoms were undertaken.

In lieu of any experimental ionic charge data on ^{252}Cf and due to the apparent unreliability of Eq. (V-3), it will be assumed that the most probable heavy fragment ionic charge is about 24 and the most probable light fragment ionic charge is about 22. The assumption that the most probable ionic charges resulting from ^{235}U fission and ^{252}Cf fission will differ slightly seems reasonable on the basis of the difference in the fragment velocities and masses in the two cases. It was further felt, due to the uncertainty in the ionic charge assignments, to be of general interest to calculate, for various atoms in this region, the K binding energies for a series of states of ionization ranging from the neutral atom to the totally ionized atom.

TABLE V-1.

	Heavy Fragment			Light Fragment		
	Mass	Velocity ($\times 10^9$ cm/sec)	Ionic Charge	Mass	Velocity ($\times 10^9$ cm/sec)	Ionic Charge
^{235}U(a)						
Eq. (V-3) ($Z_{P\ lt} = 37$, $Z_{P\ hy} = 54$)	140	0.966	16.7	96	1.409	22.6
Lassen[37] ($H\rho_{\ lt} = 6.7 \times 10^5$ gauss cm, $H\rho_{\ hy} = 6.0 \times 10^5$ gauss cm)	140	0.966	23.5	96	1.409	21.0
Cohen[40]				97		21
^{252}Cf(b)						
Eq. (V-3) ($Z_{P\ lt} = 43$, $Z_{P\ hy} = 55$)	142	1.036	18.0	106	1.383	22.1

[a] Most probable mass and velocity data for ^{235}U from Ref. 39.

[b] Most probable mass and velocity data for ^{252}Cf from Ref. 19.

The binding energy calculations were carried out using a computer program written by Roothaan and Bagus[41] employing a non-relativistic Hartree-Fock self-consistent field (S.C.F.) method. Before discussing the results of these calculations, some details of the Hartree-Fock S.C.F. method and its application in the computer program will be described.

B. The Hartree-Fock S. C. F. Method

The general Hartree-Fock method, in its various forms, has been widely used in atomic calculations. It was originally developed by Fock's[42] application of the Hartree method to determinantal wave functions.

The Hartree method consists essentially of constructing wave functions to describe atomic configurations from products of one electron orbitals for the various N electrons and solving the resulting N simultaneous nonlinear integrodifferential equations of the form

$$\left[-1/2\ \nabla_j^2 + V(r_j)\right]\ U_i(r_j) = \epsilon_i\ U_i(r_j) \quad . \qquad (V\text{-}4)$$

These equations are solved by successive approximations until the solutions are self-consistent; that is, until the final wave functions determine a final potential which agrees to a high order of accuracy with the potential determined by the preceding iteration.

Wave functions found in this manner, however, do not satisfy the restriction that they be antisymmetric which is imposed by the Pauli exclusion principle. The simplest function which does satisfy the anti-symmetry principle is a determinantal function and hence this leads to the Hartree-Fock S. C. F. method.

The Hartree-Fock method as applied to atomic calculations has received numerous and detailed treatments.[43,44] For the present purposes, therefore, the presentation which follows will be limited to a brief description of its application in the computer program. For completeness, however, the derivation of the Hartree-Fock equations for closed shells from the variational method, and Roothaan's formulation for open shells are outlined in Appendix C.

The present binding energy calculations were carried out through the use of an IBM 7090 computer program written by Roothaan and Bagus.[41] The program is based on an expansion method (developed by Roothaan[45]) which applies the procedures outlined in Appendix C to determinantal wave functions comprised of LCAO-type orbital expansions.

In applying the LCAO method, each orbital ϕ_i is expanded in terms of a given set of suitable basis functions χ_p. Advantage is taken of the symmetry properties afforded by Roothaan's open-shell formulation which permits the orbitals to be grouped in sets, each set transforming under symmetry operations according to an irreducible representation of the symmetry group. Hence, each occupied orbital of a given species and subspecies is constructed from a linear combination of the basis orbitals of the same species and subspecies such that

$$\phi_{i\lambda\alpha} = \sum_p \chi_{p\lambda\alpha} C_{\lambda pi} = \tilde{\chi}_{\lambda\alpha} \tilde{C}_{\lambda i} \quad , \qquad \text{(V-5)}$$

where the basis functions are given by

$$\chi_{p\lambda\alpha}(r,\theta,\phi) = R_{\lambda p}(r)\, Y_{\lambda\alpha}(\theta,\phi) \quad . \qquad \text{(V-6)}$$

The indices $i\lambda\alpha$ and $p\lambda\alpha$ are analogous to the quantum number nlm used to specify hydrogen-like wave functions. The radial parts of the basis functions used in the computer program are normalized Slater-type functions given by

$$R_{\lambda p}(r) = \left[(2n_{\lambda p})!\right]^{-1/2} (2\zeta_{\lambda p})^{n_{\lambda p}+1/2} r^{n_{\lambda p}-1} e^{-\zeta_{\lambda p} r} \quad . \qquad (V\text{-}7)$$

In brief, the computational process starts with a set of trial wave functions of the type given in Eq. (V-5). This requires input estimates of the Slater orbital exponents $\zeta_{\lambda p}$ and the vectors $\tilde{C}_{\lambda i}$. Using the basis functions, the integrals[46] entering the Hartree-Fock Hamiltonian are calculated, and an iterative process entered into in which the eigenvectors are solved for repeatedly until the input and output vectors agree within a certain threshold. The iterative schemes used in the program to obtain convergent solutions from as few successive iterations as possible are described in detail by Roothaan and Bagus and so will not be discussed further.

The program is designed to work with minimal, highly optimized basis sets instead of with loosely chosen, large basis sets which lead to programming and machine time complications. The basis functions are optimized by the variation of the Slater orbital exponents. The method of variation involves complete SCF calculations of the total energy for a series of values of the orbital exponent in question. An extrapolation is then performed to obtain the value of the orbital exponent which minimizes the total energy. The exponents to be varied and the amounts of variation to be applied are specified in the input data. The program provides for the optimization of basis functions in sets of one, two or three. Optimization of a set of two wave functions, for example, involves the variation of the second orbital exponent until a minimum in the total energy is found, then the first orbital is varied by the amount specified in the input, and the program again undertakes the variation of the second exponent until the total energy is again minimized. This process is repeated until both exponents in combination are fully optimized.

The output data of the SCF program consists of a listing of the final optimized orbital exponents, the final eigenvectors, and the values of the total energy, the potential energy, the kinetic energy and the Lagrangian multipliers which are referred to as orbital energies. In addition, the value resulting from the application of the virial theorem[47] and the cusp values[46] are listed as a test of the accuracy of the energy determinations and the accuracy of the eigenvectors in the region $r \rightarrow 0$, respectively. For an exact solution, the virial theorem should yield a value of -2 and the cusps shoud have the values $-Z/\lambda+1$. Further output options allow the tabulation of the orbital wave functions and the orbital densities as a function of r as well as the printing of the various matrices and intermediate data entering into the SCF calculations.

Many general problems can be handled by this SCF program including those involving open inner shells such as, for example, the configuration $1s^1\ 2s^2\ 2p^6$. Limitations of the program, however, include a maximum value of 6 for the principle quantum number, a maximum value of 3 for the angular momentum and a maximum of 20 basis functions.

C. Results of Calculations

The electron binding energies of Sr, Pd, Xe and Sm were calculated for a number of ionic charge states spanning from the neutral atom to the totally ionized atom. These particular atoms were chosen because they outline the light and heavy fission product regions and therefore make convenient bases for extrapolations to other fission product elements.

The K binding energies were obtained by computing the total energies of both the ion in question and of the ion with one 1s electron removed. The difference between these two computed total energies, then, is precisely the K binding energy of the ion. In all cases, the total energies were calculated with minimal basis sets (one basis function for each occupied orbital) using fully optimized orbital exponents.

The K binding energies for the neutral atoms are well known.[48] The K binding energies for the totally ionized atoms (ionic charge of Z-1) are easily calculable from the Sommerfeld relativistic hydrogen atom equation[49] given by

$$E_{n,\ell} = - \frac{2\pi^2 \mu e^4}{h^2} \frac{Z^2}{n^2} \left[1 + \frac{\alpha^2 Z^2}{n} \left(\frac{1}{\ell+1} - \frac{3}{4n}\right)\right]$$

$$E_{1,0} = - ChR_\infty \left(\frac{M}{M+m}\right) Z^2 \left[1 + 0.25\, \alpha^2 Z^2\right] , \qquad \text{(V-8)}$$

where α is the Sommerfeld fine structure constant and R_∞ is the Rydberg constant for an infinitely heavy nucleus. Inserting the appropriate values, this equation reduces to

$$E_{1,0} = - 13.606 \times 10^{-3}\, Z^2 \left[1 + 13.314 \times 10^{-6}\, Z^2\right] \text{keV} \quad . \qquad \text{(V-9)}$$

By comparing the calculated values for the neutral and totally ionized cases with the values obtained from Ref. 48 and Eq. (V-9), the error in the calculated values was found to range from 1.8% for strontium to 4.9% for samarium. This error was attributed to calculational error arising from the use of minimal basis sets, and to correlation and relativistic energy effects not taken into consideration by the calculation.

The percent error was very nearly the same for both the neutral and the fully ionized cases. On this basis, the percent error in the calculated values was assumed to be constant with respect to ionic charge state and a linear adjustment was made on all calculated K binding energy values such that the two extremes of ionic charge states (neutral and totally ionized) agreed with the values obtained from Ref. 48 and Eq. (V-9).

These values were then plotted as a function ionic charge and a smooth curve was fitted through the points. The adjusted K binding energy curves for Sr, Pd, Xe and Sm are shown in Figs. V-2, V-3, V-4 and V-5, respectively. These curves are believed to be accurate to better than 0.05% or in most cases to at least 0.1 keV. Similar curves are given in Figs. V-6 and V-7 for the adjusted 2s and 2p binding energies as a function of ionic charge.

As an aid to extrapolations to other elements, the percent increase in binding energy is plotted as a function of percent ionization in Fig. V-8 for Sr, Pd, Xe and Sm. The relative position of the curve representing any other element in the region may be established by calculating the point corresponding to total ionization (ionic charge = Z-1) through the use of Eq. (V-9).

The K and L electron binding energies as well as the K_α X-ray energies are listed in Table V-2 for the neutral atoms and several probable ionic charge states. It is seen that, as expected, the K_α X-ray energy is essentially unaffected by the state of ionization while the binding energies experience considerable increase.

The K binding energy increase is plotted in Fig. V-9 as a function of atomic number for several probable ionic charge states. If the most probable fission fragment charge states are assumed to be +21, +23, +24 and +26 for Sr, Pd, Xe and Sm respectively, it is seen that the binding energy increase remains nearly a constant 0.9 keV as a function of atomic number.

In order to facilitate further work in this or related areas, the remaining orbital energies for the various cases calculated are listed in Table IV-3. These values are strictly the calculated values and have not been adjusted in any way. The fully optimized orbital exponents used in these calculations are listed in Table V-4 for the neutral atom cases unless otherwise specified.

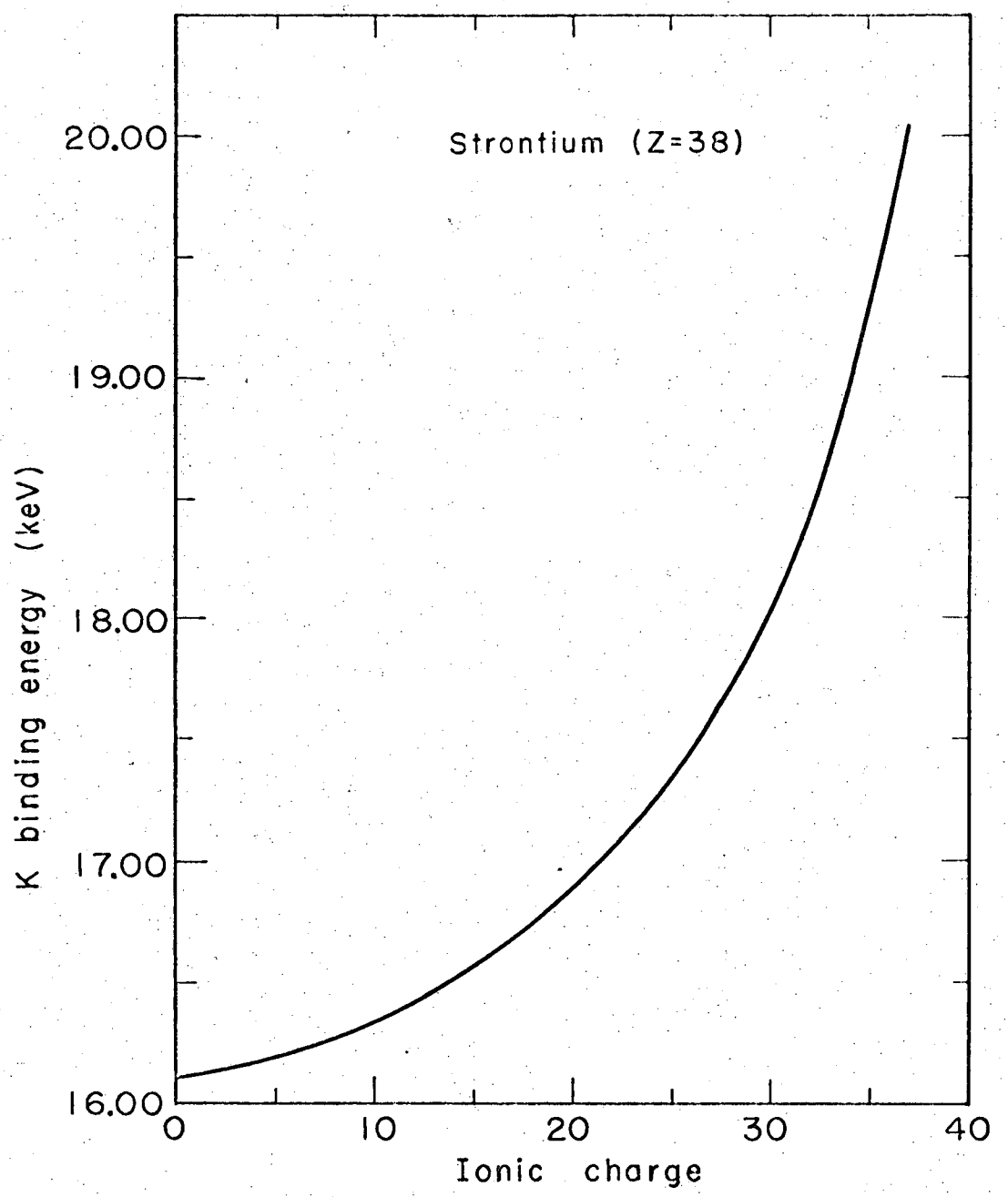

MUB-10563

Fig. V-2. Calculated K binding energy of a strontium atom as a function of its ionic charge.

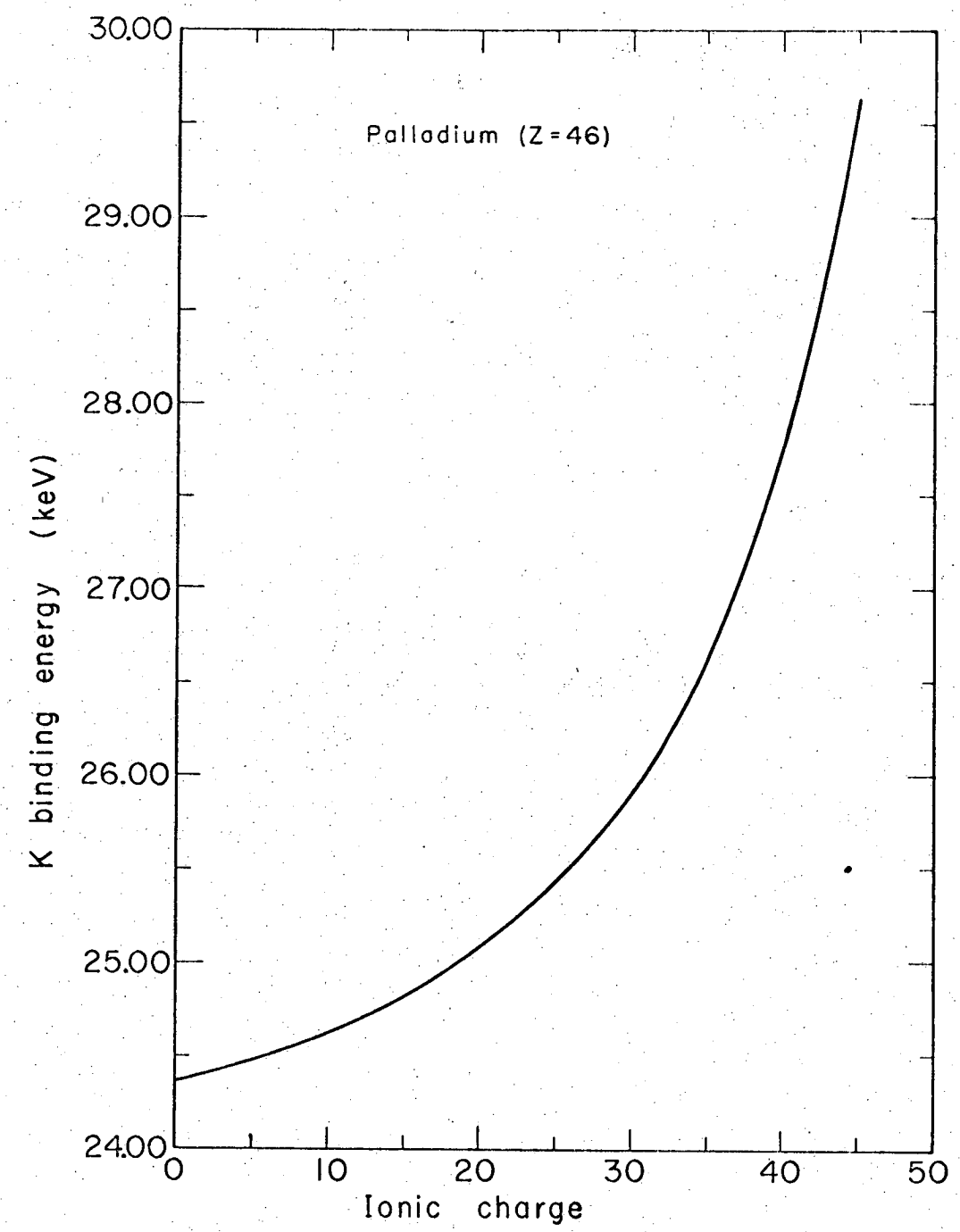

Fig. V-3. Calculated K binding energy of a palladium atom as a function of its ionic charge.

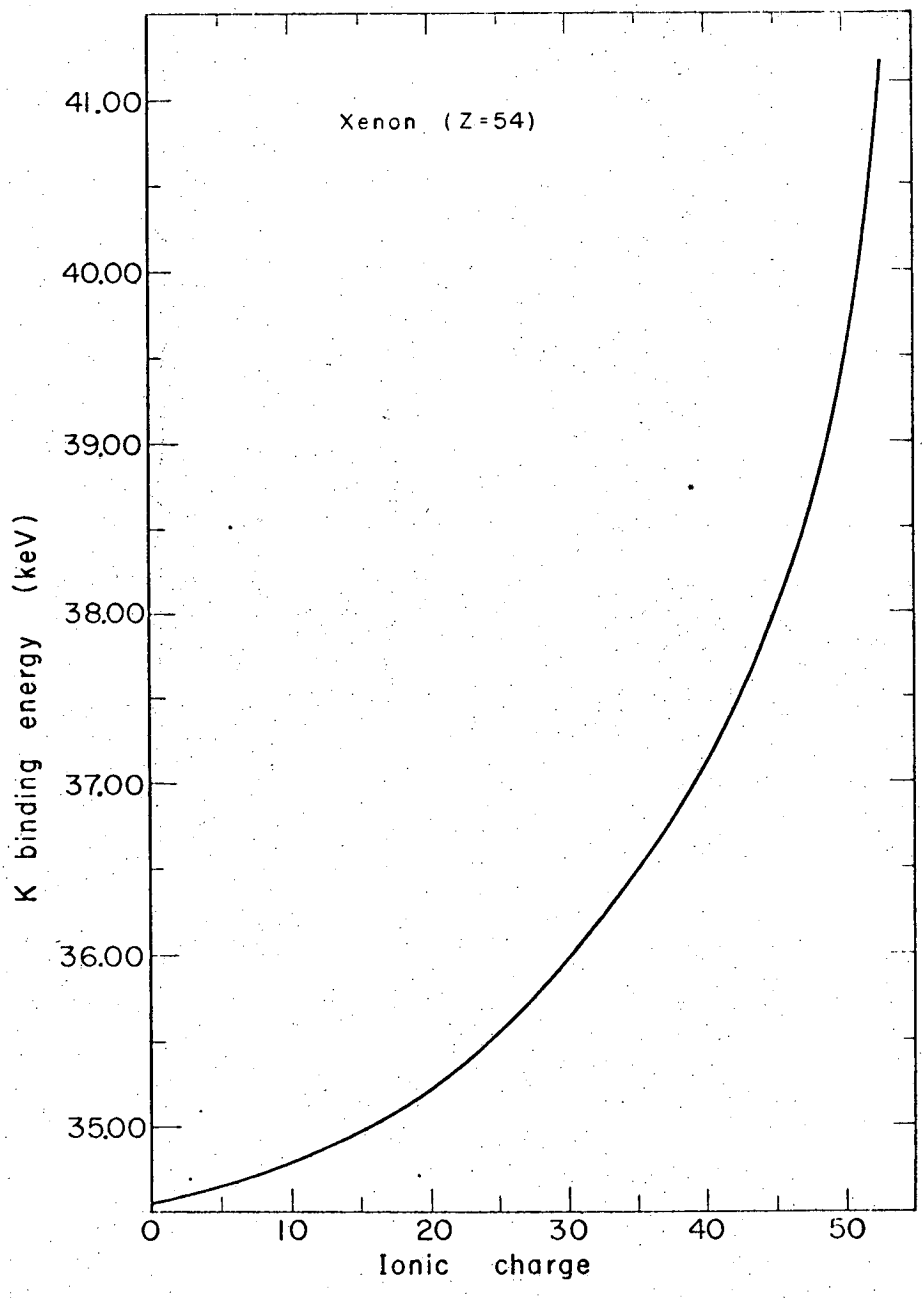

Fig. V-4. Calculated K binding energy of a xenon atom as a function of its ionic charge.

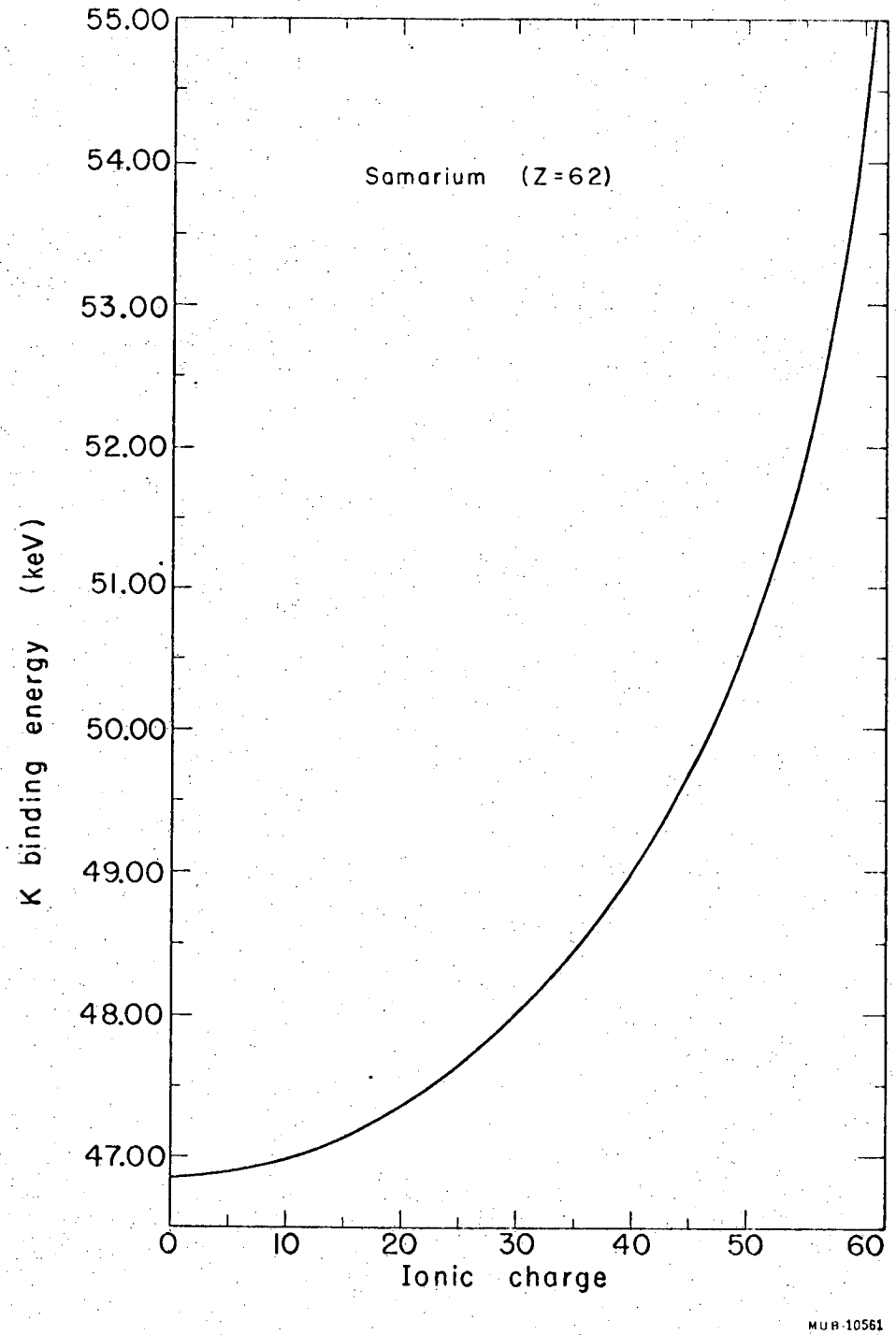

Fig. V-5. Calculated K binding energy of a samarium atom as a function of its ionic charge.

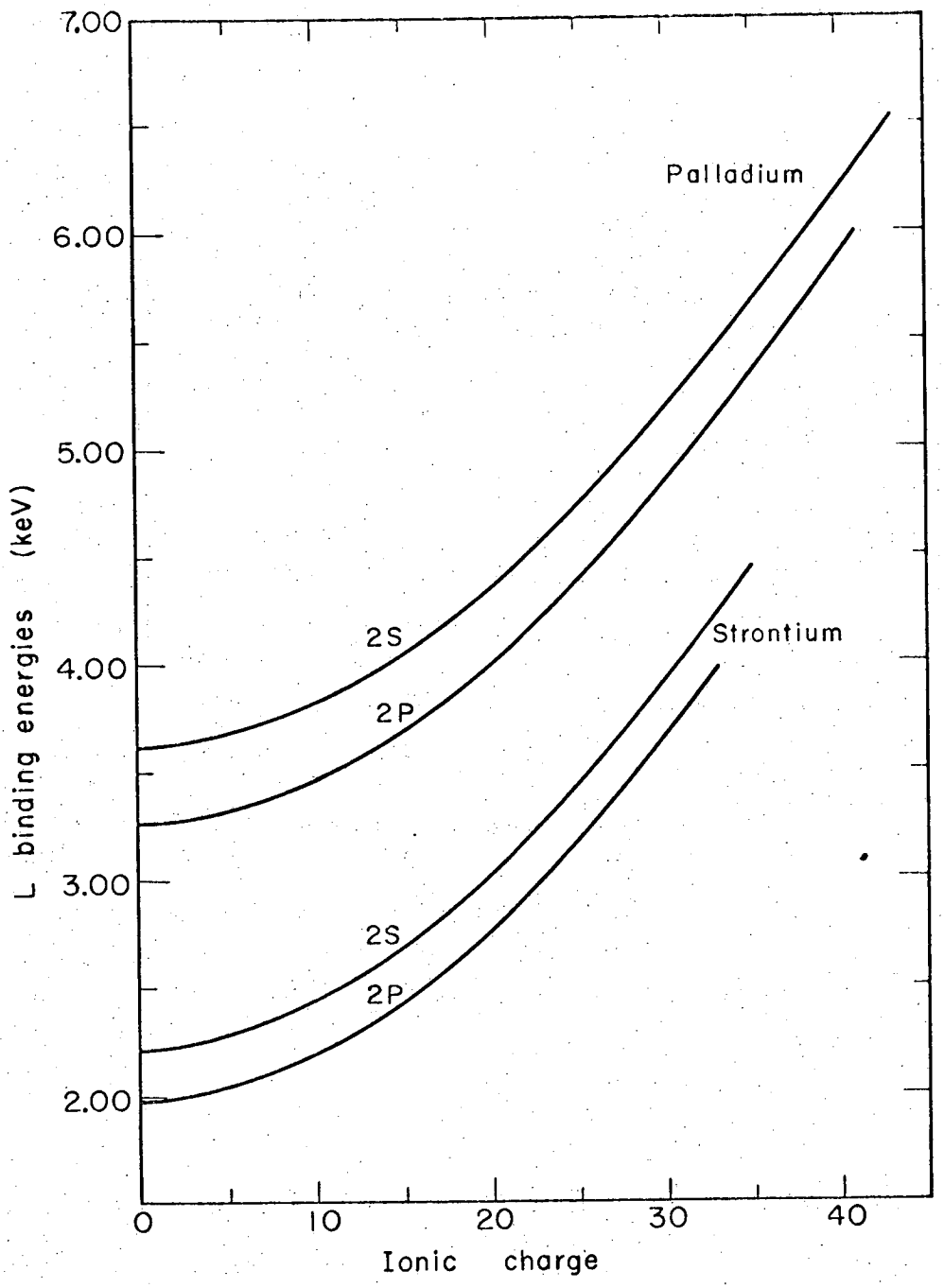

Fig. V-6. Calculated L binding energies of a strontium and palladium atom as a function of their ionic charges.

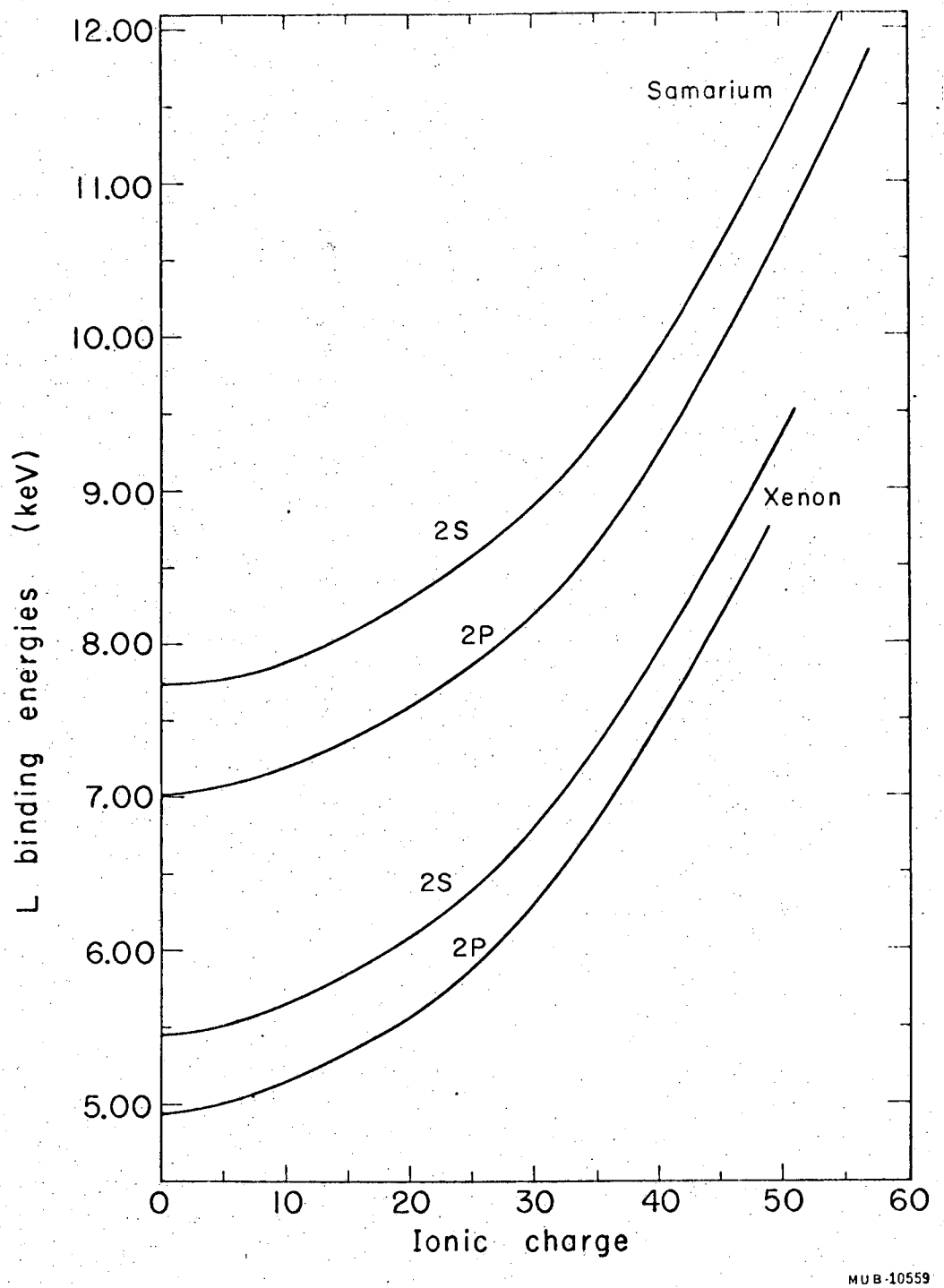

Fig. V-7. Calculated L binding energies of a xenon and samarium atom as a function of their ionic charges.

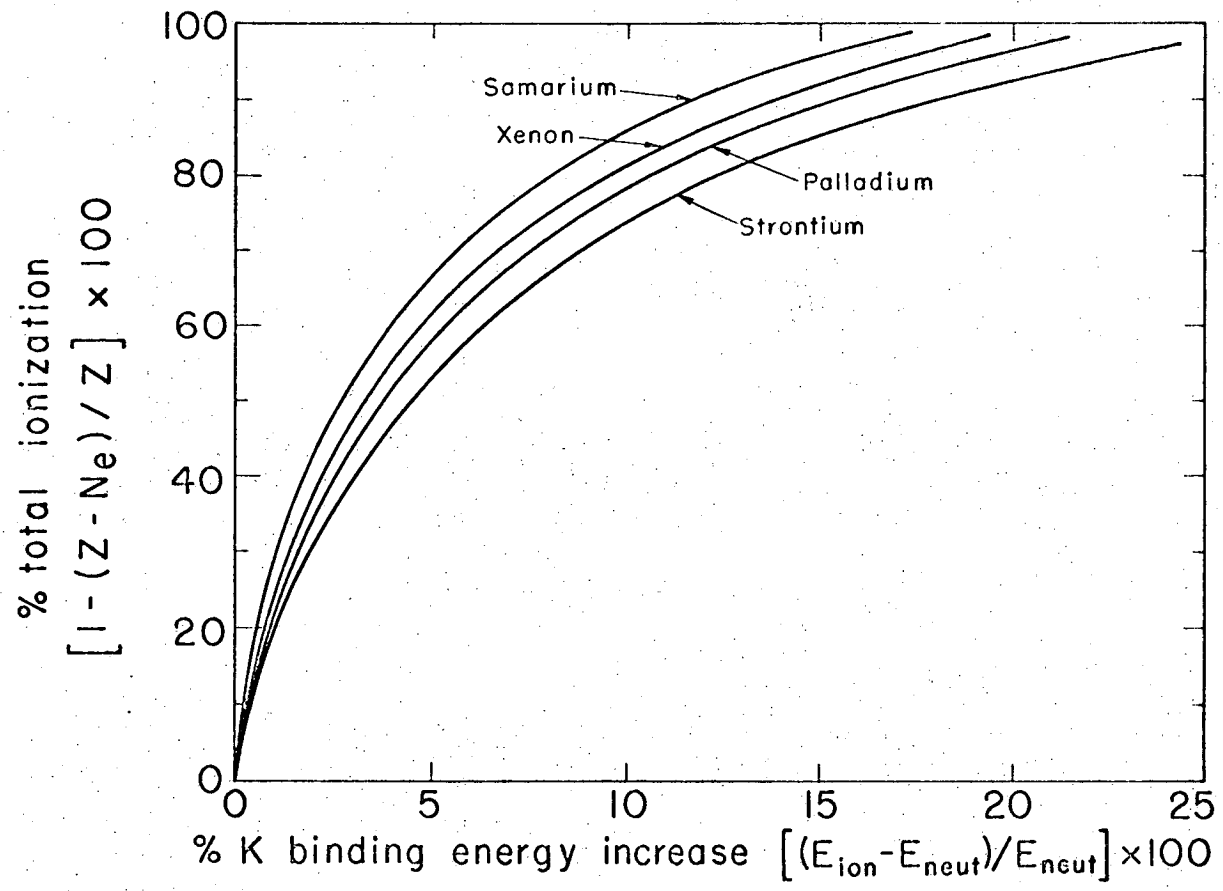

Fig. V-8. Comparison of the relative increase in K binding energy as a function of total ionization for strontium, palladium, xenon and samarium.

Table V-2. K, L and Kα energies for Sr, Pd, Xe and Sm fission fragment ions.

	Electron Binding Energy (keV)			K-α X-Ray
	1S	2S	2P	Energy (keV)
Sr Neutral	16.10	2.21	1.97	14.13
Sr^{+20}	16.89	3.02	2.76	14.13
Sr^{+21}	16.97	3.10	2.84	14.13
Sr^{+22}	17.05	3.18	2.92	14.13
Pd Neutral	24.36	3.61	3.26	21.10
Pd^{+22}	25.21	4.49	4.14	21.07
Pd^{+23}	25.28	4.57	4.22	21.06
Pd^{+24}	25.35	4.65	4.30	21.05
Xe Neutral	34.55	5.45	4.94	29.61
Xe^{+23}	35.38	6.25	5.74	29.64
Xe^{+24}	35.44	6.32	5.81	29.63
Xe^{+25}	35.50	6.38	5.88	29.62
Sm Neutral	46.85	7.74	7.02	39.83
Sm^{+24}	47.58	8.51	7.80	39.78
Sm^{+25}	47.64	8.57	7.85	39.79
Sm^{+26}	47.71	8.63	7.92	39.79

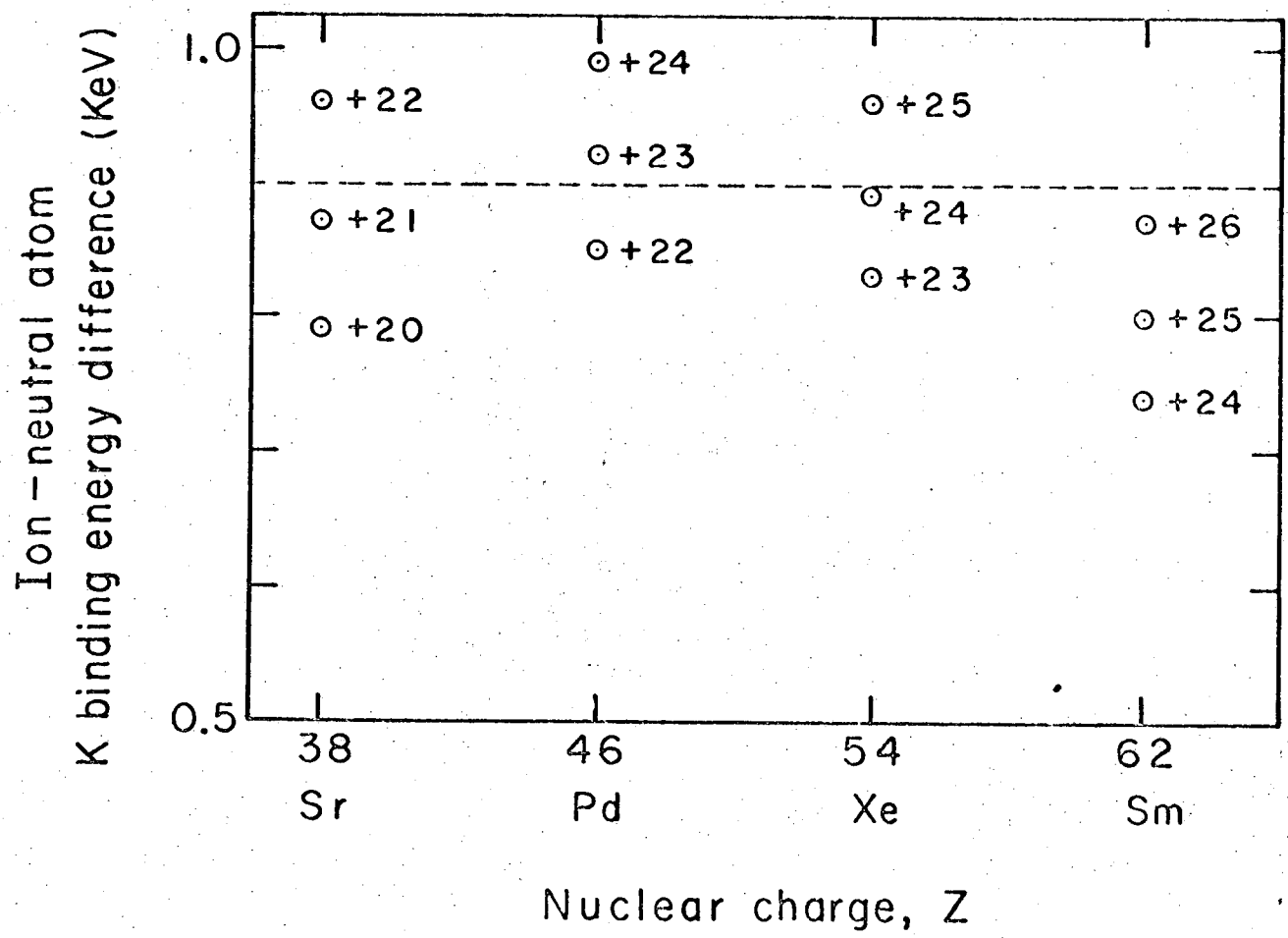

MUB-9903

Fig. V-9. The calculated increase in K binding energy for several probable fission fragment ionic charge states as a function of nuclear charge. The dashed line indicates the approximate constancy of the K binding energy increase for the probable charge states of +21, +23, +24 and +26 spanning the whole region of fission product isotopes.

Table V-3. Calculated orbital energies.

Strontium	3s	3p	3d	4s	4p	5s
Sr Neutral	0.347	0.280	0.132	0.048	0.028	0.004
Sr^{+8}	0.474	0.407	0.260	0.150		
Sr^{+20}	0.996	0.933				

Palladium	3s	3p	3d	4s	4p	4d
Pd Neutral	0.628	0.537	0.335	0.081	0.050	0.005
Pd^{+10}	0.836	0.747	0.544	0.272	0.237	
Pd^{+18}	1.085	0.998	0.800			
Pd^{+28}	1.717	1.642				

Xenon	3s	3p	3d	4s	4p	4d	5s	5p
Xe Neutral	1.058	0.948	0.690	0.200	0.157	0.067	0.022	0.010
Xe^{+8}	1.169	1.059	0.802	0.309	0.265	0.175		
Xe^{+18}	1.512	1.402	1.145	0.596	0.548			
Xe^{+26}	1.845	1.739	1.489					
Xe^{+36}	2.628	2.543						

Samarium	3s	3p	3d	4s	4p	4d	5s	5p
Sm^{+8}	1.739	1.608	1.293	0.483	0.427	0.302	0.163	0.140
Sm^{+16}	1.920	1.791	1.479	0.655	0.599	0.476		
Sm^{+26}	2.381	2.255	1.944	1.029	0.970			
Sm^{+34}	2.794	2.673	2.374					
Sm^{+44}	3.729	3.638						

Table V-4. Optimized orbital exponents.

	1s	2s	3s	4s	5s	2p	3p	4p	5p	3d	4d
Sr	37.19124	13.95111	7.55333	3.36116	1.21365	17.01516	7.38957	2.98304		7.57540	
Pd	45.06163	16.95066	9.74599	4.79658		20.96705	9.67061	4.43206		10.48086	3.40021
Xe	52.82007	20.02845	11.84913	6.50903	2.94593	24.91630	11.88862	6.23714	2.47884	13.31400	5.47198
Sm^{+8}	60.78288	22.87745	13.79440	8.43489	4.39572	28.86481	14.07045	8.04922	4.25116	16.07209	7.26007

VI. CONCLUSION

The results of these experiments have shown that the study of the conversion electrons emitted in fission is an especially attractive way in which detailed information may be obtained concerning the low-energy gamma de-excitation characteristics of fission fragments. Experimental techniques, such as the ones developed here, allow the measurement of the conversion electrons with a selectivity that is unattainable in the study of the gamma rays, both with respect to separating radiation emitted from different members of coincident fragment pairs and with respect to measuring the spectra associated with definite and well-defined time intervals after fission. It was found, however, that serious limitations are imposed upon the energy resolution obtainable in experiments designed to detect electrons in the direction perpendicular to the fragment flight path as a consequence of their emission from a moving source.

The data which have evolved from this work indicate that a large percentage of the gamma rays emitted in fission must be attributed to the decay of odd-mass nuclides. Moreover, it was found that the observed structure is in general agreement with what is expected on the basis of the systematics of neighboring nuclei. Further evidence was found for the existence of a region of stable nuclear deformation near mass 110. The large maximum in electron yield around this mass number and the characteristics of two transitions thought to be associated with ^{110}Ru both suggest rotational behavior.

The binding-energy calculations established the fact that the state of ionization common to fission fragments has a relatively large effect upon the electron binding energies. It was found that the increase in K binding energy is, on the average, 0.9 keV for highly ionized fission fragments and that this increase is approximately constant over the whole region of elements formed in fission. By virture of the fact that both the K- and L-shell electron binding energies are increased by approximately the same amounts, however, the K X-ray energies were found to remain very

nearly the same as those observed for the neutral atoms. A number of experiments are suggested by the magnitude of the dependence of the K binding energies on the large ionic charge states formed in fission. For example, if conversion electrons from any given fission fragment could be measured with enough energy precision in flight and after the fragments have come to rest (i.e. neutralized their charge), the detected shift in energy could be used to directly determine the original state of ionization. It would also be interesting to investigate the effect of ionic charge on conversion coefficients and transition lifetimes by means of fission fragments.

It is worth pointing out the applicability of the magnetic steering device used in these experiments to other types of conversion electron investigations. Experiments involving the study of conversion electrons from alpha emitters, low energy gamma and X-ray emitters, and positron emitters are particularly suited for this device which offers high detection efficiency and a means of shielding the electron detector from the interfering radiations.

Perhaps equally as important as the results of these experiments has been the demonstration of a technique which, by using fission as a means for their production, makes possible the spectroscopic study of a large number of neutron-excess isotopes. It seems certain, based upon the present work, that by the application of methods capable of improved mass determination, such as time-of-flight or mass-spectroscopic techniques, this type of experimentation will be particularly fruitful for some time to come.

ACKNOWLEDGEMENTS

I wish to express my thanks to Professor John O. Rasmussen for his direction and guidance in the conduct of this research.

The continued interest, encouragement and support of Dr. Stanley G. Thompson were greatly appreciated.

I also thank Mr. Harry R. Bowman for the use of his unpublished data and for his many helpful suggestions and discussions concerning this work.

I am greatly indebted to Mrs. Claudette Rugge for her untiring work on the computer programs used to process and analyze the multitudes of data and to Mrs. Joan Phillips for her help with various phases of the data analysis as well as with the preliminary typing of this manuscript.

For their excellent technical assistance in the experiments and for the many hours of patient instruction donated by them to my education in the fundamentals of electronics, I am very grateful to Mr. Richard Jared and Mr. Sam Nolan. The help of Mr. Eugene Miner with a number of design problems is also acknowledged.

The assistance of Mr. Ray Gatti in preparing the ^{252}Cf sources was deeply appreciated.

For providing me with a copy of the SCF computer program and instructing me in its use, I am indebted to Mr. Donald Raimondi.

I wish to thank my wife, Doris, for her encouragement, assistance and patience over the course of this work.

My association with Messrs. Judd Haverfield, John Cooper, Jerry Wilhelmy, James Lamb and Fred Bernthal during my graduate career has been extremely pleasant and has contributed greatly to my knowledge of certain laws of probability and statistics.

This work was done under the auspices of the U. S. Atomic Energy Commission.

APPENDICES

A. The Motion of a Charged Particle in an Inhomogeneous Magnetic Field

A charged particle moving in an inhomogeneous magnetic field may experience two types of drift motions. In each case the orbit of the charged particle is determined by the well known Lorentz force given by

$$\vec{F} = q(\vec{v} \times \vec{B}) \quad , \qquad \text{(VII-1)}$$

where q and v are the charge and velocity of the particle and B is the magnetic field strength.

The first type of drift motion may be understood by considering the situation depicted in Fig. VII-1. Here, the magnetic field is symmetrical about the Z axis and the field lines are slowly converging. The radius of the particle orbit, called the Larmor radius, may be obtained by writing the expression for the centripetal acceleration imposed upon the particle by the Lorentz force; namely

$$q\, v_{\perp}\, B_z = \frac{m v_{\perp}^2}{R} \quad , \qquad \text{(VII-2)}$$

where $v_{\perp}$ is the particle velocity in the plane perpendicular to the Z axis and B_z is the field strength in the z direction. Solving for R, gives

$$R = \frac{m v_{\perp}}{q B_z} \quad . \qquad \text{(VII-3)}$$

It may be shown, that in a magnetic field which varies only slowly in distances of the order of a Larmor radius, the motion of a charged particle is such as to keep its magnetic moment constant.[50] The magnetic moment is by definition given by

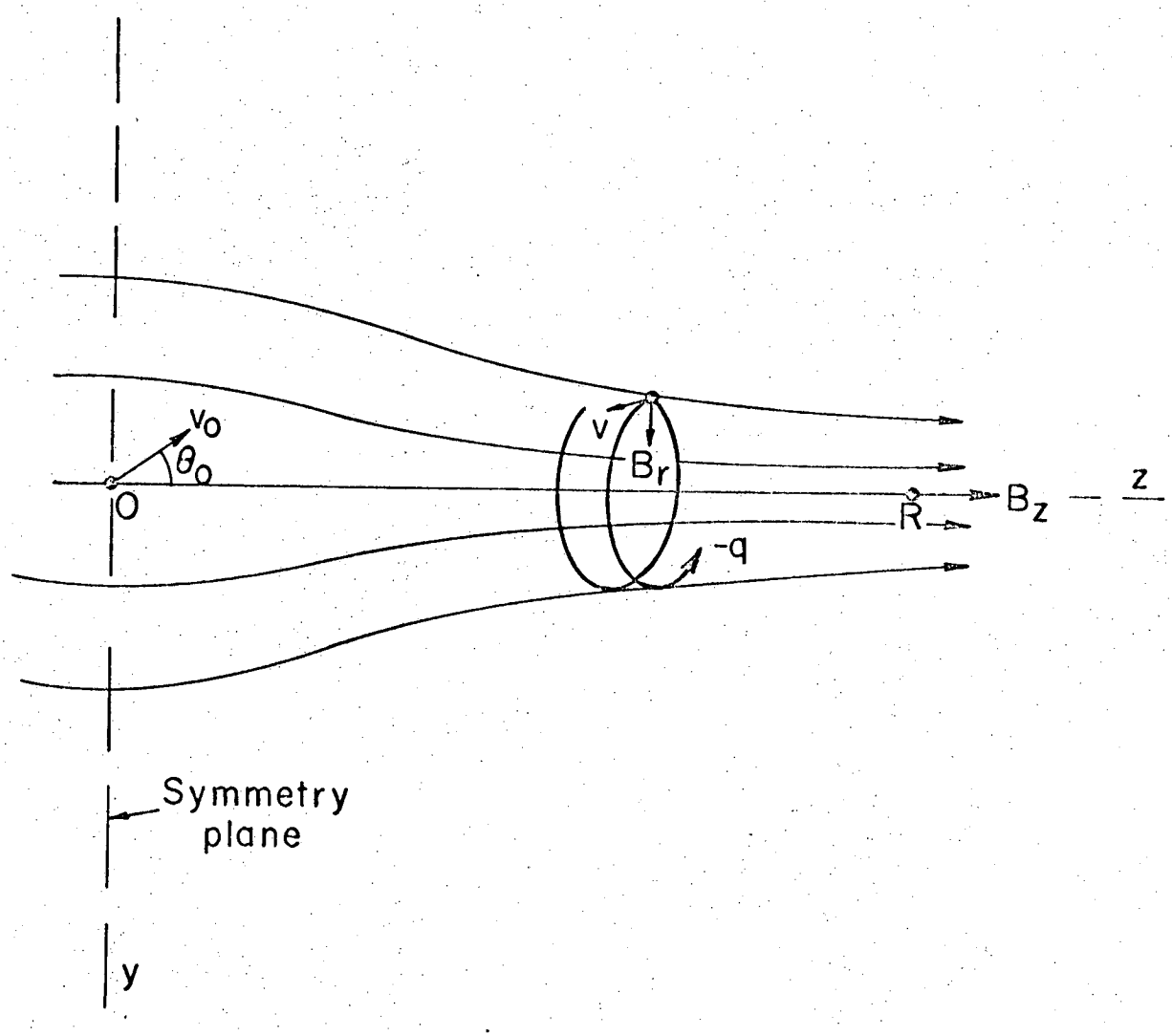

MUB-10886

Fig. VII-1. Diagram illustrating the vertical drift motion of a charged particle moving in a slowly converging magnetic field.

$$u = \text{current} \times \text{area}$$

$$= \frac{qv_\perp}{2\pi R} \times \pi R^2 = 1/2 qv_\perp R \quad . \qquad \text{(VII-4)}$$

By substituting Eq. (VII-3), this reduces to

$$u = \frac{T_\perp}{B_z} = \text{Constant} \quad , \qquad \text{(VII-5)}$$

where $T_\perp$ is the particle kinetic energy in the plane perpendicular to the magnetic field.

Now, it can be verified that there is a force tending to push the particle into the weaker magnetic field region by taking the z component of Eq. (VII-1). Thus

$$F_z = qv_\perp B_r \Big|_{r=R} = m \frac{dv_z}{dt} \quad , \qquad \text{(VII-6)}$$

where B_r is the radial component of the magnetic field. From the spatial relationship of $v_\perp$ and B_r it is evident that the force is directed such that the vertical velocities of gyrating particles which are approaching regions of stronger magnetic field are decreased.

The magnetic flux through the particle orbit is given by

$$\Phi = B_z \pi R^2 = B_z \pi \left(\frac{mv_\perp}{qB_z} \right)^2$$

$$= \frac{2\pi m}{q^2} \frac{T_\perp}{B_z} = \frac{2\pi m}{q^2} u \quad . \qquad \text{(VII-7)}$$

Since the magnetic moment is a constant of motion, the particle is constrained to move in such a way as to keep the flux through its orbit constant. In a highly convergent magnetic field, this means that the particle will gyrate in tighter and tighter helical spirals until it is reflected back into the weaker field. This is the fundamental requirement for a magnetic mirror.

In considering the conditions necessary for reflection to occur, it is evident, since the magnetic moment is a constant of motion, that

$$\frac{T_{o\perp}}{B_{oz}} = \frac{T_{R\perp}}{B_{Rz}} \quad , \tag{VII-8}$$

where the subscript o refers to the particle's starting point near the symmetry plane and the subscript R refers to the reflection point (see Fig. VII-1). If the particle is to be reflected, the component of kinetic energy parallel to the field lines, $T_{\parallel}$, must be zero at the reflection point. The total kinetic energy, T, of a particle moving in a magnetic field, however, is constant since the Lorentz force is always at right angles to the velocity and can do no work. This means that at the reflection point $T_{\perp} = T$.

Since T is constant,

$$\frac{v_{\parallel}^2}{B_z} = \frac{v^2}{B_z} - \frac{v_{\perp}^2}{B_z} \quad , \tag{VII-9}$$

but, from Eq. (VII-8)

$$\frac{v_{\perp}^2}{B_z} = \frac{v^2 \sin^2\theta_o}{B_z} \quad . \tag{VII-10}$$

Making this substitution into Eq. (VII-9), it is found that

$$v_{\|}^2 = v^2\left(1 - \frac{B_z}{B_{oz}} \sin^2\theta_o\right) \quad . \qquad \text{(VII-11)}$$

Since $v_{\|}$ goes to zero at the reflection point, the critical equation for reflection is found by setting the quantity in parentheses in Eq. (VII-11) to zero.

$$1 - \frac{B_{Rz}}{B_{oz}} \sin^2\theta_o = 0$$

$$\sin^2\theta_c \geq \frac{B_{oz}}{B_{Rz}} \quad . \qquad \text{(VII-12)}$$

Therefore, any particle starting at the symmetry plane having an initial velocity angle of θ_c will be reflected where the field lines have converged to give a field of B_{Rz}.

The second type of drift motion in an inhomogeneous magnetic field may be very simply illustrated by referring to Fig. VII-2. The dependence of the Larmor radius on the magnetic field strength, as given in Eq. (VII-3), requires that the radius of curvature be smaller in the strong-field region than in the weak-field region. This results in the drift displacement, d, after one orbit. Further details of particle drift motion are given by Simon.[51]

B. Kinematic Relations for Electrons Emitted from Moving Fission Fragments

Consider the two coordinate systems S and S' picture in Fig. VII-3 where S represents the laboratory system and S' represents the center of mass system. Choosing the x direction as the direction of motion of the fission fragment relative to the laboratory system, the following quantities are defined:

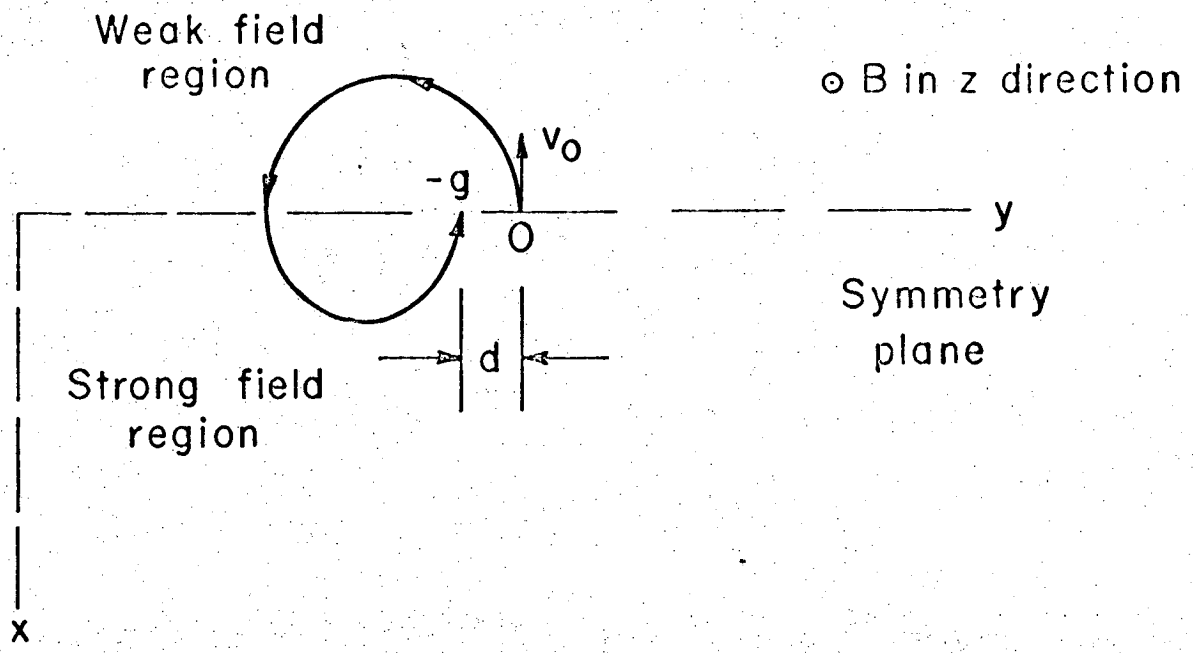

MUB-10885

Fig. VII-2. Diagram illustrating the azimuthal drift motion of a charged particle in an inhomogeneous magnetic field.

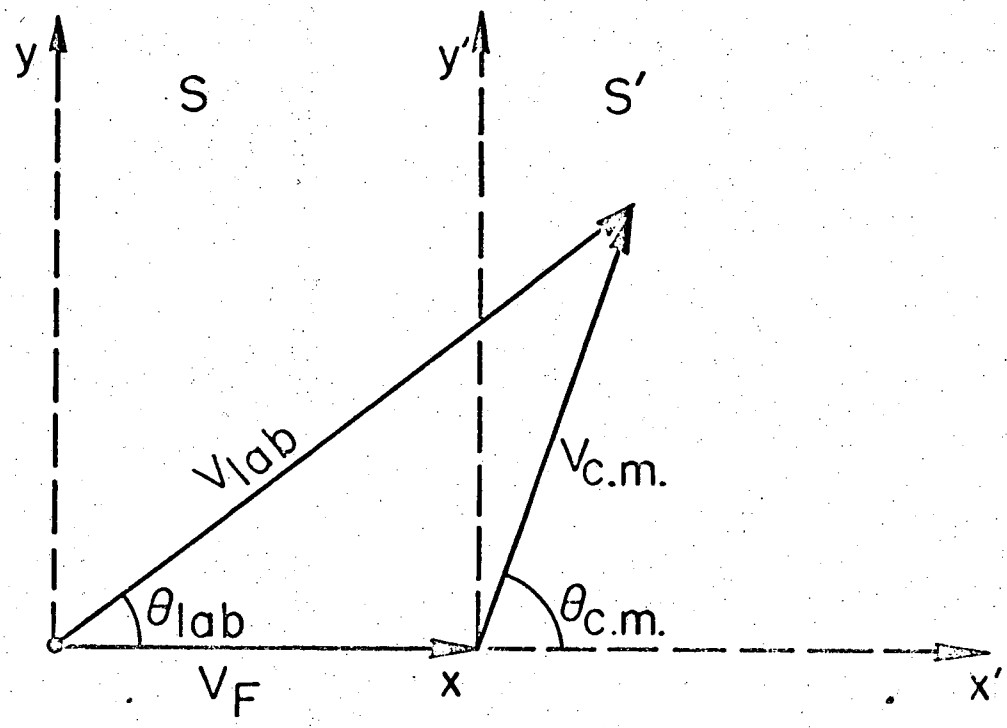

MUB-10854

Fig. VII-3. Diagram defining the laboratory and center of mass coordinate systems.

V_F = fission fragment velocity relative to the laboratory system;
V_{cm} = electron velocity relative to center of mass system;
V_{lab} = electron velocity relative to laboratory system;
θ_{cm} = electron emission angle relative to center of mass system;
θ_{lab} = electron emission angle relative to laboratory system.

The equations which relate the electron velocities in the two coordinate systems are the Lorentz transformations of special relativity:

$$V_{lab(x)} = \frac{V_{cm(x)} + V_F}{1 + \frac{V_{cm(x)}V_F}{c^2}} = \frac{V_{cm}\cos\theta_{cm} + V_F}{1 + \frac{V_{cm}V_F}{c^2}\cos\theta_{cm}}$$

$$V_{lab(y)} = \frac{V_{cm(y)}\sqrt{1 - \left(\frac{V_F}{c}\right)^2}}{1 + \frac{V_{cm(x)}V_F}{c^2}} = \frac{V_{cm}\sin\theta_{cm}\sqrt{1 - \left(\frac{V_F}{c}\right)^2}}{1 + \frac{V_{cm}V_F}{c^2}\cos\theta_{cm}} \qquad \text{(VII-13)}$$

Now

$$V_{lab} = \sqrt{V_{lab(x)}^2 + V_{lab(y)}^2}$$

So

$$V_{lab} = \frac{[V_{cm}^2 + 2V_{cm}V_F\cos\theta_{cm} + V_F^2 - V_{cm}^2\beta^2\sin^2\theta_{cm}]^{1/2}}{1 + \frac{V_{cm}V_F}{c^2}\cos\theta_{cm}} , \qquad \text{(VII-14)}$$

where $\beta = V_F/c$.

The relation between θ_{cm} and θ_{lab} may be easily obtained by noting that $\text{Tan}\,\theta_{lab} = V_{lab(y)}/V_{lab(x)}$. Utilizing this fact, substitution of Eqs. (VII-13) gives

$$\text{Tan } \theta_{lab} = \frac{V_{cm} \sin \theta_{cm} \sqrt{1 - \beta^2}}{V_{cm} \cos \theta_{cm} + V_F} \quad . \qquad \text{(VII-15)}$$

An equation giving V_{cm} as a function V_{lab} and θ_{lab} is found by simply exchanging the laboratory and center of mass subscripts and replacing V_F by $-V_F$ since the only difference between the coordinate systems S and S' is the sign of their relative velocity. Hence

$$V_{cm} = \frac{[V_{lab}^2 - 2V_{lab}V_F \cos \theta_{lab} + V_F^2 - V_{lab}^2\beta^2 \sin^2 \theta_{lab}]1/2}{1 - \frac{V_{lab}V_F}{c^2} \cos \theta_{lab}} \quad , \qquad \text{(VII-16)}$$

and similarly

$$\text{Tan } \theta_{cm} = \frac{V_{lab} \sin \theta_{lab} \sqrt{1 - \beta^2}}{V_{lab} \cos \theta_{lab} - V_F} \quad . \qquad \text{(VII-17)}$$

The laboratory velocity may now be obtained in terms of V_{cm} and θ_{lab} by re-expressing Eq. (VII-16) in the form

$$\left(\frac{V_{cm}^2 V_F^2 \cos^2 \theta_{lab} + V_F^2 c^2 \sin^2 \theta_{lab} - c^4}{c^4} \right) V_{lab}^2 + 2\cos \theta_{lab} V_F \left(1 - \frac{V_{cm}^2}{c^2} \right) V_{lab}$$

$$+ (V_{cm}^2 - V_F^2) = 0 \qquad \text{(VII-18)}$$

and solving for V_{lab}. The result is:

$$V_{lab} = \frac{\left(\frac{V_F^2 - V_{cm}^2\beta^2}{V_F} \right) \cos \theta_{lab} + [(V_{cm}^2 - V_{cm}^2\beta^2 \cos^2 \theta_{lab} - V_F^2 \sin^2 \theta_{lab})(1-\beta^2)]^{1/2}}{1 - \frac{V_{cm}^2}{c^2} \beta^2 \cos^2 \theta_{lab} - \beta^2 \sin^2 \theta_{lab}} \quad .$$

$$\text{(VII-19)}$$

The center of mass and laboratory angles may be obtained in terms of V_{cm} and V_{lab} by re-expressing Eq. (VII-14) in the form

$$\frac{V_{cm}^2 V_F^2}{c^2}\left(1 - \frac{V_{lab}^2}{c^2}\right)\cos^2\theta_{cm} + 2V_{cm}V_F\left(1 - \frac{V_{lab}^2}{c^2}\right)\cos\theta_{cm} + \left(V_{cm}^2 + V_F^2 - V_{lab}^2 - \frac{V_{cm}^2 V_F^2}{c^2}\right) = 0$$

and solving for $\cos\theta_{cm}$. This result is

$$\cos\theta_{cm} = \frac{-1 + \sqrt{\dfrac{\left(1 - \dfrac{V_{cm}^2}{c^2}\right)\left(1 - \dfrac{V_F^2}{c^2}\right)}{\left(1 - \dfrac{V_{lab}^2}{c^2}\right)}}}{\dfrac{V_{cm}V_F}{c^2}} \quad . \qquad \text{(VII-20)}$$

Again changing the sign of V_F and exchanging subscripts gives:

$$\cos\theta_{lab} = \frac{1 - \sqrt{\dfrac{\left(1 - \dfrac{V_{lab}^2}{c^2}\right)\left(1 - \dfrac{V_F^2}{c^2}\right)}{\left(1 - \dfrac{V_{cm}^2}{c^2}\right)}}}{\dfrac{V_{lab}V_F}{c^2}} \quad . \qquad \text{(VII-21)}$$

Another important expression relating the angular distribution of electrons in the center of mass system to the angular distribution of electrons in the laboratory system may be derived from the fact that the number of electrons emitted between the angles θ_{lab} and $\theta_{lab} + d\theta_{lab}$ in the laboratory system must equal the number of electrons emitted between the transformed angles θ_{cm} and $\theta_{cm} + d\theta_{cm}$ in the center of mass system.

Let

$N(\theta_{lab})$ = number of electrons emitted/unit solid angle in laboratory system;

$N(\theta_{cm})$ = number of electrons emitted/unit solid angle in center of mass system.

Then

$$N(\theta_{lab})\, \Omega_{(\theta_{lab})} = N(\theta_{cm})\, \Omega_{(\theta_{cm})} \quad ,$$

where the Ω's are laboratory and center of mass system solid angles given by

$$\Omega_{(\theta)} = \sin\theta\, d\theta \int_0^{d\pi} d\phi$$

$$= 2\pi \sin\theta\, d\theta \quad .$$

Thus

$$N(\theta_{lab})\, 2\pi \sin\theta_{lab}\, d\theta_{lab} = N(\theta_{cm})\, 2\pi \sin\theta_{cm}\, d\theta_{cm}$$

and

$$\frac{N(\theta_{lab})}{N(\theta_{cm})} = \frac{\sin\theta_{cm}}{\sin\theta_{lab}} \frac{d\theta_{cm}}{d\theta_{lab}} \quad . \qquad \text{(VII-22)}$$

From Eq. (VII-18)

$$\frac{d}{d\theta_{lab}}(\text{Tan }\theta_{cm}) = \frac{d}{d\theta_{lab}}\left(\frac{V_{lab}\sin\theta_{lab}\sqrt{1-\beta^2}}{V_{lab}\cos\theta_{lab} - V_F}\right)$$

$$\sec^2\theta_{cm}\frac{d\theta_{cm}}{d\theta_{lab}} = \frac{(V_{lab}^2 - V_{lab}V_F\cos\theta_{lab})\sqrt{1-\beta^2}}{(V_{lab}\cos\theta_{lab} - V_F)^2}$$

$$\frac{d\theta_{cm}}{d\theta_{lab}} = \frac{\cos^2\theta_{cm}(V_{lab}^2 - V_{lab}V_F\cos\theta_{lab})\sqrt{1-\beta^2}}{(V_{lab}\cos\theta_{lab} - V_F)^2} \qquad \text{(VII-23)}$$

and

$$\text{Tan }\theta_{cm} = \frac{\sin\theta_{cm}}{\cos\theta_{cm}} = \frac{V_{lab}\sin\theta_{lab}\sqrt{1-\beta^2}}{V_{lab}\cos\theta_{lab} - V_F}$$

so

$$\frac{\sin\theta_{cm}}{\sin\theta_{lab}} = \frac{\cos\theta_{cm}V_{lab}\sqrt{1-\beta^2}}{V_{lab}\cos\theta_{lab} - V_F} \qquad \text{(VII-24)}$$

and

$$\cos\theta_{cm} = \frac{V_{lab}\cos\theta_{lab} - V_F}{\left[V_{lab}^2\sin^2\theta_{lab}(1-\beta^2) + (V_{lab}\cos\theta_{lab} - V_F)^2\right]^{1/2}} \qquad \text{(VII-25)}$$

Therefore

$$\frac{N(\theta_{lab})}{N(\theta_{cm})} = \frac{V_{lab}^2(V_{lab} - V_F\cos\theta_{lab})(1-\beta^2)}{\left[V_{lab}^2(1-\beta^2\sin^2\theta_{lab}) - 2V_{lab}V_F\cos\theta_{lab} + V_F^2\right]^{3/2}} \qquad \text{(VII-26)}$$

C. Hartree-Fock Theory

1. Open Shell Theory

Proceeding according to the variational principle, the total energy of the system is to be minimized such that

$$\delta \int \Phi^* H \Phi \, dV = 0 \quad . \tag{VII-27}$$

The wave function to be used in this procedure is an antisymmetrized product of one-electron functions expressed in the form of a determinant.

$$\Phi = \frac{1}{\sqrt{2n!}} \sum_{p} (-1)^p P(\phi_1\alpha, \phi_1\beta, \ldots . \phi_n\beta) \tag{VII-28}$$

$$= \frac{1}{\sqrt{2n!}} \begin{vmatrix} \phi_1\alpha(1) & \phi_1\beta(1) & \ldots\ldots & \phi_n\alpha(1) & \phi_n\beta(1) \\ \phi_1\alpha(2) & \phi_1\beta(2) & \ldots\ldots & \phi_n\alpha(2) & \phi_n\beta(2) \\ \ldots\ldots & \ldots\ldots & \ldots\ldots & \ldots\ldots & \ldots\ldots \\ \ldots\ldots & \ldots\ldots & \ldots\ldots & \ldots\ldots & \ldots\ldots \\ \phi_1\alpha(2n) & \phi_1\beta(2n) & \ldots\ldots & \phi_n\alpha(2n) & \phi_n\beta(2n) \end{vmatrix}$$

where P is the standard permutation operator.

The Hamiltonian describing the system is

$$H = \sum_{i=1}^{2n} \left[\frac{-\hbar^2 \nabla_i^2}{2m} - \frac{Ze^2}{r_i} \right] + \sum_{i>j=1}^{2n} \frac{e^2}{r_{ij}} \quad , \tag{VII-29}$$

where the first and second terms constitute one and two-electron operators respectively. In considering the diagonal matrix elements of one and two-electron operators between determinantial wave functions, it can be shown that[52]

$$\langle A \,|F_{1\text{electron}}|\, A\rangle = \sum_{i=1}^{2n} \langle a_i \,|f|\, a_i\rangle \quad , \qquad \text{(VII-30)}$$

where $F_{1\text{electron}} = \sum_i f_{i\ 1\text{electron}}$, and

$$\langle A \,|G_{2\text{electron}}|\, A\rangle = \sum_{k>t=1}^{2n} \left[\langle a_k a_t \,|g|\, a_k a_t\rangle - \delta(\text{spin } k, \text{ spin } t)\ \langle a_k a_t \,|g|\, a_t a_k\rangle\right] \quad , \qquad \text{(VII-31)}$$

where $G_{2\text{electron}} = \sum_{i>j} g_{ij}$. Since the Hamiltonian is spin independent, only the space functions need be considered. Writing out the expression for the total energy by applying Eqs. (VII-30) and (VII-31), the following expression is obtained:

$$E = \int \Phi^* H \Phi \, dV = 2\left\{\sum_{i=1}^{n} \int \phi_i^*(1) \left(\frac{-\hbar^2\nabla^2(1)}{2m} - \frac{Ze^2}{r_1}\right) \phi_{i(1)} \, dV_1 \right.$$
$$+ \sum_{m<n=1}^{n} \left[2\iint \phi_m^*(1)\, \phi_n^*(2) \left(\frac{e^2}{r_{12}}\right) \phi_{m(1)}\, \phi_{n(2)} \, dV_1 \, dV_2 \right.$$
$$\left.\left. - \iint \phi_m^*(1)\, \phi_n^*(2) \left(\frac{e^2}{r_{12}}\right) \phi_{n(1)} \ \phi_{m(2)} \, dV_1 dV_2\right]\right\} \quad . \qquad \text{(VII-32)}$$

The first integral in the second term in Eq. (VII-32) is known as a Coulomb integral while the second integral is called an exchange integral. The factors of two in Eq. (VII-32) result from the fact that there are various combinations of spin functions which lead to the same combination of space functions and hence the summations need only be carried over the number of space orbitals (n) instead of over the number of electrons (2n).

Now letting

$$\left.\begin{aligned} H_{ii}^{\circ} &= \int \phi_i \left[\frac{-\hbar^2\nabla^2(1)}{2m} - \frac{Ze^2}{r_i}\right] \phi_i \, dV_i \\ J_{mn} &= \text{Coulomb integral} \\ K_{mn} &= \text{Exchange integral} \end{aligned}\right\} , \qquad \text{(VII-33)}$$

the total energy may be expressed as

$$E = 2\left[\sum_i H_{ii}^{\circ} + \sum_{i>j} (2J_{ij} - K_{ij})\right] . \qquad \text{(VII-34)}$$

Roothaan[53] defines Coulomb and exchange operators by the relations

$$\begin{aligned} \bar{J}_m(u)\,\phi(u) &= \left(\int \phi_m^*(\nu)\,\frac{e^2}{r_{u\nu}}\,\phi_{m(\nu)}\,dV_\nu\right)\phi(u) \\ \bar{K}_m(u)\,\phi(u) &= \left(\int \phi_m(\nu)\,\frac{e^2}{r_{u\nu}}\,\phi_{(\nu)}\,dV_\nu\right)\phi_m(u) \end{aligned} \qquad \text{(VII-35)}$$

Using the calculus of variations to minimize the energy, Eq. (VII-34) is varied by an infinitesimal amount, resulting in the following expression upon substitution of the Coulomb and exchange operators Eqs. (VII-35):

$$\delta E = 2\sum_i \int \delta\phi_i^*(1)\left[H^{\circ} + \sum_j (2\bar{J}_j - \bar{K}_j)\right]\phi_{i(1)}\,dV_1 + 2\sum_i \int \delta\phi_{i(1)}$$

$$\left[H^{\circ} + \sum_j (2\bar{J}_j - \bar{K}_j)\right]^* \phi_i^*(1)\,dV_1 . \qquad \text{(VII-36)}$$

In carrying out the variational procedure, the wave functions must be constrained to remain orthonormal; that is,

$$\delta \int \phi_i^* \phi_j \, dV = \int \delta\phi_i^* \phi_j \, dV + \int \phi_i^* \delta\phi_j \, dV = 0 \quad . \quad \text{(VII-37)}$$

The usual way of insuring this condition is to employ the method of Lagrangian multipliers.[54] The above constraint Eq. (VII-37) is applied by adding the following terms to Eq. (VII-36):

$$-2 \sum_i \sum_j \epsilon_{ji} \left[\int \delta\phi_i^*(1) \, \phi_{j(1)} \, dV_1 + \int \phi_i^*(1) \, \delta\phi_{j(1)} \, dV_1 \right] =$$

$$-2 \sum_i \sum_j \epsilon_{ji} \int \delta\phi_i^*(1) \, \phi_{j(1)} \, dV_1 - 2 \sum_i \sum_j \epsilon_{ij} \int \delta\phi_{i(1)} \, \phi_j^*(1) dV_1 \quad , \quad \text{(VII-38)}$$

where ϵ_{ji} and ϵ_{ij} are Lagrangian multipliers. In this way, the problem of finding the conditions for $\delta E = 0$ for only those $\delta\phi_i$'s which are compatible with the orthonormality constraint now becomes equivalent to finding the conditions for $\delta E' = 0$ without constraint, but at the same time giving suitable values to the Lagrangian multipliers. The result is

$$\delta E' = 2 \sum_i \int \delta\phi_i^*(1) \left\{ \left[H^o + \sum_i (2\bar{J}_j - \bar{K}_j) \right] \phi_{i(1)} - \sum_j \epsilon_{ji} \, \phi_{j(1)} \right\} dV_1 \cdot$$

$$+ \text{(Complex conjugate)} = 0 \quad . \quad \text{(VII-39)}$$

It is now required that each term in Eq. (VII-39) be identically zero. Since the variation is arbitrary, the integrands, therefore, must be zero. Hence, writing out the integrands yields the Hartree-Fock closed shell equations

$$\left[H^{o} + \sum_{j} (2\,\bar{J}_{j} - \bar{K}_{j})\right] \phi_{i(1)} = \sum_{j} \phi_{j(1)}\, \epsilon_{ji}$$

$$\left[H^{o} + \sum_{j} (2\,\bar{J}_{j} - \bar{K}_{j})\right]^{*} \phi_{i}^{*}(1) = \sum_{j} \phi_{j}^{*}(1)\, \epsilon_{ij} \quad , \tag{VII-40}$$

or, writing out the first of Eq. (VII-40) explicitly,

$$\left[\frac{-\hbar^2 \nabla_1^2}{2m} - \frac{Ze^2}{r_1}\right]\phi_{i(1)} + 2\sum_{j\neq i=1}^{n}\left[\int \phi_j^{*}(2)\, \frac{e^2}{r_{12}}\, \phi_{j(2)}\, dV_2\right] \phi_{i(1)}$$

$$- \sum_{j\neq i=1}^{n}\left[\int \phi_j^{*}(2)\, \frac{e^2}{r_{12}}\, \phi_{i(2)}\, dV_2\right] \phi_{j(1)} = \sum_{j=1}^{n} \phi_{j(1)}\, \epsilon_{ji} \quad . \tag{VII-41}$$

The Hartree-Fock Hamiltonian operator may be defined as

$$F = H^{o} + \sum_{i} (2\,\bar{J}_{i} - \bar{K}_{i}) \tag{VII-42}$$

and used to re-express Eq. (VII-41) in matrix notation:

$$\tilde{F}\,\tilde{\phi} = \tilde{\phi}\,\tilde{\epsilon} \quad . \tag{VII-43}$$

The ϕ's may now be transformed to a new set ϕ_i' by means of an arbitrary unitary transformation such that

$$\begin{aligned} \tilde{\phi}' &= \tilde{\phi} U \\ \tilde{\epsilon}' &= \tilde{U}^{+}\,\tilde{\epsilon}\,\tilde{U} \end{aligned} \tag{VII-44}$$

where

$$\tilde{U}^{+}\,\tilde{U} = \tilde{E} \quad .$$

The Hartree-Fock Hamiltonian operator matrix is invariant to such a unitary transformation since it is composed of scalar products

$$\tilde{F}' = \tilde{F} \quad , \tag{VII-45}$$

and since the matrix $\tilde{\epsilon}$ may be shown to be Hermitian, it follows that there exists a unitary matrix which will diagonalize $\tilde{\epsilon}$. There results no loss of generality in picking the representation in which $\tilde{\epsilon}$ is diagonal. In this representation the Hartree-Fock equations are given by

$$F \phi_{i(1)} = \epsilon_{ii} \phi_{i(1)} \quad , \tag{VII-46}$$

and the expression for the total energy is readily found by multiplying both sides of Eq. (VII-46) by $\phi_i^*(1)$ and expressing the resulting equation as an integral over all space after substituting Eq. (VII-42) for F. Comparison of this equation with Eq. (VII-34) yields

$$E = \sum_{i=1}^{n} (H_{ii}^{o} + \epsilon_{ii}) \quad . \tag{VII-47}$$

Equation (VII-46) is a pseudo-eigenvalue equation since the operator F is defined in terms of the solutions.

2. Open-Shell Theory

In solving the Hartree-Fock closed-shell equations, a great simplification results from the realization that the ϕ_i's must have the form of solutions of a central-field problem; that is, the orbitals must belong in sets to irreducible representations. This state of affairs stems from the fact that the Hartree-Fock problem for closed-shell atoms or ions can be shown[43] to be spherically symmetrical. Open shell cases, however, do not possess spherical symmetry and so a process of spherical averaging is required in order to get central-field type orbitals.

The customary procedure in solving open-shell problems is to set up central-field type orbitals to represent a single component of a set of degenerate total wave functions and then vary these functions such that the energy is minimized. The solution of the Hartree-Fock equations in this manner is not in general possible without the introduction of further simplifying approximations. Roothaan,[45] on the other hand, has developed a method whereby the open-shell contribution to the total energy is taken into account by summing over all members of the partially occupied degenerate set and introducing a fractional occupation number. As a result, the Hartree-Fock Hamiltonian operators are totally symmetric and the solutions are automatically central-field type symmetry orbitals. Furthermore, no additional approximations are needed.

Starting with a total function consisting of a sum of anti-symmetrized products, each of which contains a doubly occupied closed-shell core ϕ_c and a partially occupied open shell chosen from a set ϕ_o, Roothaan writes the expectation value of the energy as follows:

$$E = 2 \sum_k H_k^{\circ} + \sum_{k\ell} (2 J_{k\ell} - K_{k\ell}) + f \left[2 \sum_m H_m^{\circ} + f \sum_{mn} (2aJ_{mn} - bK_{mn}) + 2 \sum (2J_{km} - K_{km}) \right] , \qquad \text{(VII-48)}$$

where, using Roothaan's notation, the indices k and ℓ, refer to closed-shell orbitals, m and n refer to open-shell orbitals, and i and j refer to either set. In Eq. (VII-48), a and b are constants which specify the state of the configuration while f is the fractional open-shell occupation number. The first two sums represent the closed-shell energy, the next two sums represent the open-shell energy and the last sum represents the open-closed shell interaction energy.

Proceeding in a manner similar to that used in the closed-shell theory, the Coulomb and exchange operators are defined in an analogous way; this time, however, separate operators for open and closed shells are defined such that

$$\begin{aligned} \bar{J}_c &= \sum_k \bar{J}_k \\ \bar{J}_o &= f \sum_m \bar{J}_m \\ \bar{J}_T &= \bar{J}_c + \bar{J}_o \end{aligned} \qquad \text{(VII-49)}$$

and similarly for $\bar{K}_c$, $\bar{K}_o$ and $\bar{K}_T$. In addition, the following Coulomb and exchange coupling operators are defined:

$$\begin{aligned} L_i\phi &= \langle \phi_i | \bar{J}_o | \phi \rangle \ \phi_i + \langle \phi_i | \phi \rangle \ \bar{J}_o \phi_i \\ M_i\phi &= \langle \phi_i | \bar{K}_o | \phi \rangle \ \phi_i + \langle \phi_i | \phi \rangle \ \bar{K}_o \phi_i \end{aligned} \qquad \text{(VII-50)}$$

$$\begin{aligned} L_c &= \sum_k L_k & M_c &= \sum_k M_k \\ L_o &= f \sum_m L_m & M_o &= f \sum_m M_m \\ L_T &= L_c + L_o & M_T &= M_c + M_o \end{aligned} \qquad \text{(VII-51)}$$

All of the above operators are invariant under the transformation

$$\tilde{\phi}_c' = \tilde{\phi}_c \tilde{U}_c, \qquad \tilde{\phi}_o' = \tilde{\phi}_o \tilde{U}_o \ , \qquad \text{(VII-52)}$$

where $\tilde{U}_c$ and $\tilde{U}_o$ are unitary matrices.

The energy [Eq. (VII-48)] is then minimized subject to the constraint that the orbitals remain orthonormal. The result is

$$\begin{aligned}(H^{o} + 2\,\bar{J}_c - \bar{K}_c + 2\,\bar{J}_o - \bar{K}_o)\,\phi_k &= \sum_{\ell} \phi_\ell\,\epsilon_{\ell k} + \sum_{n} \phi_n\,\epsilon_{nk} \\ f(H^{o} + 2\,\bar{J}_c - \bar{K}_c + 2a\,\bar{J}_o - b\,\bar{K}_o)\,\phi_m &= \sum_{\ell} \phi_\ell\,\epsilon_{\ell k} + \sum_{n} \phi_n\,\epsilon_{nm}\end{aligned} \quad . \tag{VII-53}$$

Now, since the open and closed shell orbitals may only be transformed within themselves according to Eq. (VII-52), the above equation cannot be transformed into a pseudo-eigenvalue equation as in the closed shell case due to the presence of Lagrangian multipliers which couple open and closed shells and hence the nondiagonal Lagrangian multipliers cannot in general be removed. By re-expressing the closed-open shell coupling terms using the coupling operators [Eqs. (VII-50 and (VII-51)], however, Roothaan finds that the open-closed Lagrangian multipliers may be absorbed into the left-hand side by the substitutions

$$\begin{aligned}(2\alpha L_o - \beta M_o)\,\phi_k &= -\sum_{n} \phi_n\,\epsilon_{nk} \\ f(2\alpha L_c - \beta M_c)\,\phi_m &= -\sum_{\ell} \phi_\ell \epsilon_{\ell m}\end{aligned} \quad , \tag{VII-54}$$

where $\alpha = \frac{(1-a)}{(1-f)}$, $\beta = \frac{(1-b)}{(1-f)}$. In this manner, the open and closed shell terms may be transformed separately and their respective Lagrangian multiplier matrices diagonalized. Further manipulation allows a formulation in which the open and closed shell orbitals are solutions of the same pseudo-eigenvalue equation. In this formulation, the total energy is found to be

$$E = \sum_k (H_k^{\circ} + \epsilon_k) + f \sum_m (H^{\circ} + \epsilon_m) - f \sum_{km} (2\alpha J_{km} - \beta K_{km}) -$$

$$f^3 \sum_{mn} (2\alpha J_{mn} - \beta K_{mn}) \quad . \qquad \text{(VII-55)}$$

D. Experimental Conversion Electron Spectra

The measured electron spectra obtained in the present experiments are presented here for convenient reference. Figs. VII-4 through VII-7 show the 1 nsec delayed, electron, low energy spectra for all mass intervals contained in the first half of the light fragment region, the second half of the light fragment region, the first half of the heavy fragment region, and the second half of the heavy fragment region respectively, superimposed on single plots. The 2 nsec delayed, electron, low energy spectra are shown superimposed for the same sets of mass intervals in Figs. VII-8 through VII-11.

In Figs. VII-12 through VII-36 are shown the complete set of 1 nsec delayed, electron, low energy spectra for individual mass intervals. In those plots where two spectra appear, the larger of the two is a times 4 magnification of the smaller.

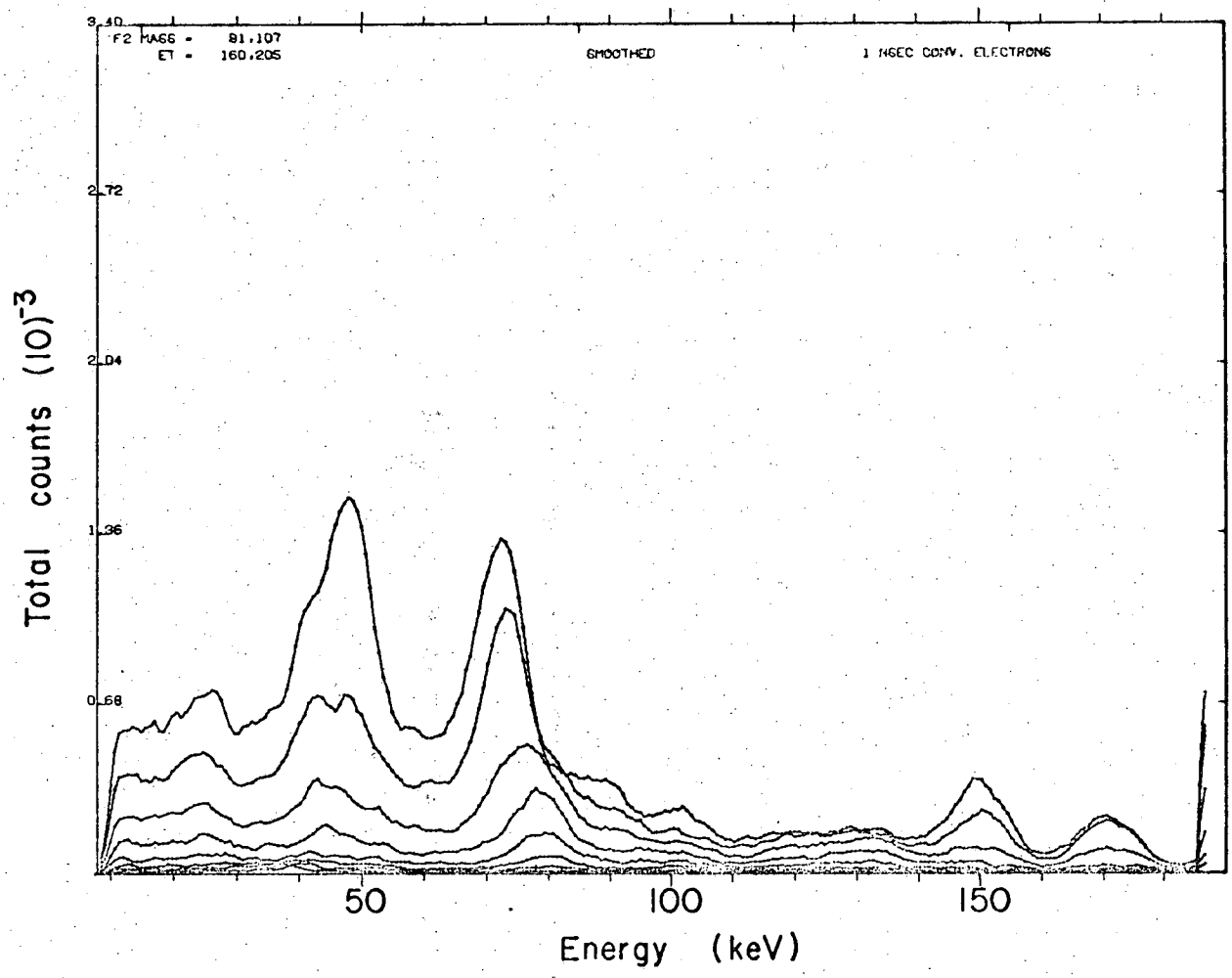
F2 MASS = 81.107
ET = 160.205
SMOOTHED
1 MSEC CONV. ELECTRONS
3.40
2.72
2.04
1.36
0.68
Total counts (10)-3
50
100
150
Energy (keV)

Fig. VII-4

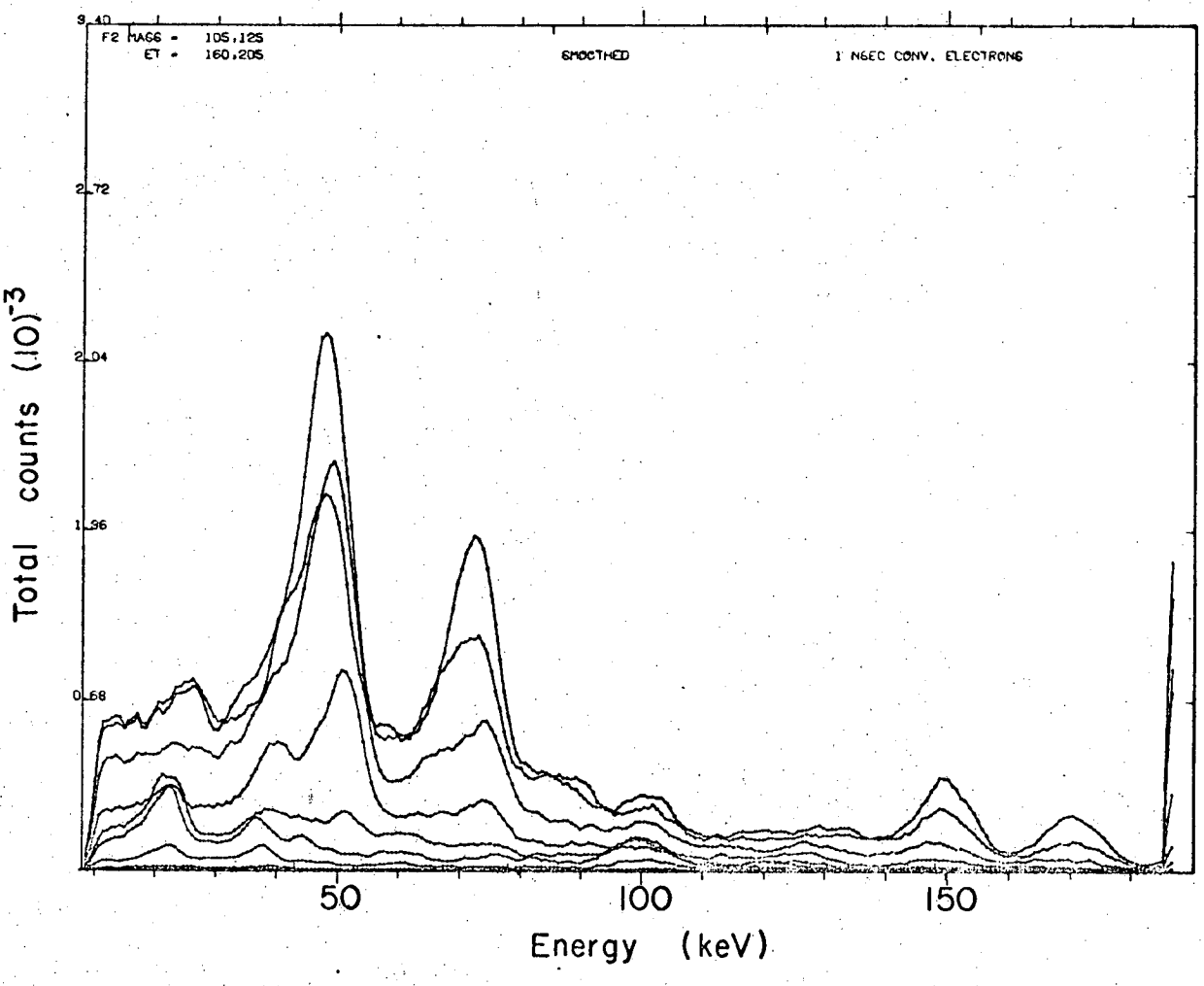
3.40
2.72
2.04
1.36
0.68
F2 MASS = 105,125
ET = 160,205
SMOOTHED
1 NSEC CONV. ELECTRONS
Total counts (10)-3
50
100
150
Energy (keV)

Fig. VII-5

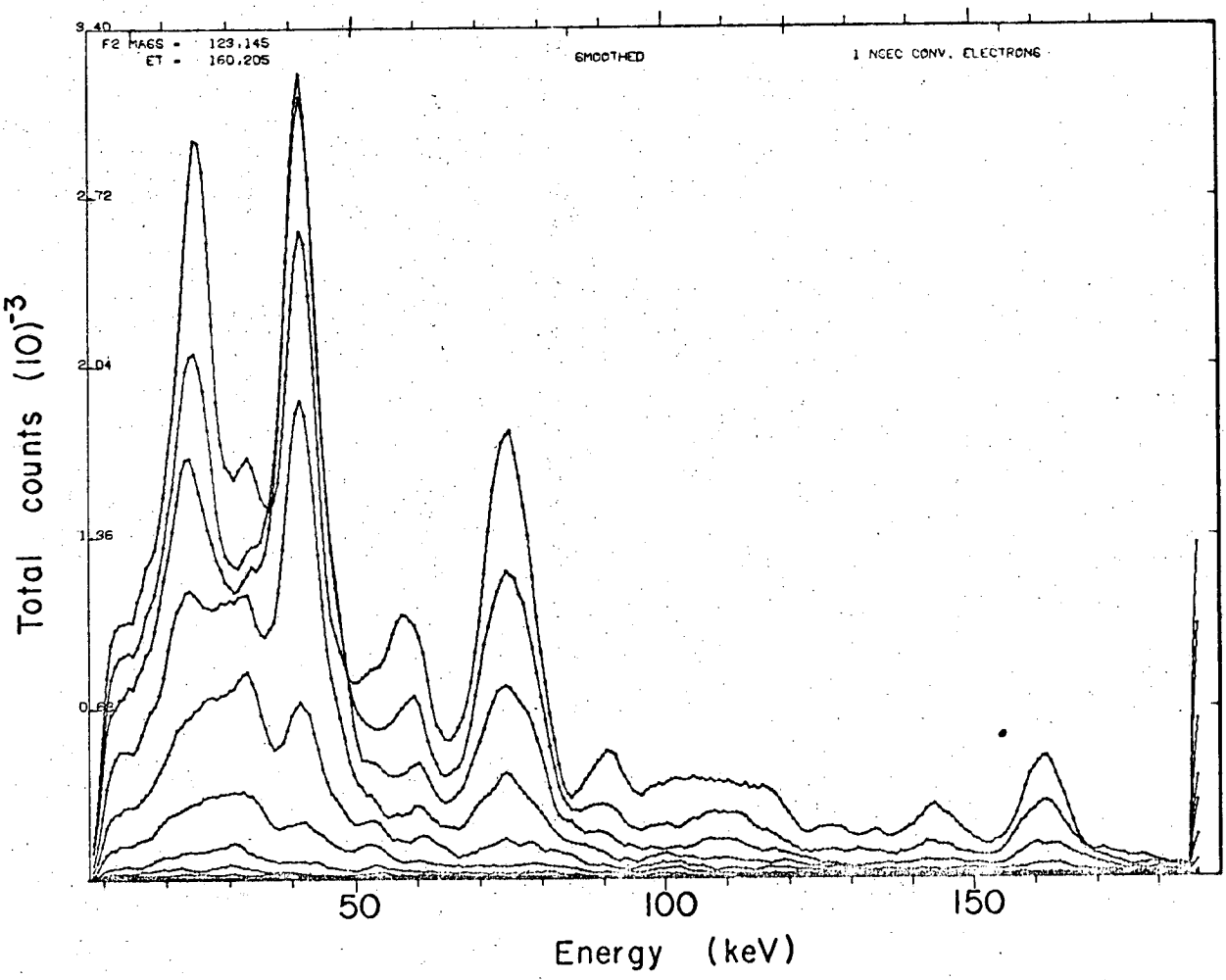
3.40
2.72
2.04
1.36
0.68
F2 MAGS = 123.145
ET = 160.205
SMOOTHED
1 NSEC CONV. ELECTRONS
Total counts (10)^-3
50
100
150
Energy (keV)

Fig. VII-6

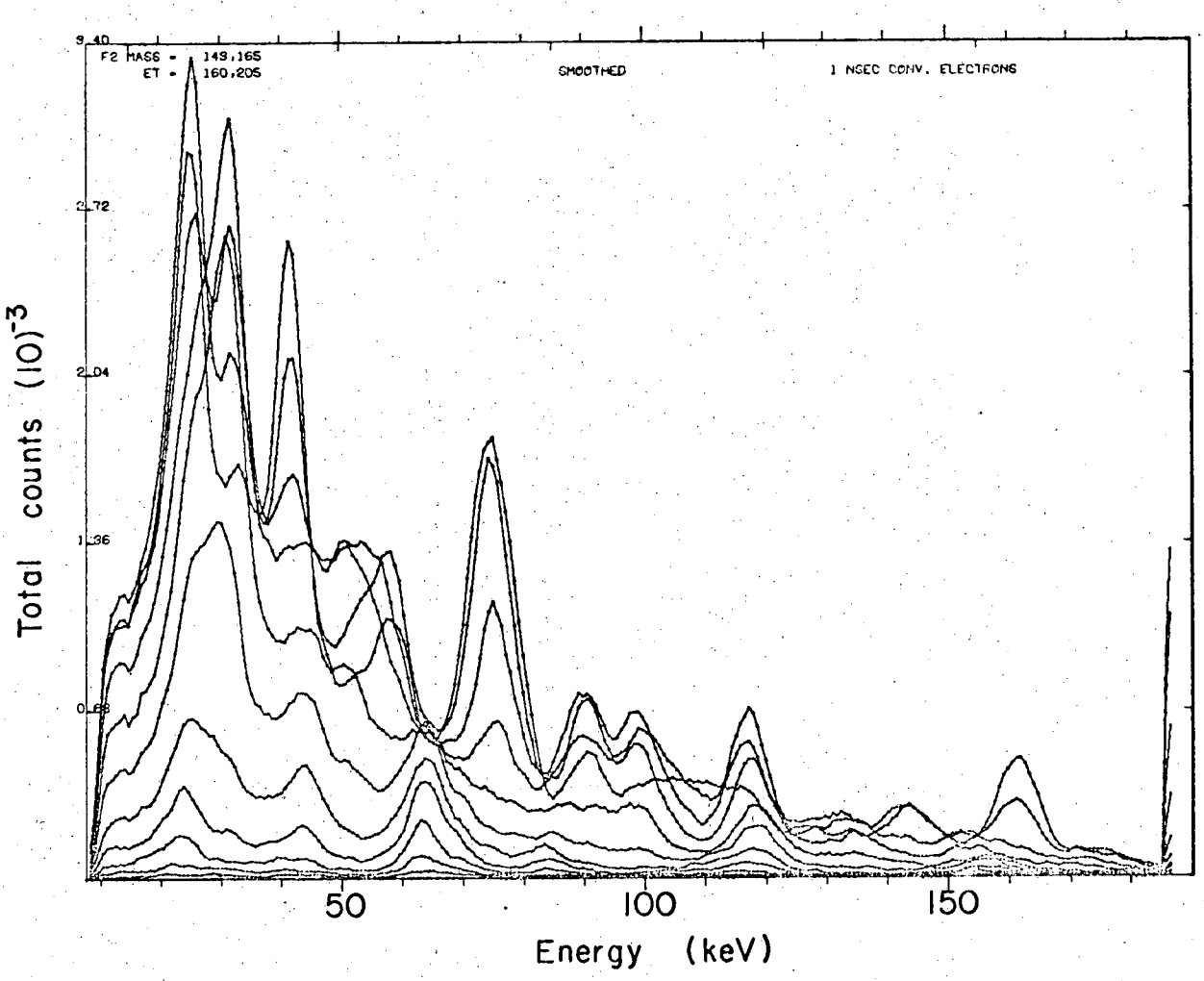
F2 MASS - 143,165
ET - 160,205
SMOOTHED
1 NSEC CONV. ELECTRONS
9.40
2.72
2.04
1.36
0.68
Total counts (10)^-3
50
100
150
Energy (keV)

Fig. VII-7

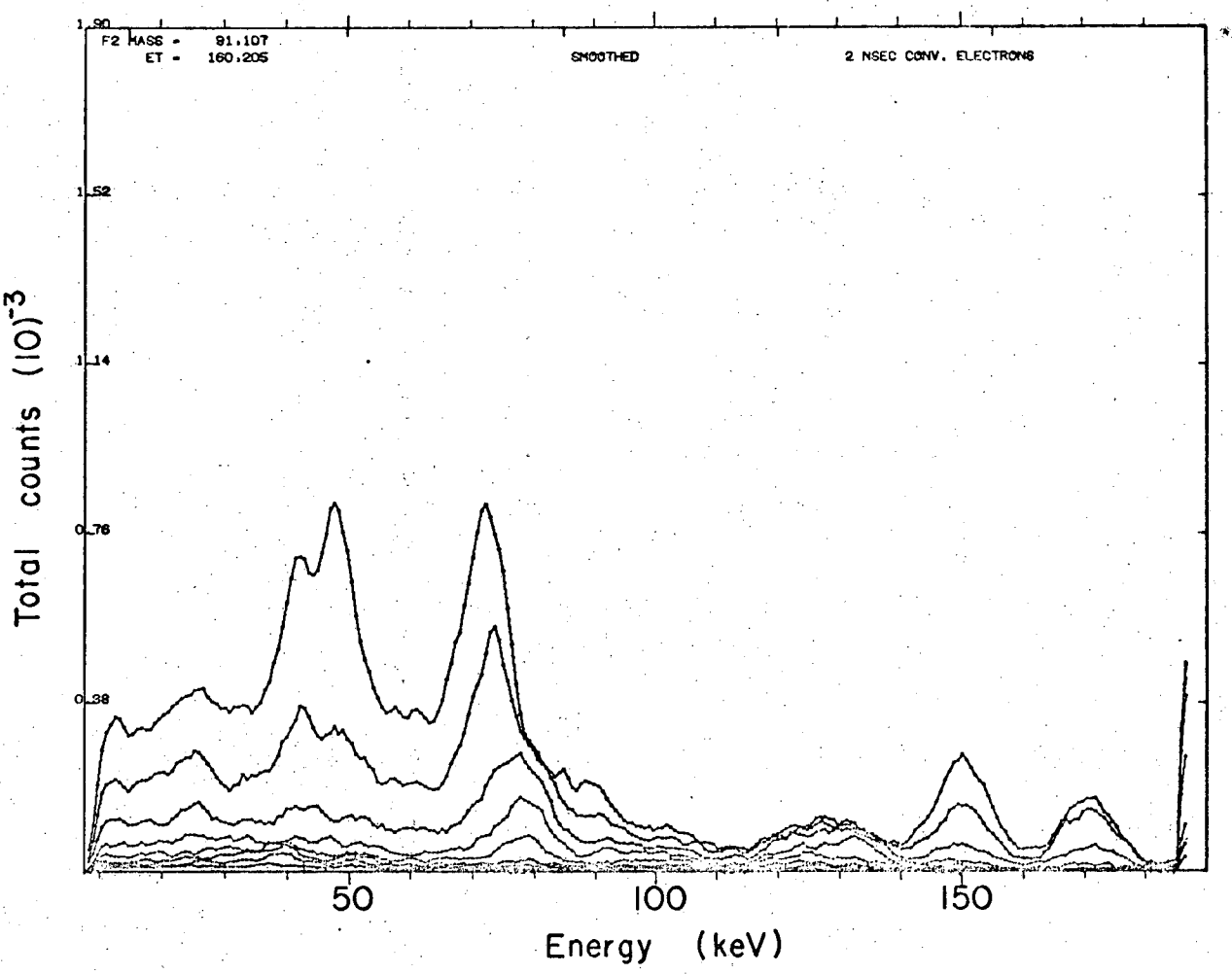
F2 MASS = 91.107
ET = 160.205
SMOOTHED
2 NSEC CONV. ELECTRONS
1.90
1.52
1.14
0.76
0.38
Total counts (10)-3
50
100
150
Energy (keV)

Fig. VII-8

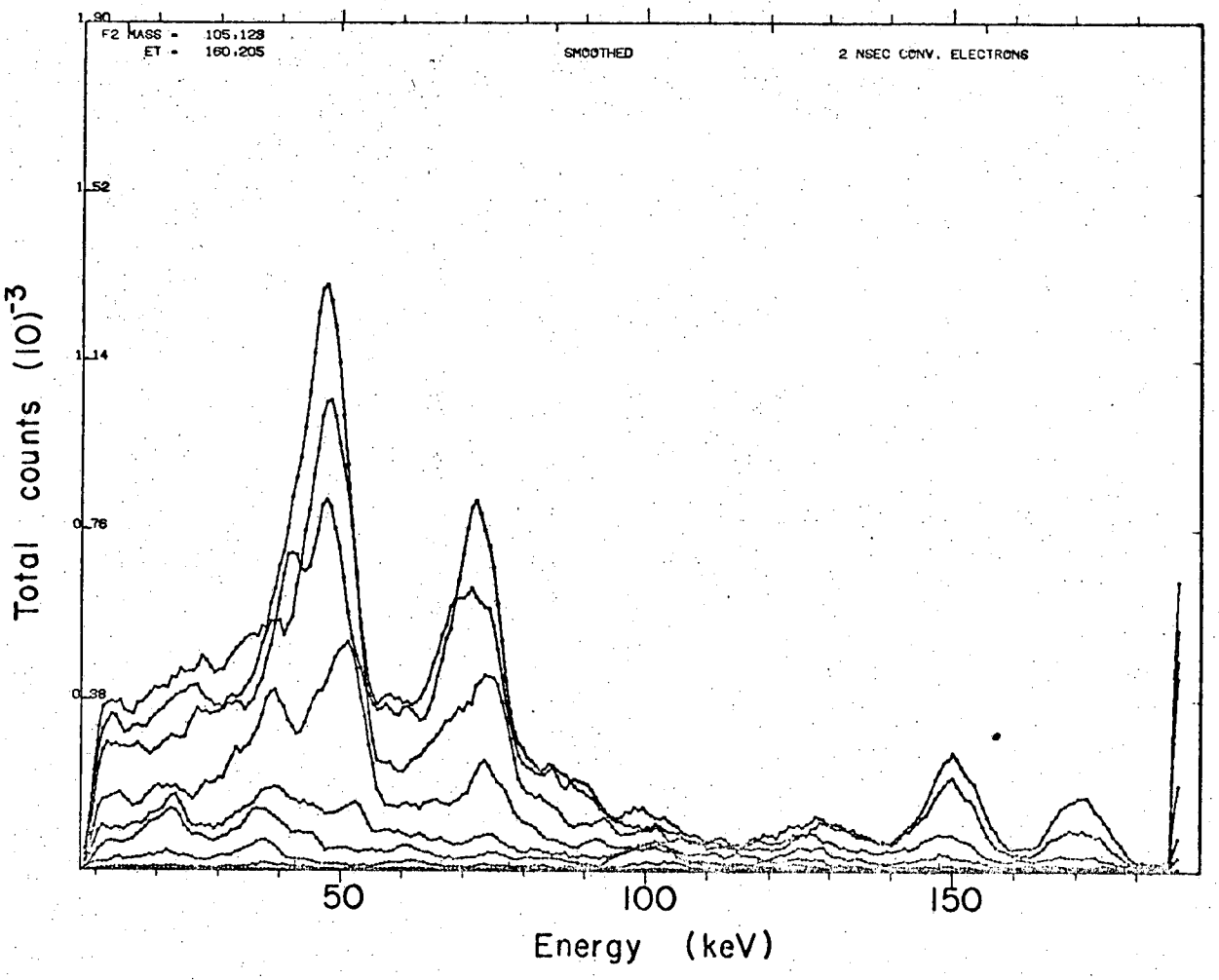
F2 MASS = 105,128
ET = 160,205
SMOOTHED
2 NSEC CONV. ELECTRONS
1.90
1.52
1.14
0.76
0.38
Total counts (10)-3
50
100
150
Energy (keV)

Fig. VII-9

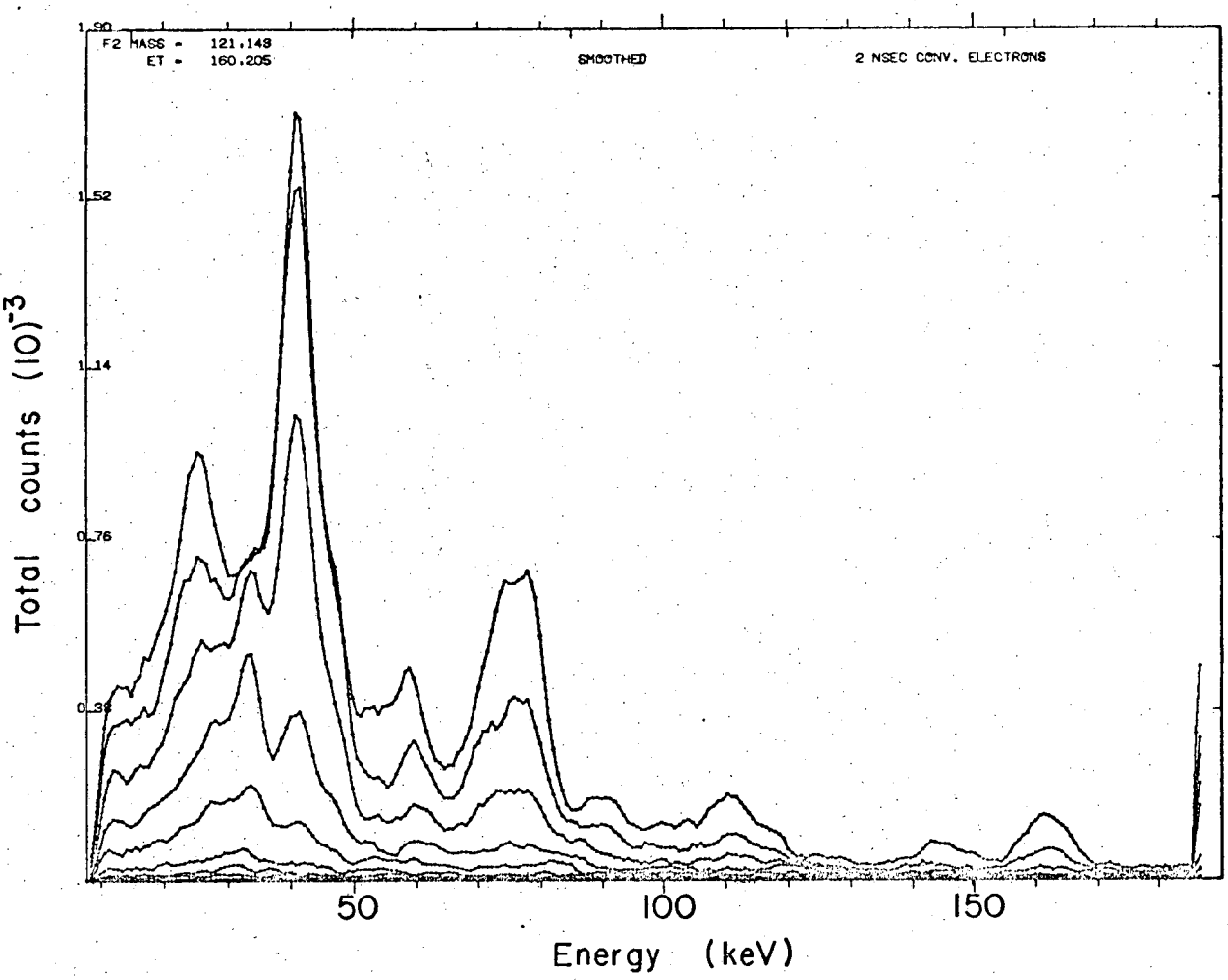
F2 MASS = 121.148
ET = 160.205
SMOOTHED
2 NSEC CONV. ELECTRONS
1.90
1.52
1.14
0.76
0.38
Total counts (10)^-3
50
100
150
Energy (keV)

Fig. VII-10

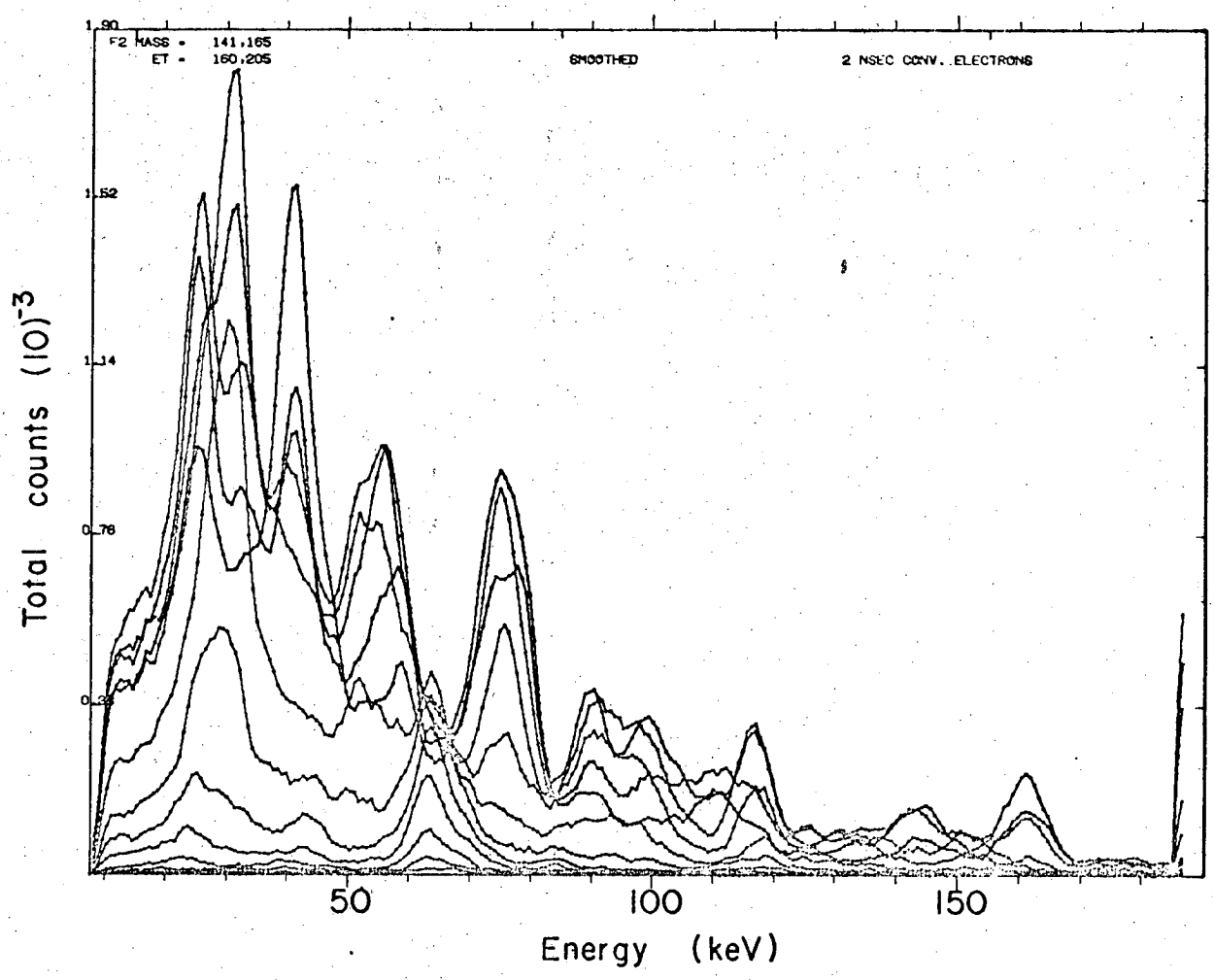
F2 MASS = 141,165
ET = 160,205
SMOOTHED
2 NSEC CONV. ELECTRONS
1.90
1.52
1.14
0.76
Total counts (10)-3
50
100
150
Energy (keV)

Fig. VII-11

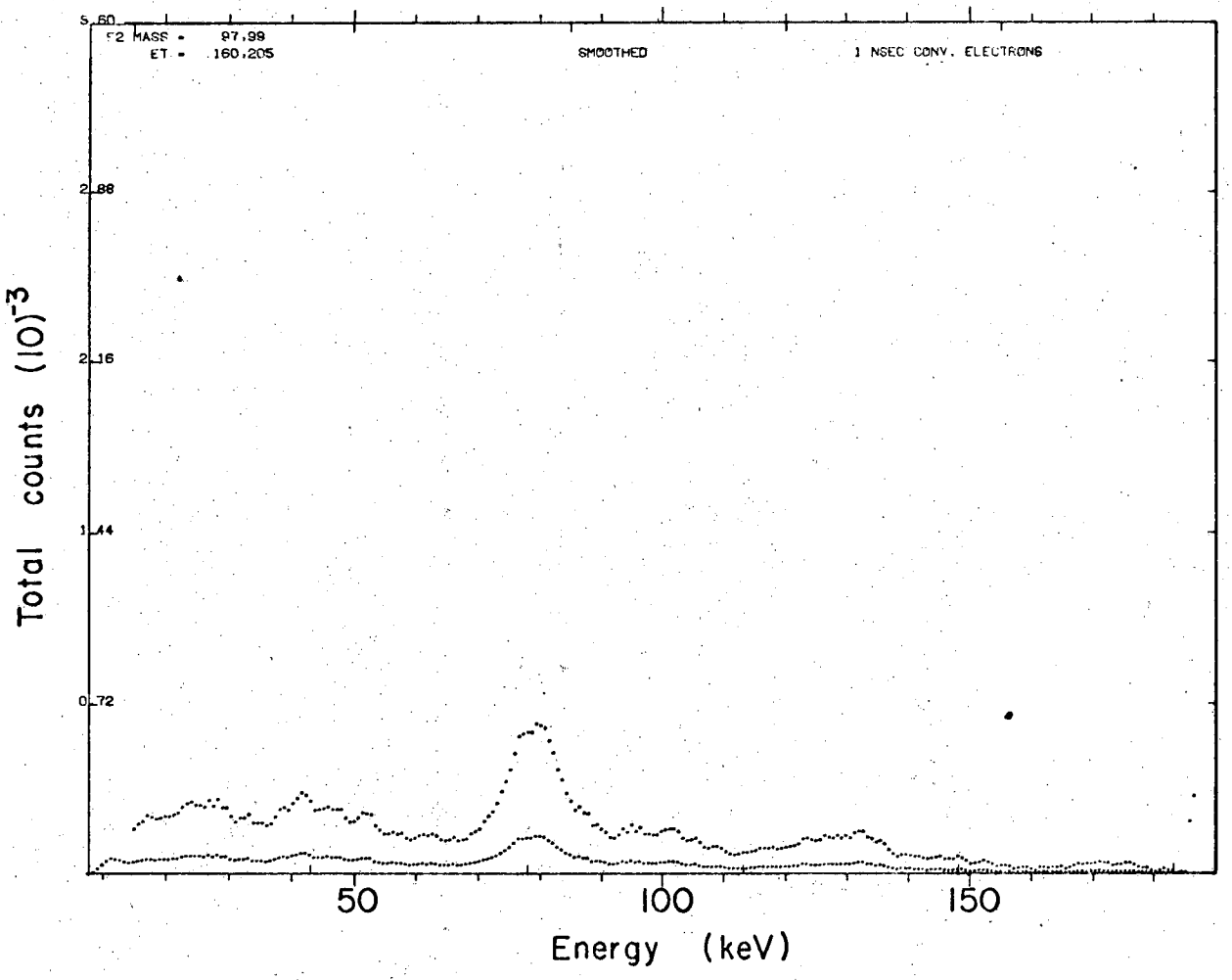
F2 MASS = 97.99
ET = 160.205
SMOOTHED
1 NSEC CONV. ELECTRONS
5.60
2.88
2.16
1.44
0.72
Total counts (10)^-3
50
100
150
Energy (keV)

Fig. VII-12

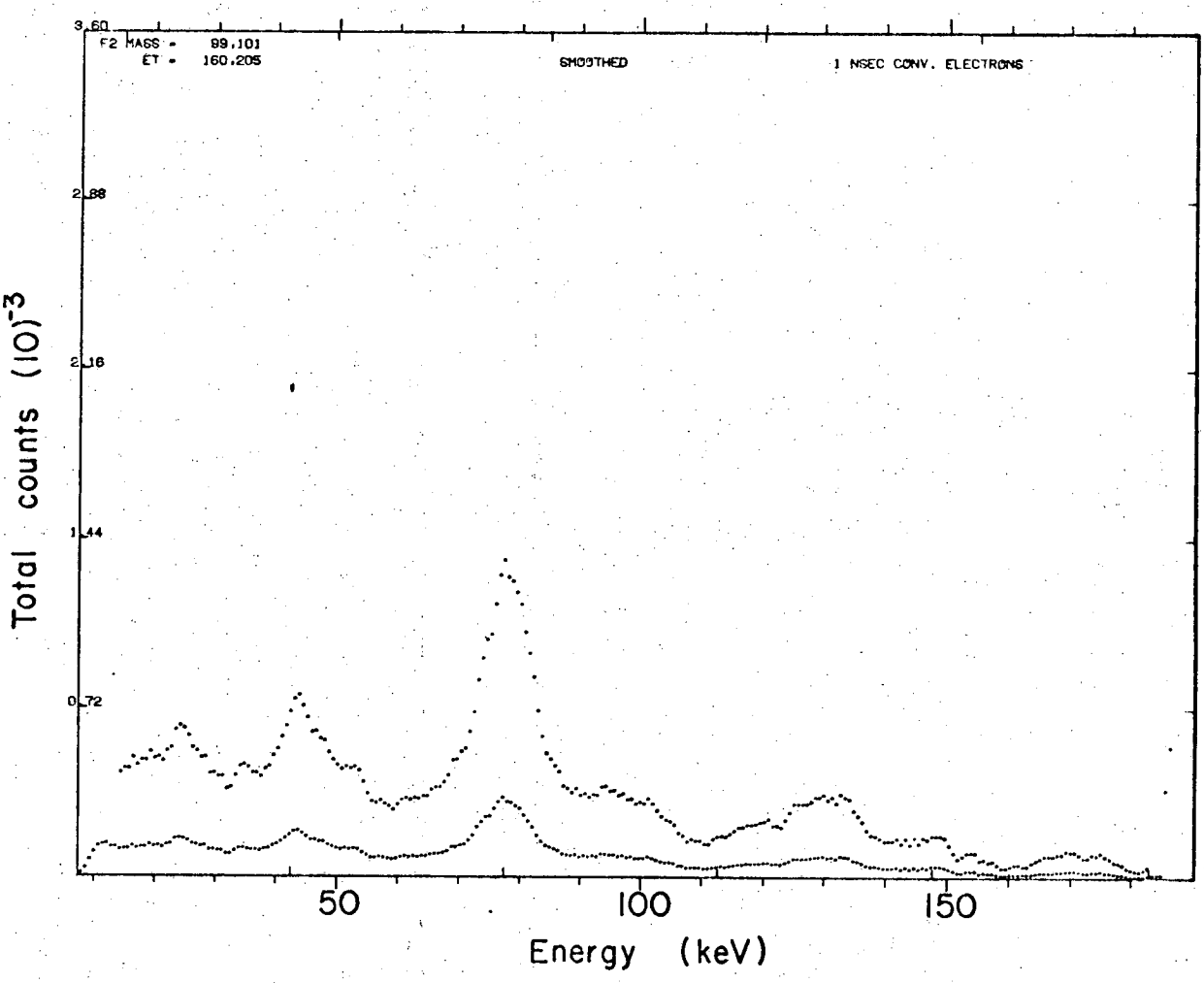
F2 MASS = 99.101
ET = 160.205
SMOOTHED
1 NSEC CONV. ELECTRONS
3.60
2.88
2.16
1.44
0.72
Total counts (10)-3
50
100
150
Energy (keV)

Fig. VII-13

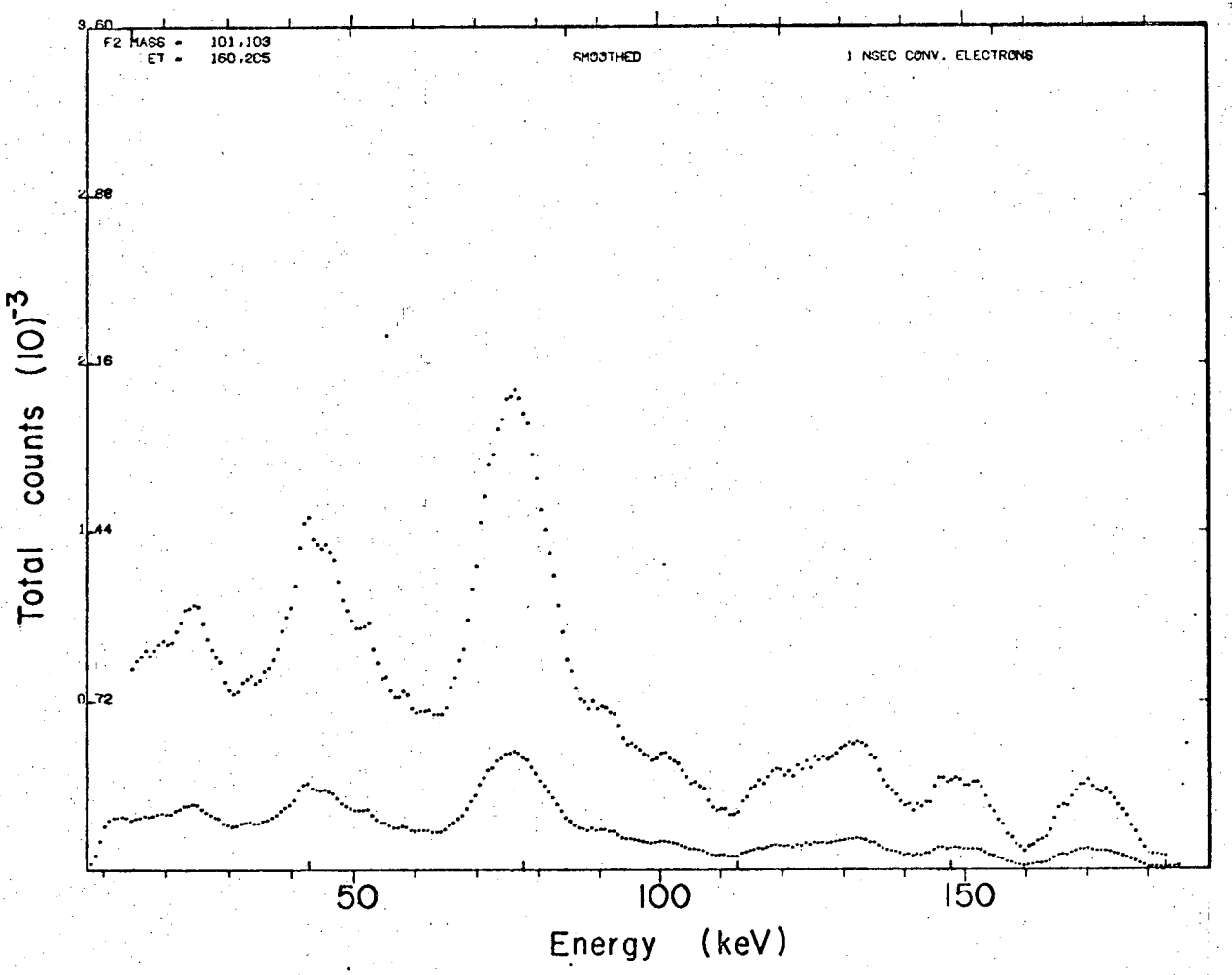
3.60
2.88
2.16
1.44
0.72
F2 MASS = 101,103
ET = 160,205
SMOOTHED
1 NSEC CONV. ELECTRONS
Total counts (10)^-3
50
100
150
Energy (keV)

Fig. VII-14

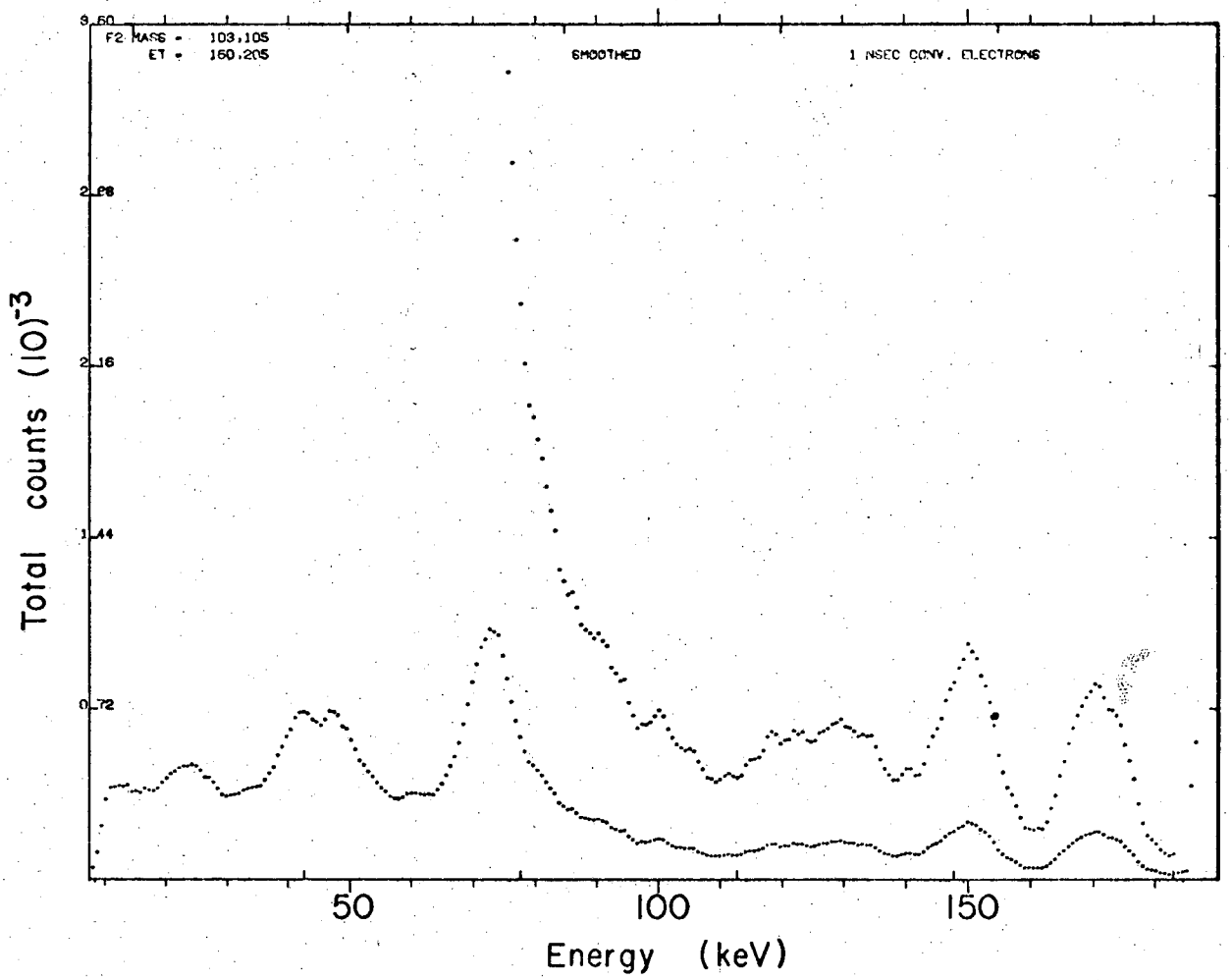
F2 MASS = 103.105
ET = 160.205
SMOOTHED
1 NSEC CONV. ELECTRONS
3.60
2.88
2.16
1.44
0.72
Total counts (10)-3
50
100
150
Energy (keV)

Fig. VII-15

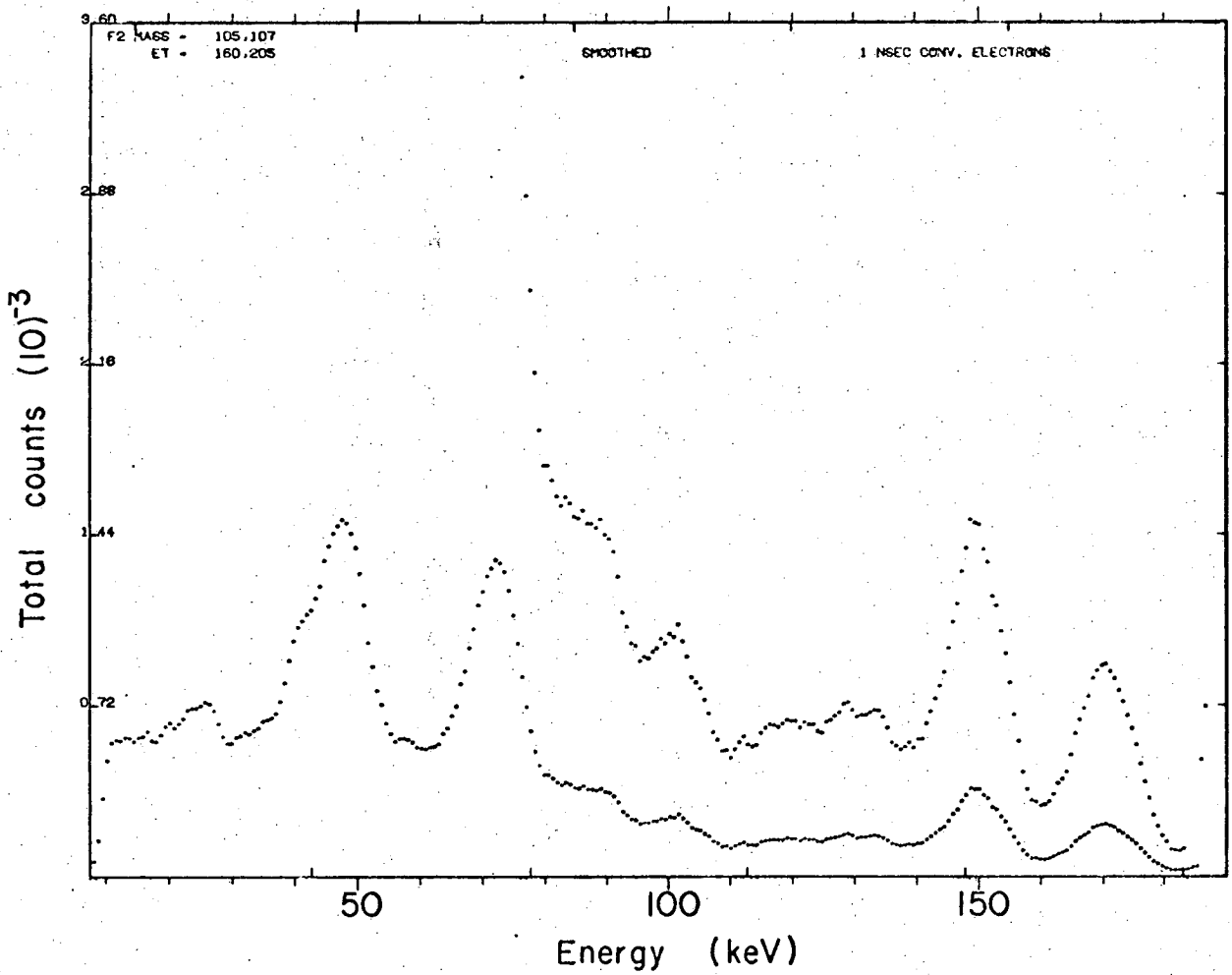
F2 MASS - 105.107
ET - 160.205
SMOOTHED
1 NSEC CONV. ELECTRONS
3.60
2.88
2.16
1.44
0.72
Total counts (10)$^{-3}$
50
100
150
Energy (keV)

Fig. VII-16

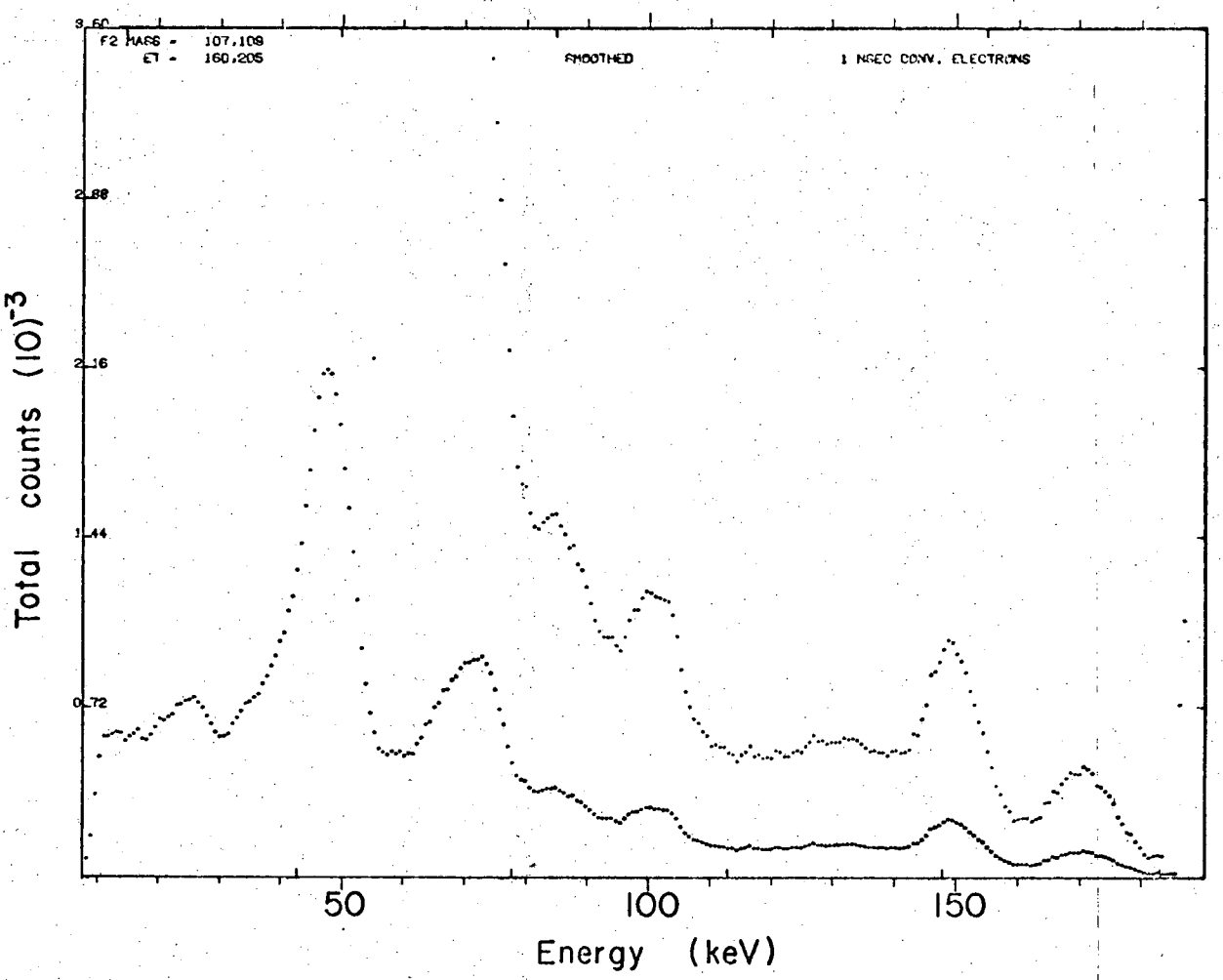
F2 MASS - 107,109
ET - 160,205
SMOOTHED
1 NSEC CONV. ELECTRONS
3.60
2.88
2.16
1.44
0.72
Total counts (10)^-3
50
100
150
Energy (keV)

Fig. VII-17

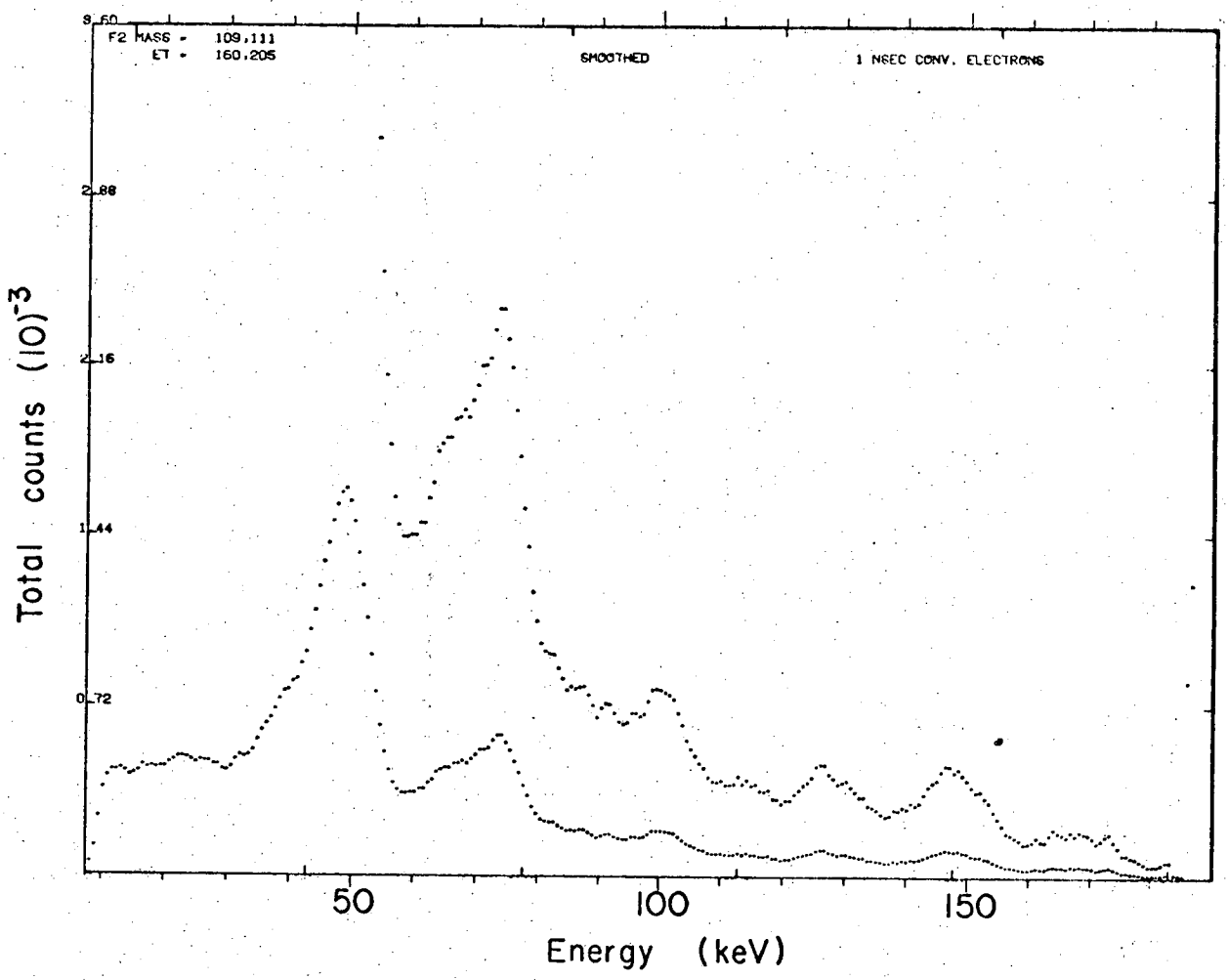
F2 MASS - 109.111
ET - 160.205
SMOOTHED
1 NSEC CONV. ELECTRONS
3.60
2.88
2.16
1.44
0.72
Total counts (10)^3
50
100
150
Energy (keV)

Fig. VII-18

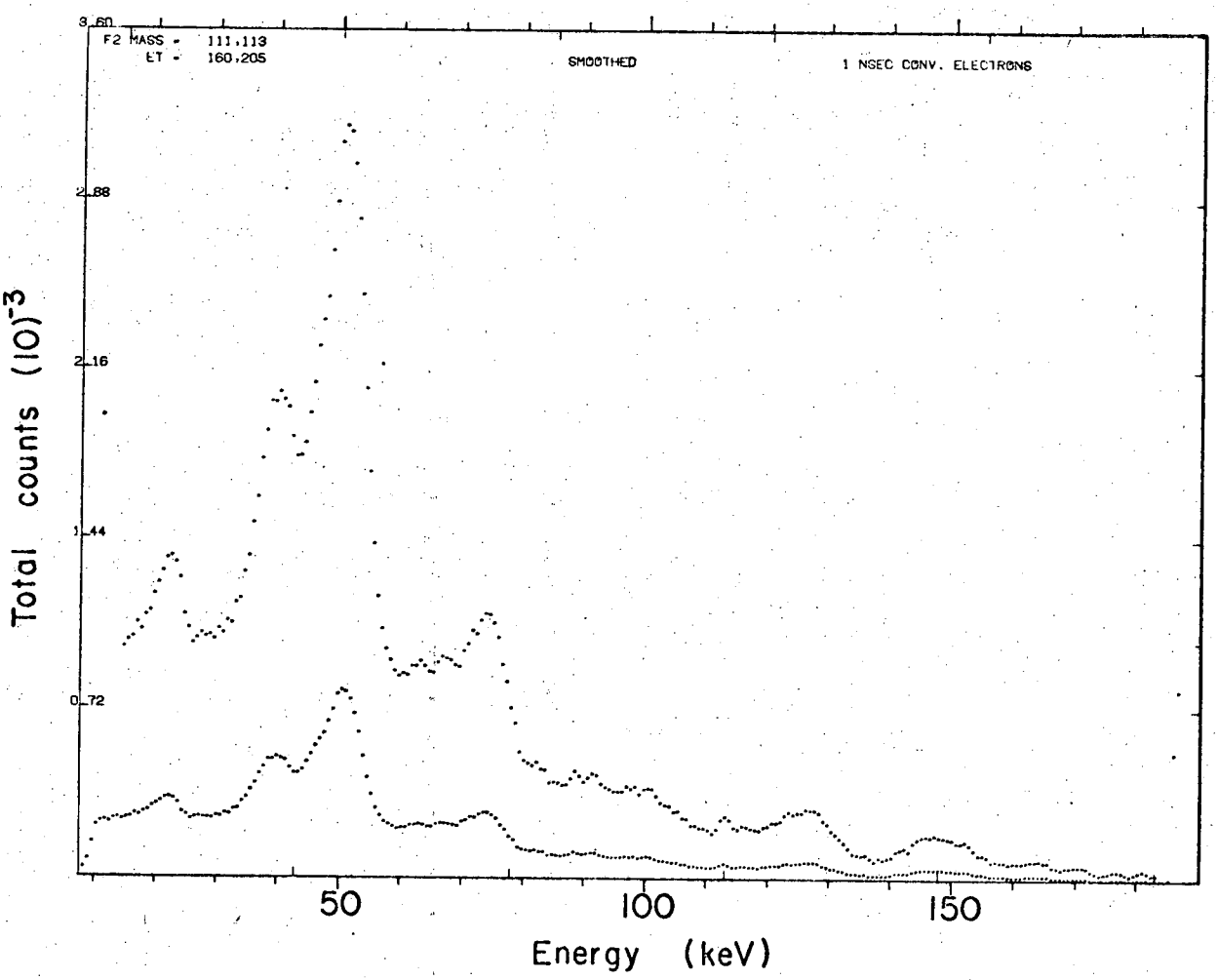
F2 MASS - 111.113
ET - 160.205
SMOOTHED
1 NSEC CONV. ELECTRONS
3.60
2.88
2.16
1.44
0.72
Total counts (10)^-3
50
100
150
Energy (keV)

Fig. VII-19

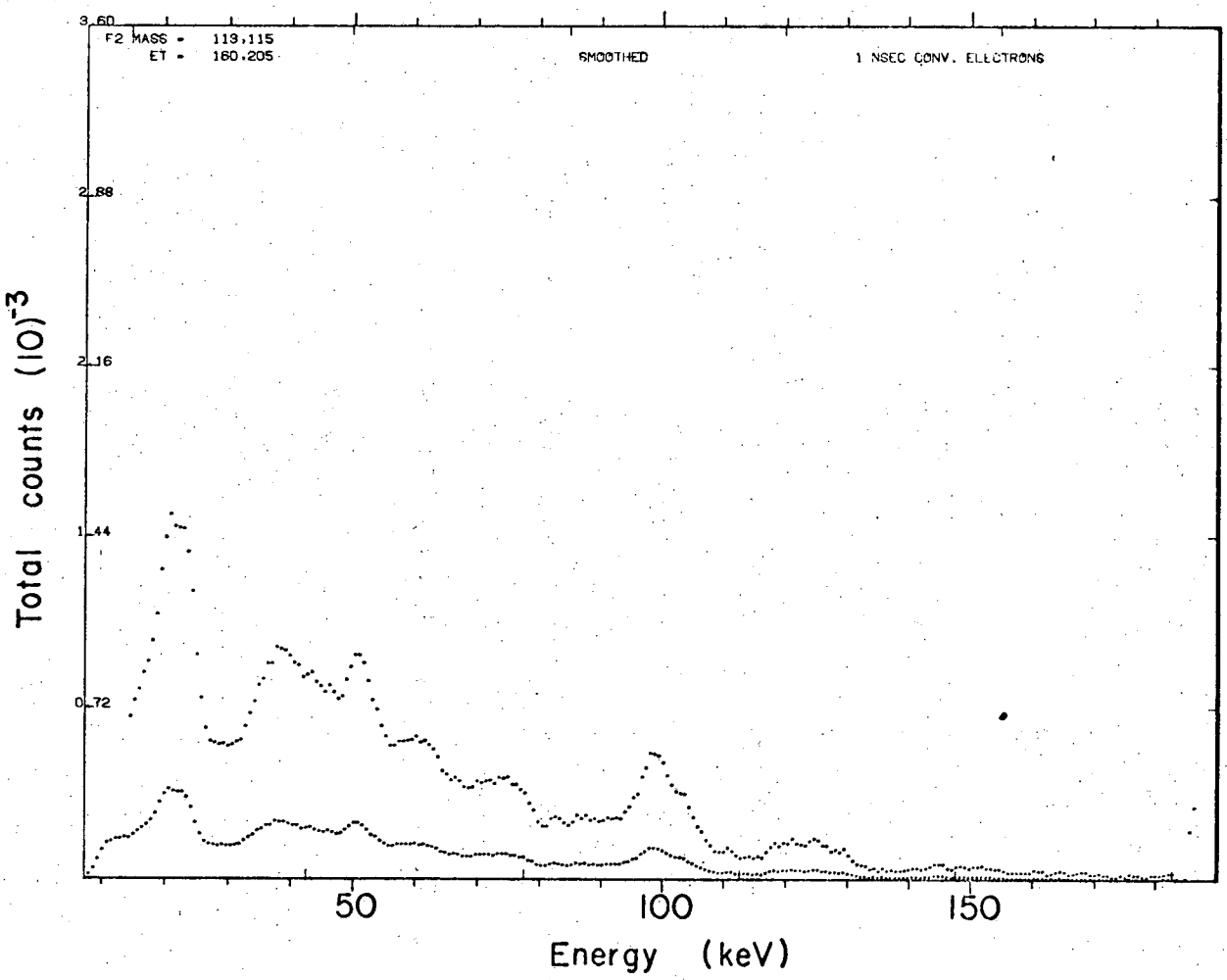
3.60
2.88
2.16
1.44
0.72
F2 MASS = 113,115
ET = 160.205
SMOOTHED
1 NSEC CONV. ELECTRONS
Total counts (10)^-3
50
100
150
Energy (keV)

Fig. VII-20

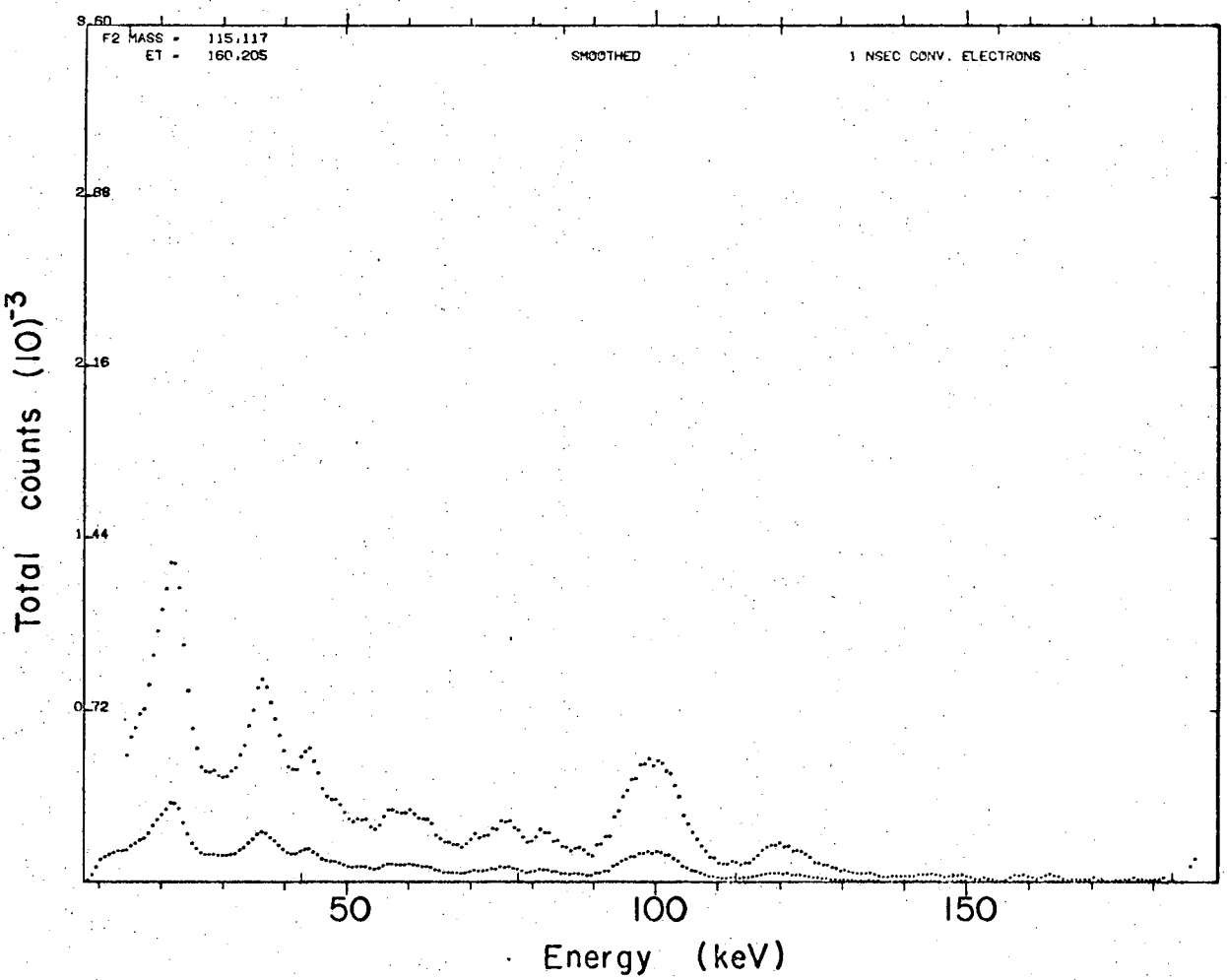
F2 MASS = 115,117
ET = 160,205
SMOOTHED
1 NSEC CONV. ELECTRONS
3.60
2.88
2.16
1.44
0.72
Total counts (10)-3
50
100
150
Energy (keV)

Fig. VII-21

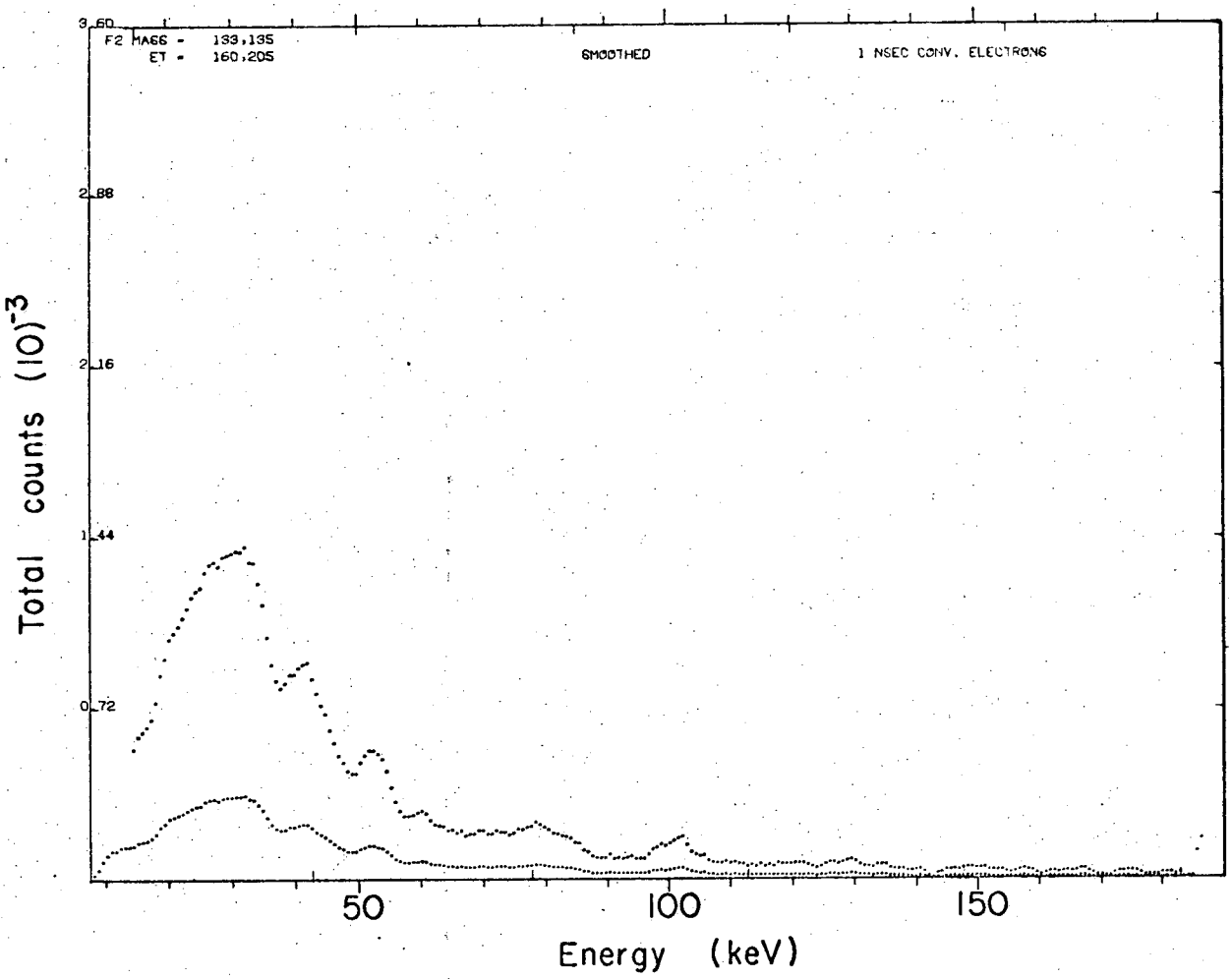
F2 MASS - 133,135
ET - 160,205
SMOOTHED
1 NSEC CONV. ELECTRONS
3.60
2.88
2.16
1.44
0.72
Total counts (10)^-3
50
100
150
Energy (keV)

Fig. VII-22

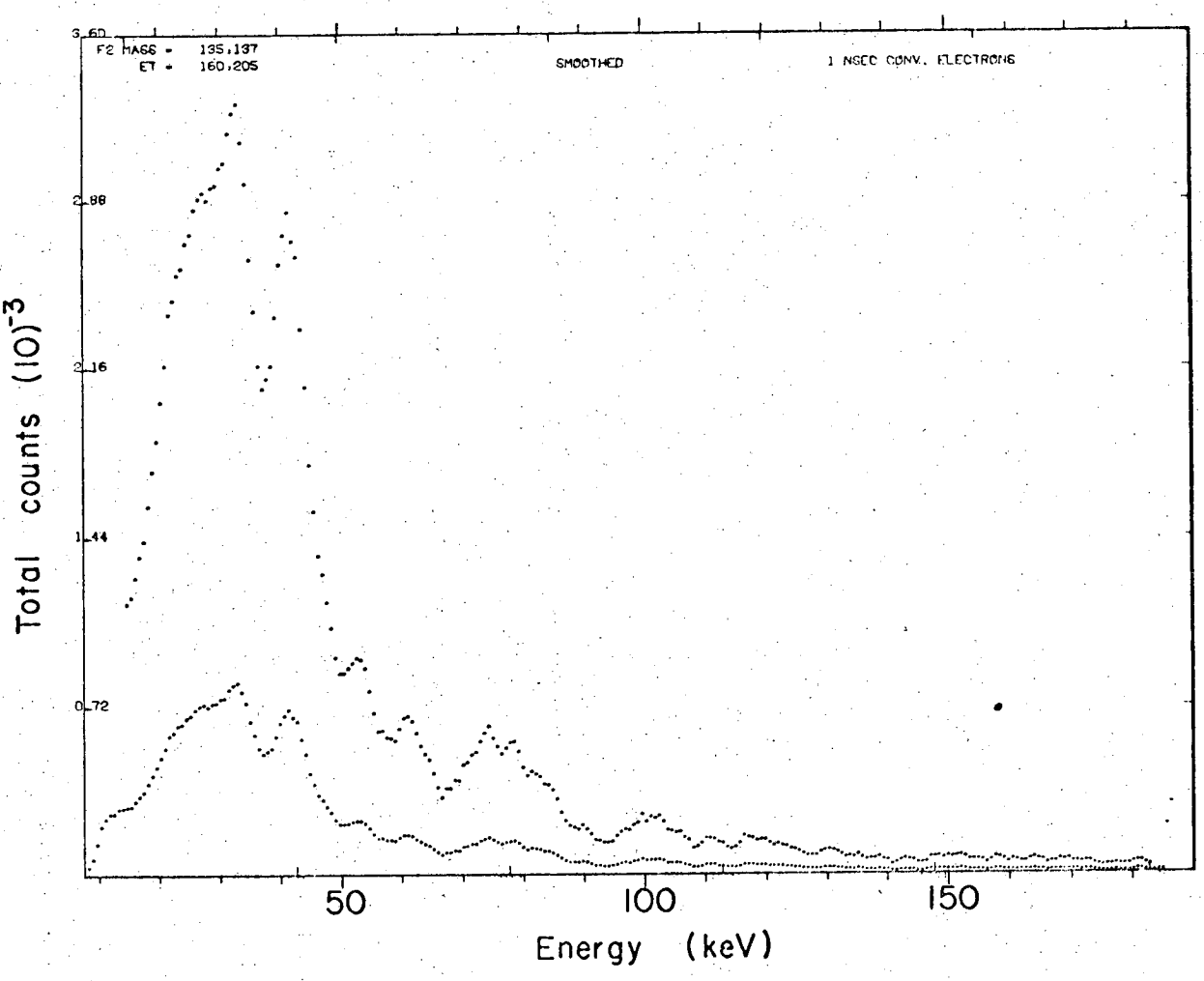
F2 MASS = 135,137
ET = 160,205
SMOOTHED
1 NSEC CONV. ELECTRONS
3.60
2.88
2.16
1.44
0.72
Total counts (10)^-3
50
100
150
Energy (keV)

Fig. VII-23

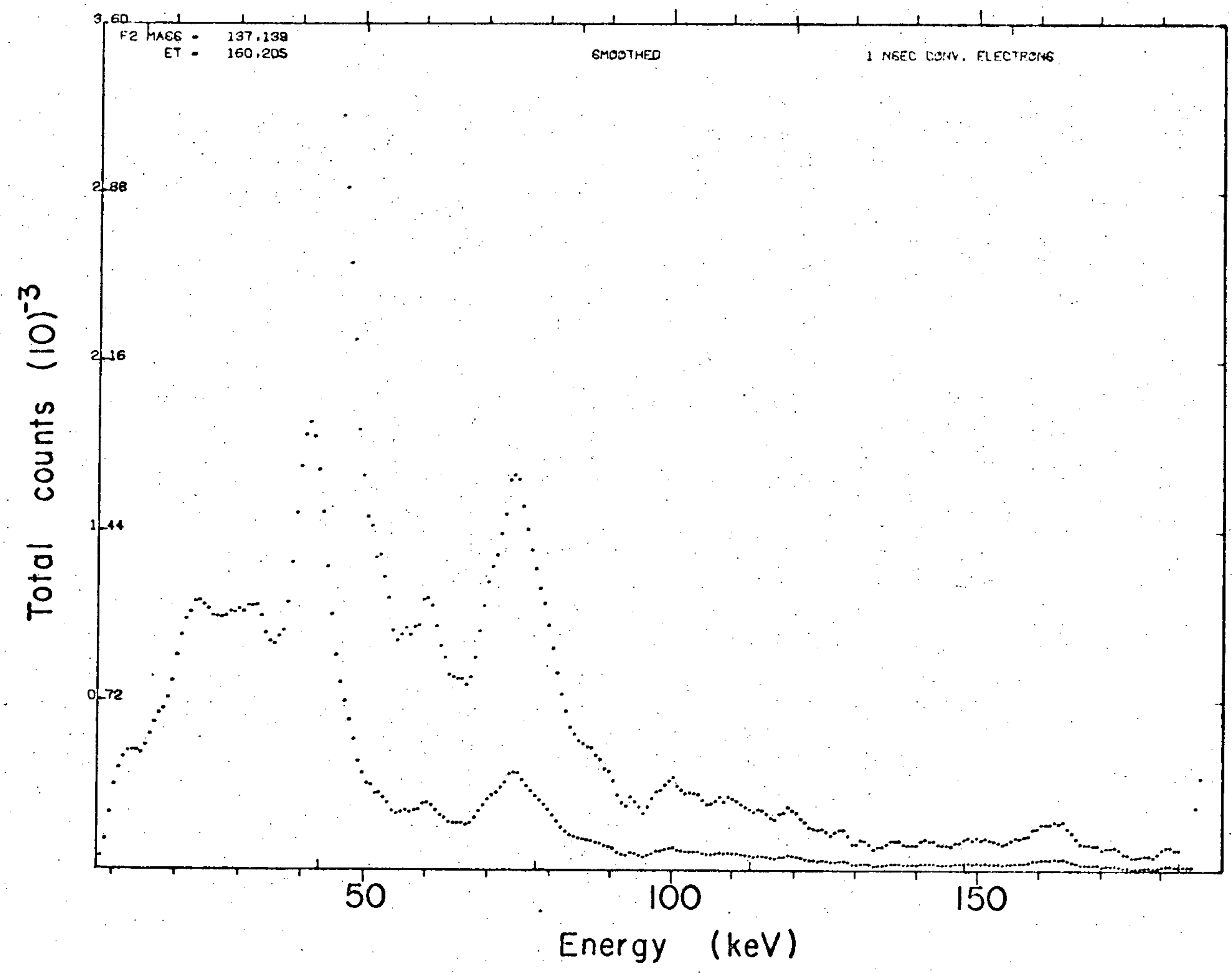
F2 MASS - 137,139
ET - 160,205
SMOOTHED
1 NSEC CONV. ELECTRONS
3.60
2.88
2.16
1.44
0.72
Total counts (10)^-3
50
100
150
Energy (keV)

Fig. VII-24

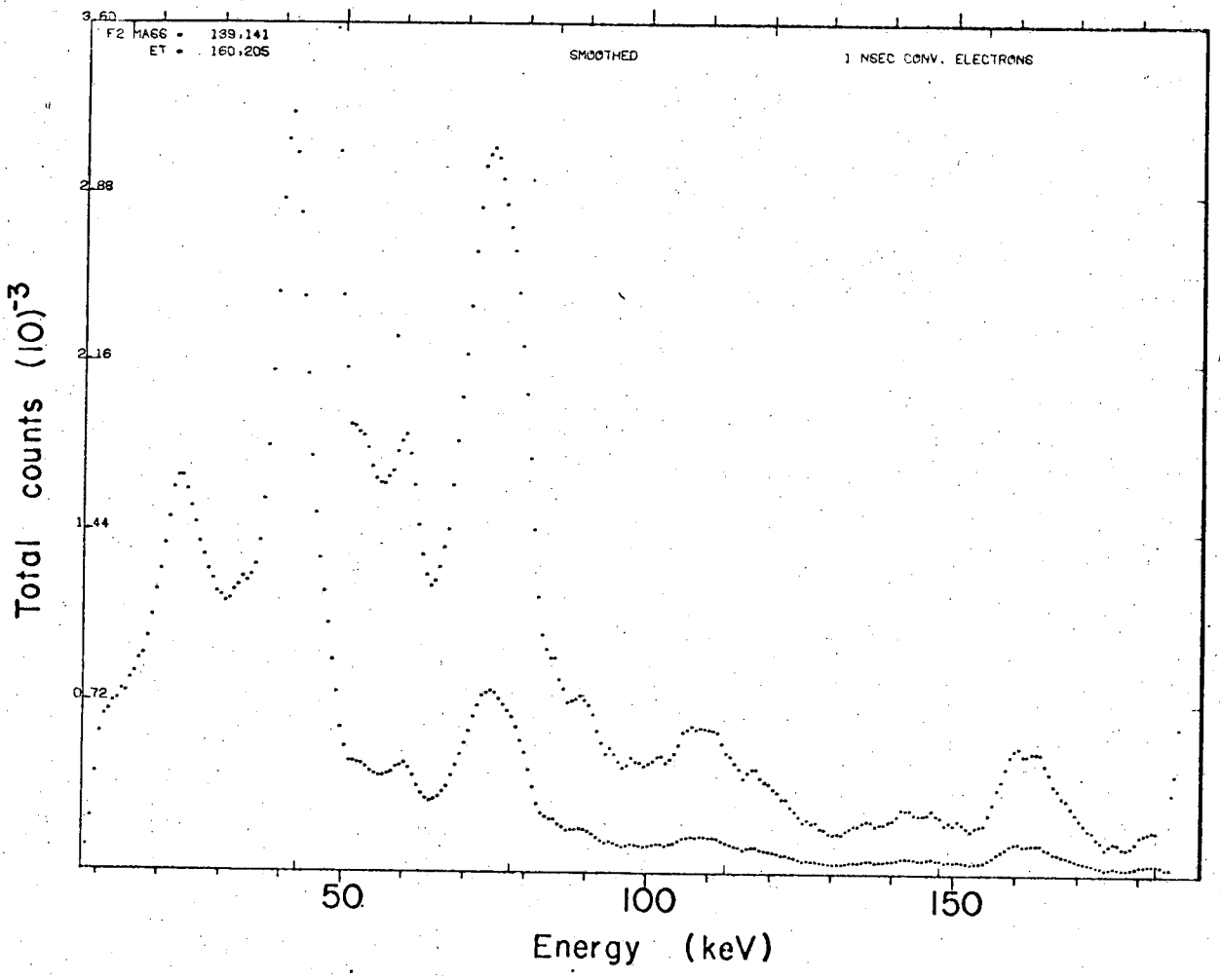
F2 MASS = 139.141
ET = 160.205
SMOOTHED
1 NSEC CONV. ELECTRONS
3.60
2.88
2.16
1.44
0.72
Total counts (10)-3
50
100
150
Energy (keV)

Fig. VII-25

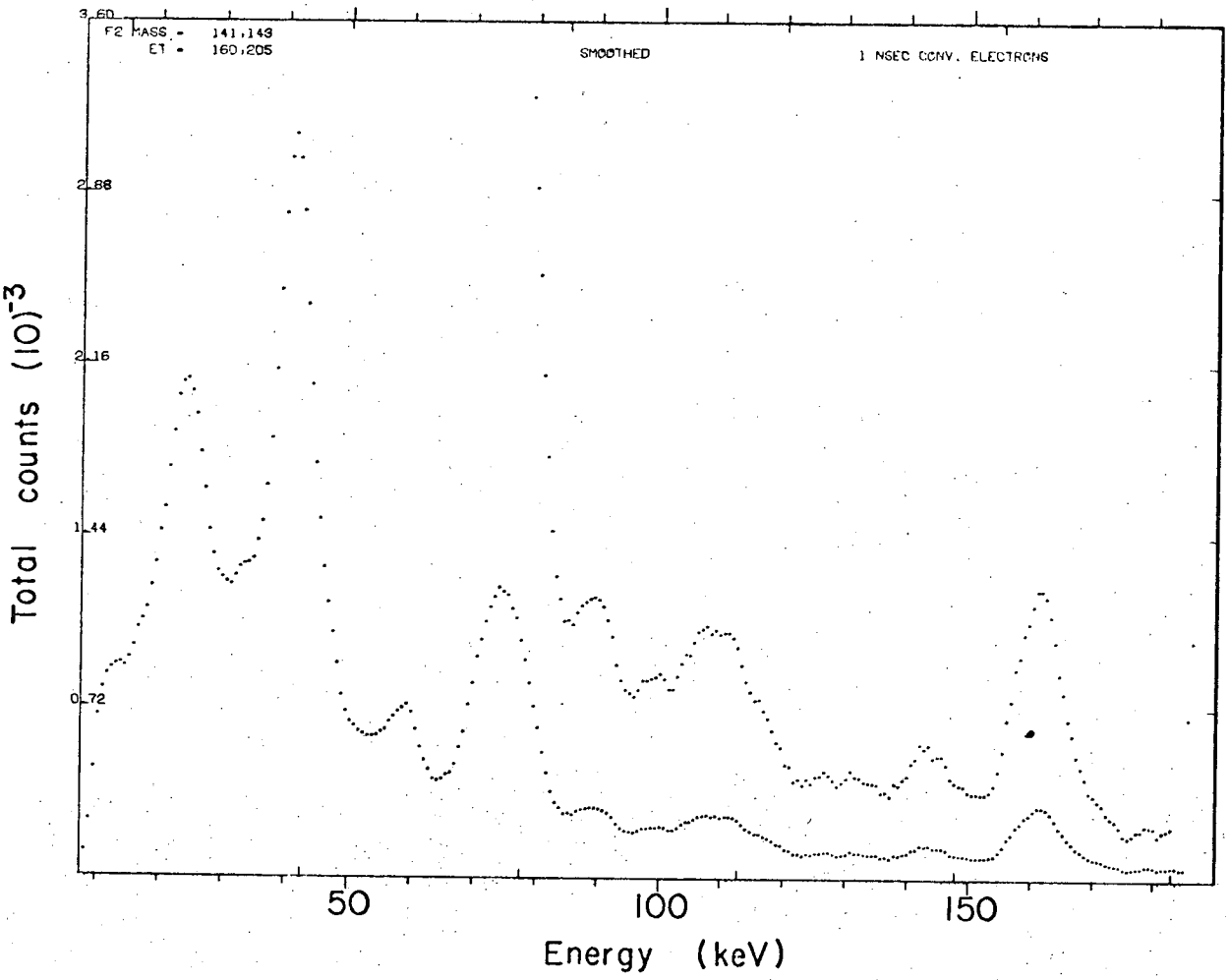
F2 MASS. - 141,143
ET - 160,205
SMOOTHED
1 NSEC CONV. ELECTRONS
3.60
2.88
2.16
1.44
0.72
Total counts (10)-3
50
100
150
Energy (keV)

Fig. VII-26

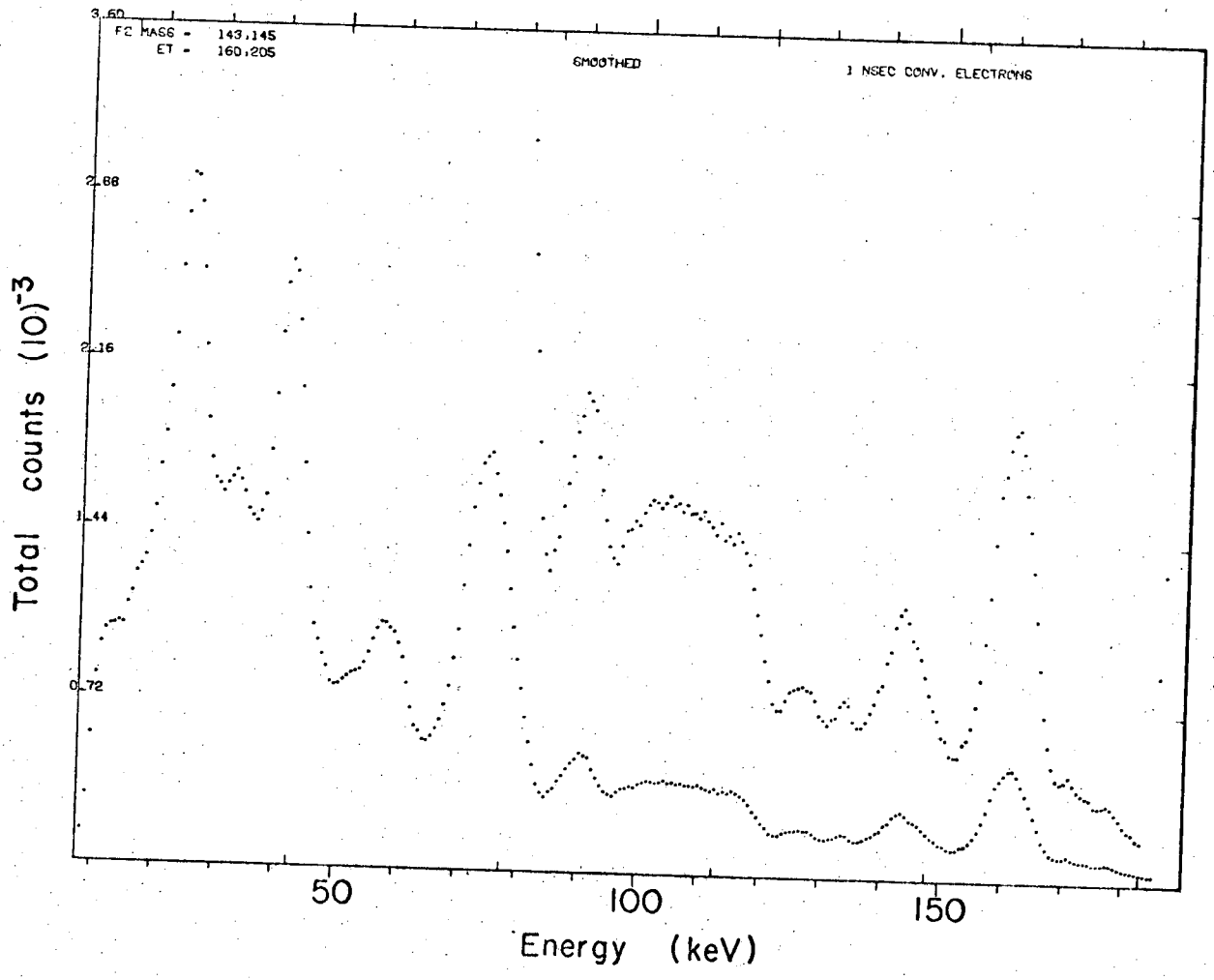
3.60
2.88
2.16
1.44
0.72
F2 MASS = 143.145
ET = 160.205
SMOOTHED
1 NSEC CONV. ELECTRONS
Total counts (10)-3
50
100
150
Energy (keV)

Fig. VII-27

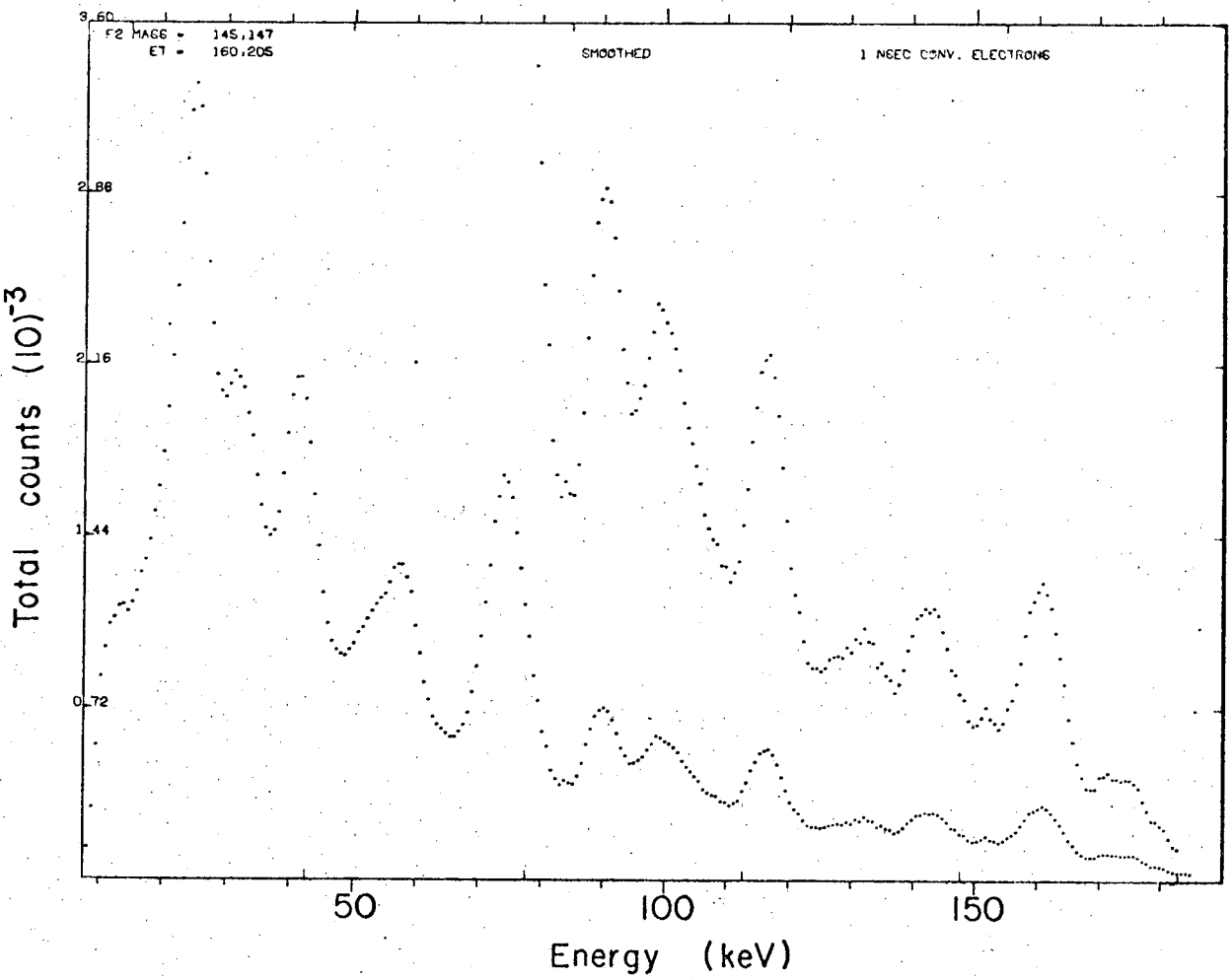
3.60
2.88
2.16
1.44
0.72
F2 MASS = 145,147
ET = 160,205
SMOOTHED
1 NSEC CONV. ELECTRONS
Total counts (10)-3
50
100
150
Energy (keV)

Fig. VII-28

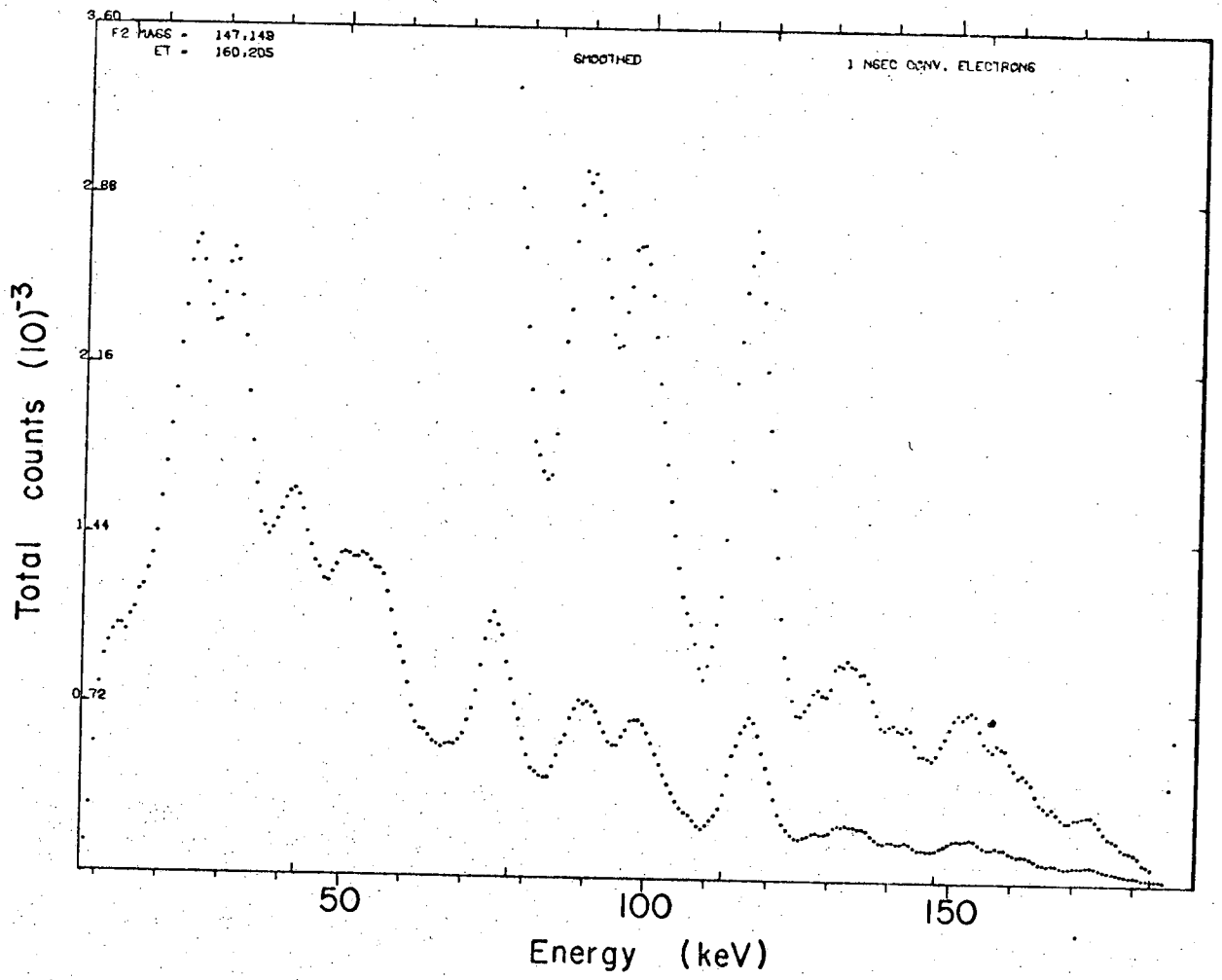
3.60
2.88
2.16
1.44
0.72
F2 MASS = 147.148
ET = 160.205
SMOOTHED
1 NSEC CONV. ELECTRONS
Total counts (10)-3
50
100
150
Energy (keV)

Fig. VII-29

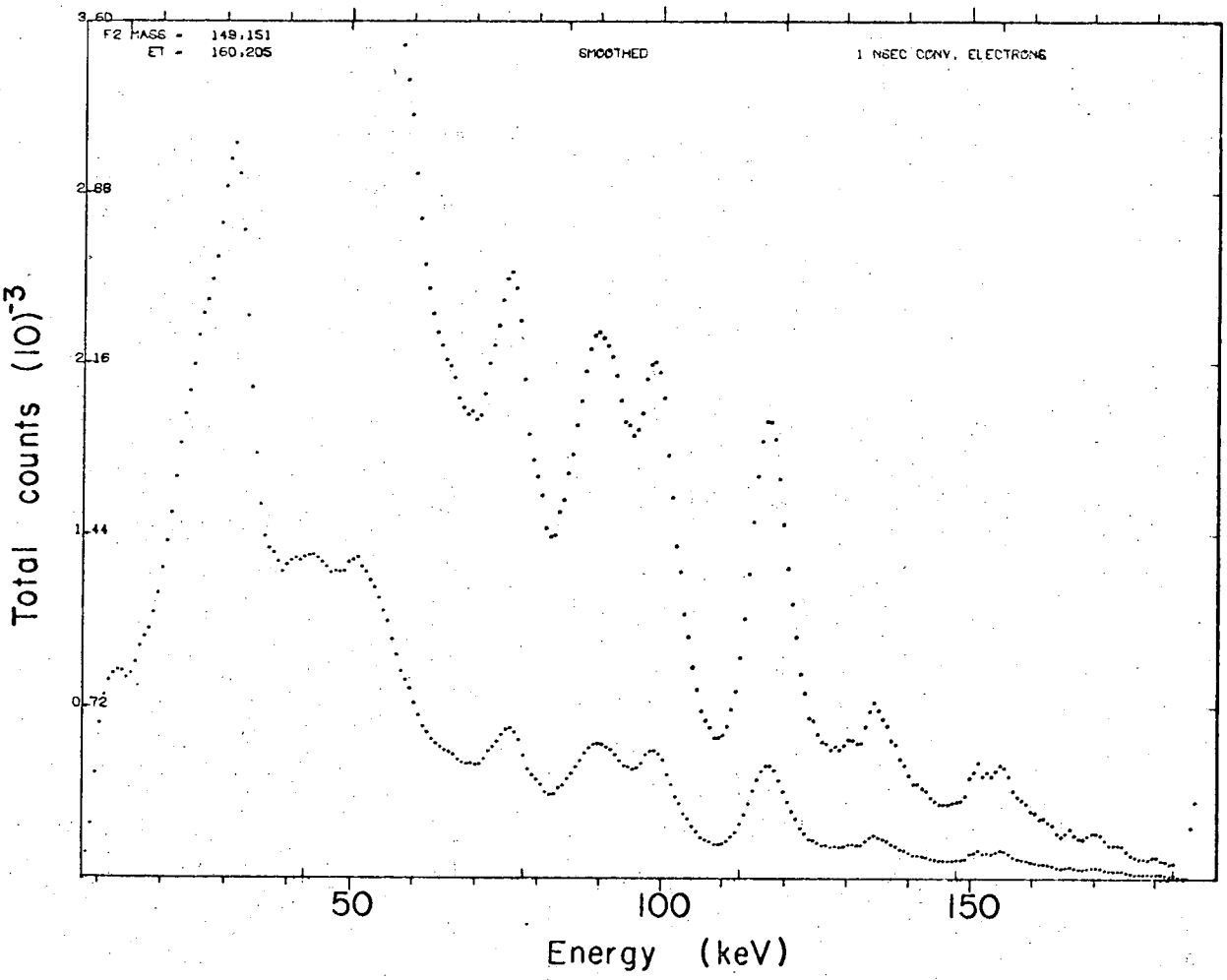
F2 MASS - 149,151
ET - 160,205
SMOOTHED
1 MSEC CONV. ELECTRONS
3.60
2.88
2.16
1.44
0.72
Total counts (10)-3
50
100
150
Energy (keV)

Fig. VII-30

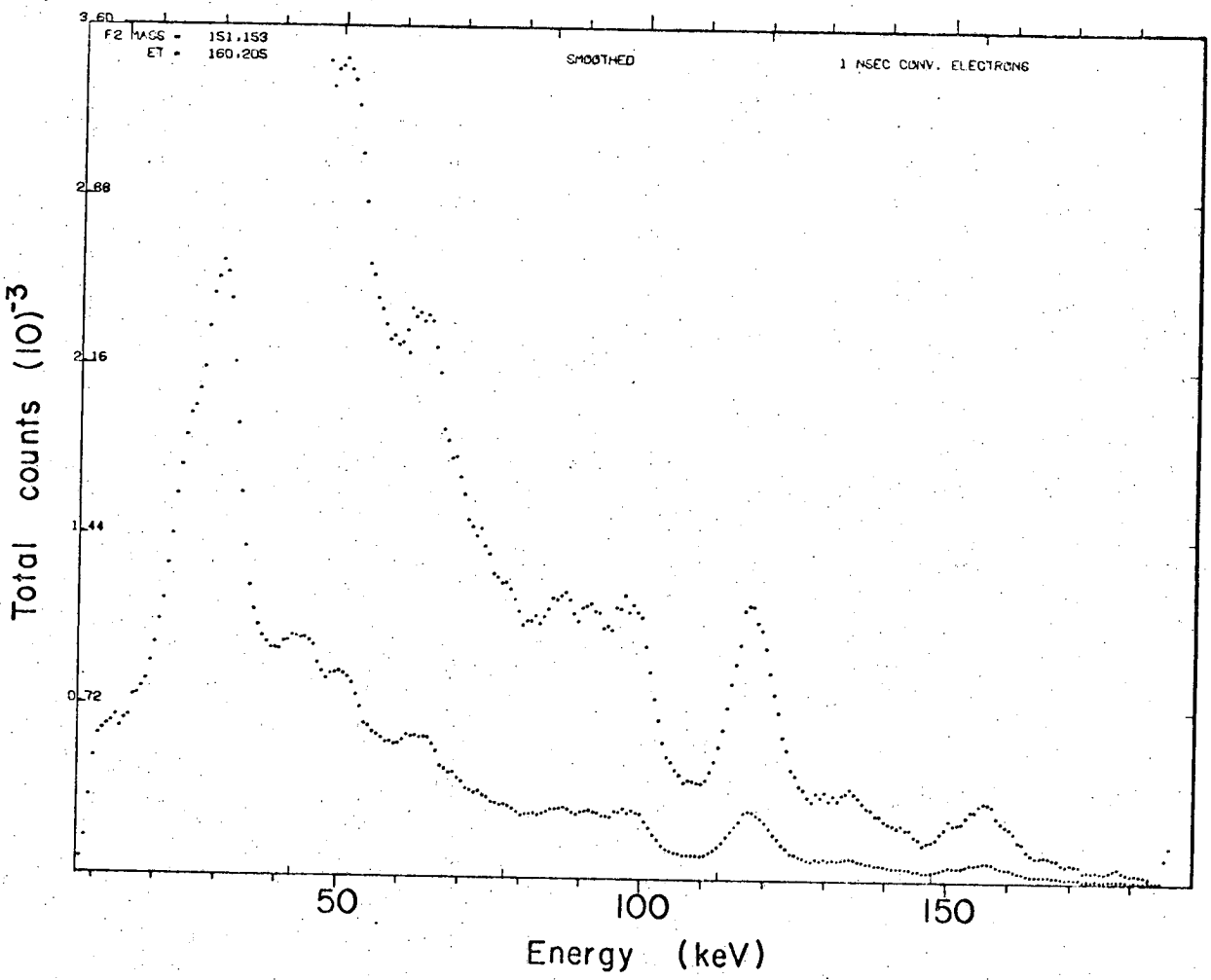
F2 MASS = 151.153
ET = 160.20S
SMOOTHED
1 NSEC CONV. ELECTRONS
3.60
2.88
2.16
1.44
0.72
Total counts (10)-3
50
100
150
Energy (keV)

Fig. VII-31

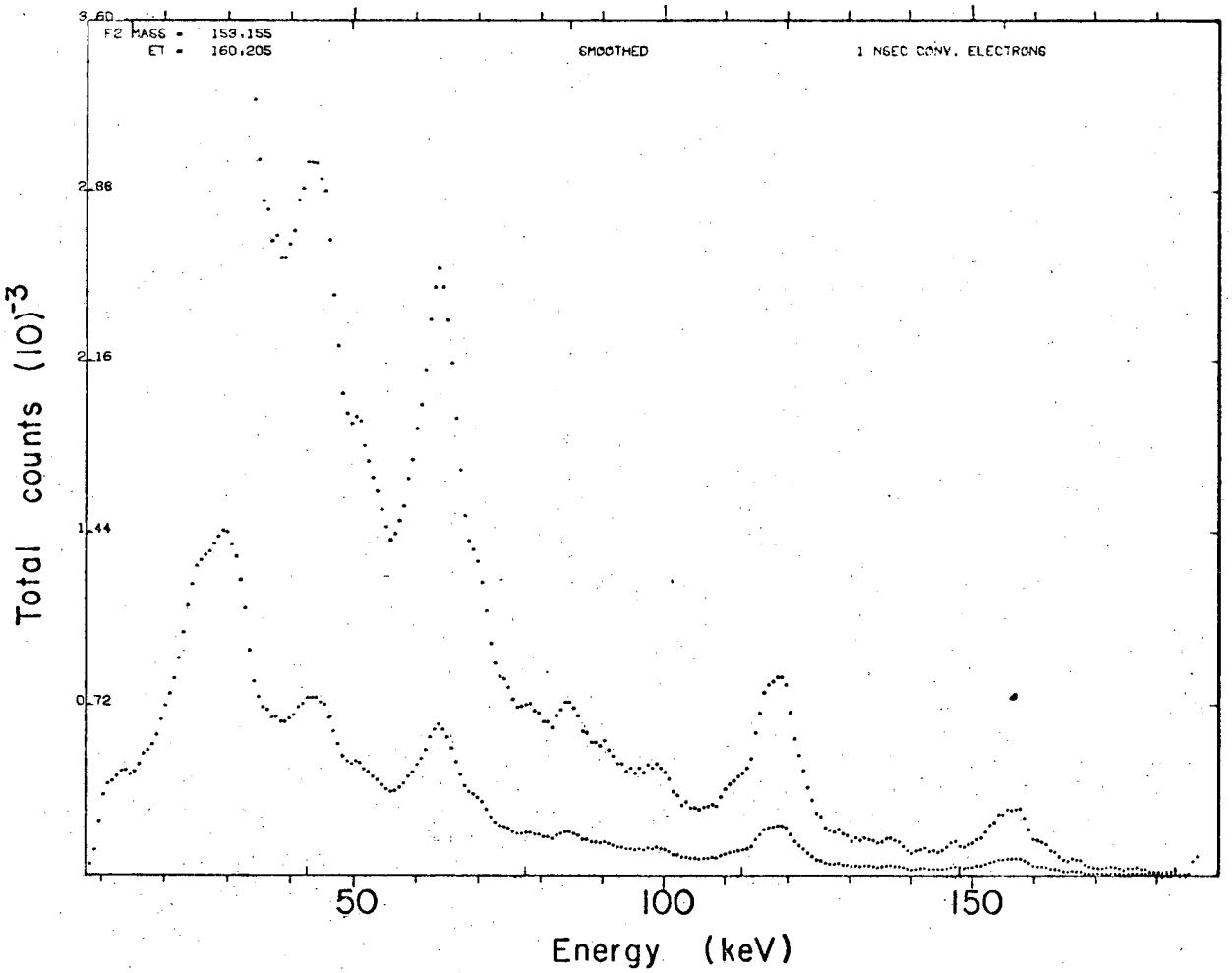
F2 MASS = 153.155
ET = 160.205
SMOOTHED
1 NSEC CONV. ELECTRONS
3.60
2.88
2.16
1.44
0.72
Total counts (10)^-3
50
100
150
Energy (keV)

Fig. VII-32

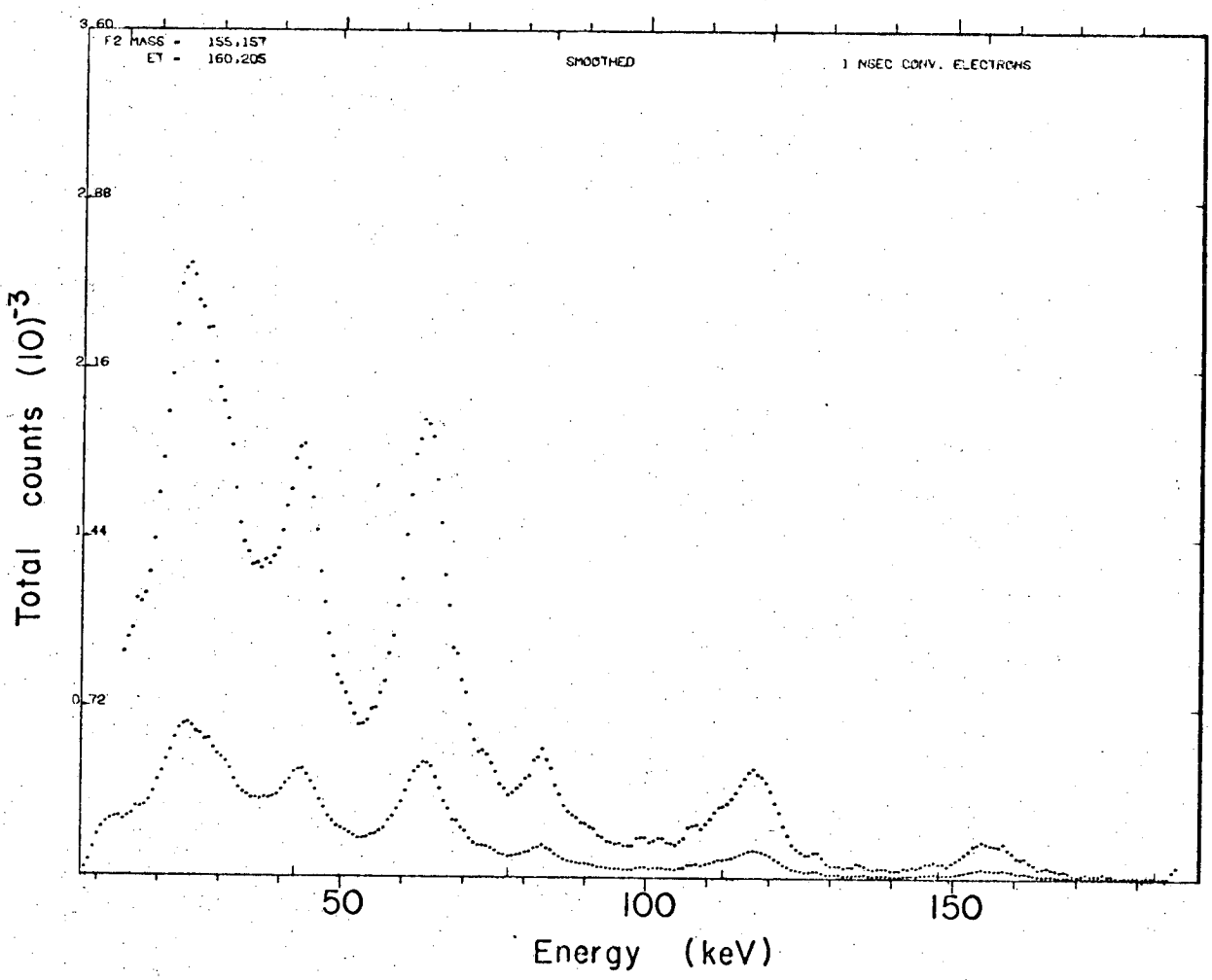
3.60
2.88
2.16
1.44
0.72
F2 MASS = 155,157
ET = 160,205
SMOOTHED
1 NSEC CONV. ELECTRONS
Total counts (10)^-3
50
100
150
Energy (keV)

Fig. VII-33

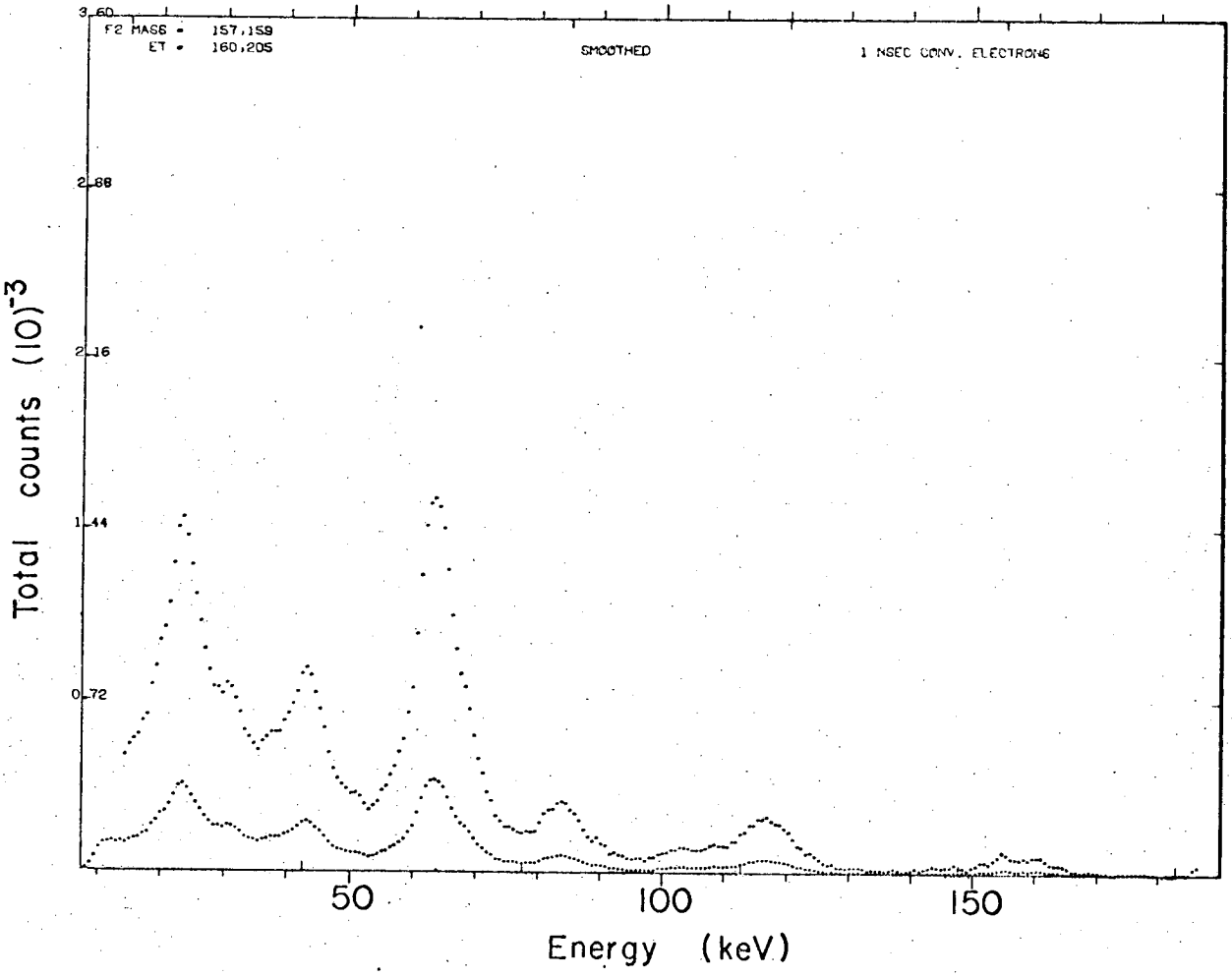
F2 MASS = 157,159
ET = 160,205
SMOOTHED
1 NSEC CONV. ELECTRONS
3.60
2.88
2.16
1.44
0.72
Total counts (10)-3
50
100
150
Energy (keV)

Fig. VII-34

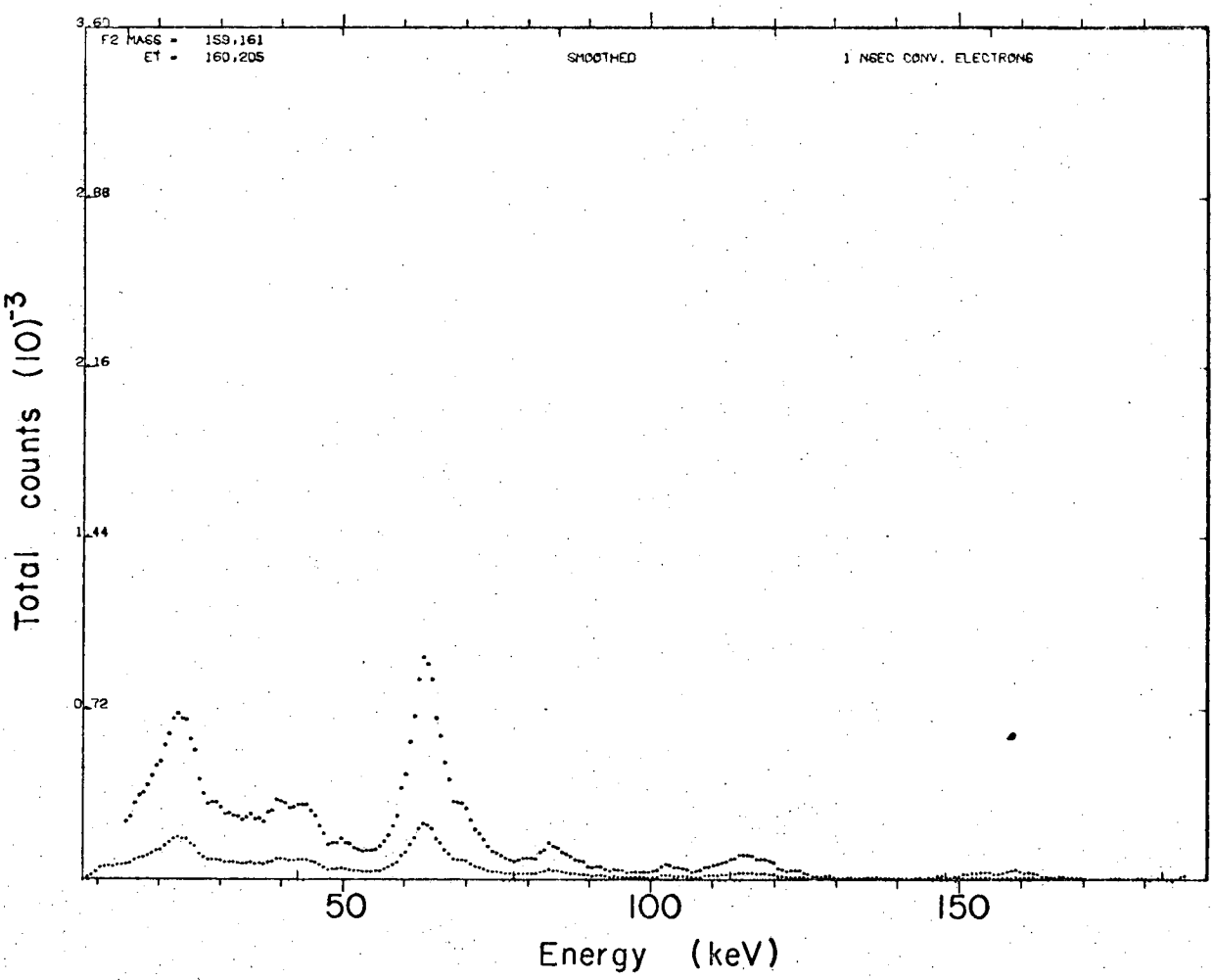
F2 MASS = 159,161
ET = 160,205
SMOOTHED
1 NSEC CONV. ELECTRONS
3.60
2.88
2.16
1.44
0.72
Total counts (10)-3
50
100
150
Energy (keV)

Fig. VII-35

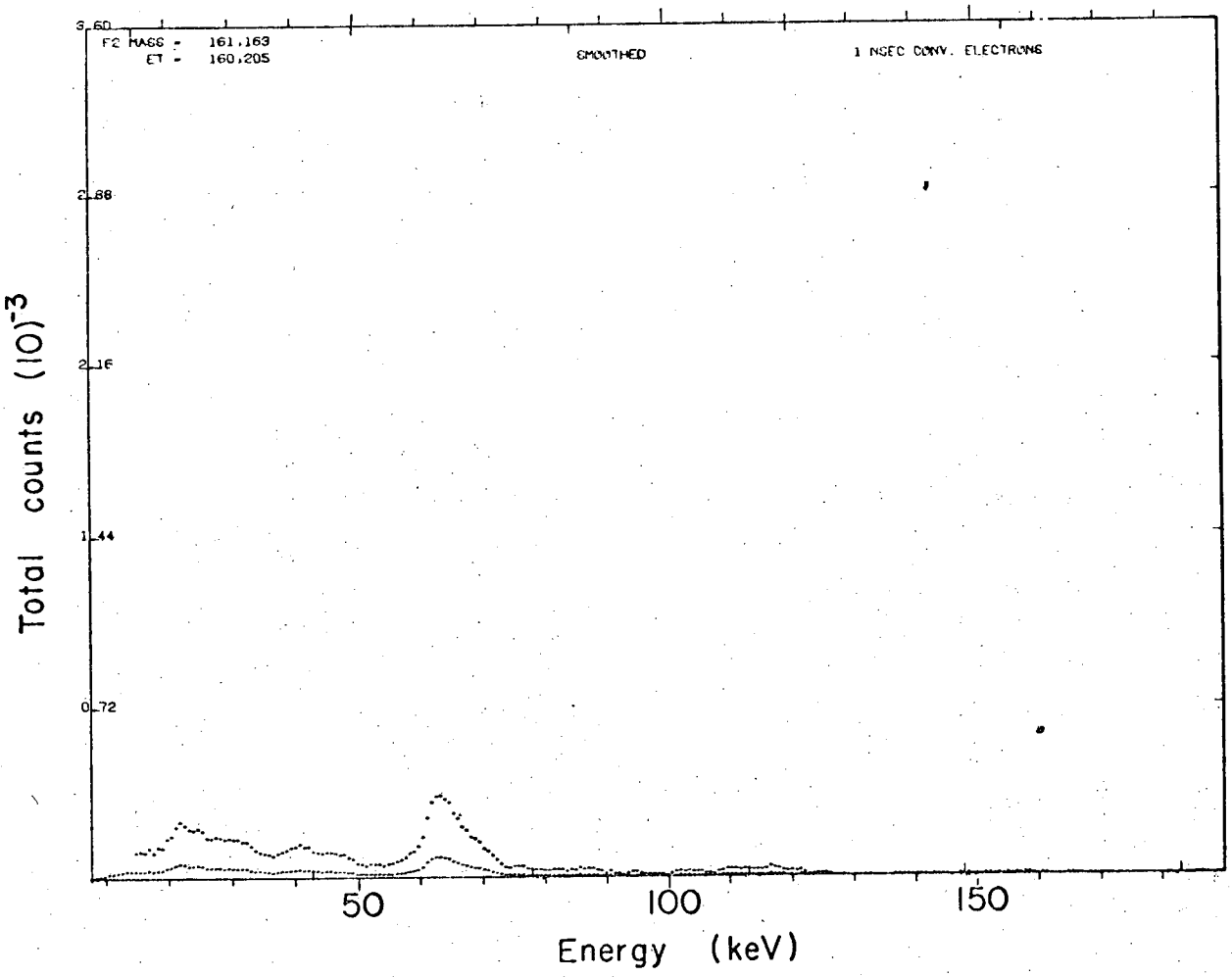
F2 MASS = 161,163
ET = 160,205
SMOOTHED
1 NSEC CONV. ELECTRONS
3.60
2.88
2.16
1.44
0.72
Total counts (10)^-3
50
100
150
Energy (keV)

Fig. VII-36

REFERENCES

1. H. R. Bowman, S. G. Thompson and J. O. Rasmussen, Phys. Rev. Letters 12, 195 (1964).
2. S. S. Kapoor, H. R. Bowman and S. G. Thompson, Phys. Rev. 140, B1310 (1965).
3. A. B. Smith, P. R. Fields and A. M. Friedman, Phys. Rev. 104, 699 (1956).
4. F. C. Maienschein, Fission Gamma-Ray Energy Release as a Function of Time After Fission, in Neutron Physics Progress Report, Oak Ridge National Laboratory Report, September 1961, p. 189.
5. H. R. Bowman and S. G. Thompson, Prompt Radiations in the Spontaneous Fission of Californium-252, in Proceedings of the Second United Nations International Conference on the Peaceful Uses of Atomic Energy, Geneva, 1958 (United Nations, Geneva, 1958), Vol. 15, p. 212.
6. S. A. E. Johansson and P. Kleinheinz, Gamma Radiation from Fission in Alpha-, Beta-, and Gamma-Ray Spectroscopy, edited by Kai Siegbahn
7. E. Elad, Nucl. Instr. Methods 37, 327 (1965).
8. M. Nakamura and R. La Pierre, A Digital Gain Stabilizer for a Multiparameter Pulse-Height-Recording System, UCRL-11494, June 1964. To be published in Nucl. Inst. Methods.
9. F. S. Goulding, Semiconductor Detectors for Nuclear Spectrometry, UCRL-16231 (1965), p. 60. To be published in Nucl. Inst. Methods.
10. E. Elad and M. Nakamura, High Resolution X-Ray and Electron Spectrometer, UCRL-16515, December 1965. To be published in Nucl. Inst. Methods.
11. F. S. Goulding, Semiconductor Detectors for Nuclear Spectrometry, UCRL-16231 (1965), p. 49. To be published in Nucl. Inst. Methods.
12. K. G. Malmfors, Arkiv För Fysik, 13 (1958), p. 237.
13. F. W. Breivogel and M. D. Holtz, Table of Kinetic Energy vs. Magnetic Rigidity for Electrons, UCRL-10494, (1962).

14. A. J. Haverfield (Lawrence Radiation Laboratory, Berkeley, California), private communication, April 1966.

15. W. Panofsky and M. Phillips, Classical Electricity and Magnetism (Addison-Wesley Publishing Co., Reading,Massachusetts; 2nd ed. 1962), p. 366.

16. P. Concus and R. L. Watson, Angular Dispersion of Coincident Fission-Fragment Trajectories Arising from a Disk Source UCRL-11965, February 18, 1965.

17. C. W. Williams, W. E. Kiker, and H. W. Schmitt, Rev. Sci. Instr. 35, 1116 (1964).

18. H. W. Schmitt, W. M. Gibson, J. H. Neiler, F. J. Walter and T. D. Thomas, in Proceedings of the IAEA Conference on the Physics and Chemistry of Fission, Salzburg, Austria, 1965 (International Atomic Energy Agency, Vienna, 1965) Vol. I, p. 385.

19. H. W. Schmitt, W. E. Kiker and C. W. Williams, Phys. Rev. 137, B837 (1965).

20. H. R. Bowman, J. C. D. Milton, S. G. Thompson and W. J. Swiatecki, Phys. Rev. 126, 2120 (1962); 129, 2133 (1963).

21. E. Takekoshi (Japan Atomic Energy Research Institute, Tokai-mura, Japan) private communication, January 1966.

22. J. Terrell, Phys. Rev. 127, 880 (1962).

23. W. E. Nervik, Phys. Rev. 119, 1685 (1960).

24. R. A. Atneosen, T. D. Thomas, W. M. Gibson, M. L. Perlman, Phys. Rev. (to be published, 1966).

25. L. E. Glendenin and H. C. Griffin, Phys. Letters 15, 153 (1965).

26. S. S. Kapoor, H. R. Bowman and S. G. Thompson, Phys. Rev. 140, B1310 (1965).

27. H. R. Bowman, University of California Lawrence Radiation Laboratory, Berkeley, California, unpublished data.

28. H. R. Bowman, S. G. Thompson and J. O. Rasmussen, Phys. Rev. Letters 12, 195 (1964).

29. H. R. Bowman, S. G. Thompson, R. L. Watson, S. S. Kapoor and J. O. Rasmussen, in Physics and Chemistry of Fission, (IAEA, Austria, 1965), p. 125.

30. L. A. Sliv and I. M. Band, in Alpha-,Beta-, and Gamma-Ray Spectroscopy, Vol. 2 edited by K. Siegbahn (North-Holland Publishing Co., Amsterdam, 1965), p. 1639.

31. S. A. E. Johansson, Nucl. Phys. 60, 378 (1964).

32. O. Nathan and S. G. Nielsson, in Alpha-,Beta-, and Gamma-Ray Spectroscopy, Vol. 2, edited by K. Siegbahn (North-Holland Publishing Co., Amsterdam, 1965), p. 651 and 652.

33. Table of Isotopes, C. M. Lederer, J. M. Hollander and I. Perlman, John Wiley and Sons, New York, 1966 (to be published).

34. L. Grodzins, Phys. Letters, 2, 88 (1962).

35. R. Vandenbosch, Physics and Chemistry of Fission, Vol. 1 (IAEA, Austria, 1965), p. 399.

36. N. Bohr, Kgl. Danske Videnskab. Selskab, Mat.-fys. Medd., 18, 8 (1940).

37. N. O. Lassen, Kgl. Danske Videnskab. Selskab, Mat.-fys. Medd., 23, 2 (1945).

38. N. O. Lassen, Kgl. Danske Videnskab. Selskab, Mat.-fys. Medd., 26, 5 (1951).

39. J. S. Fraser, J. C. D. Milton, H. R. Bowman and S. G. Thompson, Can. J. Phys. 41, 2080 (1963).

40. B. L. Cohen, Phys. Rev. 104, 1046 (1956).

41. C. C. J. Roothaan and P. S. Bagus, Methods in Computational Physics (Academic Press, New York, 1963), Vol. II, p. 85.

42. V. Fock, Z. Physik, 61, 126 (1930).

43. See for example: J. C. Slater, Quantum Theory of Atomic Structure (McGraw-Hill, New York, 1960), Vol. II.

44. D. R. Hartree, The Calculation of Atomic Structures (John Wiley and Sons, New York, 1957).

45. C. C. J. Roothaan, Rev. Mod. Phys., 32, 179 (1960).

46. C. C. J. Roothaan, L. M. Sachs, A. W. Weiss, Rev. Mod. Phys. 32, 186 (1960).

47. Eyring, Walter and Kimbal, Quantum Chemistry (John Wiley and Sons, New York, 1944), p. 355.

48. See for example: D. Strominger, J. M. Hollander and G. T. Seaborg, Table of Isotopes, Rev. Mod. Phys. 30, April 1958.

49. R. M. Eisberg, Fundamentals of Modern Physics (John Wiley and Sons, New York, 1964), p. 355.

50. J. R. Reitz and F. J. Milford, Foundations of Electromagnetic Theory, Addison-Wesley Publishing Co., Reading, Mass., 1960, p. 276.

51. A. Simon, An Introduction to Thermonuclear Research, Pergamon Press, New York, 1959, p. 35.

52. M. Tinkham, Group Theory and Quantum Mechanics (McGraw-Hill, New York, 1964), p. 162.

53. C. C. J. Roothaan, Rev. Mod. Phys., 23, 69 (1951).

54. See for example: R. Courant and D. Hilbert, Methods of Mathematical Physics, Interscience, New York, 1962.